

THESIS FOR THE DEGREE OF DOCTOR OF PHILOSOPHY

Charge-Spin Conversion and Electronic Transport in Two-Dimensional Materials and van der Waals Heterostructures

MD ANAMUL HOQUE

Department of Microtechnology and Nanoscience (MC2)

Quantum Device Physics Laboratory

CHALMERS UNIVERSITY OF TECHNOLOGY

Göteborg, Sweden 2022

Charge-Spin Conversion and Electronic Transport in Two-Dimensional Materials
and van der Waals Heterostructures

MD ANAMUL HOQUE

Göteborg, Sweden 2022

ISBN 978-91-7905-752-7

COPYRIGHT ©MD ANAMUL HOQUE, 2022

Doktorsavhandlingar vid Chalmers tekniska högskola

Ny serie Nr 5218

ISSN 0346-718X

Quantum Device Physics Laboratory

Department of Microtechnology and Nanoscience (MC2)

Chalmers University of Technology

SE-412 96 Göteborg, Sweden

Telephone: +46 (0)31-772 1000

Cover

Schematic illustrations of charge-spin conversion, nanoribbon field-effect transistor and memristor devices based on 2D materials.

Printed by Chalmers Reproservice

Göteborg, Sweden 2022

Charge-Spin Conversion and Electronic Transport in Two-Dimensional Materials
and van der Waals Heterostructures
MD ANAMUL HOQUE
Quantum Device Physics Laboratory
Department of Microtechnology and Nanoscience (MC2)
Chalmers University of Technology

ABSTRACT

Applications related to artificial intelligence (AI), 5G communication, cloud computing, Internet of Things (IoT) will necessitate wide range of data collection, communication and processing. Current charge-based technology using conventional materials suffers adverse effects with down-scaling the device size and has limited efficiency in meeting the future demands for computation and data storage. The exploration of alternative device technology along with new materials is important to enhance computing performance and energy efficiency. In this thesis, I investigated new materials for future memory and logic technologies. Recently developed 2D materials such as graphene, semiconductors, and semimetals exhibit remarkable new properties that promise faster and energy efficient non-volatile memory and logic functionalities. For non-volatile memory technologies, increasing efforts are being directed towards exploiting charge-spin conversion phenomena in high spin-orbit coupling (SOC) materials to realize all-electric magnetic memory.

Interestingly, magnetic memory devices have been demonstrated on an industrial scale; however, the moderate efficiency and fundamental limitations of the conventional materials employed limit their use in consumer electronics. This thesis addresses some of these critical challenges and presents charge-spin conversion mechanisms in layered high SOC materials such as topological insulators, semimetals, and two-dimensional (2D) materials heterostructures. At the same time, this thesis contributes in the direction of integrating memory and logic devices by investigating 2D semiconductor devices with sub-20 nm narrow channel width and memristive switching in field-effect transistors using 2D semiconductors with graphene contacts. Such 2D semiconductors have enormous prospects for next-generation high-performance and energy-efficient nanoscale field-effect transistors and integration with memory technologies. These studies of charge and spin transport in 2D materials and heterostructures can open the door for nanometer-scale memory, logic and sensing technologies.

Keywords: Spintronics, Nanotransistor, Graphene, Two-dimensional materials, van der Waals heterostructure, Charge-spin conversion, Nanoribbons, Chemical vapor deposition, Spin-orbit coupling, Proximity effect.

ACKNOWLEDGEMENTS

I am very grateful to my thesis supervisor, Prof. Saroj Prasad Dash, for giving me the opportunity to pursue my PhD study at MC2, Chalmers University of Technology and for his continuous support during this time. I am so lucky to have Saroj as my supervisor. I really liked your suggestion of having a plan B in the research approach, which helped to explore new topics.

I would also like to thank my co-supervisor, Dr. Witlef Wiecezorek, and examiner, Prof. Dag Winkler, for their prompt support during this journey. Of course, this thesis is the result of many people's enthusiastic contributions. Special thanks to Prof. Jaroslav Fabian, Klaus Zollner, Dr. Timur Shegai, Dr. Battulga Munkhbat, Prof. Andrey Turchanin, Dr. Antony George, Prof. Sergey Kubatkin and Dr. Samuel Lara Avila for the great collaboration. I am particularly grateful to Aleksandr Poliakov and Bing Zhao for the nice and productive time spent together in the clean room and for helping out with the fabrications.

I am very lucky to be able to work with great colleagues in MC2, especially in the Quantum Device Physics Laboratory. I want to express my appreciation to Prof. Avgust Yurgens, Prof. Tord Claeson, Prof. Elsebeth Schröder, Prof. Floriana Lombardi, Prof. Thilo Bauch, Prof. Attila Geresdi, Prof. Per Lundgren, Dr. Alexei Kalaboukhov and Dr. Andrey Danilov.

I am very thankful to Annika Holtringer, Debora Perlheden, Susannah Carlsson and Linda Brånell. You are the most esteemed personnel in the MC2 department.

My earnest gratitude to the cleanroom team at Myfabs, MC2, particularly Bengt Nilsson, Henrik Frederiksen, Marcus Rommel and Lars Jönsson for their cordial help in maintaining the tools for sample fabrication and measurements.

Many many thanks to my colleagues Dmitrii, Bogdan, Bing, Lars, Munis, Nerman, Richa, Navin, Annathu, Roselle, Bekmurat, Mazhar and Jakaria who introduced me to all the measurement equipment and for making MC2 an enjoyable workplace. I never felt lost at MC2 because of you!

Very grateful to Ivo and Paul for their time at MC2, especially for the chess matches and at the padel ground. I want to give a huge thanks to my friends in Gothenburg from Bangladesh for managing their time to play badminton, cricket and football every now and then.

Special love to my wife, Jerin Sultana, for being my source of strength and motivation. Thank you so much, for your support especially in the last six months of the PhD journey for not getting angry when I could not manage time for you and many other stuff. I am thankful to my parents and sisters for their endless love and moral support! I have to admit that without your support I would not have thought to complete this journey. I am very lucky to have you all in my life.

Most importantly, I want to thank Allah (SWT) for making me hopeful to pursue this PhD journey. Besides, my heartfelt gratitude to Prophet Muhammad (PBUH) and one of his best companions, Omar Bin Khattab (PBUH), for being my source of tranquility.

Last but not the least, I acknowledge the financial support from the EU Graphene Flagship (Core 3, No. 881603), Swedish Research Council (No. 2021-04821), FlagEra project H2O (funded by VR) and 2DSOTECH (VR No. 2021-05925), 2D TECH VINNOVA (No. 2019-00068), and Graphene center, EI Nano, AoA Energy and AoA Materials program at the Chalmers University of Technology.

LIST OF PUBLICATIONS

This thesis is based on the work contained in the following appended papers:

- [I] A. M. Hoque, S. Lars, B. Zhao, D. Khokhriakov, and S. P. Dash, “Room temperature nonlocal detection of charge-spin interconversion in a topological insulator”, Under review in ACSNano.
- [II] A. M. Hoque, D. Khokhriakov, B. Karpiak, and S. P. Dash, “Charge-spin conversion in layered semimetal TaTe₂ and spin injection in van der Waals heterostructures”, Physical Review Research **2**, 033204 (2020).
- [III] A. M. Hoque, B. Zhao, D. Khokhriakov, P. Muduli, and S. P. Dash, “Charge to Spin Conversion in van der Waals Metal NbSe₂”, arXiv:2205.08327 (2022).
- [IV] A. M. Hoque, D. Khokhriakov, K. Zollner, B. Zhao, B. Karpiak, J. Fabian, and S. P. Dash, “All-electrical creation and control of spin-galvanic signal in graphene and molybdenum ditelluride heterostructures at room temperature”, Communications Physics **4**, 1–9 (2021).
- [V] A. M. Hoque, V. Ramachandra, A. George, E. Najafidehaghani, Z. Gan, R. Mitra, B. Zhao, D. Khokhriakov, A. Turchanin, S. Lara-Avila, S. Kubatkin, and S. P. Dash, “Spin-valley coupling and spin-relaxation anisotropy in all-CVD Graphene-MoS₂ van der Waals heterostructure”, Under revision in Physical Review Materials.
- [VI] A. M. Hoque, A. Poliakov, A. V. Agrawal, B. Zhao, R. Mitra, S. Kubatkin, S. Lara-Avila, T. O. Shegai, and S. P. Dash, “Ultra-narrow Semiconductor WS₂ Nanoribbon Field-effect Transistors with Atomically Designed Zig-zag Edges”, Manuscript in preparation.

OTHER PUBLICATIONS NOT INCLUDED IN THIS THESIS

1. Kovács-Krausz, Zoltán, Anamul Md Hoque et al. "Electrically controlled spin injection from giant Rashba spin-orbit conductor BiTeBr." *Nano letters* 20, no. 7 (2020): 4782-4791.
2. Zhao, Bing, Dmitrii Khokhriakov, Yang Zhang, Huixia Fu, Bogdan Karpiak, Anamul Md Hoque, Xiaoguang Xu, Yong Jiang, Binghai Yan, and Saroj P. Dash. "Observation of charge to spin conversion in Weyl semimetal WTe₂ at room temperature." *Physical Review Research* 2, no. 1 (2020): 013286.
3. Karpiak, Bogdan, Aron W. Cummings, Klaus Zollner, Marc Vila, Dmitrii Khokhriakov, Anamul Md Hoque, André Dankert et al. "Magnetic proximity in a van der Waals heterostructure of magnetic insulator and graphene." *2D Materials* 7, no. 1 (2019): 015026.
4. Zhao, Bing, Bogdan Karpiak, Dmitrii Khokhriakov, Annika Johansson, Anamul Md Hoque, Xiaoguang Xu, Yong Jiang, Ingrid Mertig, and Saroj P. Dash. "Unconventional Charge-Spin Conversion in Weyl-Semimetal WTe₂." *Advanced Materials* 32, no. 38 (2020):2000818.
5. Khokhriakov, Dmitrii, Anamul Md Hoque, Bogdan Karpiak, and Saroj P. Dash. "Gate-tunable spin-galvanic effect in graphene-topological insulator van der Waals heterostructures at room temperature." *Nature communications* 11, no. 1 (2020): 1-7.
6. Khokhriakov, D., Karpiak, B., Hoque, A. M., & Dash, S. P. (2020). Two-dimensional spintronic circuit architectures on large scale graphene. *Carbon*, 161, 892-899.
7. Khokhriakov, D., Karpiak, B., Hoque, A. M., Zhao, B., Parui, S., & Dash, S. P. (2020). Robust spin interconnect with isotropic spin dynamics in chemical vapor deposited graphene layers and boundaries. *ACS nano*, 14(11), 15864-15873.
8. Zhao, B., Hoque, A. M., Khokhriakov, D., Karpiak, B., & Dash, S. P. (2020). Charge-spin conversion signal in WTe₂ van der Waals hybrid devices with a geometrical design. *Applied Physics Letters*, 117(24), 242401.

ABBREVIATIONS AND SYMBOLS

1D	One-dimensional	SCC	Spin-to-charge conversion
2D	Two-dimensional	SOC	Spin-orbit coupling
3D	Three-dimensional	SEM	Scanning electron microscope
BSTS	$\text{Bi}_{1.5}\text{Sb}_{0.5}\text{Te}_{1.7}\text{Se}_{1.3}$	SML	Spin-momentum locking
CNP	Charge neutrality point	SV	Spin valve
CSC	Charge-to-spin conversion	SHE	Spin Hall effect
CSIC	Charge-spin interconversion	SCC	Spin-charge conversion
CVD	Chemical vapour deposition	SGE	Spin-galvanic effect
DOS	Density of states	SLG	Single-layer graphene
DP	D'yakonov-Perel	STT	Spin transfer torque
EBL	Electron beam lithography	SOT	Spin-orbit torque
EY	Elliott-Yafet	TI	Topological insulator
FM	Ferromagnet	TMR	Tunnel magnetoresistance
Gr	Graphene	TB	Tunnel barrier
HS	Heterostructure	TMDC	Transition metal dichalcogenide
ISHE	Inverse spin Hall effect	TRS	Time reversal symmetry
ICSC	Inverse charge-to-spin conversion	VZ	Valley-Zeeman
IV	Current-voltage characteristic	WAL	Weak antilocalization
MR	Magnetoresistance	WL	Weak localization
MTJ	Magneto tunnel junction	Symbols	
NL	Non-local	L	Channel length
NM	Non-magnetic materials	τ_s	Spin lifetime
SB	Schottky barrier height	τ_p	Momentum scattering time
SBH	Schottky barrier height	P	Spin polarization
		P_i	Injector's spin polarization

P_d	Detector's spin polarization	ζ	Spin lifetime anisotropy ratio
σ	Conductivity	τ_{\perp}	Lifetime of out-of-plane spins
D_s	Spin diffusion coefficient	τ_{\parallel}	Lifetime of in-plane spins
D_c	Charge diffusion coefficient	θ_{SH}	Spin Hall angle
λ_s	Spin diffusion length	α	Conversion efficiency of the spin-galvanic effect
n	Carrier concentration	Δ_{EY}	Effective SOC strength of EY mechanism
n_s	Spin density	Δ_{DP}	Effective SOC strength of DP mechanism
μ	Mobility	β	Angle of the magnetic field
V	Voltage	R_{sq}	Sheet resistance of graphene
V_g	Gate voltage	λ_{IEE}	Inverse Edelstein effect length
V_{nl}	Nonlocal voltage	Constants	
E_f	Fermi energy	e	Electron charge: $e = 1.602 \times 10^{-19} \text{ C}$
v_f	Fermi velocity	ϵ	Relative dielectric constant: $\text{SiO}_2 = 3.9$
$\mu_{\downarrow\uparrow}$	Spin-dependent electrochemical potential	ϵ_0	Vacuum dielectric constant: $\epsilon_0 = 8.854 \times 10^{-12} \text{ Fm}^{-1}$
I	Bias current	h	Planck's constant
W	Channel width	\hbar	Reduced Planck's constant
ω_L	Larmor spin precession frequency	μ_B	Bohr magneton: $\mu_B = 9.274 \times 10^{-24} \text{ JT}^{-1}$
g	Landé factor		
B	Magnetic field		
B_{\parallel}	Magnetic field parallel to the easy magnetization direction		
B_{\perp}	Out-of-plane magnetic field		
T	Temperature		
λ	SOC strength		
k	Electron wave vector		

CONTENTS

Abstract	iii
Acknowledgements	v
List of publications	vii
Abbreviations and Symbols	ix
Contents	xi
1 Introduction	1
2 Concepts and theory	5
2.1 Spin-polarized electron transport in graphene	5
2.2 Spin-orbit and spin-valley coupling in 2D materials	7
2.3 Proximity-induced spin-orbit coupling in graphene and 2D van der Waals materials	9
2.4 2D semiconductors	10
3 Recent advancements	13
3.1 Advances on charge-spin conversion in 2D materials and their het- erostructures	13
3.1.1 Charge-to-spin conversion in topological insulators	14
3.1.2 Spin-charge conversion in TMDCs	15
3.1.3 Proximity-induced spin-charge conversion in graphene and 2D materials heterostructures	17
3.1.4 Proximity-induced spin-lifetime anisotropy in graphene and 2D materials heterostructures	19
3.2 2D semiconductor nano-transistors	21
4 Charge-spin conversion in layered topological insulator and semimetals	25
4.1 Charge-spin conversion in topological insulator (TI)	25
4.1.1 Device geometry and charge-spin conversion signals in TI	26
4.1.2 Asymmetric components of the charge-spin conversion Hanle signal.	27
4.1.3 Geometry and bias current dependence of charge-spin con- version signal	29

4.1.4	Gate dependence of inverse charge-spin conversion signal in TI	31
4.1.5	The inverse charge-spin conversion (ICSC) signal in TI . . .	33
4.2	Charge-spin conversion in TaTe ₂	35
4.2.1	Measurements of charge-spin conversion effects in TaTe ₂ . .	36
4.2.2	Gate dependence of charge to spin conversion signal in TaTe ₂	38
4.2.3	Bias dependence of charge to spin conversion signal in TaTe ₂	39
4.3	Charge-spin conversion in NbSe ₂	40
4.3.1	Device properties and superconductivity of NbSe ₂	41
4.3.2	Charge to spin conversion in van der Waals metal NbSe ₂ . .	42
4.3.3	Temperature dependence of charge-spin conversion in NbSe ₂	45
5	Proximity-induced spin-orbit coupling in graphene and TMDC het- erostructures	49
5.1	Proximity-induced spin-galvanic effect in MoTe ₂ -Graphene heterostruc- ture	49
5.1.1	Spin-galvanic signal in MoTe ₂ -graphene heterostructure . .	50
5.1.2	Spin-galvanic signal with perpendicular FM	53
5.2	Spin dynamics in all-CVD Graphene-MoS ₂ heterostructure	54
5.2.1	Device properties and electronic transport across the all- CVD graphene-MoS ₂ heterostructure	55
5.2.2	Spin-lifetime anisotropy in the graphene-MoS ₂ heterostructure	57
6	WS₂ nanoribbon and all-CVD MoS₂-graphene FETs	61
6.1	Ultra-narrow semiconductor WS ₂ nanoribbon FETs	61
6.1.1	Device architecture and fabrication processes of WS ₂ nanorib- bon FETs	62
6.1.2	Transport measurements of WS ₂ nanoribbon FETs	63
6.1.3	Narrow channel effects in WS ₂ nanoribbon FETs	65
6.1.4	Temperature dependence of transport properties in WS ₂ nanorib- bon	66
6.1.5	Gate and bias induced metal to insulator transition in WS ₂ nanoribbon	67
6.2	All-CVD MoS ₂ -graphene heterostructure FET	70
6.2.1	Gate tunable Schottky barrier at the all-CVD MoS ₂ -graphene heterostructure	72
7	Conclusion and Outlook	75
	References	79
	Appended papers	97

1 Introduction

In the near future, new applications associated with healthcare, agriculture, security and manufacturing industries will greatly depend on artificial intelligence (AI), 5G communication, cloud computing, Internet of Things (IoT) for a wide range of data collection, communications and computation [1–3]. These processes will dramatically increase the need for energy-efficient computing and memory technology to manage gigantic data storage and neural network-based algorithms [4, 5]. Modern computer technology uses von Neumann architecture, where the memory units are separated from the central processing unit (CPU) and these units are connected via a system bus [1, 6]. This separation of the memory and CPU constraints efficiency of modern computation for AI algorithms, known as the von Neumann bottleneck [1, 4, 5]. This is because sending data back and forth between different components imposes excessive power consumption and a time delay on the CPU by keeping it idle during data communication.

The integration of memory and logic functionalities like the brain can reduce the energy loss associated with transferring data between memory and processor units, cut the time needed for computing operations and shrink the amount of space required on chips [4, 7, 8]. In the brain, neurons are connected via synapses and communicate with electrochemical impulses (synaptic weight). These synaptic weights are modifiable by electrochemical impulses and serve as memory functionality, data communication for the brain’s cognitive activities [9]. Brain-inspired computation (known as neuromorphic computation) can outperform modern computers in energy efficiency, speed and self-learning functionalities by locally storing data and processing it ad hoc [1, 4, 10]. Current computation device, such as field effect transistor (FET), is unsuitable to combine logic and memory functionality locally in compact device design. Hence, the integrated circuits (ICs), fabricated with traditional materials, used so far have limited efficiency in meeting the future demands in computing performance and energy consumption [11, 12]. On the other hand, recently developed 2D materials such as graphene, semiconductors, and semimetals exhibit remarkable new properties that promise to overcome the issues of non-volatile memory and logic functionalities [13–15]. These materials demonstrate prospects to fabricate compact devices for compute-in-memory applications like the brain’s neurons and synapses.

Besides, modern FET technology also suffers from down-scaling issues [16, 17]. The basic building block of modern computation and memory technology is conventional materials (Silicon) based FET for about the last five decades. This

current human era is, therefore, coined as the “Silicon Age” (also known as Digital Age or Information Age) [18, 19]. It has been a remarkable journey for the transistor technology that has emerged from few thousand in the 1970s to a few billion units in 2020s in the IC owing to mainly down-scaling techniques by adopting modern fabrication facilities, like updated lithography techniques, silicon-germanium channel, high-K dielectrics, vertical “fins” (FINFET) [20–22]. These transistor scaling eras were triggered mainly by Moore’s law in conjunction with Dennard’s guidelines, which infer the transistors in IC double every two years by reducing their dimension with constant power density due to down-scaling the operating voltage and current of the transistors with its size [23, 24]. Interestingly, the operating voltage and current of the FET do not downscale as predicted because smaller transistors with reduced channel length and thinner oxide layers become prone to leakage current. As a result, the power density in IC increases with the shrinking transistor’s dimension. High-k dielectric, protruding channel into 3D “fins” in FINFET helped further scaling the transistor in the post-Dennard era (after 2005). For instance, the current state-of-the-art sub 10nm technology node has a fin width of 7nm and gate length of 18nm with an operating supply voltage of around 0.6V [25]. Further scaling will need advanced fabrication technologies that will eventually increase the price of ICs. It has been predicted that current silicon-based (conventional bulk materials) technology node transistor will continue to scale until 2025, aided by extreme UV lithography (EUV), innovative fabrication processes such as buried power rails, and design technology co-optimization in the back-end-of-line (BEOL) and front end-of-line (FEOL) in IC fabrication [16, 26, 27]. Concurrently, to continue scaling and enhancing the performance of FETs and memory devices to meet the demand will necessitate further decreasing of the FET’s footprint by fabricating gate-all-around (GAA) FET based on nanosheets [28]. These new proposals based on 3D materials render critical fundamental challenges like dangling bonds and surface roughness in the sub-5nm node, leading to substantial degradation of charge carrier mobility due to strong charge carrier scattering [17]. There is a critical limit for FET-scaling with conventional 3D materials, e.g., Si, Ge. Hence, alternative device architectures and new nanoscale materials are crucial for near-future computation and memory chips [13, 29–32].

Spintronics is considered an emerging field that utilizes the spin quantum property (magnetic moment) of the charge carriers for next-generation nanoelectronic devices compatible with compute-in-memory implementations [33]. The spin degree of freedom of the charge carriers (electrons or holes) in conjunction with the charge property can provide a suitable platform for low power and faster data encoding and processing applications, including neuromorphic computing [4, 34, 35]. Spintronics allow to engineer the device architecture for different functions, like logic and memory, using similar materials. The spintronics research field flowered after the discoveries of giant magnetoresistance (GMR) and tunnel magnetoresis-

tance (TMR) effects with subsequent uses in the hard disk drive, magnetic sensors, actuators and non-volatile memory devices [36]. Current spintronic devices are fabricated by stacking dozens of conventional 3D magnetic (Co, Ni, CoFeB) and non-magnetic (e.g., oxide barrier) materials [37–39]. To illustrate, non-volatile magnetic random-access memories (MRAMs) are fabricated as magnetic tunnel junctions (MTJs), where spin-transfer torque (STT) and spin-orbit torque (SOT) mechanisms are used to store the information. Improving these devices using conventional materials for versatile applications poses crucial challenges since the ultrathin interfaces intermix in the stack during annealing and greatly influence the device’s performance [15, 40]. Furthermore, these devices below 20nm node consume high power density, lack thermal stability, and suffer from physical and chemical damages on the cell side wall during patterning. Therefore, the exploration of new materials is ever more important for future spintronic devices.

Interestingly, two-dimensional (2D) materials host a vast range of charge, spin and orbital physics that can be used and combined in van der Waals (vdW) heterostructures with atomically smooth interfaces down to atomic layers for both spintronic and FET applications [17, 41–43]. 2D materials constitute a plethora of electronic properties like metallic, semimetallic, semiconducting, insulating, ferromagnetic, topological and are atomically thin in monolayer form including smooth interfaces without dangling bonds and surface roughness [30, 44]. Besides their fascinating intrinsic properties, these materials can be stacked together in appropriate functionalities and orientations in vdW heterostructure to engineer artificial materials via the proximity or interface effects [45–47]. To get the benefits of these novel 2D materials, substantial investigations need to be carried out to identify the most potential candidates for a future spin and charge-based commercial devices. The key challenges for low-power all-electric spintronic memory and logic devices using 2D materials and their vdW heterostructures are the generation, detection, transport, and manipulation of spin-polarized signals [41, 45].

For spin-based FET and non-volatile memory technologies, increasing efforts are being directed towards exploiting the charge-spin conversion phenomena in high spin-orbit coupling (SOC) material to create spin-orbit torque (SOT) magnetization switching of an adjacent ferromagnet [40, 48]. SOT-based magnetic memory devices have been demonstrated on an industrial scale; however, the moderate efficiency and fundamental limitations of the conventional materials employed limit their use in consumer electronics [39]. This thesis addresses some of these critical challenges and investigates charge-spin conversion mechanisms in high SOC materials such as topological insulators, semimetals, and 2D materials heterostructures.

The following chapter, (chapter 2), provides some fundamental concepts on spin and charge transport mechanisms in 2D materials that are used to discuss the presented results in this thesis. Chapter 3 discusses the recent advancements

in spin and charge transport phenomena in 2MDs and their vdW heterostructures. Next, we present the findings on layered topological insulator (TI) and TMDCs for robust spin generation and detection effects at room temperature in Chapter 4 using charge-spin conversion processes. We take advantage of the remarkable spin transport properties of graphene to explore such functionalities in TI and TMDCs by fabricating vdW heterostructure spintronic devices [49]. We demonstrate that the properties of these 2D materials can be used as non-magnetic spin-sources in spintronic devices. Next, we show the spin manipulation functionalities of MoS₂ in a graphene spin channel at room temperature owing to the proximity-induced spin-valley coupling property in Chapter 5. Furthermore, the proximity-induced spin-galvanic effect in MoTe₂ and graphene heterostructures is presented in the same chapter. The proximity-induced SOC effects can be harnessed for spin filtering, gate-dependent spin manipulation and charge-spin interconversion (CSIC) processes in spin-logic, memory and spin-valleytronics devices.

Additionally, 2D semiconducting TMDCs have enormous prospects for next-generation high-performance and energy-efficient nanoscale FET technology by extending the FET-scaling down to atomically thin monolayer (sub-1 nm) [13, 30–32]. However, atomic-scale control of their nanostructures has been challenging. This thesis also contributes to the direction of integrating memory and logic devices by investigating FETs using 2D semiconductors with nanoribbon channels and with graphene contacts to realize memristive switching. Importantly, controlling edge structures in nanoribbons is one of the main interests because electronic properties of the edge-states become increasingly relevant in such nanoscale transistors [50–52]. In chapter 6, we present the charge transport properties of 2D semiconducting FETs with sub-20 nm narrow channel width.

Furthermore, memristive switching-based random access memory (RRAM) promises to perform computation-in-memory for AI algorithms without moving the data between CPU and memory units [10]. Memristive switching in semiconducting 2D material (MoS₂) is realized with conventional 3D contact materials (Au) [53, 54]. For flexible and energy efficient large area applications, memristive switching in all CVD 2D materials is highly sought-after phenomenon. We show gate-tunable memristive-switching in all-CVD MoS₂ FET with graphene contacts in chapter 6. Finally, in chapter 7, we conclude the experimental results and discuss future outlooks to study spin and charge transport properties in 2D materials. These studies of charge and spin transport properties in 2D materials and their heterostructures have prospects to be used in future nanometer-scale memory, logic and sensing technologies.

2 Concepts and theory

This chapter provides some fundamental concepts on spin and charge transport mechanisms in two dimensional (2D) materials that are used to discuss the presented results in the following chapters. The first section highlights different spin signals in graphene and parameters extracted from these signals like spin polarization, spin lifetime, spin diffusion length. In the second section, spin-orbit and spin-valley coupling, different charge-spin interconversion (CSIC) techniques such as, spin-Hall effect (SHE), Rashba Edelstein effect (REE) and their inverse effects are discussed. The final section briefly introduces the charge transport properties in 2D semiconducting materials.

2.1 Spin-polarized electron transport in graphene

Ferromagnetic (FM) electrodes, such as cobalt and nickel are used as spin source materials to inject and detect spin-polarized carriers in a graphene channel [49]. Electrical spin injection and transport in graphene are usually studied by non-local measurements geometry (Fig. 2.1a). In this measurement geometry, the spin injection current probe (I) is separated from the spin detection voltage probe (V) to avoid spurious effects from electron's charge and FM contacts like anisotropic magnetoresistance (AMR) [56, 57]. Spin-polarized current is injected from FM contact into the graphene channel and diffuses towards the detector circuit. The spin population from the injector FM decreases exponentially with the distance during the diffusion process. The spin chemical potential for up (blue) and down spin (red line) is illustrated by the band diagram in Fig. 2.1b. The voltage probe (V) measures the potential difference ($\Delta\mu_{\downarrow,\uparrow}$) of the corresponding spin chemical potential aligned with the detector's magnetization in relation to the neutral chemical potential (dash line) [58, 59].

A changing in-plane magnetic field (B_y) switches the relative magnetization of the injector and detector FM electrodes from parallel to antiparallel orientation, and renders a non-local spin valve (NLSV) signal, as shown in Fig. 2.1c. Besides, varying out-of-plane magnetic field (B_z) manifests the Hanle spin precession signal (Fig. 2.1d) while keeping the magnetization of the detector FM contact along the in-plane orientation. B_z induces spin precession in addition to diffusion and dephasing, which results in a reduction of the spin signal as the detector probes only the projection of the spin orientation onto the FM contact. If the injected spin is parallel to the detector's FM magnetization (Fig. 2.1a), the Hanle signal is

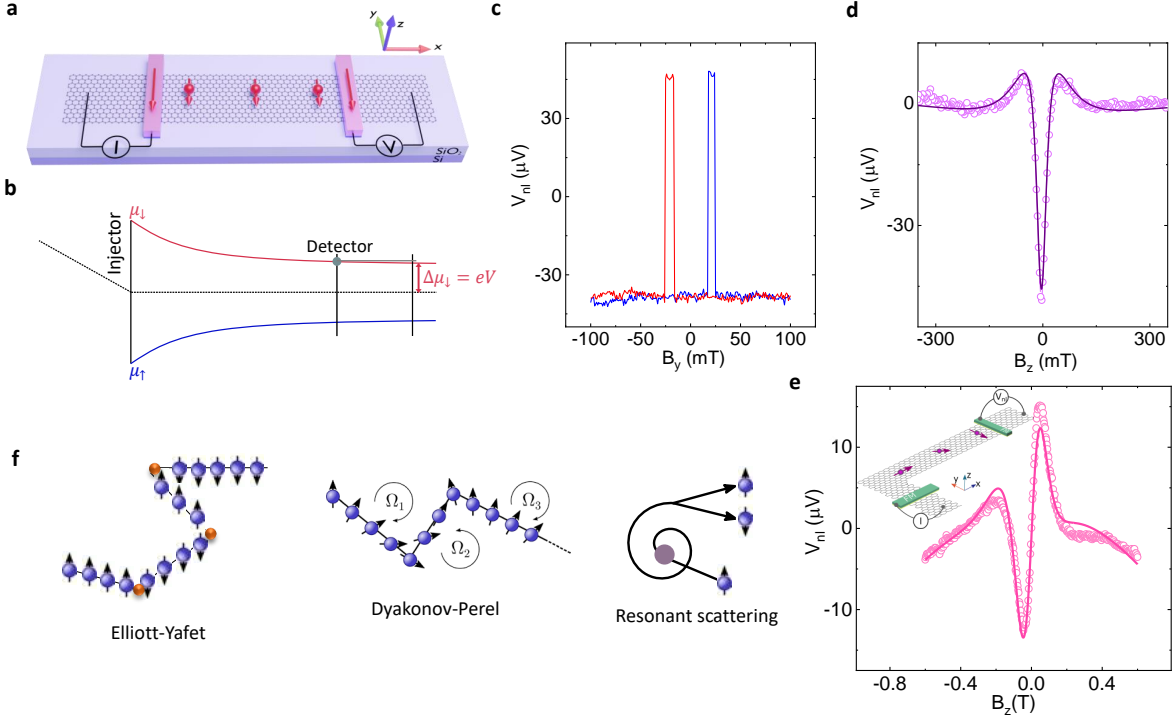


Figure 2.1: Non-local spin transport in graphene. (a) Measurement configuration for non-local spin transport in graphene, where injector current probe (I) and detector voltage (V) probe are separated. Ferromagnetic contacts are used to inject and detect spin-transport properties in the graphene channel. (b) Band diagram to show chemical potential for up (blue) and down (red) spin in the channel in the diffusive transport regime. (c) Non-local spin valve signal as a function of changing in-plane magnetic field (B_y). (d) Non-local Hanle spin precession signal by changing out-of-plane magnetic field (B_z). (e) Non-local antisymmetric Hanle spin precession signal by changing out-of-plane magnetic field (B_z) for the measurement geometry shown in the inset. (f) Pictorial illustrations for dominant spin scattering mechanisms in graphene, e.g., Elliot-Yafet, Dyakonov-Perel, and resonant scattering (adapted from ref. [49, 55]).

symmetric (Fig. 2.1d). On contrary, when the injected spin is perpendicular to the detector's FM magnetization (Fig. 2.1e inset), the Hanle signal is antisymmetric (Fig. 2.1e).

The symmetric and antisymmetric Hanle signals can be fitted to the following equation to get spin transport parameters in the channel [58, 59].

$$V_{NL}^{sym}(B_{\perp}) \propto \int_0^{\infty} \frac{1}{\sqrt{4D_s t}} e^{-L^2/4D_s t} \cos(\omega_L t) e^{-t/\tau_s} dt \quad (2.1)$$

$$V_{NL}^{asym}(B_{\perp}) \propto \int_0^{\infty} \frac{1}{\sqrt{4D_s t}} e^{-L^2/4D_s t} \sin(\omega_L t) e^{-t/\tau_s} dt \quad (2.2)$$

Here, D_s is the spin diffusion coefficient, τ_s is the spin lifetime, L is the channel length and $\omega_L = g\mu_B B_z/\hbar$ is the Larmor spin precession frequency, where g is

the Landé g-factor and μ_B is the Bohr magneton. The spin diffusion length ($\lambda_s = \sqrt{D_s \tau_s}$) in the graphene channel could also be extracted using (2.1) [60].

Using the spin transport parameters from the Hanle signal measurements, the polarization of the FM contacts can be calculated using the following equation [58]:

$$\Delta V_{NL} = \frac{P_{FM}^2 R_{\square} I \lambda_s}{W_{Gr}} \exp\left(\frac{-L}{\lambda_s}\right), \quad (2.3)$$

where ΔV_{NL} is the amplitude of the non-local signal, R_{\square} and W_{Gr} are the sheet resistance and the width of the graphene channel, respectively, λ_s is the spin diffusion length of the graphene channel and L is the channel length [58]. Here, it is assumed that both injector and detector FM contacts have identical polarizations. Using equation 2.1 and 2.3, we estimated $\tau_s = 320\text{ps}$, $D_s = 0.03\text{m}^2\text{s}^{-1}$, $\lambda_s = 3.34\mu\text{m}$ and $P_{FM} = 15\%$ for CVD graphene on SiO_2 substrate.

During the diffusion process, spin transport in graphene is mainly governed by three main scattering mechanisms, as illustrated in Fig.2.1f. The Elliot-Yafet (EY) mechanism originates from spin-orbit coupling that scatters spin during momentum scattering (τ_p) events, thus $\tau_s \propto \tau_p$ [49]. Interestingly, Dyakonov-Perel (DP) spin-relaxation mechanism also originates from SOC due to breaking inversion symmetry, which leads to spin-split bands. The induced SOC acts as an internal magnetic field that induces precession of the electron's spin and thus, scatters spin [55]. Unlike EY, spin relaxation is $\tau_s \propto \tau_p^{-1}$ for DP mechanism. Moreover, magnetic moments from adatoms in graphene can also lead to additional resonant spin relaxation mechanisms by inducing spin-flip exchange interaction [49]. At the resonant condition, the electron is trapped at the impurity site and precesses along the magnetic moment. While escaping from the site, there is an equal probability to flip the spin or maintain the same spin orientation. According to theory, including EY and DP spin relaxation mechanisms, graphene should demonstrate $1\mu\text{s}$ of a spin lifetime that is two orders of higher than the experimentally realized (10ns) on exfoliated graphene on hBN substrate [61]. However, resonant scattering yields a spin lifetime of few 100ps, which is usually observed in graphene in SiO_2 substrate [61]. With the above-mentioned scattering phenomena, commercial CVD-graphene exhibits excellent long-distance spin transport properties, reaching $34\mu\text{m}$, stems from the high carrier mobility [62, 63]. Recently, all-electric universal and reprogrammable spin logic is demonstrated at room temperature using CVD graphene with FM electrodes [64].

2.2 Spin-orbit and spin-valley coupling in 2D materials

2D materials with high spin-orbit coupling (SOC) properties have received considerable attention for spintronic applications, mainly for charge-spin interconversion

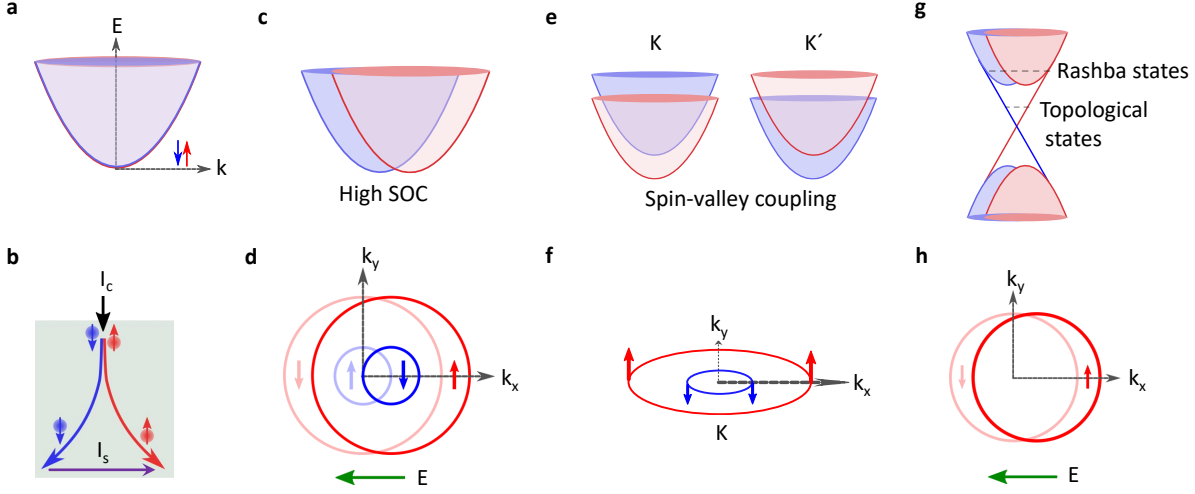


Figure 2.2: Spin-orbit and spin-valley coupling in 2D materials. (a) Spin degenerate band diagram for a free electron with opposite spins. (b) Spin Hall effect in high SOC materials, where spin current (I_s) is created due to transverse charge current (I_c). (c) Band diagram with high SOC with Rashba spin-split bands where spin-degeneracy is lifted. (d) Electric field (E)-induced generation of the spin population in the Rashba spin-split bands. (e) Spin-split bands in K and K' valleys due to spin-valley coupling. (f) Out-of-plane spin polarization in the K valley. (g) Band diagram to illustrate topological bands in the gap-less surface states and non-topological Rashba states in the bulk due to band inversion from strong SOC. (h) Electric field-induced spin polarization in the surface states.

(CSIC) and spin modulation processes [45]. A free electron in the materials with negligible SOC maintains time reversal and inversion symmetries, promoting spin-degenerate band structure (Fig. 2.2a), e.g., graphene [65]. The high SOC in the materials breaks these symmetries that results in spin dependent scattering in the system, which can be utilize for CSIC processes. A charge current can create a transverse spin current (Fig. 2.2b) owing to spin-Hall effect (SHE), or its inverse effect (ISHE)-where spin current produces an orthogonal charge current [66]. Furthermore, high SOC also leads to Rashba spin-split band structure with lifted spin-degeneracy (Fig. 2.2c) [67]. The materials (BiTeBr) with Rashba spin-split bands can engender spin-polarized current upon the application of electric field (E) via Rashba-Edelstein effect (REE), as shown in Fig. 2.2d [68].

Charge carriers in 2D MoS₂ exhibit valley degree of freedom aided by spin-valley coupling that shift spin-degenerate bands towards energy axis analogous to Zeeman effect (Fig. 2.2e) [67, 69]. The spin orients towards perpendicular to the monolayer plane (Fig. 2.2f), which can be used as spin-filter or polarized light-induced generation of spin-population. Moreover, band inversion in topological insulators leads to topologically protected surface states along with Rashba states (Fig. 2.2g). The surface states are spin-polarized such that spin orientations are locked to their momenta that results in topological spin-momentum locking

(TSML) properties features. Charge carriers in TI depending on the Fermi surface can have a winding spin texture for both Rashba states and TSML, which will be offset from the equilibrium position by the additional electron momentum that is caused by an applied electric field (Fig. 2.2h)[70].

2.3 Proximity-induced spin-orbit coupling in graphene and 2D van der Waals materials

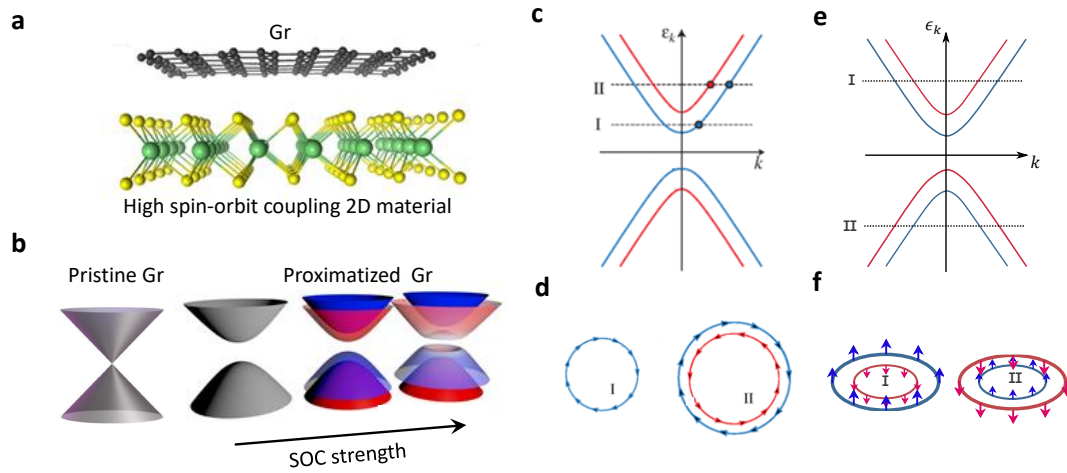


Figure 2.3: Proximity-driven spin-orbit coupling in van der Waals heterostructures (a) Heterostructure device geometry of graphene and high SOC materials, such as MoS_2 , WSe_2 . (b) Evolution of Gr band diagram due to proximity SOC, showing orbital-gap, trivial spin-split bands and non-trivial spin inversion bands, adapted from ref. [71]. (c) Proximity-induced Rashba spin-split bands in Gr. (d) Spin-windings for regions I and II shown in c (adapted from [72]). (e) Proximity-induced Zeeman spin-split bands in Gr. (f) Spin-windings for regions I and II shown in e.

2D materials and their der Waals (vdW) heterostructures have the ability to manipulate spin transport properties using proximity effects [33, 41, 73]. For instance, graphene (Gr) is well-known for long-distance spin transport due to its low spin-orbit coupling (SOC) [62], which preclude the ability to manipulate spin-orientation therein. Significant efforts have been made to enhance SOC in Gr to realize gate-tunable spintronic functionalities. One way to achieve sizable SOC in Gr is by employing chemically-adsorbed heavy adatoms; however, doping can introduce defects in Gr and compromise the fascinating electronic properties [74]. Alternatively, the vdW heterostructures of Gr with high-SOC 2D materials, such as transition metal dichalcogenides (TMDCs), magnetic insulators ($\text{Cr}_2\text{Ge}_2\text{Te}_6$), and topological insulators (TI), have emerged as a promising platform for proximity-induced SOC, while preserving their electronic properties [45].

Pristine monolayer Gr exhibits linear dispersion in the energy spectrum due to Dirac fermions, resulting high carrier mobility (Fig. 2.3a, b) [75]. First principle calculations show that Gr in proximity to high SOC breaks inversion symmetry that induces a spin-degenerate orbital gap in graphene [71, 76]. In addition to that, high SOC materials imprint Rashba and valley Zeeman spin-split bands in graphene (Fig. 2.3a, b) [71, 72]. Further increasing SOC strength can lead to topological non-trivial band inversion [77]. These proximity-induced Rashba, valley-Zeeman and Ising SOC in graphene are explored experimentally by weak anti-localization (WAL), spin relaxation anisotropy, penetration field capacitance measurements [78, 79].

The Rashba SOC in Gr orients the spin toward the in-plane direction, whereas, the valley-Zeeman and Ising SOC turn the spin polarization out-of-plane direction [72, 80]. Proximity-induced Rashba spin-split band structure in Gr is shown in Fig. 2.3c. The spin winding bands for regions I and II (denoted in Fig. 2.3c) are depicted in Fig. 2.3d. Note that proximity-induced Rashba SOC has similar spin-split bands for electrons and holes that can lead to gate-dependent sign change of charge-spin conversion signals. Figure 2.3e shows the spin-split bands in Gr due to the proximity-induced valley-Zeeman effect. In this case, the spin windings for the conduction band (I) and valance band (II) are opposite orientation (Fig. 2.3f).

2.4 2D semiconductors

There are enormous interest in two-dimensional (2D) semiconducting transition metal dichalcogenides (TMDCs), such as MoS₂, WS₂ for a wide range of potential applications [17, 32]. In addition to direct band-gap semiconductors, dangling-bond-free surfaces, atomically thin bodies, and ultrahigh optical absorption coefficients make them potential candidates for next-generation field-effect transistors, tunnel transistors, rectifiers, light-emitting diodes, and solar energy harvesting devices [83–86]. Devices with 2D semiconducting TMDCs are fabricated with conventional 3D materials and render high contact resistance [87]. Furthermore, 2D semiconductor exhibit bias and gate-induced metal-to-insulator transition due to percolation transport mechanisms [82]. This section is dedicated to discussing the junction between 2D TMDCs and contact electrodes, and the percolation transport processes.

The contacts on 2D semiconductor materials play an important role to define the device performances [87, 88]. 2D semiconductors form Schottky contact with metal electrodes increase the contacts resistance and decrease carrier transport. The Schottky contact renders an energy barrier and emerges due to the mismatch of the band alignment between 2D TMDC semiconductor's electron affinity and work-function of the metal with respect to the vacuum level (Fig. 2.4a, b) [89]. Electrons need to surmount this energy barrier, termed as Schottky barrier (SB),

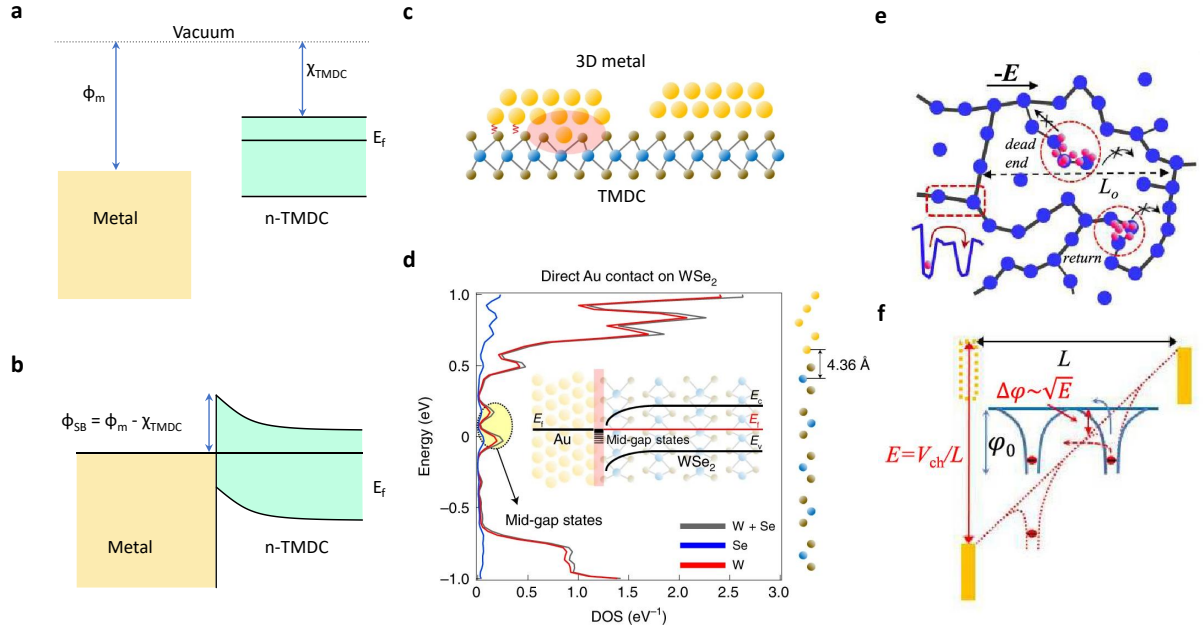


Figure 2.4: Contact properties and metal-insulator transition in 2D semiconductors (a) Band diagram of metal electrode and n-TMDC semiconductor material before making any contact between them. ϕ_m and χ_{TMDC} indicate the work function of metal and electron affinity in TMDC with respect to vacuum level, respectively. (b) The formation of Schottky barrier ($\phi_{SB} = \phi_m - \chi_{TMDC}$) in the metal and TMDC interface [81]. (c) Pictorial illustration to show the defects associated to direct metal deposition on TMDC and interface with vdW contact. (d) Density functional theory calculations of density of states of WSe₂ with direct Au contact and the inset shows the Fermi level pinning effect from gap-states in TMDC. (e) Percolation transport in the presence of charge traps that lead to bias and gate-induced metal-insulator transition. (f) Effect of bias voltage to deform potential barrier and enhance carrier transport. (c,d) are adapted from ref. [81] and (e,f) are from ref. [82].

for transport to the TMDC material. SB is defined by the Schottky-Mott rule and can be estimated by the thermionic emission model, as given below [90, 91].

$$I_{ds} = AT^{3/2} \exp \frac{-q\phi_{SB}}{k_b T} \left(1 - \exp \frac{-qV_{ds}}{k_b T} \right), \quad (2.4)$$

To minimize the SB, low work-function materials (Ti, Sc) are preferred with n-type TMDC to lower the barrier and facilitate electron transport [92], but these metals also give rise to Fermi level pinning due to dislocation, defects and interface gap-states (Fig. 2.4c) [81, 85]. Density functional theory (DFT) calculations of the electronic band structure of direct Au contact on TMDC (WSe₂) clearly show the emergence of gap-states in TMDC due to penetration of metallic states into the TMDC (Fig. 2.4d) [85]. Instead of direct deposition of the metals on TMDC, vdW electrodes and semimetallic contacts (Bi, graphene) on TMDC can alleviate Fermi-level pinning and interface gap-states [81, 93].

Surprisingly, semiconductor TMDC shows metal-to-insulator transition (MIT) with bias (V_{ds}) and gate-voltage (V_g) due to percolation transport process [82, 94, 95]. The percolation transport can be explained by considering charge trap centers (dead end, return sites in Fig. 2.4e) due to structural impurities in the 2D TMDC and from the highly interactive substrate [96]. These trap centers act as coulomb potential barrier for the charge carriers in the material. Increasing carriers with V_g screens these potential barriers and enhances carrier transport. Furthermore, applying an electric field (E) between source-drain contacts (V_{ds}) also lowers the height of the potential barrier that increases hopping conduction in channel (Fig. 2.4f). In this condition, the 2D TMDC exhibits bias-induced metallic properties with temperature [82].

3 Recent advancements

Two-dimensional (2D) materials are very promising for the charge-spin interconversion (CSIC) effects since they host high SOC and broken symmetries. In addition, 2D materials in van der Waals (vdW) heterostructures are prominent candidates for proximity-induced spin-orbit coupling (SOC), which can be used for spin modulation in the channel and CSIC processes. Substantial milestones have been achieved in the field of 2D materials-based CSIC processes in the last few years by exploring new materials and vdW heterostructures. These advances are categorized into three main sections in this chapter. First, we address the recent experimental advances in CSIC processes followed by proximity-induced SOC in 2D materials and their heterostructures for spintronics applications. In addition, semiconducting 2D materials have attracted tremendous interest due to atomically thin thickness for next-generation nanoscale transistors for logic, memory and sensor applications. This chapter finally discusses the recent experimental achievements of 2D materials-based ultra-narrow and vdW heterostructure transistors.

3.1 Advances on charge-spin conversion in 2D materials and their heterostructures

CSIC consists of two processes, which are charge-to-spin conversion (CSC) and its inverse effect, spin-to-charge conversion (SCC) or inverse charge-to-spin conversion (ICSC). CSC (SCC) is the process to generate (detect) spin-current or -accumulation by charge (spin) current. These processes are the cardinal aspects for all electric spintronic devices because they allow control of charge and spin properties in the materials electrically, without using a magnetic field [97]. The CSIC processes can emerge in materials and heterostructures due to the spin Hall effect (SHE) in bulk, the Rashba-Edelstein effect from the spin-split bands and the topological spin-momentum locking (TSML) feature of the surface states (SS) in topological materials [45]. We start this section by presenting a critical summary of the recent experimental progresses made on CSIC effects in layered topological insulators (TI) and their vdW heterostructures. Thereafter, the recent experimental landmarks on CSIC effects in 2D TMDCs and their vdW heterostructures are discussed.

3.1.1 Charge-to-spin conversion in topological insulators

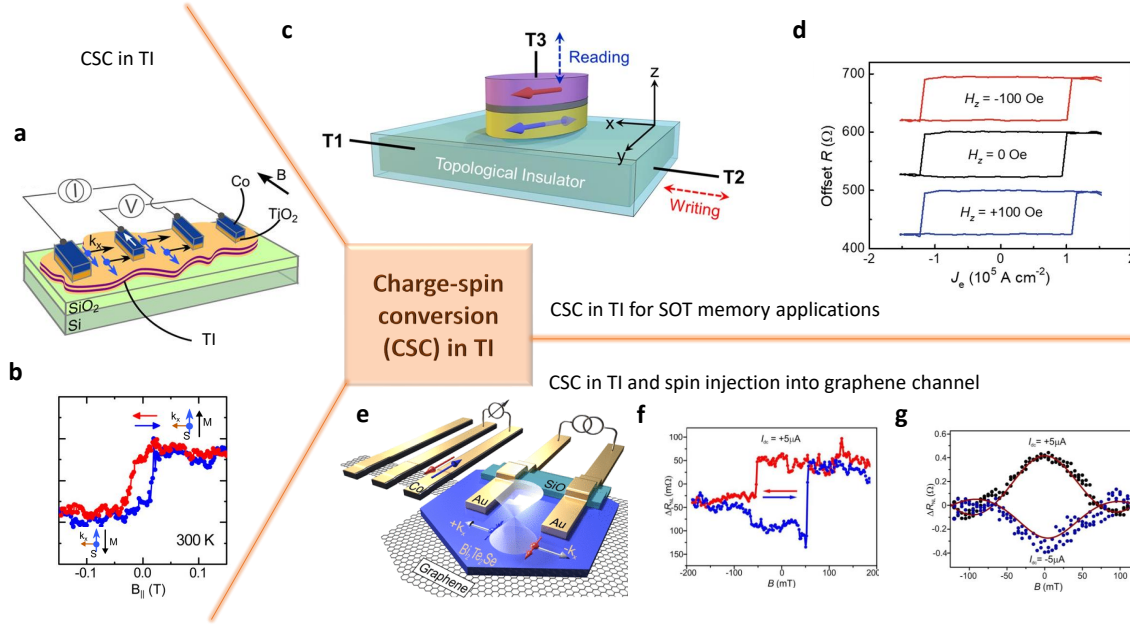


Figure 3.1: Charge-to-spin conversion (CSC) in TI. (a) Schematic of device structure along with potentiometric measurement geometry to measure the current-induced spin-polarization in TI. (b) Characteristic hysteretic switching of the CSC effect in Bi₂Se₃ TI with varying external B field at room temperature. (c) Sketch of a SOT-MRAM device using a TI and magnetic tunnel junction (MTJ) cell along with 3-terminal (3T) electrical connections. (d) Current-induced SOT switching for deterministic switching mechanism with and without external field. (e) Schematic with electrical connections in graphene-TI heterostructure for creation, injection and detection of CSC in TI. (f) Characteristic non-local spin-switch hysteretic signal for spin creation and injection from TI into graphene channel with a varying in-plane B field. (g) Hanle spin precession measurements at Low temperature ($T = 1.3$ K) for positive and negative bias currents. (a), (b) are adapted from [98]; (c), (d) are adapted from [99]; (e), (f), (g) are imported from [100].

The CSC effects in TIs have been investigated using ferromagnetic (FM) tunnel contacts on the TI in potentiometric measurements (Fig. 3.1a) up to room temperature [98, 101–106]. A varying in-plane external magnetic (B) field results in characteristic hysteretic spin-switching of the CSC signal (Fig. 3.1b) in TI. The applied B field switches the magnetization of the detector's FM contact and detects current-induced CSC signal supposedly due to TSML from the SS in TI. However, the background voltage in local measurement geometries and TI/FM interfaces raise concerns about the actual origin of the measured signals, and detailed control experiments have to be conducted [107].

The high SOC properties in TIs can be used to switch the magnetization of an adjacent FM material by CSC effect owing to the spin-orbit torque (SOT) mechanism [108]. This SOT-based switching is considered the leading candidate

for ultra-low power memory and logic devices. A Schematic of a TI-based SOT-driven MRAM cell is presented in Fig. 3.1c with three terminal (3T) measurement connections [99]. In this measurement configuration, the writing current is applied in TI (between T1 & T2 contacts) to switch the magnetization of the adjacent soft FM layer (yellow layer) using SOT mechanism. The reading process is carried out between T1 and T3 contacts using the tunneling magnetoresistance (MTR) effect in the MTJ cell. Figure 3.1d shows current-induced SOT switching for the deterministic switching mechanism without having any effect from the external field, i.e., field-free switching. TI-MTJ based SOT switching is observed in both MBE and sputtered devices, which is compatible with industrial applications with large charge-spin conversion efficiency [99].

In addition to the switching effect, current-driven spin polarization due to the CSC effect in TI can be injected in a vdW graphene channel for long-distance spin transport, useful for future all 2D materials-based in-chip memory and logic applications [41, 42]. Figure 3.1e presents a schematic with electrical connections of a graphene-TI ($\text{Bi}_2\text{Te}_2\text{Se}$) vdW heterostructure for the creation of spin polarization in TI and later, injecting and detecting spin polarized carriers in the graphene channel using FM electrode in non-local measurement geometry [100]. The non-local (NL) measurement geometries enable the measurement of pure spin currents without any artifacts from charge current contribution [49, 109]. Spin-valve (SV) and Hanle spin-precession measurements are successfully reported as depicted in Fig. 3.1(f, g) in TI-graphene vdW device. However, the measured NL spin signals were only detected at very low temperatures up to $T = 15\text{K}$ [100], limiting its practical applications.

3.1.2 Spin-charge conversion in TMDCs

Two-dimensional (2D) transition metal dichalcogenides (TMDCs) are ideal hosts for realizing current-driven spin-polarized electronic states due to the high SOC accompanied by broken symmetries in the crystal structure. Recently, layered TMDCs (WTe_2 , MoTe_2 , NbSe_2 , MoS_2 , TaTe_2) have paved the way for utilizing various CSIC processes (spin Hall effect, Rashba-Edelstein effect) for SOT applications up to room temperature [110, 114–118]. Moreover, exerted out-of-plane torque in the lower symmetric crystals can enable field-free perpendicular magnetization switching for high-density magnetic memory and logic devices. Schematic of a device structure of WTe_2 /Permalloy (Py) heterostructure for SOT applications has been shown in Fig. 3.2a [110]. Spin torque ferromagnetic resonance (ST-FMR) experiments in WTe_2 /Py heterostructure device for opposite applied B field directions (40° & 220°) are shown in Fig. 3.2b. The output voltages [$V_{\text{mix}}(40^\circ)$ and $-V_{\text{mix}}(220^\circ)$] substantially differ, revealing that the reduced WTe_2 crystal symmetry has significant influence in current-driven torques, unlike heterostructures of 3D materials (Pt/Py) [110].

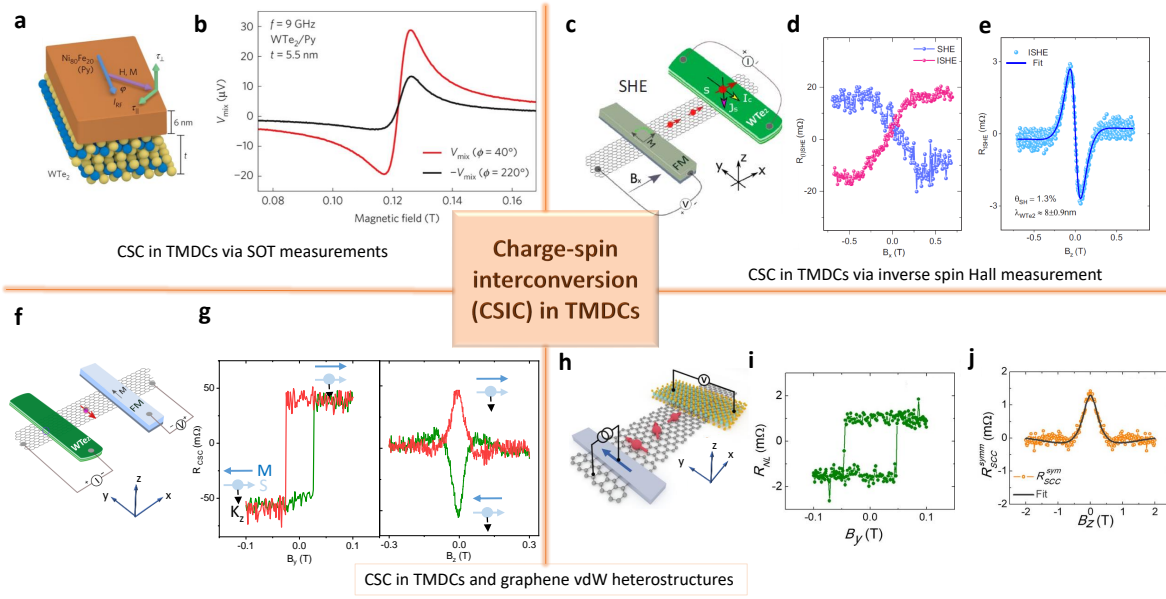


Figure 3.2: Charge-spin interconversion (CSIC) in TMDCs (a) Device schematic of WTe₂/Permalloy (Py) heterostructure. (b) ST-FMR signal in WTe₂/Py device for opposite magnetization orientations. (c) Schematic of graphene-WTe₂ heterostructure for SHE and ISHE measurement schemes. (d) SHE and ISHE signals with magnetic field (B_x) sweep along x-axis. (e) ISHE signal and Hanle fitting curve with B_z field sweep. (f) Measurement configuration for the detection of unconventional charge-spin conversion in WTe₂. (g) The spin-switch and Hanle spin-precession measurements across the WTe₂-graphene junction for opposite magnetization of the detector FM contact. (h) Sketch of the device geometry and measurement configuration to measure SCC signal in the graphene-MoTe₂ heterostructure. (i) Non-local SCC signal (R_{NL}) as a function of applied magnetic field along the y-axis (B_y), the easy axis of the FM electrode. (j) Hanle spin-precession measurement of the SCC signal in MoTe₂. (a, b) are adapted from [110]; (c, d, e) are adapted from [111]; (f, g) are adapted from [112]; (h, i, j) are adapted from [113].

Furthermore, 2D TMDCs with vdW heterostructures with graphene have been extensively studied for CSIC mechanisms. CSIC can originate from the spin Hall effect (SHE), Rashba-Edelstein effect (REE), and surface states [111]. In SHE measurement scheme (Fig. 3.2c), a charge current in 2D TMDCs (e.g., WTe₂) creates a spin polarization that is injected into a graphene channel and detected using a ferromagnetic contact in a nonlocal geometry. The current and voltage probes interchange in inverse-SHE (ISHE) measurement configuration, where a spin polarization is created by the FM contact in the graphene channel that is injected into WTe₂ and voltage probes measure induced charge current due to the spin-to-charge conversion (SCC) effect across the WTe₂ flake [111]. Typical SHE and ISHE signals with varying B_x field toward the in-plane magnetic hard axis of the FM magnetization is shown in Fig. 3.2d [111]. An out-of-plane changing magnetic field in this measurement scheme results in an anti-symmetric Hanle

signal presented in Fig. 3.2e and spin Hall angle is estimated about 1.3% with Edelstein length of about 8nm. Similar studies confirm conventional CSIC in metallic TMDC (NbSe₂) and Rashba material (BiTeBr) [68, 119].

Besides conventional CSIC in TMDCs, unconventional CSIC in WTe₂ and MoTe₂ have been reported [112]. In the unconventional CSIC process due to breaking symmetries, spin polarization, charge and spin current do not need to abide by the orthogonal orientation (right-hand rule). Figure 3.2(f,g) show the device structure of WTe₂-graphene heterostructure and corresponding spin-switch and Hanle spin precession measurements. Unconventional spin-to-charge conversion (SCC) in MoTe₂ is realized while measuring the SCC signal across the MoTe₂ flake [113]. In this measurement scheme (Fig. 3.2h), spin-polarized carriers from a FM diffuse through a graphene channel and are absorbed by the TMDC material. The absorbed spins convert to voltage signals due to the SCC effect across the TMDC material. The spin-switch (Fig. 3.2i) and symmetric Hanle spin precession (Fig. 3.2j) measurements reveal the unconventional SCC effect ($s||j_c$) in MoTe₂ due to broken crystal symmetries [113]. The TMDCs with conventional and unconventional CSIC effects can be used as spin-source and -detector for all-electric all-2D room temperature spintronics applications.

3.1.3 Proximity-induced spin-charge conversion in graphene and 2D materials heterostructures

The SOC is the fundamental physical phenomenon that gives rise to fascinating CSIC effects in non-magnetic 2D materials due to SHE, REE, and TSML [45]. The CSIC in 2D materials is of great interest, but true potential of 2D materials lies in forming vdW heterostructures to synthesize artificial materials by inducing proximity coupling, e.g. SOC. It has been predicted that proximatized graphene with high SOC materials can engender CSIC effects that can be controlled by gate voltage, which is unlikely to be realized in bulk materials [72]. Figure 3.3a shows a device schematic for proximity-induced SOC in graphene from TMDC (WS₂) for CSIC processes [120]. Proximatized graphene can acquire spin-split bands with in-plane (s_y) and out-of-plane (s_z) components (Fig. 3.3b) [72].

In this device geometry with spin-split bands, accumulation of spins in the heterostructure region from the FM creates a transverse electric field (E) during SCC process, or inversely, E can create spin population in the heterostructure region that can be detected by the FM due CSC process [120, 123]. Furthermore, s_z component of the spins are measured as R_{ISHE} due to proximity-induced SHE and s_y component owing to proximity-induced REE that is measured as spin-galvanic effect (SGE), R_{SGE} [120, 121, 123]. The measured R_{ISHE} (red points) and R_{SGE} (blue points) as a function of applied V_g are shown in Fig. 3.3c at room temperature along with the graphene channel resistance R vs. V_g (black solid line). It is evident that the R_{SGE} changes its sign with tuning charge carriers

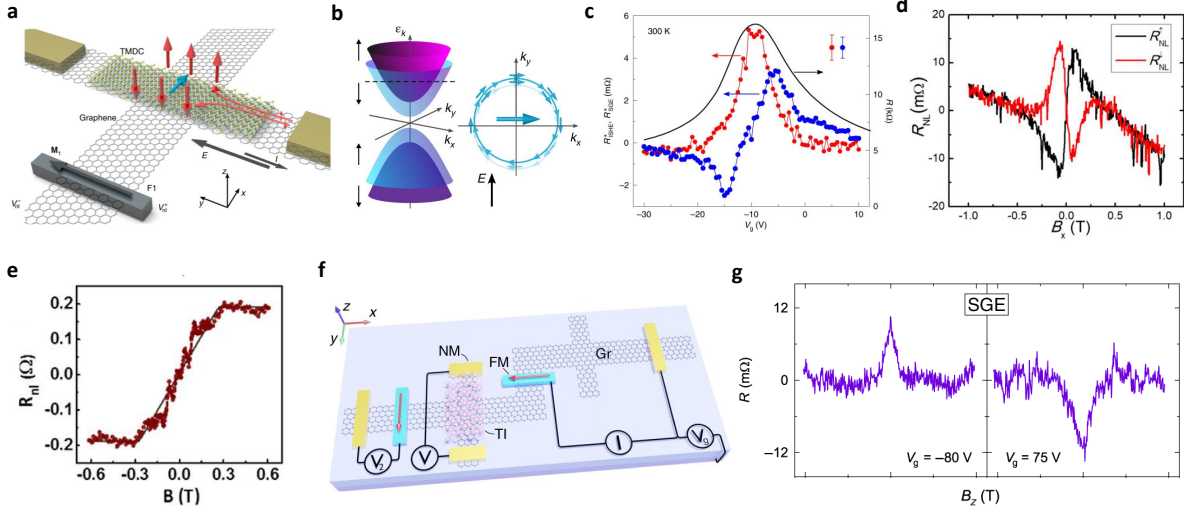


Figure 3.3: Proximity-induced charge-spin interconversion (CSIC) in graphene and 2D materials heterostructures. (a) Pictorial illustration of device geometry to manifest proximity-induced spin-charge conversion in graphene and 2D material vdW heterostructure. (b) Induced-SOC in proximatized graphene with 2D materials tailors spin-split bands with out-of-plane and in-plane components. Accumulating spin population in the heterostructure region generates a transverse electric field (E) owing to CSIC processes, or vice versa. (c) Gate (V_g) dependent CSIC effects for ISHE (red), SGE (blue) in graphene and WS_2 heterostructure. The solid black line is graphene channel resistance (R) vs. V_g . (d) Spin-to-charge conversion due to induced SHE in the proximatized graphene with MoS_2 for opposite magnetization of the injector FM. The changing B field is applied along the in-plane magnetic hard axis of the FM. (e) Proximity-induced (inverse) Rashba-Edelstein effect (I)REE in graphene- WS_2 heterostructure. (f) Device structure and measurement geometry of graphene Hall cross with a TI flake. In this measurement configuration, a perpendicular FM tunnel contact is used to inject spin current into graphene-TI heterostructure region, and the corresponding SGE signal is measured as a voltage signal across the graphene-TI Hall cross. (g) The opposite SGE signals ($R = V/I$) measured with the in-plane magnetic field for electron- and hole-doped regimes. (a, b, c) are adapted from ref. [120]; (d) is adapted from ref. [121]; (e) is adapted from ref. [122]; (f, g) are adapted from ref. [123].

from electrons to holes by V_g . R_{ISHE} delineates similar V_g dependence at low temperature, but it is smeared at room temperature supposedly due to charge puddling and thermal broadening [120]. Furthermore, spin-to-charge conversion using ISHE measurement configuration is observed in multilayer graphene- MoS_2 heterostructure, could be due to proximity-induced SOC in graphene from MoS_2 or from the bulk MoS_2 effect [121].

Moreover, another study in proximatized graphene with WS_2 shows charge-spin interconversion (CSIC) owing to proximity-induced SHE and REE [122]. An in-plane changing magnetic field (B_x) along the magnetic hard axis (x -axis in Fig. 3.3a) is applied to rotate and saturate the magnetization of the FM toward $\pm x$ -axis while measuring the corresponding voltage signal due to (I)REE) in non-

local measurement geometry (Fig. 3.3e). Interestingly, the stray magnetic field from a FM contact in bare graphene can mimic the CSIC signals in such measurement configuration [124]. One way to get rid of this confusion is to put a perpendicular FM contact with respect to the heterostructure region, as shown in Fig. 3.3f [123, 125]. In this measurement configuration, B_x switches the FM magnetization sharply, rather than slowly rotating the FM magnetization along the magnetic hard axis. An out-of-plane field (B_z) renders opposite Hanle precession spin signals for electron- and hole-doped regimes (Fig. 3.3g) [123]. These experiments prove the spin-origin of the SGE (similar to SCC) signals due to (I)REE in SOC-induced graphene from high SOC material. These much-needed experimental proofs of such gate-tunable SCC effects in proximity-induced SOC graphene-2D materials vdW heterostructure would considerably boost its utilization in emerging spintronic technologies.

3.1.4 Proximity-induced spin-lifetime anisotropy in graphene and 2D materials heterostructures

Another exciting aspect of proximity-induced SOC in graphene is the spin-lifetime anisotropy ($\xi = \tau_{\perp}/\tau_{\parallel}$), which results in spin filtering functionalities due to the different spin relaxation time for spins along different orientations [71, 127]. Pristine graphene shows isotropic spin, $\xi = 1$, whereas proximatized graphene with high SOC shows $\xi \geq 10$ [127]. To estimate ξ in graphene and its heterostructure, non-local measurement device geometry is used (Fig. 3.4a) [126]. High SOC from the TMDC can imprint complex spin-texture in graphene, giving rise to spin-split bands, as shown in Fig. 3.4b with out-of-plane spin component mainly due to the valley-Zeeman effect [126]. In the non-local measurement geometry, spin-polarized electrons from the injector's FM diffuse to the detector's FM in the graphene channel through the heterostructure region, where its orientation is modulated. Figure 3.4b shows pictorial illustrations for spin orientation in opposite valleys of high SOC graphene in proximity with high SOC materials [127]. Intervalley scattering (τ_{iv}) controls in-plane spin (τ_{\parallel}), whereas momentum scattering (τ_p) regulates the out-of-plane spin (τ_{\perp}) component.

In the heterostructure, ξ greatly depends on intervalley scattering (τ_{iv}) that has an inverse effect on in-plane spin component (τ_{\parallel}) (Fig. 3.4c). In the absence of intervalley scattering, similar spin-lifetime for in-plane and out-of-plane spin components are calculated and ξ becomes unity. Furthermore, the number of charge scatterers (n) can influence ξ , as shown in the inset of Fig. 3.4c. When the n is higher, τ_{\perp} and τ_{iv} decrease and the ξ approaches to unity in comparison to the scenario where n is lower [127].

The difference between in-plane and out-of-plane Hanle spin signals (Fig. 3.4d) demonstrates large spin-lifetime anisotropy in graphene- WS_2 heterostructure [126]. Figure 3.4e shows the data points of normalized non-local resistances ($R_{nl,\beta}/R_{nl,0}$)

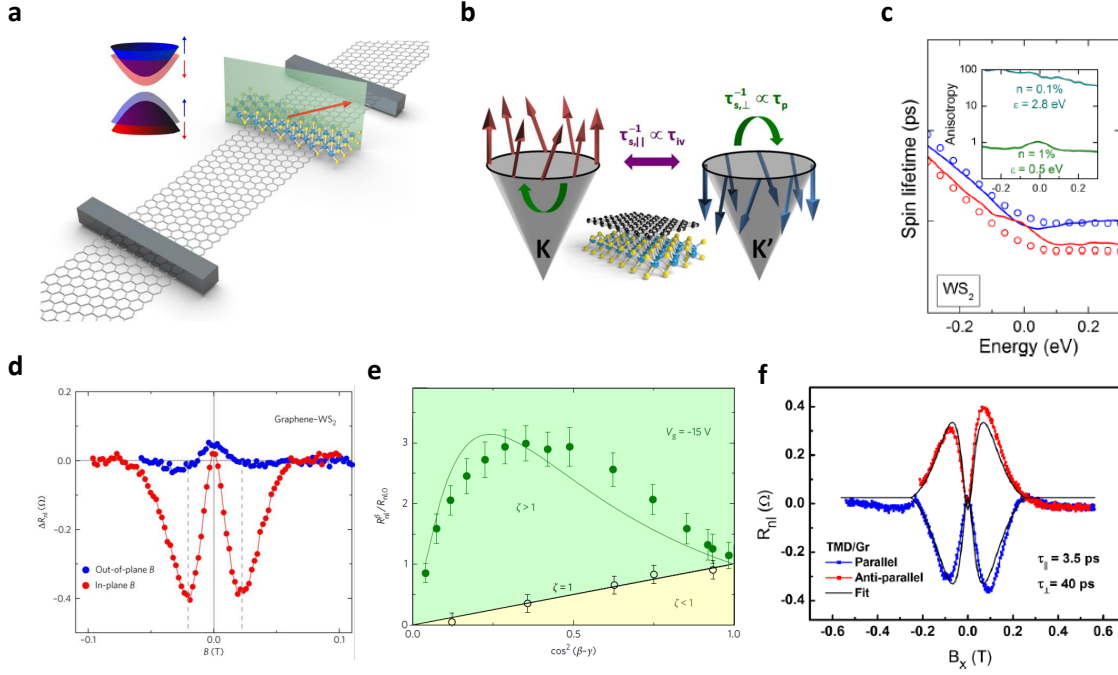


Figure 3.4: Spin-lifetime anisotropy in graphene-TMDCs heterostructures. (a) Schematic illustration of the graphene-TMDC heterostructure device and non-local measurement scheme. Pictorial depiction of the band diagram of graphene in heterostructure region with spin-split bands along out-of-plane spin component. (b) Pictorial illustrations for spin orientation in opposite valleys (K and K') of high SOC graphene in proximity with a TMDC. The arrows indicate the spin orientations in the valleys. (c) Spin-lifetime in graphene-WS₂ heterostructure without intervalley scattering, resulting in isotropic spin-lifetime phenomena. The red and blue circles indicate out-of-plane and in-plane spin-lifetime, respectively. (d) Hanle signal R_{nl} with out-of-plane and in-plane magnetic field sweep to demonstrate spin-lifetime anisotropy in graphene-WS₂ heterostructure. (e) Data points of normalized non-local resistances ($R_{nl,\beta}/R_{nl,0}$) as a function of $\cos^2(\beta - \gamma)$ along with the fitting function to estimate anisotropy. (f) Hanle spin precession measurements (R_{nl}) in graphene-MoSe₂ with opposite FM magnetization. Magnetic field (B) is applied along the in-plane magnetic hard axis of the FM contact. (a, d, e) adapted from [126]; (b, c) adapted from [127]; (f) adapted from [128].

as a function of applied effective magnetic field direction, $\cos^2(\beta - \gamma)$, along with the fitting function to estimate ξ [126]. It is observed that ξ in graphene-WS₂ can also be modulated by gate voltage (V_g). Moreover, in-plane Hanle signals with the opposite magnetization of the injector's FM also reveal higher $\xi \geq 10$ in graphene-MoSe₂ (Fig. 3.4f) [128]. So far, exfoliated devices consisting of graphene with WS₂, MoS₂, MoSe₂ and WSe₂ demonstrate $\xi \geq 10$ due to enhanced spin-valley coupling in graphene in proximity with the aforementioned TMDCs [126, 128].

3.2 2D semiconductor nano-transistors

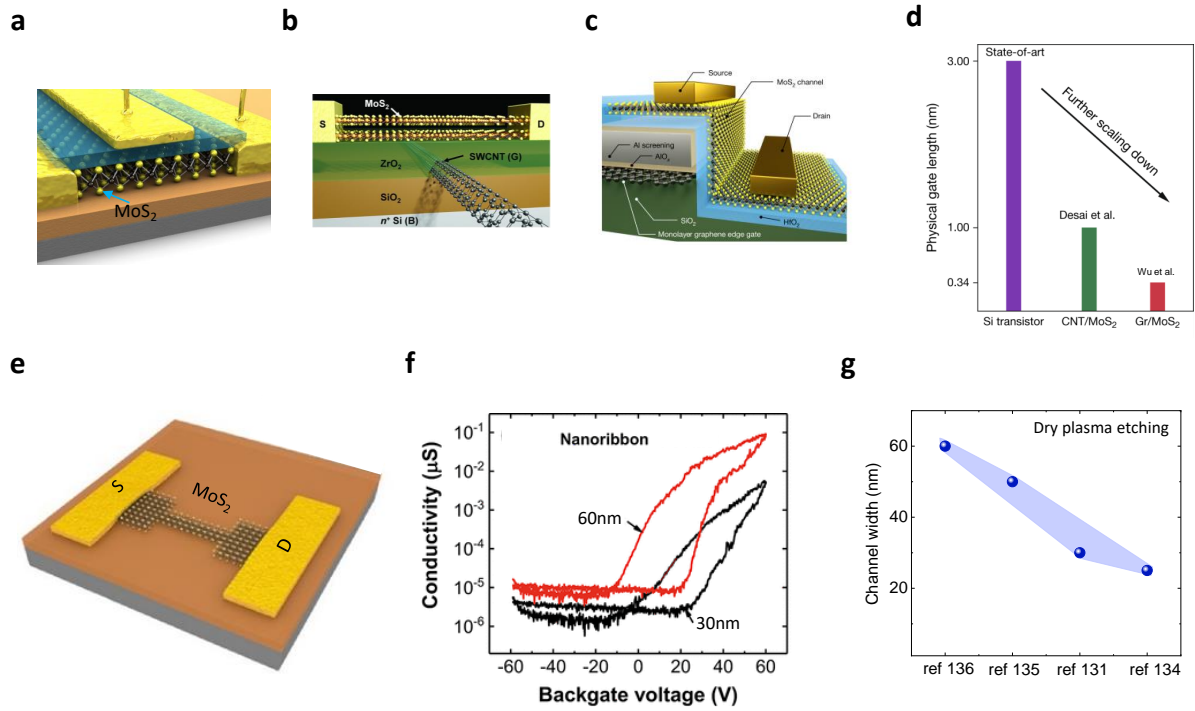


Figure 3.5: Recent milestones of 2D semiconductor nano-transistors. (a) Schematic view of MoS₂ FET with dual gate (top and bottom) electrodes. (b) 3D view of a bilayer MoS₂ FET with 1nm single-wall carbon nanotube (SWCNT) gate. (c) Device sketch of a vertical monolayer MoS₂ FET with 0.34nm single-layer graphene gate. (d) Ultimate scaling of gate length from state-of-the-art Si FET and 2D material's FETs. (e) Device schematic of a single layer MoS₂ FET with a narrow channel. (f) Channel conductivity as a function of backgate voltage of MoS₂ nanoribbon FETs with channel width 60nm (red) and 30nm (black). (g) Milestones of the nanoribbon channel-width of 2D TMDC FETs that are fabricated by dry plasma etching, limited to 25nm. (a) adapted from [129]; (b) adapted from [130]; (c, d) adapted from [131]; (e, f) adapted from [132].

2D semiconducting TMDCs have attracted tremendous interest due to their atomically thin body and dangling-bond-free surface for the next-generation field-effect transistors (FET), tunnel transistors, rectifiers, light-emitting diodes, and solar energy harvesting devices [13, 30–32, 83–86]. Besides, theory reveals that the band structures of the TMDCs nanoribbons are different from their bulk properties. To illustrate, zigzag terminated nanoribbon shows metallic and ferromagnetic behavior, in contrast to the armchair counterpart, which is semiconducting [51, 133]. The design and control of semiconducting TMDC-based FETs and engineering their properties at an atomic scale are challenging and of paramount importance for advances in basic science and technology [30, 43]. After realizing monolayer high mobility MoS₂ FET (Fig. 3.5a) [129], considerable efforts have

been devoted to scale-down the channel length and width of the TMDC-based FETs. Devices with planar and vertical TMDC FET structures with carbon nanotube (1nm) and graphene (0.34nm) gate are realized (Fig. 3.5b, c) [130, 131]. Figure 3.5d shows the comparison of ultimate gate length scaling of state-of-the-art Si-FET and 2D material's FETs [131].

Although TMDC-based FETs with sub-10nm channel length and sub-nm gate dimensions have been recently demonstrated [130, 131, 134], the channel width of the devices is mostly limited to be more than 25 nm due to limited resolution of lithography processes and physical etching techniques used so far [132, 135–137]. Device schematic of a single layer MoS₂ FET with narrow channel (fabricated by dry plasma etching) is depicted in Fig. 3.5e [132]. Transport properties of that monolayer MoS₂ nanoribbon FETs with channel widths down to 30nm are manifested (Fig. 3.5f) [132]. Figure 3.5g shows the state-of-the-art nanoribbon channel-widths of 2D material-based FETs down to 25nm wide channel, fabricated by dry plasma etching that is limited by the lithography resolution [132, 135–137]. Furthermore, the edge properties are not controlled and perfect, which limit the transport in the dry-etched nanoribbons by increasing scattering processes. Nanoribbon 2D TMDC transistors with well-defined edges (zigzag and armchair) have not been investigated so far.

In addition to the remarkable achievements in realizing 2D nano-transistor FETs, major issues regarding high contact resistance on 2D semiconductor FETs need to be addressed [87, 88]. In 2D semiconductors, the interface between the contact and semiconductor determines the overall device performance. Bulk metal electrodes on top of 2D semiconductors (Fig. 3.6a) usually render high contact resistance due to lack of covalent bonds and high Schottky barrier (SB) originating from mismatched work functions of metal and electron affinity in 2D semiconductor. Interestingly, the metal that can make covalent bonds (e.g., Ti on MoS₂) hybridizes the 2D semiconductor properties by forming metallic states (Fig. 3.6a, b) [30, 87, 88]. A strong hybridized interface usually increases the contact resistance mainly because of Fermi level pinning, increasing 2D surface inhomogeneity and impurities, and metal-induced gap states (MIGS), as shown in Fig. 3.6d [93]. To better realize the effects mentioned earlier, the dependence of SB between multilayer MoS₂ and different metals is shown in Fig. 3.6c [87]. It can be seen that the estimated SB weakly depends on the metal work functions, with slope $S = 0.09$ and SB is pinned around 100-150 meV. Besides controlling SB, another approach to reduce contact resistance is to reduce MIGS at the metal-semiconductor interface by introducing a contact material with a Fermi level that matches the conduction band minimum of the 2D semiconductor (Fig. 3.6e). A recent study shows fairly low contact resistance ($\sim 100\Omega\mu\text{m}$) between semimetallic Bi and monolayer MoS₂ (blue star in Fig. 3.6h) by mitigating MIGS at the interface in contrast to few k Ω s- M Ω s with conventional metallic electrodes [93].

Besides 3D metals or semimetals, 2D metals (e.g, 1T' MoS₂) and semimetals

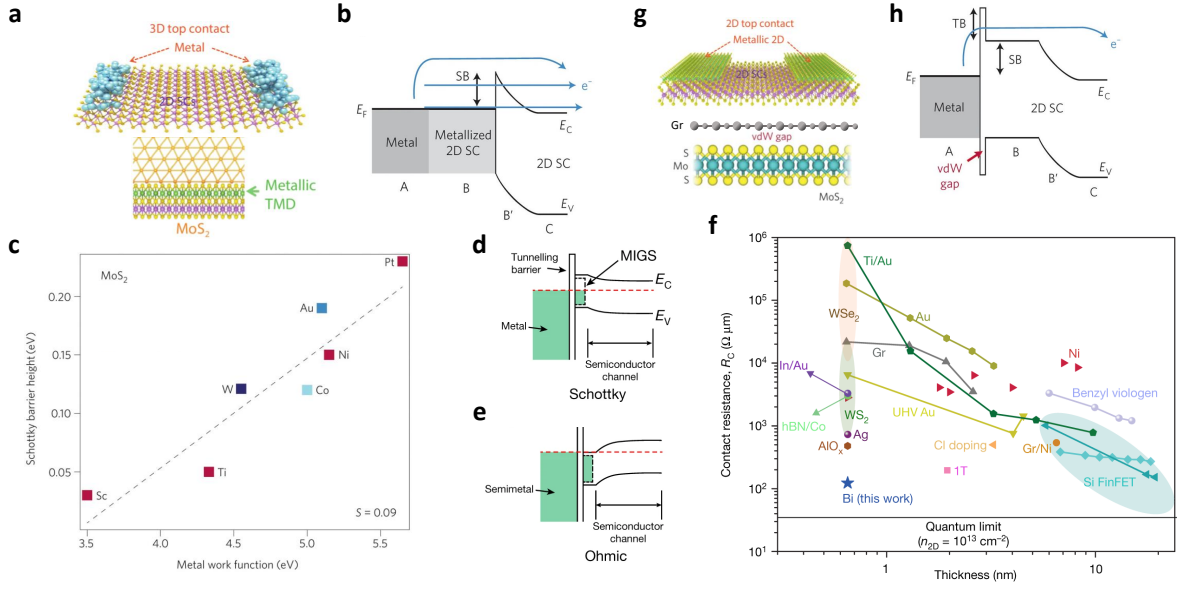


Figure 3.6: Contact properties of 2D semiconductor FETs. (a) Sketch of a 2D semiconductor FET with top 3D metallic contacts along with a pictorial view of hybridized TMDC and metal. (b) Band diagram of hybridized metal/2D semiconductor interface. (c) Dependence of Schottky barrier height in multilayer MoS₂ for metals with different work functions. (d) Conventional metal and 2D semiconductor interface, where gap-states give rise to Fermi level pinning. (e) Band diagram of semimetal-2D semiconductor interface, where gap-states are mitigated by matching Fermi-level of the semimetallic contact and 2D semiconductor. (f) Contact resistance of Bi (semimetallic) contacts on monolayer MoS₂ FET and its comparison with conventional metallic contact. (g) Sketch of a 2D semiconductor FET with top 2D material contacts along with pictorial view of vdW gap between 2D semiconductor (MoS₂) and top 2D electrode. (h) Band diagram of 2D semiconductor and 2D material electrode interface. (a, b, c, g, h) adapted from [87, 88]; (d, e, f) adapted from [93].

(e.g., Gr) have possibilities to reduce the contact resistance by matching Fermi level, thus eliminating SB and forming chemical bonds [88, 90]. 2D electrodes in 2D material FET (Fig. 3.6g) can be achieved by phase engineering, direct CVD growth and intercalation treatments [88, 90]. Charge carriers in this device geometry need to tunnel through the vdW gap (Fig. 3.6g, bottom panel) in the interface and surmount SB height (Fig. 3.6h). Furthermore, Fermi-level tunability, high carrier mobility and functionalizing ability make graphene a potential candidate for contact electrodes for optical and flexible electronic applications [138–140].

Further research on all-CVD grown graphene and 2D semiconductor vdW heterostructures can shed some light to investigate their prospects for large area applications and can open new possibilities, e.g, memristor applications. To illustrate, a memristor device combines resistor and memory functions and applied voltage can change its resistance state from a low-resistance state (LRS) to a

high-resistance state (HRS) or vice versa [141]. Memristors are highly sought-after devices for neuromorphic computation [142]. Such memristive device functionalities are observed in 2D TMDCs (MoS_2) with conventional 3D contacts and memristive switchings originate from the motion of grain boundary, defects and Schottky barrier modulation with applied bias [53, 54]. It would be interesting to observe memristive switchings in all-CVD graphene- MoS_2 vdW devices for future flexible and high-performance memory and logic applications.

4 Charge-spin conversion in layered topological insulator and semimetals

Charge-spin interconversion (CSIC) processes are essential aspects to realize all-electric spintronic devices. CSIC processes are crucial for injecting and detecting spin polarized electrons in a channel. This chapter presents the charge-to-spin conversion (CSC) and its inverse effect (ICSC) in layered topological insulator (TI) and semimetals (i.e., TaTe₂ and NbSe₂), sequentially. These materials possess high spin-orbit coupling (SOC) properties that render novel spin-textures and hence (I)CSC effect upon application of an electric field. These high SOC materials are combined in vdW heterostructure with graphene spin-valve devices. Here, graphene is used as a spin channel material because it has been shown to exhibit a robust and long distance spin transport at room temperature [62, 64, 143]. Systematic measurements with gate voltage and bias current are presented to show spin injection and detection by these materials in heterostructure with a graphene channel. Demonstration of charge-spin interconversion (CSC & ICSC) at room temperature using non-local geometry can open doors for the exploration and testing of new materials and devices for future spintronic applications.

4.1 Charge-spin conversion in topological insulator (TI)

TIs are emerging materials for next-generation nanoelectronic devices, thanks to the non-trivial spin-momentum locking of their topological surface states. Although CSC has previously been reported in TIs by potentiometric measurements [98, 101–106], reliable nonlocal (NL) detection has so far been observed only at cryogenic temperatures up to $T = 15$ K [100]. This section presents the nonlocal detection of CSC and its inverse effect (ICSC) in a TI compound Bi_{1.5}Sb_{0.5}Te_{1.7}Se_{1.3} at room temperature using a van der Waals heterostructure with a graphene spin valve device. The lateral nonlocal device design with graphene allows observation of both spin switch and Hanle spin precession signals for generation, injection and detection of spin currents by the TI. Detailed bias- and gate-dependent measurements in different geometries prove the robustness of

the (I)CSC effects in the TI. These findings demonstrate the possibility of using topological materials to make all-electrical room-temperature spintronic devices.

4.1.1 Device geometry and charge-spin conversion signals in TI

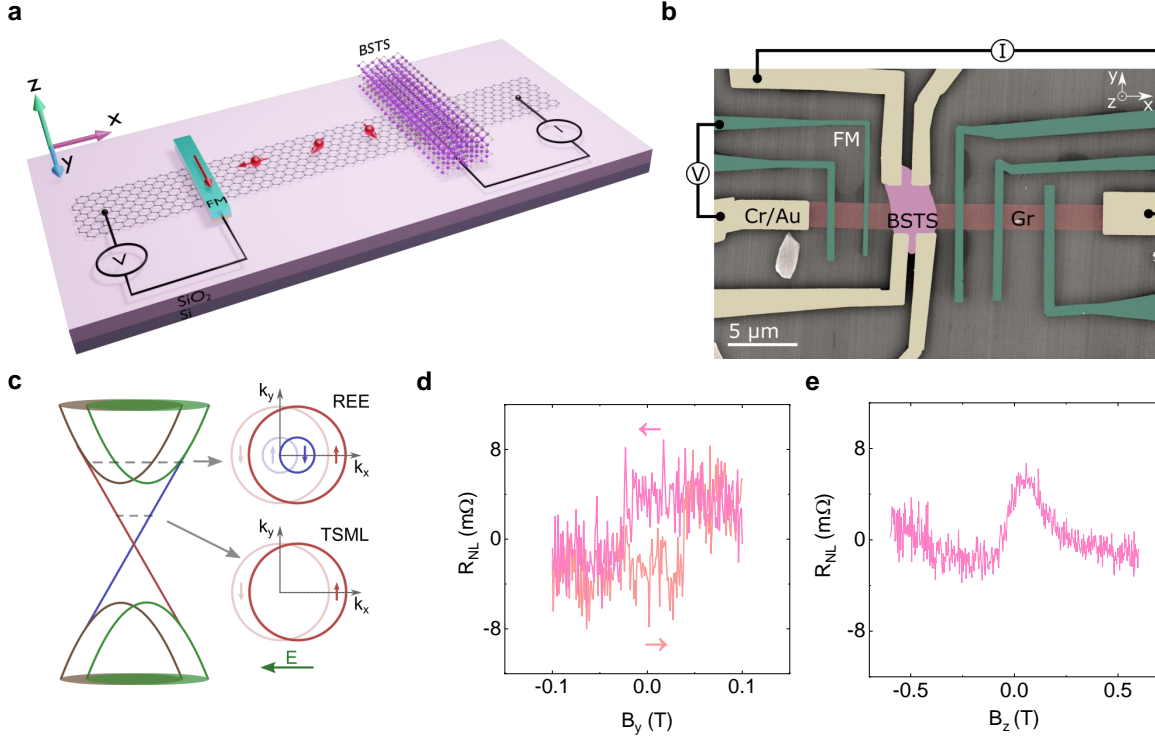


Figure 4.1: Graphene/BSTS heterostructure device for nonlocal detection of charge-spin conversion at room temperature. (a, b) Schematics and coloured SEM image of the graphene/BSTS heterostructure device with non-local (NL) measurement geometry, with reference nonmagnetic (Cr/Au) and FM (TiO_2/Co) contacts. The scale bar shown is $5\ \mu\text{m}$. (c) Schematic of two CSC mechanisms: the Rashba-Edelstein effect (REE) and topological spin-momentum locking (TSML). (d) Spin switch signal ($R_{NL} = V_{NL}/I$) for spin injection from BSTS with B_y magnetic field sweep. (e) Hanle signal R_{NL} with B_z magnetic field sweep. The measurements were performed at $T = 295\ \text{K}$ for a bias current of $I = 150\ \mu\text{A}$ and a gate voltage of $V_g = -70\ \text{V}$. Linear backgrounds of $25\ \text{m}\Omega$ and $35\ \text{m}\Omega$ have been subtracted from the measured data in (d) and (e), respectively.

To detect CSC in the TI, a BSTS and graphene heterostructure-based spin valve device is utilized, as shown in Fig. 4.1a-b. The graphene/BSTS vdW heterostructure is fabricated with reference non-magnetic (Cr/Au) and FM (TiO_2/Co) contacts for spin injection and detection in the graphene channel. Here, the TiO_2 oxide layer acts as a tunnel barrier to help mitigate issues like conductivity mismatch with the graphene channel [144–146]. The CSC in TIs can arise due to

the bulk spin Hall effect (SHE), the Rashba-Edelstein effect (REE) of the bulk states or the trivial surface states, and/or the topological spin-momentum locking (TSML) of the surface states [66, 147]. As shown in Fig. 4.1c, the Fermi surface has a winding spin texture for both REE and TSML, which will be offset from the equilibrium position by the additional electron momentum that is caused by an applied electric field [70, 122]. Importantly, BSTS has been found to have dominant TI properties below 90 K [148], which means that the bulk SHE and the bulk REE can contribute to CSC at room temperature, although the TSML may still be present.

In the measurement geometry (Fig. 4.1a), an applied charge current creates a spin density due to CSC in the TI that is then injected into the graphene spin channel. The diffused spin polarization in the graphene channel is detected as a non-local (NL) voltage by a remote FM electrode placed at a channel length of $L = 3.4 \mu\text{m}$ (center-to-center distance) away from the TI flake. First, spin switch measurements were performed while sweeping an in-plane magnetic field along the y axis (B_y), which is the easy axis of the FM electrodes. The applied magnetic field results in switching of the magnetization orientation of the FM detector from parallel to antiparallel orientation with respect to the injected spin-polarized electrons from the TI into the graphene channel. This results in a change in NL resistance ($R_{NL} = V_{NL}/I$) as shown in Figure 4.1d, where V_{NL} is the measured voltage and I is the applied charge current across the graphene/TI structure. In order to prove the spin origin of the signal, Hanle spin precession measurements were conducted by sweeping the magnetic field out-of-plane along the z axis (B_z). This causes the in-plane spins to precess and dephase while diffusing along the graphene channel, and reach the FM detector electrode with a finite angle with respect to the contact magnetization direction[109]. As shown in Figure 4.1e, the measured Hanle signal R_{NL} depends on B_z , as it changes the projection of the spin polarization onto the FM contact magnetization direction. The observation of both spin switch and Hanle spin precession signals is a confirmation of the spin injection from the TI into the graphene channel due to an efficient CSC effect. By using data from the CSC signals and reference measurements (see below), the spin polarization of the BSTS flake could be estimated to about 0.1 %.

4.1.2 Asymmetric components of the charge-spin conversion Hanle signal.

The Hanle signals were further investigated with the magnetization direction of the FM detector electrode in parallel and antiparallel orientations ($\pm y$), respectively, as shown in Fig. 4.2a. Depending on the FM magnetization direction, the Hanle signal has either a minimum or a maximum around $B_z = 0$. The two curves for opposite magnetization were averaged to get rid of any non-spin-related background. As the observed signals are not symmetric, the averaged

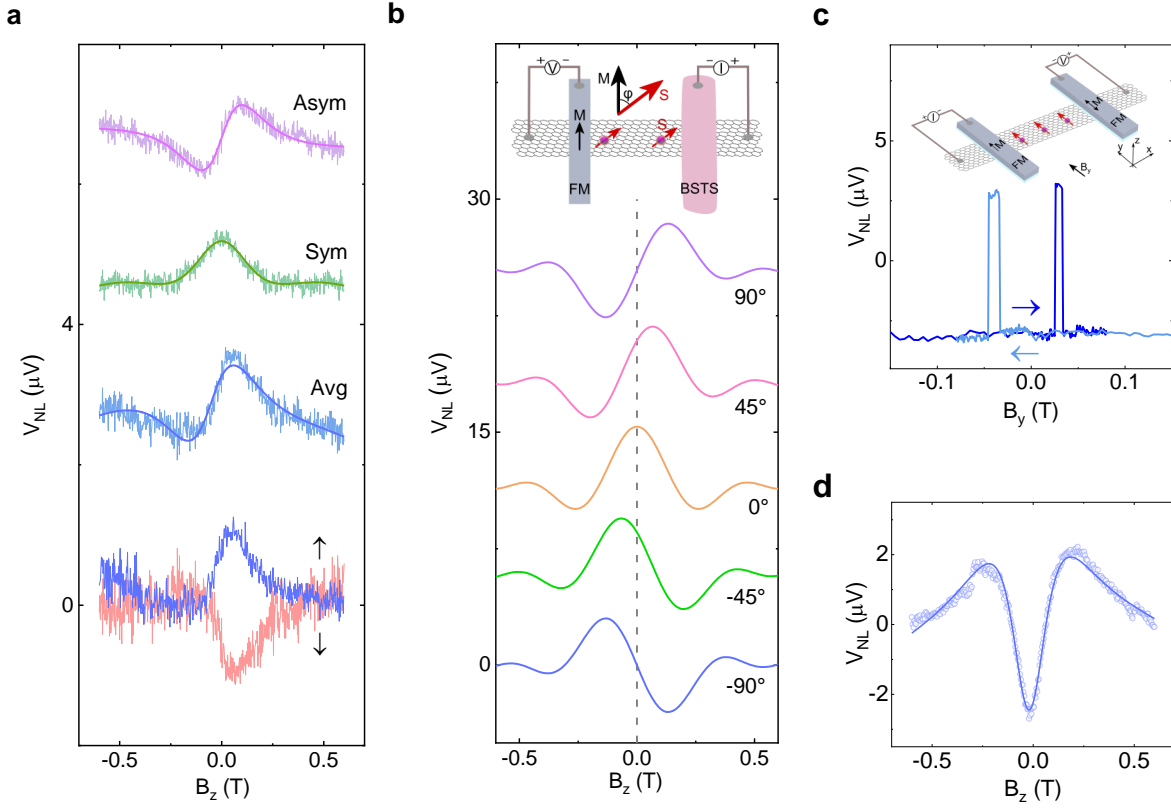


Figure 4.2: Asymmetric components of the charge-spin conversion Hanle signal.

(a) Hanle spin precession signals with FM contact magnetization along the $+y$ (\uparrow) and the $-y$ (\downarrow) direction, respectively, as well as the averaged signal (Avg) and the symmetric (Sym) and the antisymmetric (Asym) components of the averaged signal. The green and purple solid lines are fits of the respective signal components, and the blue solid line is a guide to the eye for the averaged signal. The measurements were performed for $I = 150 \mu A$ and $V_g = -70 V$. A linear background has been subtracted and the data are shifted vertically for clarity. (b) Simulation of the evolution of the CSC signal with the tilt angle of the injected spin polarization in the device. Inset: The top view of the CSC measurement geometry with the tilt angle (ϕ) of spins S injected from the BSTS with respect to the magnetic moment M of the FM spin injector. (c) A reference spin valve signal measured in pristine graphene with FM contacts used as both spin injector and spin detector. The measurement was performed for $I = -50 \mu A$ and $V_g = -70 V$. Inset: Schematic of the measurement setup with pristine graphene. (d) Hanle spin precession signal for measurement in pristine graphene. The solid line is a fit of the detected signal. The measurement was performed for $I = -100 \mu A$ and $V_g = -70 V$.

signal was then deconvoluted into its symmetric and antisymmetric components and subsequently fitted. From this, values for the spin lifetime τ_s and the spin diffusion length λ_s in the graphene were extracted as 75 ps and $1.5 \mu m$, respectively. The relative contribution of the symmetric and antisymmetric components

depends on the angle between the polarization of the spin current that is injected from the BSTS flake into the graphene and the magnetization direction of the FM detector contact [62, 68, 111], and this angle could here be estimated to $\phi = \tan^{-1}(V_{NL}^{Asym}/V_{NL}^{Sym}) = 67 \pm 1^\circ$. Simulated Hanle signals for different values of ϕ are illustrated in Fig. 4.2b [68, 111].

The asymmetric characteristic of the Hanle signals can have different origins, however, the most likely one is the bias current distribution in the TI. Because of the positions of the two electrodes (one on TI and the other on graphene) that the bias current is applied between, the charge current through the BSTS flake has nonzero x , y and z components. Due to the mechanism of the CSC, the generated in-plane spin polarization (which is detected in the Hanle measurements) will be perpendicular to the charge current. The injected spin from the TI into the graphene channel will therefore have nonzero x and y components, corresponding to asymmetric Hanle signals [62, 68, 111–113, 123].

For comparison, signals from spin valve and Hanle measurements in a pristine graphene region of the same device with FM electrodes as both spin injector and detector [143] are shown in Fig. 4.2c-d. In contrast to the CSC-based measurements, the Hanle signal for pristine graphene is symmetric, because the injected spin and the detector contact magnetization are always either parallel or antiparallel. The spin transport parameters that were extracted from Fig. 4.2d are $\tau_s = 45$ ps and $\lambda_s = 0.85 \mu\text{m}$. Similar Hanle measurements for the graphene channel across the vdW heterostructure give $\tau_s = 103$ ps and $\lambda_s = 1.0 \mu\text{m}$. The variation in transport parameters between the three different measurements is most likely because of differences in contact and channel properties. By comparing the results from the pristine graphene to those from the vdW heterostructure, it can be concluded that there is little or no spin absorption by the TI flake.

4.1.3 Geometry and bias current dependence of charge-spin conversion signal

In order to investigate the origin of the CSC, experiments were performed for the different measurement geometries shown in Fig. 4.3a. In the first geometry, the bias current I_1 is applied on the $+x$ side of the BSTS flake and the NL voltage V_1 is detected on the $-x$ side of the flake. In the second setup, an opposite geometry is used with I_2 and V_2 . Both setups have similar channel lengths of $3.4 \mu\text{m}$ and $3.2 \mu\text{m}$, respectively. As shown in Fig. 4.3b, there is a sign change for the spin switch signal between the two measurement geometries: setup 1 gives a high NL voltage when the contact magnetization of the detector is in the $+y$ direction and a low NL voltage for $-y$ contact magnetization, while setup 2 gives the opposite. The origin of the CSC must therefore be odd with the x component of the charge current, but may also depend on the y and z components. This behavior indicates that the origin of the spin current can be due to either of

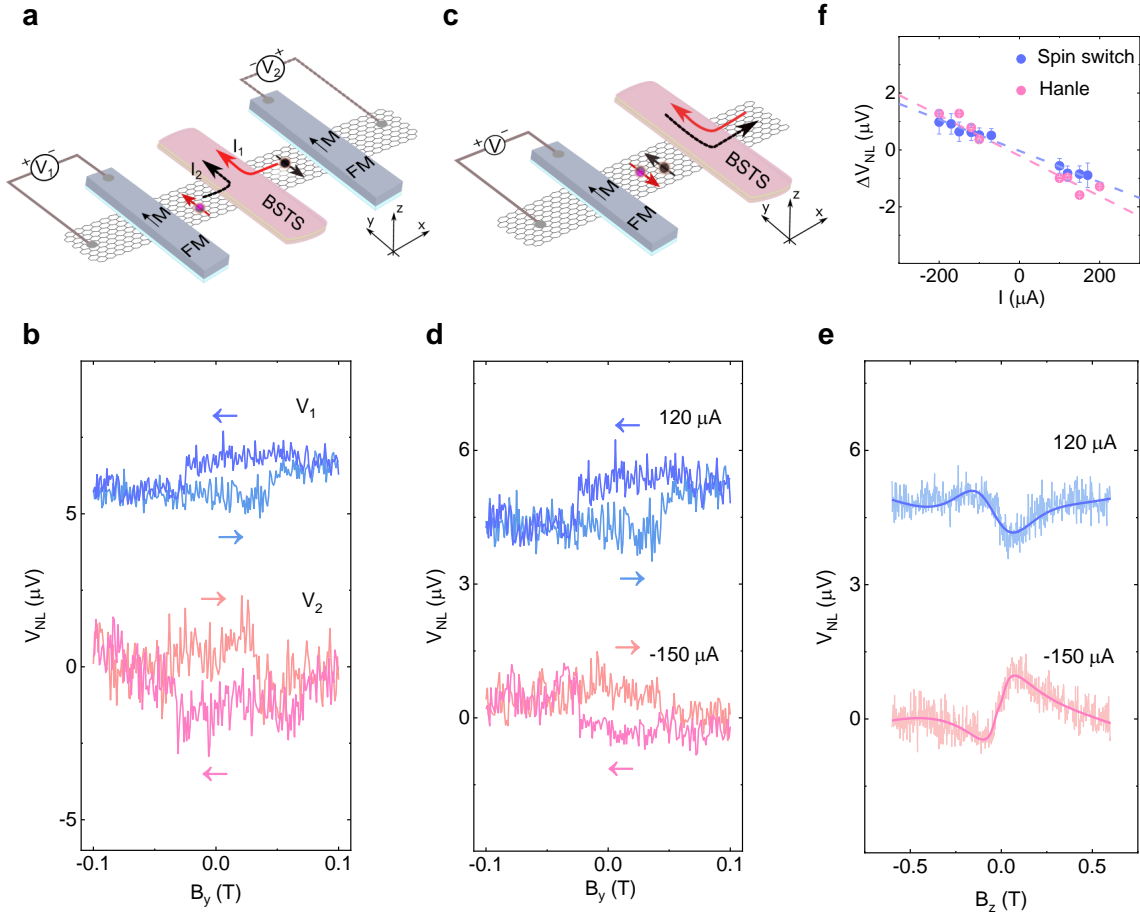


Figure 4.3: Geometry and bias current dependence of charge-spin conversion signal in graphene/BSTS junction. (a) Schematic of the device and the two different CSC measurement geometries. (b) Spin switch signals for each of the two measurement geometries. The measurements were performed at room temperature for $I = 120 \mu A$ and $V_g = -60 V$ and for $I = 300 \mu A$ and $V_g = -75 V$, respectively. (c) Schematic of the device and measurement geometry with arrows indicating the direction of positive and negative bias currents. (d, e) Spin switch and Hanle signals for $I = 120 \mu A$ and $I = -150 \mu A$. The Hanle signals are presented with corresponding guides to the eye. The measurements were performed at room temperature for $V_g = -60 V$ and $V_g = -70 V$, for spin switch and Hanle signals, respectively, and the data are shifted vertically for clarity. (f) The amplitude of the measured spin switch and Hanle signals as a function of bias current, and linear fits. Some error bars are smaller than the data points.

the conventional SHE, REE or TSML, since all of these effects depend on the in-plane charge current direction [66, 123, 147]. These control experiments, however, rule out any unconventional CSC mechanism in the TI, as recently reported in the case of WTe_2 , where the latter showed a CSC which is independent of the x component of the charge current [112]. It should be noted that differences in amplitude between the two signals in Figure 4.3b can arise from different detector

FM contacts being used, which may have different polarizations and/or interface resistances with the graphene.

The bias current dependence of the spin signal was examined through both spin switch and Hanle measurements with an experimental setup as shown in Fig. 4.3c. Both the spin switch (Fig. 4.3d) and the Hanle (Fig. 4.3e) signals show a sign change with reversed bias current. Furthermore, Fig. 4.3f shows a linear bias dependence of the amplitude of both the spin switch and the Hanle signals. Here, the Hanle signal is larger than the spin switch signal. This is logical because the Hanle amplitude is the vector addition of the symmetric and the antisymmetric components, and therefore consists of both the x and the y components of the injected spin polarization from BSTS into graphene, due to the precession of spins in the xy plane. The spin switch signal, on the other hand, consists of only the y component of the spin, since there is no precession and the FM detector is only sensitive to spin components in the y direction.

Furthermore, considering that reversing the bias current means changing between injection and extraction of polarized spin, the observation of a sign change of the spin signal is as expected [68]. In principle, the linear bias dependence is also expected, since a larger charge current enables a larger spin polarization. The observation of linear bias dependence also rules out any spurious thermal effects in data within the measured bias ranges.

4.1.4 Gate dependence of inverse charge-spin conversion signal in TI

The gate dependence of the spin signal was investigated using the device geometry shown in Fig. 4.4a, with use of the $n^{++}\text{Si}/\text{SiO}_2$ substrate as the back gate. Fig. 4.4b shows the Dirac curves of the graphene channel, both for pristine graphene and in the graphene/BSTS heterostructure region. The Dirac points at $V_g = 43$ V (for the heterostructure region) and $V_g = 41$ V (for pristine graphene) indicate negligible contribution from doping of graphene by the TI and band misalignment between the graphene and BSTS, which could have offset the charge carriers. The difference in the resistances comes from the longer channel for the graphene/BSTS heterostructure. The mobility of the charge carriers was calculated [149] to be $\mu_{HS} = 1200 \text{ cm}^2/\text{Vs}$ for the heterostructure graphene and $\mu_{pr} = 1000 \text{ cm}^2/\text{Vs}$ for the pristine graphene, similar to what has been reported in literature [60, 123, 125, 150].

The gate dependence was measured for spin switch and Hanle spin precession, as shown in Fig. 4.4c-d. As the TI is not very sensitive to gate voltage in the experiments (because of shielding by the graphene and the thickness of the TI flake itself), the modulation of the Fermi level in graphene from p- to n-doped regime for $V_g = \pm 70$ V causes only a small Fermi level tuning of BSTS and does not change the sign of the signal, proving the spin origin of the signal and ruling out

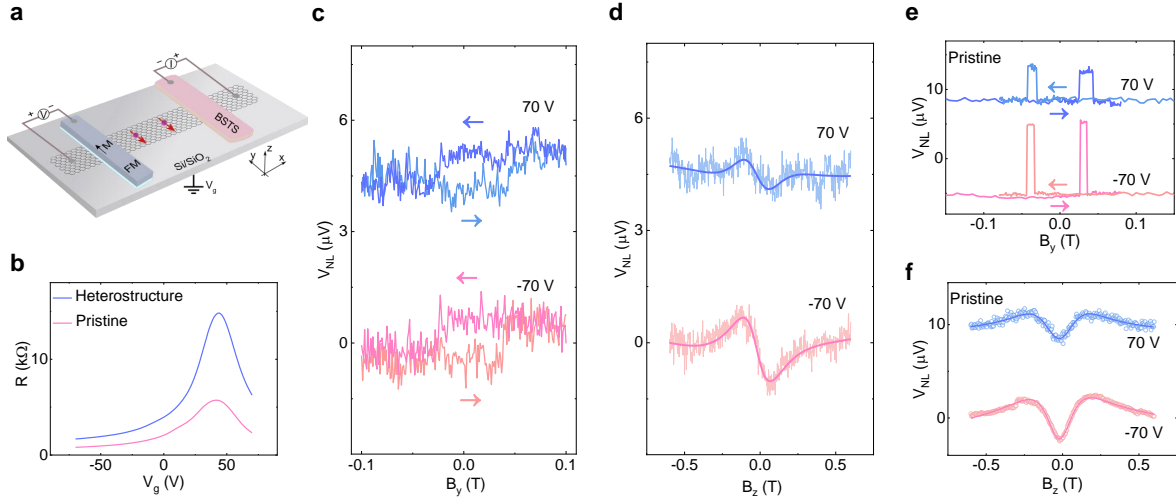


Figure 4.4: Gate voltage dependence of charge-spin conversion signal in graphene/BSTS junction. (a) Device geometry for gate dependence measurements with back gate. (b) The Dirac curve of heterostructure and pristine graphene regions of the device. (c, d) Spin switch and Hanle spin precession signals for electron and hole doped graphene regimes measured at $V_g = \pm 70$ V and $I = 150 \mu\text{A}$ at room temperature. The Hanle signals are presented with guides to the eye. Linear backgrounds have been subtracted and the data are shifted vertically for clarity. (e, f) Spin valve and Hanle signals of the pristine graphene region at electron and hole doped graphene regimes, measured at $V_g = \pm 70$ V and $I = -100 \mu\text{A}$ at room temperature.

any artifact arising from the stray magnetic field from the detector FM contacts on the graphene [107]. The absence of a sign change of the spin signal also indicates that the CSC does not originate from proximitized graphene in the device [123]. This is because both the proximity-induced SHE and the proximity-induced REE would have given rise to a sign change of the spin polarization with change in the carrier type in graphene [120, 123, 151]. The possibility that the change of the charge carrier type would be prevented by screening of the electric field in graphene due to the proximity to the TI [152] was deemed very unlikely because a sign-change of the proximity-induced REE signal has previously been observed with change of carrier type in similar CVD graphene/TI heterostructures [123].

Furthermore, the contribution from the bulk SHE and the bulk REE in the TI are, however, not expected to cause a sign change, since this would necessitate the Fermi level to be tuned across the TI band gap and would therefore require a very large applied gate voltage [123, 125]. The TSML does not give a sign change either, even when the Fermi level is tuned across the TI Dirac point, due to the opposite chirality of the TSML above and below the Dirac point, which counteracts the effect of the changed charge carrier types [123, 148]. It should furthermore be noted that the device geometry is not very suitable for observing

proximity-induced CSC, since these effects require the charge and spin currents to be perpendicular at the graphene/BSTS interface [113]. While it is possible for some charge current to flow in the y direction at the interface, this is not the main contribution of the charge current direction. Additionally, the proximity-induced SHE further requires out-of-plane spin polarization [113], which is not observed in the spin switch and Hanle measurements. However, because of the aforementioned similarities between the bulk SHE, the bulk REE and the TSML, it is not possible to further narrow down the exact contributions of the CSC at room temperature.

For comparison, signals from spin valve and Hanle measurements in pristine graphene, with FM electrodes as both spin injector and detector, are shown in Fig. 4.4e-f. Gate voltage modulation results in a behavior that is very similar to the case with CSC, with the main difference being the symmetry of the Hanle signals, as already discussed above.

4.1.5 The inverse charge-spin conversion (ICSC) signal in TI

Inverse CSC (ICSC) experiments were also performed with the TI to verify the Onsager reciprocity of the system, by injecting spin current from the FM contact into the graphene channel. The spin current in graphene is absorbed by the TI and produces a NL voltage, as shown in Fig. 4.5a for two different measurement geometries. The spin polarization causes the Fermi surface spin textures of the TI to shift from the equilibrium position in the way shown in the inset of Fig. 4.5a, which gives rise to a charge current. Spin switch measurements indeed showed ICSC effects (Fig. 4.5b), which was measured at room temperature. It can clearly be seen that the CSC (Fig. 4.3d, bottom signal) and the ICSC (Fig. 4.5b) obey the Onsager reciprocity by generating spin signals of opposite sign for similar bias current and the same geometry, due to the spin diffusion current having opposite directions in the two cases.

The spin polarization of BSTS in the ICSC measurement was determined to about 0.2%, slightly higher than for the CSC counterpart. The reason for this slight difference could be due to different spin injection and detection efficiencies of the graphene/BSTS and the graphene/FM contacts with and without bias voltages. Moreover, it is important to mention that the electric field across the BSTS flake in the CSC measurement, which is different from the ICSC measurement, can also reduce the measured spin polarization. Measurements in two geometries with opposite x components of the spin current showed a change in sign of NL voltage when the polarization of the injected spin current was reversed (Fig. 4.5b-c). This means that the ICSC has a dependence on the x component of the spin current, similarly to the direct CSC. This, combined with the fact that no sign change of the ICSC signal was detected for reversal of the gate voltage in both n- and p-doped graphene regimes (Fig 4.5d), agrees with the results from

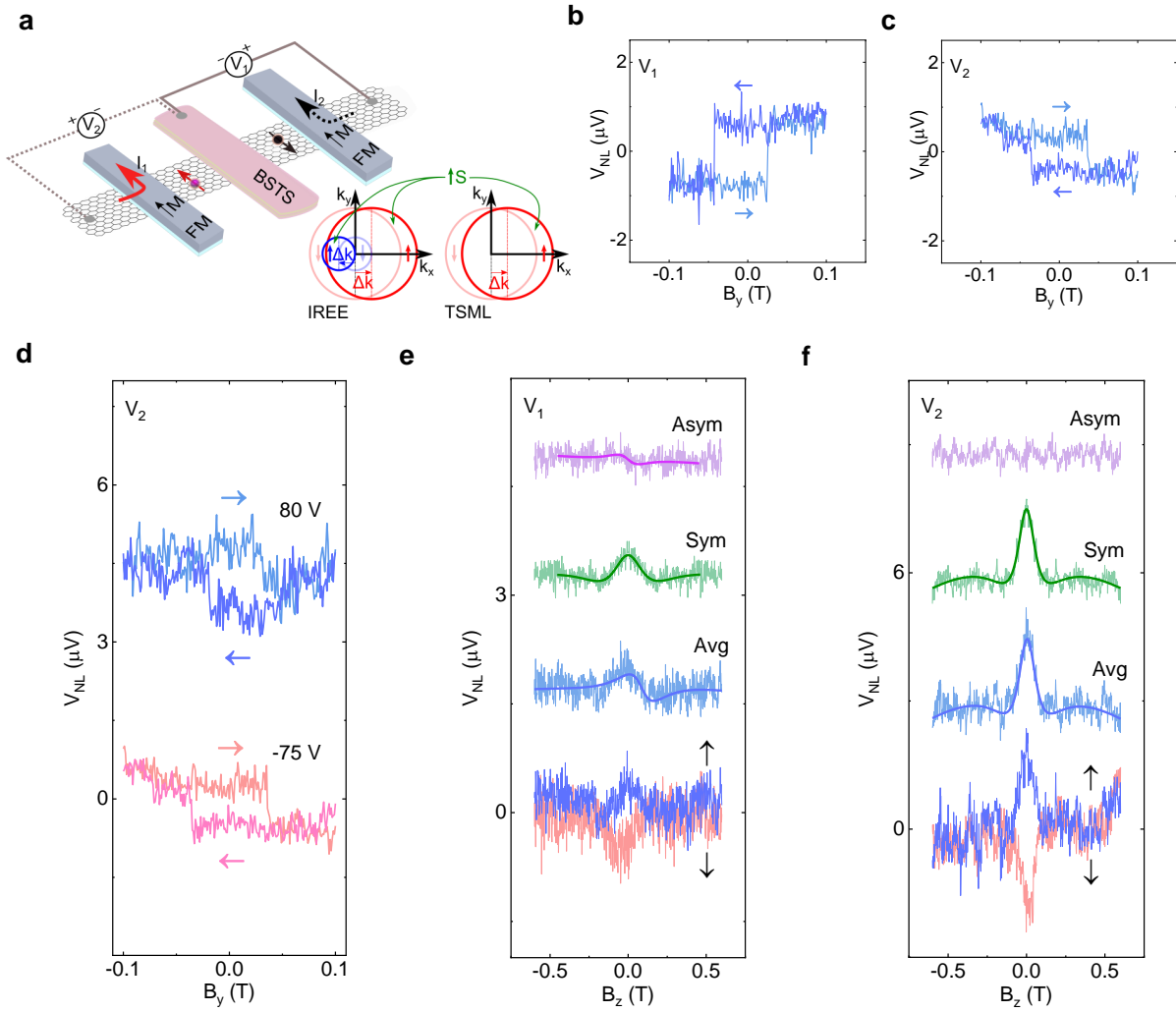


Figure 4.5: The inverse charge-spin conversion signal in graphene/BSTS junction. (a) Schematic of the device and the two different measurement setups for measuring ICSC. Inset: Schematic of ICSC through the inverse Rashba-Edelstein effect (IREE) and TSML. (b, c) Spin switch NL signals for each of the two measurement setups in (a). The measurements were performed for $I = -150 \mu\text{A}$ and $V_g = -70$ V and for $I = -100 \mu\text{A}$ and $V_g = -75$ V, respectively. (d) Spin switch NL signals for $V_g = 80$ V and $V_g = -75$ V at $I = -100 \mu\text{A}$ in measurement geometry 2. (e, f) Hanle spin precession signals for the two measurement setups with FM contact magnetization along the $+y$ (\uparrow) and the $-y$ (\downarrow) direction, respectively, as well as the averaged signal (Avg) and its symmetric (Sym) and antisymmetric (Asym) components. The green and purple solid lines are fits of the respective signal components, and the blue solid lines are guides to the eye for the averaged signals. The measurements were performed for $I = 130 \mu\text{A}$ and $V_g = -75$ V. The data are shifted vertically for clarity.

the CSC experiments and indicates that the ICSC comes from the TI and not from proximitized graphene.

The Hanle spin precession measurements in the two geometries are shown in Figures 4.5e-f. The signals for opposite contact magnetization direction were averaged and subsequently deconvoluted into symmetric and antisymmetric components in the same way as described for the CSC signals. The angles between the polarization of the injected spins from the FM contact and the SML of the TI were calculated to be $\phi = 24 \pm 8^\circ$ and $\phi = 7.2 \pm 0.2^\circ$ for the two geometries, respectively. The most likely explanation for the difference in asymmetry between the CSC (4.2a) and the ICSC (4.5e-f) signals is that the charge current of the CSC effects has a distribution along different paths through the interface and/or the BSTS flake with and without the application of a bias.

The spin Hall angle was estimated [113, 150, 153] to be $\theta_{SHE} \geq 2.8\%$ and the spin Hall length scale was subsequently calculated [113, 150] as $\lambda_{SHE} = \theta_{SHE} \lambda_s^{BSTS} \geq 0.55 \text{ nm}$, where λ_s^{BSTS} is the spin diffusion length of the BSTS. Similarly, the REE efficiency parameter was calculated [123] to be $\alpha_{REE} = 2.8\%$ and the Rashba-Edelstein length scale was estimated [123] to $\lambda_{REE} \leq \alpha_{REE} \lambda_s = 16.7 \text{ nm}$, where the spin diffusion length of graphene, λ_s , is chosen as an upper bound of the heterostructure spin diffusion length. However, these values are only to be regarded as rough estimates, due to the used models not being accurate for this measurement geometries.

In summary, CSC and its inverse effect are demonstrated at room temperature in the TI BSTS, using a hybrid device with a graphene spin valve. The lateral nonlocal spin switch and precession measurements, supported by the detailed dependence on bias current, gate voltage, different geometries and magnetization orientations, prove the robustness of the CSC effects in BSTS. It can be concluded that both the CSC and the ICSC originate from the bulk SHE or REE, from the TSML of the TI surface states or from a combination of these effects. These results prove CSC effects in TIs at room temperature, which is considered a potential candidate for SOT-based memory, logic and neuromorphic computing technologies [73]. With the recent progress in graphene spintronics [62, 64, 143], the attainment of TIs as spin injectors/detectors can also provide substantial advances in all-electrical spin-based devices and integrated circuits in 2D architectures.

4.2 Charge-spin conversion in TaTe₂

In addition to TI, a spin-polarized current source using nonmagnetic high conducting semimetallic layered materials is promising for next-generation all-electrical spintronic science and technology. This section presents electrical generation of spin polarization in a layered semimetal tantalum ditelluride (TaTe₂) via charge-spin conversion processes. Using a hybrid device of TaTe₂ in a van der Waals heterostructure with graphene (Gr), the spin polarization in TaTe₂ is efficiently injected and detected by nonlocal spin-switch, Hanle spin precession, and inverse spin Hall effect measurements. Systematic experiments at different bias currents

and gate voltages in a vertical geometry prove the TaTe₂ as a nonmagnetic spin source at room temperature. These findings demonstrate the possibility of spintronic devices in a two-dimensional heterostructure for spin-orbit technology.

4.2.1 Measurements of charge-spin conversion effects in TaTe₂

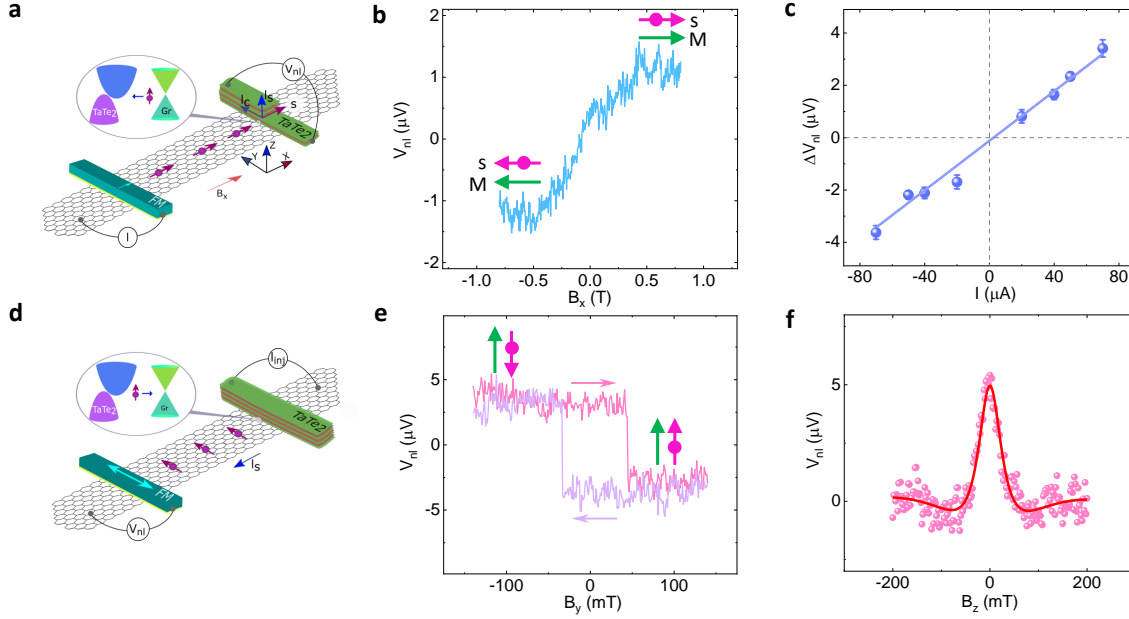


Figure 4.6: Charge-spin conversion effects in TaTe₂ at room temperature. (a) Measurement geometry to detect the inverse spin Hall effect (ISHE) in TaTe₂ by injecting a spin current from the FM via graphene channel into TaTe₂ and detecting a voltage signal across the TaTe₂ in a NL geometry. (b) ISHE signal V_{nl} measured with an in-plane magnetic field (B_x) sweep for $I = -50 \mu\text{A}$ at $V_g = 40 \text{ V}$ at room temperature. (c) Bias current dependence of the ISHE signal amplitude ΔV_{nl} with a linear fit (solid line). (d) Measurement geometry where TaTe₂ is used as a spin-polarized current source for vertical injection of spins into the graphene channel, which is finally detected by a FM contact in a NL geometry. (e,f) The spin-switch and Hanle spin precession measurements for spin injection from TaTe₂ with a B_y and B_z sweep, respectively, with an application of an $I = -30 \mu\text{A}$ at $V_g = 40 \text{ V}$. The up and down magnetic sweep directions are indicated by arrows in e for spin-switch experiments. A linear background is subtracted from the data.

First, the spin-to-charge conversion (SCC same as ICSC) experiments (measurement geometry in Fig. 4.6a) were performed in TaTe₂ via the inverse spin Hall effect (ISHE), when the Gr-TaTe₂ interface resistance, $R_{\text{int.}}$, was low. In this condition, the spin current is injected from an FM into the graphene channel is strongly absorbed by TaTe₂. The spin current in TaTe₂ subsequently gives rise to a transverse charge current due to the efficient SCC process in TaTe₂, which is

detected as a voltage signal (V_{nl}) across the TaTe₂ (Fig. 4.6b). By sweeping an in-plane magnetic field along the x-axis, B_x , the V_{nl} varies anti-symmetrically at low field and saturates at $B = \pm 0.4$ T as the magnetization of the injector FM rotates completely toward the x-axis. Considering the symmetry of the system with the spin current being absorbed from graphene into TaTe₂ along the z-direction, spin polarization (≥ 0.4 T) in the x-direction and manifested orthogonal charge current (I_c) is in the y-direction can be due to the ISHE or Edelstein effect (EE) in TaTe₂ [111]. The V_{nl} signal has been measured at different spin injection bias currents at room temperature, which scales linearly (Fig. 4.6c).

A large SCC signal is observed at room temperature in TaTe₂ with signal amplitude, $\Delta R_{SCC} = \Delta V_{nl}/I_{bias} = -1.69 \mu V / -20 \mu A \sim 84 \text{ m}\Omega$, which is about few times larger than in WTe₂, MoS₂ and Pt in heterostructure with graphene, one order of magnitude larger than in graphene-MoTe₂ heterostructure and few orders of magnitude higher than in Pt/Cu heterojunction but comparable to the graphene-TaS₂ heterostructure system [111–113, 151, 153–155]. It is to be noted that spin-orbit torque experiments using TaTe₂/FM heterostructure reported a dominating Oersted field contribution by local measurements [117], which is avoided in the NL measurements. From the manifested data, it is not possible to calculate the exact spin Hall angle ($\theta_{SH} \propto J_s/J_c$) in TaTe₂, as the spin diffusion length λ_{TaTe_2} , is unknown. Furthermore, the larger width of TaTe₂ flake ($2.6 \mu m$) compared to the spin diffusion length in graphene ($\sim 2.5 \mu m$) restrains the use of available model [111, 153, 154]. An estimation of θ_{SH} found to be in the range of 0.2 - 0.6 using a simple model and considering $\lambda_{TaTe_2} = 10 - 110 \text{ nm}$ and R_{int} of 10 - 100 Ω . Moreover, the estimated inverse Edelstein effect (IEE) of TaTe₂ through IEE length, $\lambda_{IEE} = \theta_{SH} * \lambda_{TaTe_2}$, is found $\lambda_{IEE} \approx 6 - 60 \text{ nm}$ as a function of λ_{TaTe_2} (10 - 110 nm).

Next, CSC mediated vertical spin injection (VSI) of in-plane spin polarization from TaTe₂ into a graphene channel at room temperature is realized (see Fig. 4.6d for measurement geometry). In the spin-switch experiment, the measured spin signal V_{nl} as a function of an in-plane magnetic field B_y sweep, which switches the magnetization of the FM detector contact from parallel to anti-parallel orientation with respect to the in-plane injected spin polarization from TaTe₂ (Fig. 4.6e). The amplitude ($\Delta R_{nl} = \Delta V_{nl}/I_{bias}$) of the CSC signal is about 240 m Ω . A confirmatory test of the in-plane spin polarization using a Hanle spin precession measurement was performed in the same NL geometry, where a perpendicular magnetic field (B_z) was swept while keeping the magnetization of the detector FM contact in the in-plane orientation. Figure 4.6f shows the Hanle data measured along with the fitting at room temperature while injecting spin from TaTe₂ into graphene channel. The spin lifetime $\tau_s = 195 \pm 26 \text{ ps}$ and spin diffusion length $\lambda_s = \sqrt{\tau_s D_s} = 1.98 \pm 0.3 \mu m$ are estimated in a channel length of $L = 3.75 \mu m$. The spin polarization of the FM detector contact is calculated about $P_{FM} \approx 6.13\%$. Subsequently, knowing the P_{FM} , the for the current-induced spin-polarization of

TaTe₂ is approximated to be about $P_{\text{TaTe}_2} = 1.34 \pm 0.26\%$.

4.2.2 Gate dependence of charge to spin conversion signal in TaTe₂

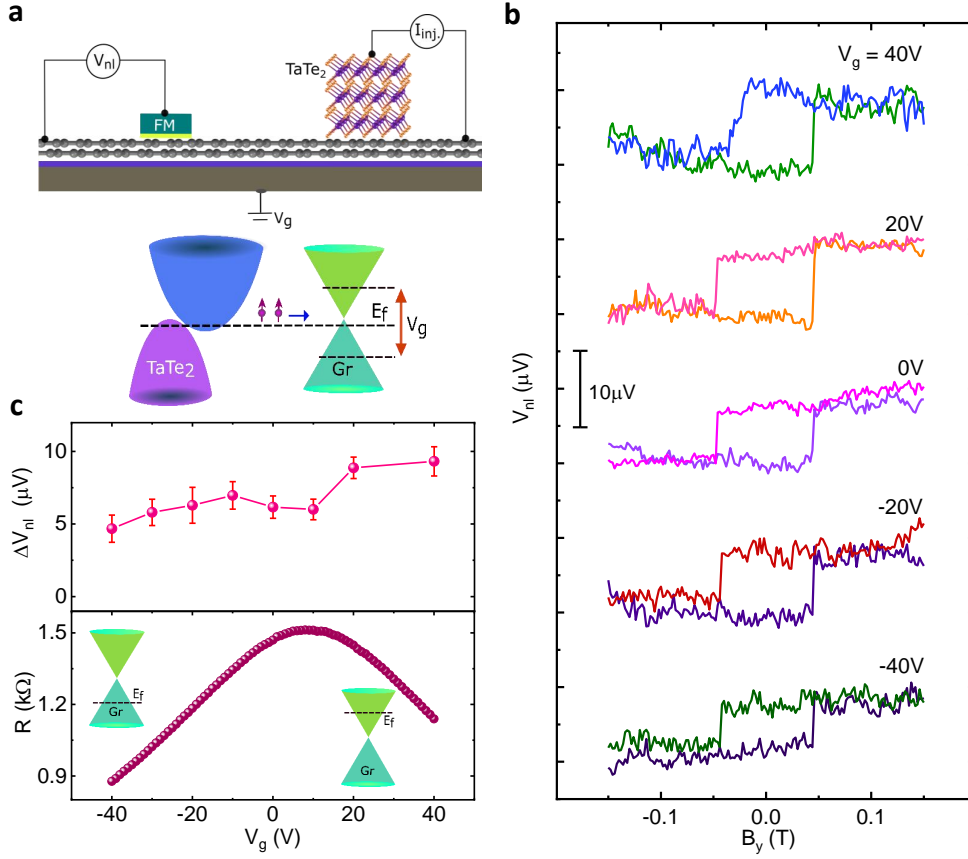


Figure 4.7: Gate dependence of CSC signal in TaTe₂-graphene heterostructure. (a) Measurement setup and band diagram of TaTe₂ and graphene with an application of a back-gate voltage (V_g) across the Si/SiO₂ substrate. (b) The measured NL spin-switch signals at various $V_g = -40$ V to 40 V for both n and p doped graphene regime with a bias current $I = -20 \mu A$ and room temperature. (c) The magnitude of the signal ΔV_{nl} as a function of V_g (top panel). The V_g dependence of the graphene-TaTe₂ heterostructure channel resistance (bottom panel) along with the Fermi-level position in the graphene band structure.

The back-gate (V_g) dependence of the VSI spin-switch signal due to CSC process in TaTe₂ as a spin injector is further investigated. Figure 4.7a shows a sketch of the graphene-TaTe₂ heterostructure and the change in the Fermi level position in graphene with an application of V_g for electron- and hole-doped regimes, whereas no change is expected in TaTe₂ due to its metallic properties. The measured spin-switch signals (V_{nl}) at various V_g in the range from -40 V to 40 V are depicted in Fig. 4.7b. The gate dependent magnitude of the spin signals ΔV_{nl}

($\Delta R_{nl} \approx 250 - 400 m\Omega$) is presented in Fig. 4.7c (top panel), which shows that the V_{nl} signal direction remains unchanged in the hole and electron transport regime. To compare ΔV_{nl} with heterostructure channel properties, the gate dependence of graphene-TaTe₂ heterostructure channel resistance is presented in the bottom panel of Fig. 4.7c, where the charge neutral point (V_{CNP}) is ~ 10 V with field-effect mobility of about $1074 \text{ cm}^2 \text{V}^{-1} \text{s}^{-1}$. These results rule out any contribution of the stray Hall effect produced by the fringe field from the FM detector contact edges on the graphene since this effect should change its sign with carrier types in graphene [107].

4.2.3 Bias dependence of charge to spin conversion signal in TaTe₂

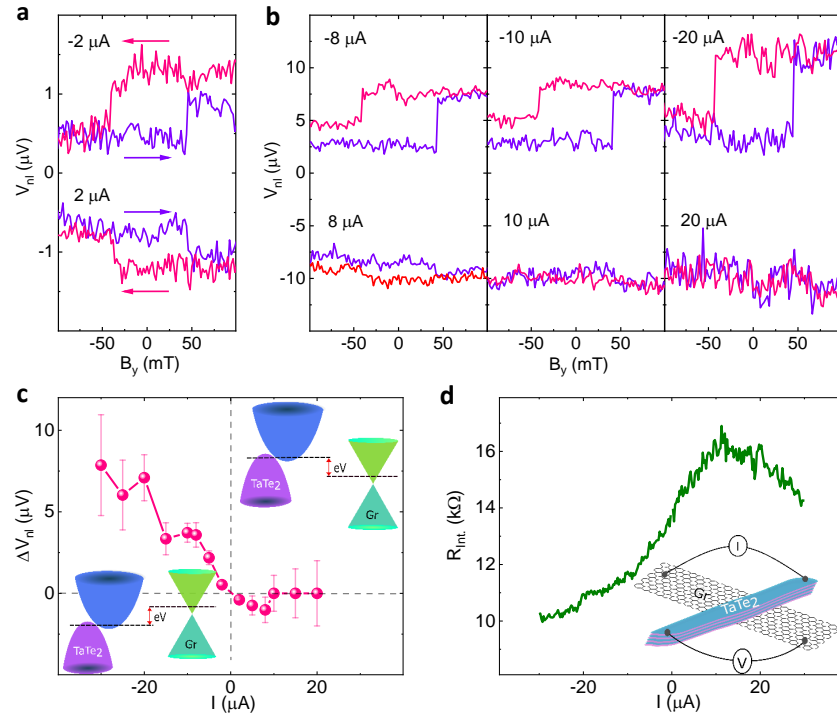


Figure 4.8: Electrical control of CSC signal in TaTe₂ and spin injection into graphene. (a) NL spin-switch signals (V_{nl}) with bias currents of $I = \pm 2 \mu\text{A}$ at $V_g = 20$ V. (b) The V_{nl} at different bias currents, measured at $V_g = 20$ V. The data are vertically shifted for clarity. (c) Bias dependence of the magnitude of the signal ΔV_{nl} . Insets: The schematic of the non-equilibrium Fermi level positions for positive and negative applied bias conditions. (d) The graphene-TaTe₂ interface resistance ($R_{int.}$) characteristics with bias current (I) measured in four-terminal geometry (inset).

Next, the electrical bias-controlled switching of the spin injection from TaTe₂ was measured. Figure 4.8a shows the spin-switch signal (V_{nl}) with injection bias currents of $I = \pm 2 \mu\text{A}$. Reversing the current direction creates opposite spin

polarization in TaTe₂ and hence accumulation of opposite spins in the graphene channel, which results in the opposite direction of the hysteretic behavior of the measured V_{nl} . A full bias dependent measurement was carried out at larger biases to understand the detailed energy dependence of the spin injection mechanism at the graphene-TaTe₂ junction (see Fig. 4.8b and 4.8c). In the -I range, an increase of the ΔV_{nl} with bias currents is observed, where the amplitude of the spin to charge conversion signal is about $\Delta R_{nl} = 300 \text{ m}\Omega$. However, for the +I, the ΔV_{nl} increases linearly for low biases up to $I = 8 \text{ }\mu\text{A}$ and disappears at larger bias within the measurement noise. One of the reasons for such bias dependence can be ascribed to the energy dependence of spin polarization in TaTe₂ or the availability of spin-polarized density of states near the Fermi level in TaTe₂. In contrast to local detection of spin signal as the measurements were performed in the NL geometry without any bias across the detector FM contact; any spurious effects originating from the detector can be ruled out. This asymmetric feature of the bias dependent spin injection effect in graphene-TaTe₂ heterostructure can be correlated to an electronic diode, where instead of controlling the charge current with bias in the conventional diode, it is possible to control the spin injection in the heterostructure. To examine the asymmetric bias dependent ΔV_{nl} , the bias dependence of the graphene-TaTe₂ interface resistance ($R_{int.}$) is checked (see Fig. 4.8d). Interestingly, $R_{int.}$ is observed to be asymmetric with bias, which can be the origin of the asymmetry in the spin injection signal due to a conductivity mismatch issue between the TaTe₂ spin source and graphene channel [144, 145].

To conclude, this section demonstrates efficient charge-spin conversion in semimetal TaTe₂ as an efficient spin injector and detector in a graphene-based spintronic device at room temperature. Detailed bias- and gate-dependent measurements of the CSC signals indicate that the origin of spin polarization can be mainly because of the SHE or REE in TaTe₂. Such a nonmagnetic spin source based on the charge-spin conversion effect shows great potential to replace the ferromagnetic injector in all-electrical 2D spintronic circuits and is suitable for spin-orbit technologies.

4.3 Charge-spin conversion in NbSe₂

Van der Waals metals with high spin-orbit coupling and novel spin textures have attracted significant attention for an efficient charge to spin conversion (CSC) process. This section presents electrical generation of spin polarization due to CSC in NbSe₂ up to room temperature. Characterization of NbSe₂ shows superconducting transition temperature, $T_c \sim 7\text{K}$. To probe the CSC process in NbSe₂, a graphene-based non-local spin-valve device is used, where the spin-polarization in NbSe₂ is efficiently injected and detected using non-local spin-switch and Hanle spin precession measurements. A significantly higher CSC in NbSe₂ is observed at a lower temperature. Systematic measurements provide the possible origins of the spin

polarization to be predominantly due to the spin Hall effect or Rashba-Edelstein effect in NbSe₂, considering different symmetry allowed charge-spin conversion processes.

4.3.1 Device properties and superconductivity of NbSe₂

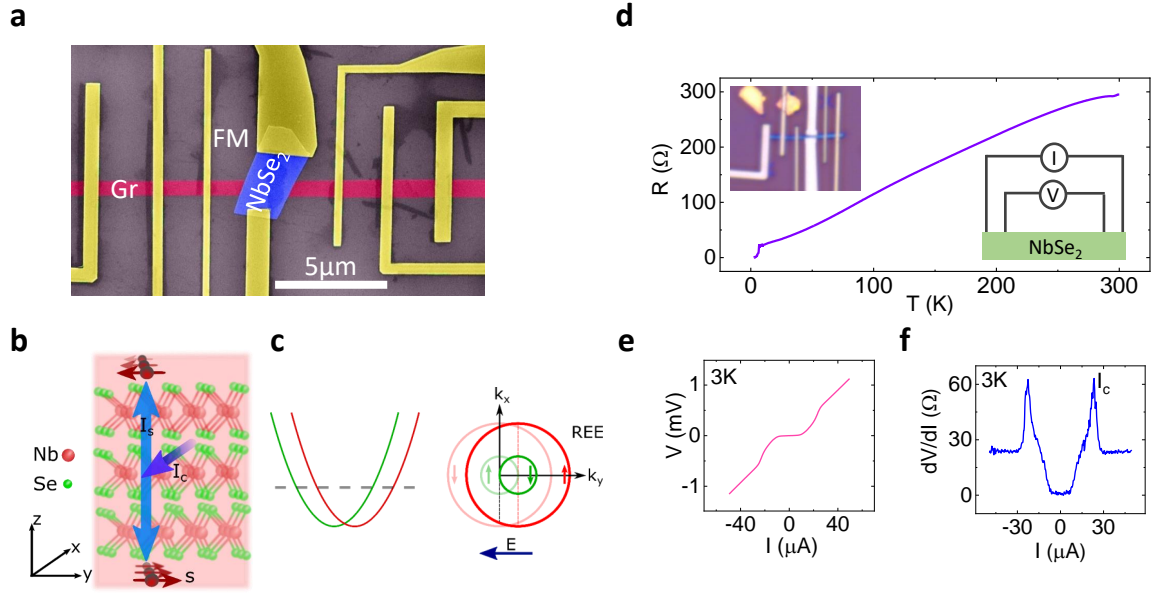


Figure 4.9: Device architecture and superconductivity of NbSe₂. (a) Colored scanning electron microscopic (SEM) image of a fabricated device consisting of CVD graphene, multilayer NbSe₂ flake (blue), and multiple FM contacts (yellow). The scale bar is 5 μm. (b) Schematic illustration of charge to spin conversion process due to conventional spin Hall effect. (c) Charge current from the applied electric field (E) induced spin polarization due to the Rashba-Edelstein effect (REE) at the Fermi surface in a high spin-orbit coupling system. (d) Temperature dependence of the longitudinal resistance of multilayer NbSe₂ flake, where superconducting critical temperature (T_c) around 6.8 K is evident. Insets are the device picture (top) and four-terminal measurement geometry (bottom). (e, f) The four-probe IV measurements and corresponding differential resistance as a function of the bias current in the multilayer NbSe₂ flake at 3 K.

Figure 4.9a presents the scanning electron microscopic (SEM) image of a NbSe₂-graphene vdW heterostructure device along with ferromagnetic (FM) contacts to characterize the spin transport properties in the heterostructure. As a high SOC material, NbSe₂ can give rise to current-induced in-plane (y-axis) spin polarization via conventional spin Hall effect (shown in Fig. 4.9b), where charge current (I_c) along the x-axis creates a transverse spin current (I_s) along the z-axis. Furthermore, high SOC in conjunction with breaking inversion symmetry in layered NbSe₂ crystal can result in Rashba spin splitting in the band structure with he-

lical spin texture with opposite spin-subbands, as shown in Fig. 4.9c. Upon application of an electric field (E), the charge current can shift the helical Fermi surface in the k-space and create net spin polarization via the Rashba-Edelstein effect. The created spin polarization in NbSe₂ can be injected into a graphene spin-channel in vdW heterostructure and detected by NL measurement geometry to realize a pure spin signal.

Next, superconducting properties of exfoliated multilayer NbSe₂ flake by measuring the temperature dependence of longitudinal resistance is shown in Fig. 4.9d. A DC bias current of 1 μ A is used and the superconducting critical temperature (T_c) in this flake is found to be 6.8K. The IV measurement with DC bias current and corresponding differential resistance (dV/dI) as a function of the bias current at 3K for the NbSe₂ flake are shown in Fig. 4.9e and 4.9f, respectively. The nonlinear IV is due to superconductive properties in NbSe₂ and from the dV/dI plot, the estimated critical current density is found, $J_c = 0.7 \times 10^6$ A/cm² for the multilayer NbSe₂ at 3K, consistent with the recent study [156].

4.3.2 Charge to spin conversion in van der Waals metal NbSe₂

In order to investigate the charge-spin conversion (CSC) effect in NbSe₂, a charge current is applied in a multilayer NbSe₂ flake to create a non-equilibrium spin polarization. The spins are injected into the graphene channel and finally detected by an FM contact in NL measurement geometry. Figure 4.10a shows a schematic illustration of the measurement geometry, used to detect the CSC effect in NbSe₂ along with the axis orientation and corresponding spin (s), charge current (I_c) and spin current (I_s). According to the measurement geometry in Fig. 4.10a by considering conventional SHE in NbSe₂, a charge current along x-axis can create an out-of-plane (z-axis) spin current, which renders spin polarization along y-axis. It is worth mentioning that the spin diffusion current in graphene spin channel is along x-axis in the measurement geometry with spin orientation towards y-axis after spin is created in NbSe₂ and injected into graphene. In the experiments, the non-local (NL) voltage is measured at the FM contact (left nearest contact to the NbSe₂ flake, shown in Fig. 4.9b) by applying varying magnetic fields along with the B_y and B_z directions. A varying magnetic field along the magnetic easy axis (y-axis) switches the magnetization of the FM contact and renders a switching signal which detects non-equilibrium in-plane spin in graphene injected from the NbSe₂ flake. The spin-switch signal, presented in Fig. 4.10b, is measured with $I = 400$ μ A at $V_g = -40$ V. The amplitude of the signal estimated from the change in NL resistance corresponding to the opposite magnetization of the FM contact is about $\Delta R_{nl} = 1.77 \pm 0.6$ m Ω .

Furthermore, an out-of-plane varying magnetic field (B_z) in this measurement geometry should render a Hanle spin precession signal, which unequivocally confirms the CSC process in the NbSe₂ and spin transport in the graphene spin

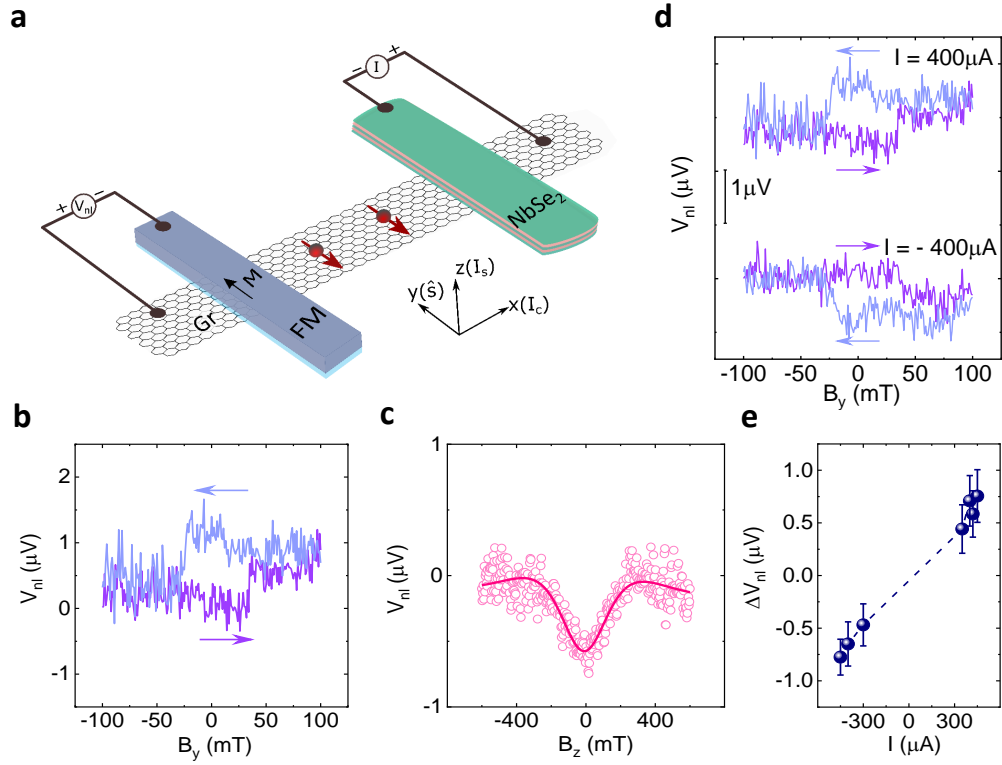


Figure 4.10: Charge-spin conversion in NbSe₂ at room temperature. (a) Schematic illustration of non-local (NL) measurement geometry to detect the charge-spin conversion effect in NbSe₂ by injecting spin current into the graphene spin channel. (b, c) The spin-switch and Hanle spin precession measurements for spin injection from NbSe₂ with a B_y and B_z sweep, respectively. For spin-switch experiments, the up and down magnetic sweep directions are indicated by arrows. A linear background is subtracted from the data. (d) NL spin-switch signals (V_{nl}) at room temperature with bias currents of $I = \pm 400$ μA and $V_g = -40$ V. A shift is added in the y-axis for clarity. (e) The magnitude of the spin-switch signal (ΔV_{nl}) with applied bias current in NbSe₂-graphene heterostructure. The error bars are calculated from the noise level of the non-local signal. All the measurements were conducted at room temperature.

channel. Figure 3(c) shows the manifested Hanle spin signal measured with $I = +420$ μA and $V_g = -40$ V while injecting spin from NbSe₂ into the graphene channel along with the fitting. The estimated spin lifetime, $\tau_s = 23 \pm 6$ ps and spin diffusion length, $\lambda_s = \sqrt{\tau_s D_s} = 0.65 \pm 0.05$ μm are found, considering the channel length $L = 2.4$ μm (distance between the center of the NbSe₂ flake to the center of the detector's FM electrode). In NbSe₂-graphene heterostructure, the lower τ_s in graphene spin channel after spin is injected from NbSe₂ can be attributed to the influence of long-range disorders, lattice deformation, and extrinsic interstitials in the graphene crystal that acts as spin-defect centers [157]. These imperfections might be introduced during processing CVD graphene, NbSe₂ transfer, and device fabrication processes. Additionally, spin absorption by NbSe₂ can also give rise to

lower τ_s because of the transparent NbSe₂-graphene interface. Interestingly, only a symmetric Hanle component is observed, although the NbSe₂ flake in the device is at an angle to the graphene spin channel [158]. Furthermore, any contribution from the spin injection from the FM contact on NbSe₂ can be eliminated from the spin switch signal, because the influence of any FM magnetization would have manifested typical spin valve signal with double spin-valve switching while sweeping B_y . Besides, Hanle measurement rules out any effect of stray fields from the detector FM contact on the manifested CSC signals, since the stray Hall effect would have rendered linear Hall signal for an out-of-plane field (B_\perp) [107].

Next, the spin polarization of NbSe₂ is found about $P_{NbSe_2} = 1 \pm 0.3\%$, estimating the spin polarization of FM contact on bare CVD graphene is $P_{Co} = 1.5 \pm 0.6\%$ [58]. The efficiency of the CSC process due to spin Hall effect in NbSe₂ can be characterized by the spin Hall angle ($\theta_{SH} \propto J_s/J_c$) and by using a simple model, the θ_{SH} of NbSe₂ is approximated from 0.68 ± 0.15 to 0.30 ± 0.06 by assuming the variation of spin diffusion length in NbSe₂, $\lambda_{NbSe_2} = 5$ nm to 40 nm [111, 153–155]. This estimation of θ_{SH} is consistent with the recently reported theoretical study, where θ_{SH} in NbSe₂ is predicted to be ≈ 0.5 by light irradiation [159]. Note that the spin diffusion length (λ_{NbSe_2}) in NbSe₂ is not experimentally reported yet. Moreover, the calculated Rashba-Edelstein length scale, $\theta_{SH} \cdot \lambda_{NbSe_2}$ (nm), associated with the CSC in NbSe₂ (5-13nm), is comparable to the recently reported length scale in layered TMDCs, e.g., 5nm in WSe₂ and 1.15nm in MoTe₂ [113, 160]. Another plausible origin of the measured CSC signal could be the Rashba-Edelstein effect (REE) due to Rashba spin-split bands in NbSe₂ and its proximity effect in the NbSe₂-graphene heterostructure region [161]. The characteristic efficiency parameter (α_{RE}) of the REE is calculated to be $5.3 \pm 1.8\%$, which is consistent with the recent studies on 2D material heterostructures [113, 122, 123, 125, 151].

To control the spin polarization in NbSe₂, the electrical bias dependence of the CSC signal in NbSe₂ is measured systematically. Figure 4.10d shows the spin-switch signal (V_{nl}) with bias currents of $I = \pm 400 \mu A$. It is evident that reversing the bias current direction results in opposite spin-switch signals due to the reversal of the accumulated spin polarization direction. A full bias-dependent spin-switch measurement was carried out and the amplitudes of the spin-switch signal (ΔV_{nl}) at different bias current are summarized in Fig. 4.10e with a linear fitting (dashed line). It can be seen that with increasing bias current the ΔV_{nl} increases linearly because a larger bias current generates more spin polarization in NbSe₂, which is eventually injected and measured in the graphene spin channel.

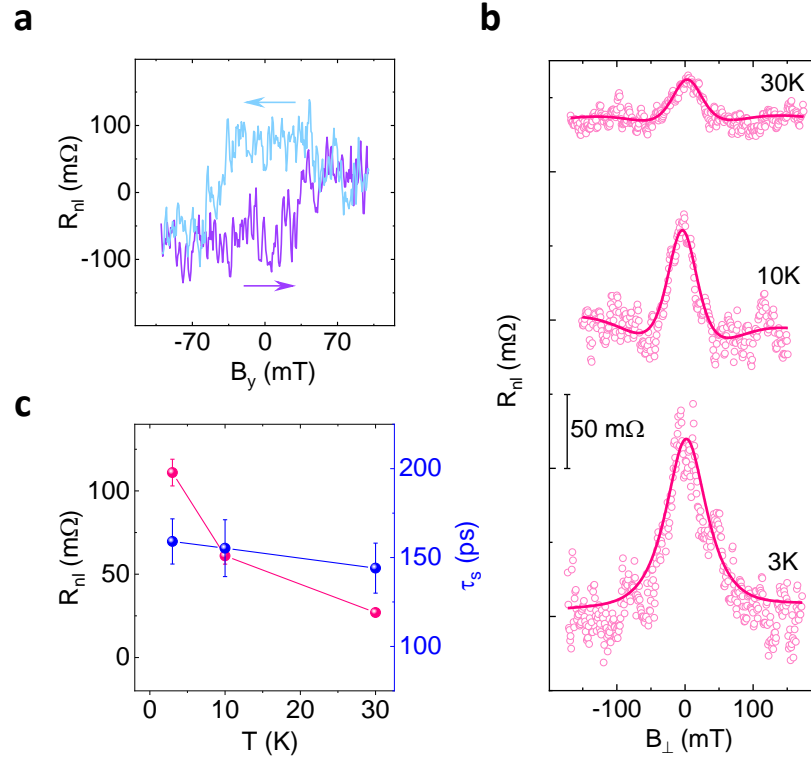


Figure 4.11: Temperature dependence of charge-spin conversion effect in NbSe₂. (a) Spin-switch signal for charge-spin conversion effect in NbSe₂ resulting in spin injection from NbSe₂ into graphene at 3K. (b) Hanle spin precession measurements along with the fitting (solid line). Measurements were performed in a bias current range of 200 - 500 μ A and at $V_g = -40$ V. A linear background is subtracted from the data and shifted along the y-axis for clear visualization. (c) The magnitude of the Hanle spin signal ΔR_{nl} and extracted spin lifetime (τ_s) at different temperatures.

4.3.3 Temperature dependence of charge-spin conversion in NbSe₂

The temperature dependence of the CSC process in NbSe₂ was measured to observe the evolution of spin polarization in NbSe₂ with temperature. Figure 4.11a shows the non-local spin-switch signal arising due to the CSC effect in NbSe₂ and subsequent spin injection into graphene at 3K. The magnitude of the CSC signal is found to be $\Delta R_{nl} \approx 106 \pm 27$ mΩ. Next, the Hanle spin precession signal above and below T_c of NbSe₂ is measured to validate the manifested spin-switch signal is a spin-related phenomenon. Fig. 4.11b shows the Hanle signals along with the fitting. The magnitude of the Hanle spin signal, ΔR_{nl} , and extracted spin lifetime τ_s at different temperatures (3 to 30K) have been shown in Fig. 4.11c. Interestingly it is observed that the ΔR_{nl} increases drastically below T_c , but τ_s remains unchanged around 150 ps, below and above T_c , because spin transport parameters

of graphene are known to be weakly dependent on temperature [112, 162]. Note that, as τ_s remains mostly unchanged, the larger ΔR_{nl} can be attributed to more efficient CSC conversion effect below T_c . However, the increase in CSC signal with decreasing temperature could also be due to the decrease of NbSe₂ resistivity (ρ_{NbSe_2}) and conductivity mismatch between NbSe₂ and graphene interface [163]. Interestingly, a recent report demonstrates multidirectional spin-to-charge conversion in graphene/NbSe₂ van der Waals heterostructures [119].

It is expected that quasiparticle mediated CSC process to be enhanced in the superconducting state of the corresponding material [164–166]. Besides, the spin lifetime can be extremely high in the superconducting state of NbSe₂ because it takes a longer time for the quasiparticles to scatter by the spin-orbit impurities in comparison to the normal electron scattering rates [164, 167]. Although the CSC signal is observed in NbSe₂ at 3K (below $T_c \sim 7K$), but it is to be noted that the NbSe₂ is not in the superconducting state in the CSC measurements as the applied bias current density ($\sim 4 \times 10^6$ A/cm²) is much higher than the critical current density ($\sim 0.7 \times 10^6$ A/cm² at 3K). It is needed to optimize the bias current magnitude to maximize the CSC signal at different temperatures to surmount the noise level of the signals, which vary due to the conductivity mismatch of the NbSe₂ and detector FM contact with the graphene spin channel.

The possible origins of the CSC effect in NbSe₂ are discussed here. First and foremost, the NL spin-switch and Hanle spin-precession measurements confirm that the detected signals are due to the in-plane (y-axis) spin-polarized current that is created in NbSe₂ and injected into graphene. We can rule out the spin polarization via proximity induced SHE because this effect would have resulted in an out-of-plane spin polarization (s_z) in the heterostructure region, which is not observed [121]. The CSC signal was observed only in the p-doped regime of graphene with higher negative gate voltage, most likely due to the conductivity mismatch issues of the graphene channel with NbSe₂ and FM contacts in the n-doped regime of graphene [144, 163]. Hence, proximity induced REE can neither be ruled out or nor be claimed to be the origin of the observed CSC signal with these measurements. Furthermore, the unconventional CSC process, which is recently reported in multilayer TMDCs (WTe₂ and MoTe₂), cannot also be disregarded in NbSe₂ since it is a layered material with structural inversion asymmetry in the crystal structure that can be further enhanced by the induced strain at the vdW heterostructure device geometry [112, 113]. Finally, considering the symmetry principle [113], the spin polarization direction (s) is set perpendicular to the applied charge current (I_c) and spin current (I_s) direction; the SHE and REE in NbSe₂ most likely merge or independently produce the observed CSC signal in NbSe₂.

The CSC effect in the normal metallic state of NbSe₂ up to room temperature is demonstrated. The engendered spin polarization can be injected into the graphene channel and detected in non-local measurement geometry via spin-switch and

Hanle spin precession measurements. A higher CSC signal in NbSe₂ is detected at a lower temperature, however, in its non-superconducting state. The spin-switch and Hanle signals reveal that the possible origins of the in-plane spin polarization are predominantly due to the spin Hall effect or Rashba-Edelstein effect in NbSe₂ considering different symmetry-permitted CSC processes. Such features of current-induced spin polarization in NbSe₂ have promising potentials to be used as a non-magnetic spin source in future all-electric spintronic devices and spin-orbit technologies.

5 Proximity-induced spin-orbit coupling in graphene and TMDC heterostructures

Graphene (Gr) is well-known for Dirac fermions and high carrier mobility along with long-distance spin transport due to its low spin-orbit coupling (SOC) [62, 64, 75, 80, 162]. Introduction of SOC in Gr can induce new basic phenomena and provide ways to control the spin polarization. Significant efforts have been made to enhance SOC in Gr to realize gate tunable spintronic functionalities [45]. One way to achieve sizable SOC in Gr is by employing chemically-adsorbed heavy adatoms [74, 168], however, doping can introduce defects in Gr and compromise the fascinating electronic properties [169]. Alternatively, the vdW heterostructures of Gr with high-SOC 2D materials, such as transition metal dichalcogenides (TMDCs) and topological insulators (TI), have emerged as a promising platform for proximity-induced SOC [42, 109], while preserving their electronic properties [71, 76, 77, 123]. This chapter, first, presents proximity-induced gate-tunable spin-galvanic effect (SGE) in vdW heterostructures of graphene with semi-metallic molybdenum ditelluride (MoTe_2) at room temperature. Next, proximity-driven spin-valley coupling and spin-relaxation anisotropy in graphene- MoS_2 heterostructure devices, prepared from scalable chemical vapor deposited (CVD) materials, are presented.

5.1 Proximity-induced spin-galvanic effect in MoTe_2 -Graphene heterostructure

The ability to engineer new states of matter and control their spintronic properties by electric fields is at the heart of future information technology. This section reports a gate-tunable spin-galvanic effect (SGE) in van der Waals heterostructures of graphene (Gr) with a semimetal of molybdenum ditelluride (MoTe_2) at room temperature. The observed SGE is stemmed from the proximity-induced SOC in Gr from MoTe_2 that renders efficient spin-charge conversion (SCC) process. Measurements in different device geometries with control over the spin orientations exhibit spin-switch and Hanle spin precession behavior, confirming the spin origin of the signal. The experimental spin-galvanic signals are supported by theoretic-

cal calculations considering the spin-orbit induced spin-splitting in the bands of the graphene in the heterostructure. The calculations also reveal an unusual spin texture in graphene heterostructure with an anisotropic out-of-plane and in-plane spin polarization. These findings open opportunities to utilize graphene-based heterostructures for gate-controlled spintronic devices.

5.1.1 Spin-galvanic signal in MoTe₂-graphene heterostructure

The charge-spin conversion (CSC) due to the proximity-induced SOC in Gr-MoTe₂ heterostructure can be measured by employing a direct Rashba-Edelstein effect (REE) or its inverse phenomenon (IREE) based methods [66]. The charge current-induced REE can be detected by a FM contact due to CSC. In contrast, for the IREE measurements, a spin current is injected from a FM into a heterostructure region and, consequently, a voltage signal is measured due to a SCC. Figure 5.1a shows the schematics of the NL measurement geometry used for the detection of SGE. The device consists of Hall-bar shaped Gr-MoTe₂ heterostructure region for spin-to-charge conversion, graphene channel for spin transport, Co/TiO₂ ferromagnetic contacts (FM) on graphene for spin injection, and Ti/Au contacts on graphene for detection of the voltage signal and also as reference electrodes, and Si/SiO₂ substrate acts as a global back gate. Due to the IREE in the Gr-MoTe₂ heterostructure region with a possibility of spin-split bands (5.1b), the diffused spin-polarized carriers create a non-equilibrium spin density across the heterostructure with a net momentum along the $\pm y$ -axis depending on the spin direction ($\pm s$).

The SGE measurements were performed in various device geometries such as magnetization rotation, spin switch, and Hanle spin precession methods. First, the results from magnetization rotation experiments in a device are demonstrated where the ferromagnetic contact is placed parallel to the Gr-MoTe₂ heterostructures, as shown in the schematics (Fig. 5.1a). In this measurement method, the spin current is injected from a FM contact into the graphene channel and diffused into the Gr-MoTe₂ heterostructure that is finally detected as a voltage signal (V_{SGE}) across the Hall-bar structure with non-magnetic Ti/Au contacts on graphene. A changing magnetic field is applied along the magnetic hard axis (B_x) of the FM magnetization that rotate the FM's magnetization orientation from magnetic easy axis (y -axis) to hard axis (x -axis). While sweeping the B_x , the corresponding voltage signal due to SGE is detected, $V_{SGE}(I_c) \propto \hat{z} \times n_s(I_s)$; here, I_c , \hat{z} and n_s are the induced charge current, out-of-plane direction and non-equilibrium spin density accumulated via spin current I_s , respectively. The direction of the injected spin is along $\pm x$ -axis at $B_x \gtrsim 0.4T$ and the V_{SGE} is controlled by sweeping a magnetic field in the x -direction ($\pm B_x$). Here, B_x induces spin precession together with rotation and saturates the magnetization of the injector FM (Fig. 5.1c).

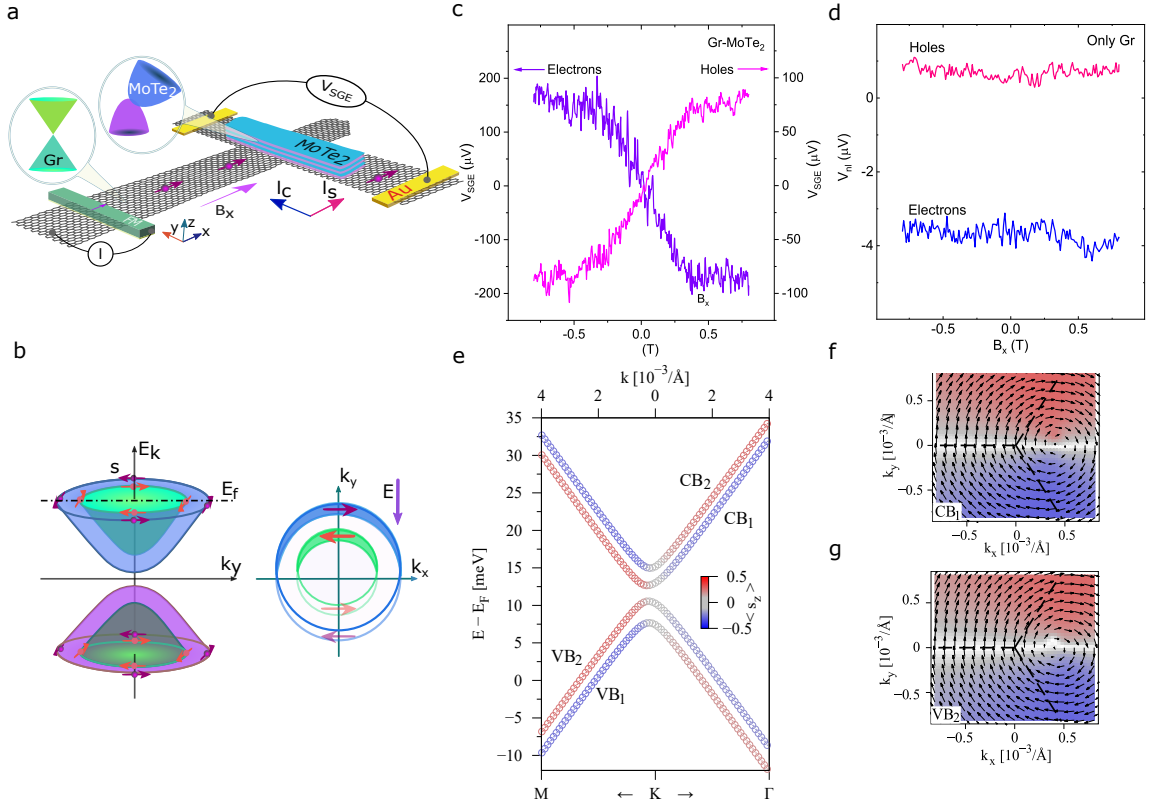


Figure 5.1: Proximity-induced spin-galvanic effect in graphene-MoTe₂ van der Waals heterostructure at room temperature. (a) The spintronic device schematic with the measurement scheme consisting of graphene-MoTe₂ heterostructure on Si/SiO₂ substrate, ferromagnetic (FM) and non-magnetic (Ti/Au) contacts on graphene. (b) A schematic band diagram of modified graphene in a heterostructure with MoTe₂, showing Rashba spin-split conduction and valence bands in accordance with the energy in momentum space (E_k), where Fermi energy (E_f) is in the conduction band. (c) Measured spin-galvanic signal (V_{SGE}) by sweeping a magnetic field along the x-axis (B_x) at room temperature in graphene-MoTe₂ heterostructure with $I = 80 \mu A$ in the electron and hole doping regimes, respectively. A linear background is subtracted from the data. (d) Measured non-local signals (V_{nl}) in pristine graphene Hall cross by sweeping a magnetic field in the x-direction (B_x) for electron- and hole-doped regions with $I = 100 \mu A$. (e) The low energy band structure of graphene in proximitized to MoTe₂ from density functional theory calculations. (f) Density functional theory calculations for similar clockwise spin texture in the outermost conduction (ϵ_1^{CB}) and valence band (ϵ_2^{VB}) in graphene-MoTe₂ heterostructure.

The spin precession due to the applied x-field ($\pm B_x$) will be in the y-z plane, and the projection of spin polarization along the x-axis will be the same during the spin precession. Nevertheless, the accumulated non-equilibrium spin density (n_s) depends on the spin direction towards the x-axis ($\pm x$) in the measurement system of IREE. Due to the unchanged spin projection along the x-axis during the spin precession, together with changing magnetization of the injector FM contact, the

resulting IREE signal increases with B_x until the saturation of FM magnetization (0.4T) without any contribution of spin precession. Accordingly, the measured V_{SGE} increases in the low field range and saturates at magnetic fields above $B \approx \pm 0.4T$. A giant spin-galvanic signal has been obtained at room temperature with an amplitude up to $\Delta R_{SGE} = \Delta V_{SGE}/I \sim 4.96\Omega$ (with $I = -80 \mu A$ at $V_g = 40 V$) and lower bound of the efficiency (α_{RE}) of I_{REE} is estimated to be 7.6% [121, 151].

In order to demonstrate the electric field-controlled switching of the SGE, V_{SGE} is measured for the electron (n) and hole (p) doped regimes of the Gr-MoTe₂ heterostructure. The applied gate voltage (V_g) modulates the Fermi level (E_f) position in the Gr-MoTe₂ hybrid bands for probing the spin-split REE-induced non-equilibrium spin accumulation (n_s) with different charge carrier types. Figure 5.1c shows the opposite signs of V_{SGE} signals for two different doping regimes, electrons (violet) at $V_g = 20V$ and holes (magenta) at $V_g = -10V$ at room temperature. The proximity-induced REE effect in graphene is predicted to be dependent on the conduction charge carrier type, i.e., electrons and holes, since spin polarity in Rashba contour remains unchanged in valence and conduction bands, unlike the spin-momentum locking in topological insulators [72, 170]. The observed SGE produces a charge current (I_c) perpendicular to the injected spin densities (n_s), which changes its direction because of a unidirectional accumulation of electrons and holes ($-q$ for electrons and $+q$ for holes) in the heterostructure with specific spin orientations. So, it can be concluded that the measured SGE signal and the sign change of the V_{SGE} is inherently due to induced IREE in Gr-MoTe₂ heterostructure. To compare the induced SGE in Gr-MoTe₂ with pristine graphene, NL signals (V_{nl}) are measured for electron- and hole-doped regions, depicted in Fig. 5.1d, with $I = 100\mu A$ at $V_g = 70V$ and $-50V$, respectively. The resultant signals can be considered as null noise-signals because of the absence of REE in pristine graphene.

To understand the experimental findings of SGE, density functional theory (DFT) calculations of the electronic band structure of Gr-MoTe₂ heterostructure were carried out to identify the Rashba spin texture to verify the enhanced SOI strength in the heterostructure [171, 172]. The low energy band structure of the graphene and 1T'-MoTe₂ heterostructure is presented in Fig. 5.1e and four states ($\epsilon_{1/2}^{VB/CB}$) of Rashba spin-splitting with SOI strength of around 2.5meV are found. It can also be noticed that the bands display a clear signature of Rashba SOI, as the spin in the outermost conduction (ϵ_1^{CB}) and valence band (ϵ_2^{VB}) is aligned clockwise (Fig. 5.1f, g), while the corresponding spin-orbit split partner bands (for example, ϵ_1^{CB} and ϵ_2^{CB}) show a counter-clockwise sense of spin-alignment. The calculations have also revealed an unusual proximity-induced spin texture in graphene: the out-of-plane spin polarization is highly anisotropic around K, and the in-plane spin polarization (Rashba) vortex is shifted from K. Such a spin texture in the graphene valence and conduction band in the heterostructure can

explain the measured SGE signal, where the sign of the SGE signal is efficiently controlled by the application of a gate voltage.

5.1.2 Spin-galvanic signal with perpendicular FM

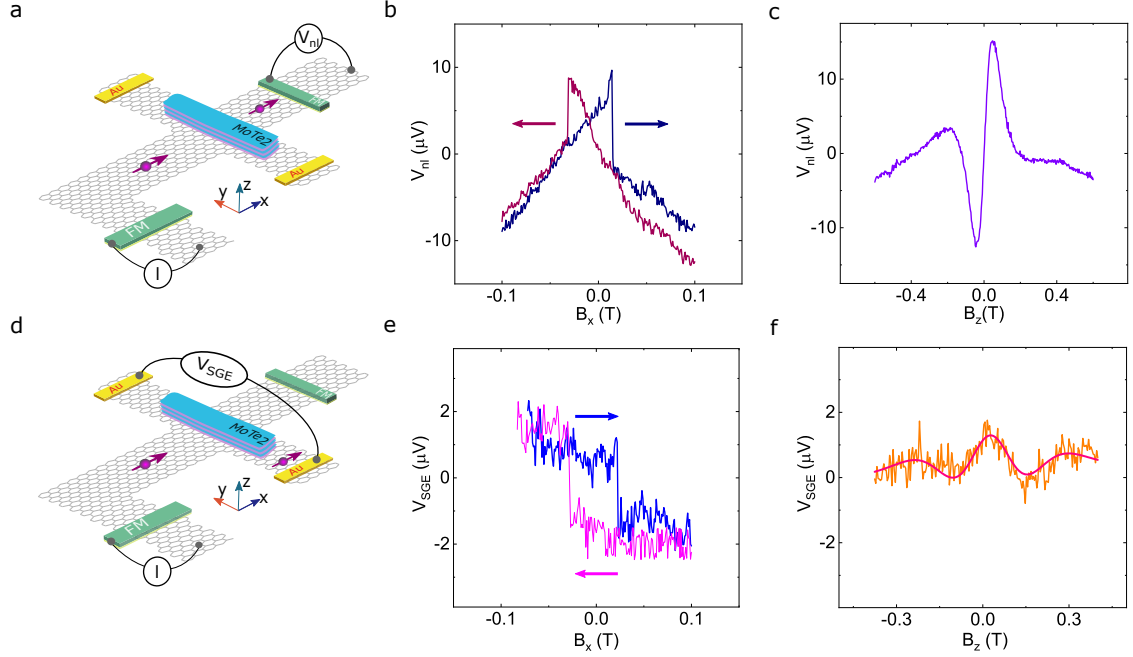


Figure 5.2: Spin-galvanic signal with an injector ferromagnet (FM) perpendicular to the graphene-MoTe₂ heterostructure. (a) A schematic of the device and measurement geometry to measure the non-local spin signal with a ferromagnetic detector in graphene across the graphene-MoTe₂ heterostructure. (b, c) Spin valve and Hanle spin precession measurements, respectively. A linear background is subtracted from the data. (d) A schematic of the device and measurement geometry to measure the non-local spin-galvanic signal (V_{SGE}) with non-ferromagnetic detectors (Ti/Au) along the Hall-cross of graphene-MoTe₂ heterostructure. (e) The spin-galvanic signal, V_{SGE} , is measured with varying in-plane magnetic field (B_x) at room temperature. (f) The spin-galvanic signal was detected via Hanle spin precession with varying out-of-plane magnetic field (B_z) along with Hanle fitting.

To substantiate the proximity-induced SGE in Gr-MoTe₂ heterostructure via spin-switch and Hanle spin precession measurements [123], a different device is fabricated where an injector FM is placed perpendicular (x-axis) to the heterostructure. At first, the spin transport properties in graphene across the Gr-MoTe₂ heterostructure have been verified. Figure 5.2a depicts the schematic of the device and measurement geometry to measure the non-local spin signal with a FM detector in graphene across the Gr-MoTe₂ heterostructure. The non-local spin valve (V_{nl}) in graphene is depicted in Fig. 5.2b with $I = -300\mu A$ at $V_g = -50V$,

where the magnetic field is applied along the easy axis of the injector's magnetization (x-axis). The Hanle spin precession signal in graphene is presented in Fig. 5.2c with $I = -50 \mu\text{A}$ at $V_g = -50\text{V}$. The characteristic switching in spin-valve and antisymmetric Hanle are due to the perpendicular magnetization of the injector (x-axis) and detector (y-axis) FM contacts. Next, the non-local SGE signal in the Gr-MoTe₂ has been investigated. Figure 5.2d shows the schematic of the device and measurement geometry to measure non-local SGE signal (V_{SGE}) with Ti/Au contacts along the Hall-cross of Gr-MoTe₂ heterostructure. In this measurement geometry, it is expected that applying a changing magnetic field along the easy axis (x-axis) of the FM injector should have manifested a spin switch signal across the Hall-cross due to proximity-induced SGE. The SGE signal with varying in-plane magnetic field (B_x) at room temperature is presented in Fig. 5.2e with $I = -100 \mu\text{A}$ at $V_g = -50\text{V}$. As the graphene channel was highly doped in this device, a complete gate-dependent measurement could not be performed, as the signal became noisy at positive gate voltages. As a confirmation of the spin-related origin of the observed SGE, Hanle spin precession with out-of-plane field B_z is measured and shown in Fig. 5.2f along with fitting for $I = -100 \mu\text{A}$ at $V_g = -50\text{V}$. The spin lifetime and spin diffusion length in Gr-MoTe₂ heterostructure are extracted to be around $\tau_s = 20 \text{ ps} \pm 1 \text{ ps}$ and $\lambda_s = 155 \text{ nm} \pm 5 \text{ nm}$.

In short, this part demonstrated the electrical detection and control of proximity-induced Rashba spin-orbit interaction in vdW heterostructures at room temperature. The observed SGE in the heterostructure of semi-metallic MoTe₂ and large-area CVD graphene can offer unique advantages for faster and low-power spin-charge conversion-based spintronic devices. The proximity effect enables graphene to acquire strong SOI and a spin texture with spin-split conduction and valence bands, which is ideal for tuning by a gate voltage. Controlling the magnitude and sign of the spin voltage by an external electric field at room temperature can be efficiently used for gate tunable spin-orbit torque (SOT) based magnetic random-access memory (MRAM) [39] and logic technologies [173].

5.2 Spin dynamics in all-CVD Graphene-MoS₂ heterostructure

Two-dimensional (2D) van der Waals (vdW) heterostructures fabricated by combining 2D materials with unique properties in one ultimate unit can offer a plethora of fundamental phenomena and practical applications. Recently, proximity-induced quantum and spintronic effects have been realized in heterostructures of graphene with 2D semiconductors and their twisted systems. However, these studies are so far limited to exfoliated flake-based devices, limiting their potential for scalable practical applications. This section reports spin-valley coupling and spin-relaxation anisotropy in graphene-MoS₂ heterostructure devices prepared

from scalable chemical vapor deposited (CVD) 2D materials. Spin precession and dynamics measurements reveal an enhanced spin-orbit coupling (SOC) strength in the heterostructure in comparison to the pristine graphene at room temperature. Consequently, a large spin relaxation anisotropy is observed in the heterostructure, providing a method for spin filtering due to spin-valley coupling. These findings open a scalable platform for all-CVD 2D vdW heterostructures design and their novel device applications.

5.2.1 Device properties and electronic transport across the all-CVD graphene-MoS₂ heterostructure

Figure 5.3a shows the schematic of a device structure consisting of CVD grown Gr-MoS₂ heterostructure along with multiple contacts on Si/SiO₂ substrate, which allows to apply back-gate voltage (V_g). The bottom panel in Fig. 5.3a illustrates the band diagram of Gr and MoS₂ with spin-split bands for up and down spins. Interestingly, in the vdW heterostructure region, MoS₂ can induce SOC into graphene via proximity effect and modify the band structure (presented by the band diagram) and spin transport in the channel [71, 126]. An optical micrograph of a fabricated device is presented in Fig. 5.3b, where the CVD graphene strip is covered with a single layer of CVD MoS₂, which was transferred by wet transfer technique [174]. Subsequently, e-beam lithography was performed to make contacts of TiO₂ (~ 1 nm)/Co (~ 80 nm) to manifest charge and spin transport properties.

First, the individual CVD-grown single-layer material is characterized to inspect their electrical properties. The transport properties (source-drain current I_{ds} vs. gate voltage V_g) of single-layer MoS₂ are depicted in Fig. 5.3c for different bias voltages V_{ds} , along with I_{ds} vs. V_{ds} at different V_g in the inset. The channel current (I_{ds}) increases monotonically with increasing V_{ds} and the I_{ds} increase with increasing V_g for a fixed V_{ds} due to increasing carrier concentration in the MoS₂, which corresponds to n-type transport properties as expected for the MoS₂ [129]. The estimated field-effect mobility is found by $\mu = (Lg_m)/(WC_gV_{ds}) = 1.21 \text{ cm}^2\text{V}^{-1}\text{s}^{-1}$; where L , W , C_g and g_m are the channel length, width, gate capacitance per area ($1.15 \times 10^{-8} \text{ Fcm}^{-2}$ for 285nm SiO₂) and transconductance, respectively.

Next, charge transport properties are measured for Gr-MoS₂ vdW junction. Figure 5.3d shows the measured I_{ds} as a function of applied V_{ds} at various V_g along with the measurement geometry. The asymmetric I_{ds} for positive and negative V_{ds} with diode-like behavior could be due to work function mismatch between the electrodes and the materials [87, 89]. The transfer characteristic (I_{ds} vs. V_g) of the Gr-MoS₂ heterostructure for $V_{ds} = 1\text{V}$ is depicted in Fig. 5.3e, both in a linear and log-scale. An increase of I_{ds} with increasing positive V_g is observed that is derived mainly from the transport properties of MoS₂, where graphene acts as

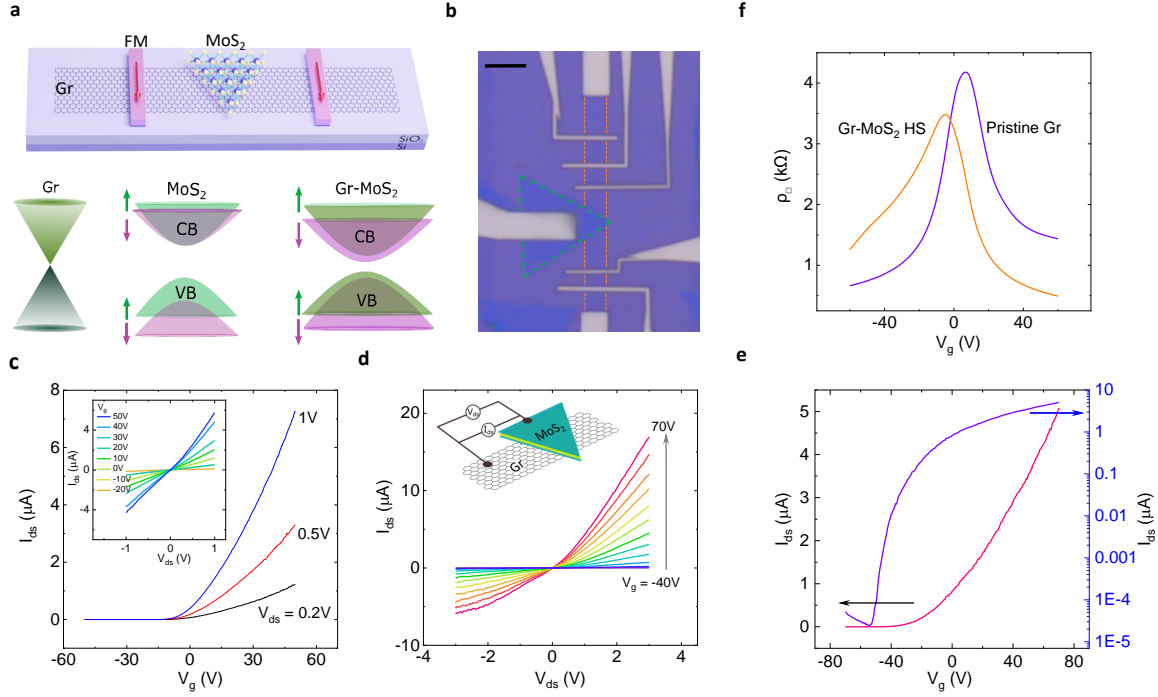


Figure 5.3: All-CVD graphene-MoS₂ heterostructure spintronic device and electrical properties. (a) Graphical representation of the Gr and MoS₂ vdW heterostructure device on Si/SiO₂ substrate along with the FM contacts. Pictorial depiction of the band diagram of Gr, MoS₂, and their heterostructure with spin-split bands. (b) Optical image of CVD Gr (orange dotted line) and CVD MoS₂ (green dotted line) vdW heterostructure along with the different FM (Co/TiO₂) contacts. The scale bar is 5 μm . The width and the shapes of the FM contacts are designed on Gr to facilitate spin injection and detection. (c) Source-drain current I_{ds} as a function of the applied back-gate voltage (V_{g}) of single-layer of CVD MoS₂ field-effect transistor with different source-drain bias voltages V_{ds} . Inset shows I_{ds} vs. V_{ds} at different V_{g} . (d) I_{ds} vs. V_{ds} plots at different gate voltages between Gr-MoS₂ along with the measurement geometry in the inset. (e) Transfer properties (I_{ds} vs. V_{g}) between Gr-MoS₂ at $V_{\text{ds}} = 1\text{V}$ in linear (pink) and log (violet) scale. (f) Gate-dependent resistivity of Gr channels in pristine and heterostructure regions probed in four-terminal measurement geometry.

vdW contact. The field-effect mobility μ is estimated to be $12.4 \text{ cm}^2\text{V}^{-1}\text{s}^{-1}$ in the Gr-MoS₂ heterostructure, which is one order of magnitude higher than the pristine MoS₂. This enhancement of mobility of MoS₂ with graphene contact is attributed to lesser defect states in the MoS₂ contact region and smaller Schottky barrier in the vdW interface [89, 175, 176]. Figure 5.3f presents the V_{g} dependent Gr resistivity ($\rho_{\square} = (R_{\text{AT}}W)/L$) in the pristine and Gr-MoS₂ heterostructure region, with Dirac point at 6.8V and -5V, respectively. The μ is estimated to be $2340 \text{ cm}^2\text{V}^{-1}\text{s}^{-1}$ for pristine Gr and $3000 \text{ cm}^2\text{V}^{-1}\text{s}^{-1}$ for the Gr-MoS₂ heterostructure regions. The electrical properties of the heterostructure region indicate the ex-

cellent quality of materials, and wet transfer of CVD MoS₂ on CVD Gr does not have a detrimental effect on its phenomenal electrical transport properties [62, 143].

5.2.2 Spin-lifetime anisotropy in the graphene-MoS₂ heterostructure

It is predicted that graphene in proximity to high SOC materials can give rise to large spin lifetime anisotropy ($\xi = \tau_{\perp}/\tau_{\parallel}$) in the system, mainly by means of induced Rashba SOC or spin-valley coupling [127]. The SOC associated with Rashba spin-split bands gives rise to a higher in-plane spin lifetime ($\tau_{\parallel} > \tau_{\perp}$) and anisotropy of less than unity ($\xi < 1$). On the other hand, induced spin-valley coupling in the heterostructure renders higher out-of-plane spin polarization ($\tau_{\parallel} < \tau_{\perp}$) and results in $\xi > 1$ because of dominant out-of-plane spin polarization in different valleys (K and K') of the TMDC [58, 126, 128]. To verify the dominant SOC mechanism in all-CVD Gr-MoS₂ heterostructure region, anisotropy (ξ) was estimated by employing oblique magnetic field-dependent evolution of Hanle spin precession signals [177]. In this measurement scheme (Fig. 5.4a), the changing magnetic field (B) is applied at an angle (β) to the FM contact in the yz-plane and let the spins perpendicular to the external magnetic to dephase. Hence, the manifested NL resistance only measures the projection of the dephased spin onto that applied field direction. Figure 5.4b shows measured Hanle spin precession signals for different magnetic field directions.

Figure 5.4c shows the normalized value of the non-local resistances ($R_{nl,\beta}/R_{nl,0}$) as a function of $\cos^2(\beta^*)$ for the respective applied field (B) direction in the dephased regime, which is highlighted by the shaded region in Fig. 5.4b. Here, β^* is the angle with a smaller correction of the out-of-plane tilting angle of the FM contacts due to the external magnetic field [177]. The average value of data points is accounted to reduce the effect of the measurement noise in the analysis. The data points is fitted with the following equation 5.1 (Fig. 5.4c).

$$\frac{R_{NL}^{\beta}}{R_{NL}^0} = \sqrt{\cos^2(\beta) + \frac{1}{\xi} \sin^2(\beta)}^{-1} \exp \left[-\frac{L}{\lambda_{\parallel}} \left(\sqrt{\cos^2(\beta) + \frac{1}{\xi} \sin^2(\beta)} \right) \right] \cos^2(\beta^*) \quad (5.1)$$

Here, L represents the heterostructure channel length, and λ_{\parallel} is the in-plane spin diffusion length. The anisotropy, $\xi \approx 1.6 \pm 0.13$ is found in the Gr-MoS₂ heterostructure channel. Consequently, the spin-valley coupling is estimated in the Gr-MoS₂ heterostructure by using the following equation [127]:

$$\xi = \left(\frac{\lambda_{VZ}}{\lambda_R} \right)^2 \frac{\tau_{iv}}{\tau_p} + \frac{1}{2} \quad (5.2)$$

Here, λ_{VZ} and λ_R are the valley Zeeman and Rashba SOC constants; τ_{iv} and

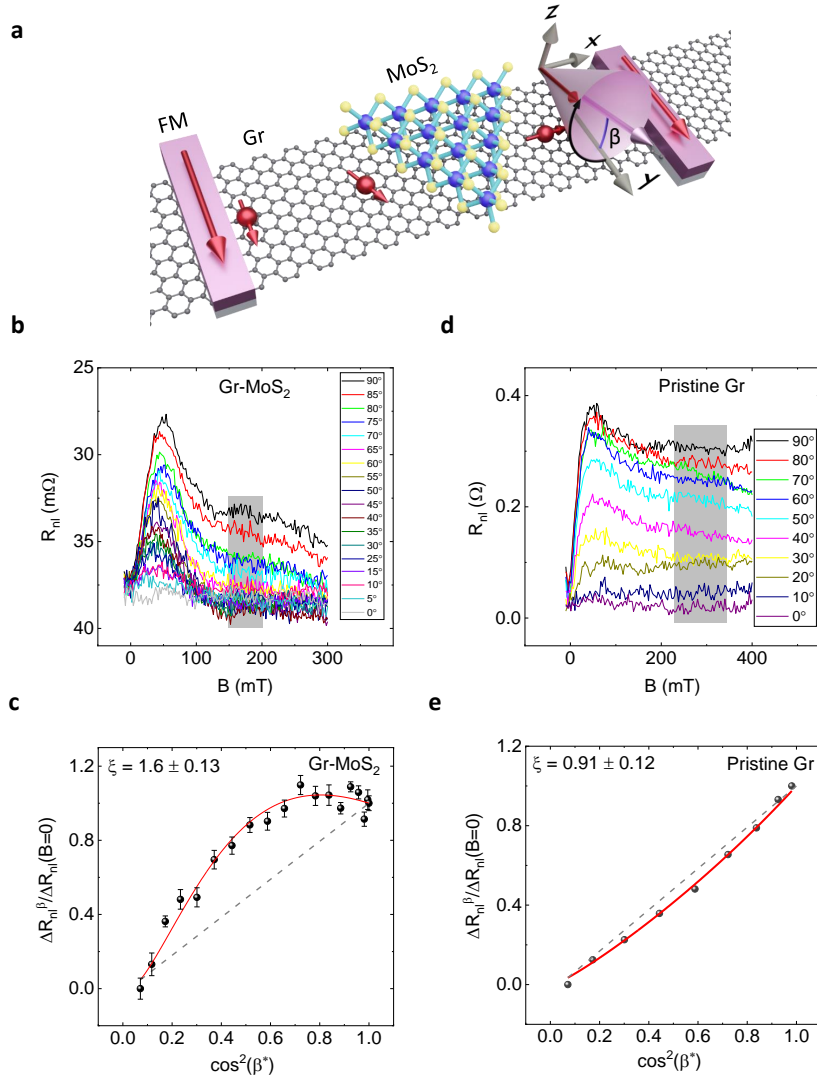


Figure 5.4: Spin-lifetime anisotropy in the Gr-MoS₂ heterostructure (a) Schematic illustration of the device and measurement scheme for spin precession in Gr-MoS₂ heterostructure with an oblique magnetic field. The applied magnetic field is at an angle β along the magnetic easy axis of the FM contacts (y-axis) in the yz-plane. (b) Spin precession signals as a function of changing B field at different angles with $I = -350 \mu\text{A}$ at $V_g = 40\text{V}$. (c) Data points denote normalized non-local resistances ($R_{nl,\beta}/R_{nl,0}$) as a function of $\cos^2(\beta^*)$ along with the fitting (red line) to equation 5.1 to estimate anisotropy. (d) Spin precession signals as a function of changing B field at different angles with $I = -100\mu\text{A}$ at $V_g = 20\text{V}$ in pristine graphene. (e) Data points denote normalized non-local resistances ($R_{nl,\beta}/R_{nl,0}$) as a function of $\cos^2(\beta^*)$ along with the fitting (solid line) to equation 5.1 to estimate anisotropy in pristine graphene. The gray dashed lines in c and e visualize isotropic case.

τ_p are the intervalley and momentum scattering lifetimes. It is observed that $\lambda_{VZ} \sim 238\mu\text{eV}$ by considering $\tau_{iv} \approx \tau_p$ and $\lambda_R = 227\mu\text{eV}$. The exact ratio of $\frac{\tau_{iv}}{\tau_p}$

is difficult to estimate; however, the relatively lower ξ must be compatible with the assumption, whereas the theoretical study report an anisotropy of $\xi = 20$, considering $\tau_{iv} \sim 5\tau_p$ [127].

To compare the estimated anisotropy in the heterostructure channel with the pristine graphene channel, oblique Hanle spin precession signals in pristine graphene at different magnetic field directions were measured, shown in Fig. 5.4d. Figure 5.4e shows the normalized value of the non-local resistances ($R_{nl,\beta}/R_{nl,0}$) as a function of β^* for the respective B direction in the fully dephased regime, which is highlighted by the shaded region in Fig 5.4d. The fit to equation 5.1 with the data points provides an estimation of anisotropy close to unity, $\xi \approx 0.91 \pm 0.12$, shown in Fig. 5.4e. It is expected that graphene on SiO₂ substrate should render isotropic spin lifetime [127, 143].

According to the theoretical calculations and recent experiments in exfoliated Gr-TMDC heterostructures, the anisotropy ξ can be in the range of 1 to 10 [126–128, 178]. For instance, exfoliated Gr-MoSe₂ and Gr-WSe₂ heterostructures show $\xi > 10$ at 75K, whereas Gr-WS₂ heterostructure shows $\xi \approx 10$ at room temperature [126, 128]. Furthermore, the anisotropy in exfoliated Gr-MoS₂ heterostructure is estimated to be higher than unity ($\xi > 1$) at room temperature [126]. The estimated spin lifetime anisotropy of $\xi = 1.6$ in the all-CVD Gr-MoS₂ heterostructure using oblique Hanle measurements can be due to proximity-induced spin-valley locking in graphene from MoS₂. Interestingly, the anisotropy in the Gr-TMDC heterostructure significantly depends on the intervalley (τ_{iv}) and momentum scattering (τ_p) lifetimes, which also depend on the charge scatterers (n) in the spin transport channel [127]. The proximity SOC strength and anisotropy can also be influenced by the interfacial interstitials, twist-angle and band alignment in the all-CVD Gr-TMDC heterostructure channels [174, 179].

In summary, this section demonstrated spin-valley coupling and spin-relaxation anisotropy in scalable all-CVD grown Gr-MoS₂ vdW heterostructure devices at room temperature. The CVD-grown materials and their heterostructures showed excellent charge and spin transport properties, showing the good quality of the hybrid devices and interfaces. The spin transport and Hanle precession in the heterostructure channel showed increased SOC strength in the proximitized graphene, which is three times higher than that in pristine graphene. The spin relaxation anisotropy properties evaluated using oblique Hanle spin precession measurements revealed an anisotropic spin dynamic of $\xi \sim 1.6$ in the proximitized graphene, compared to $\xi \sim 1$ in the pristine graphene channel. The associated spin-valley coupling strength of 238 μeV is estimated in the Gr-MoS₂ heterostructure. The observation of increased SOC strength and spin relaxation anisotropy between the in-plane and perpendicular spin polarization in all-CVD Gr-MoS₂ heterostructures have enormous prospects for making spin filtering devices in scalable all-2D materials.

6 WS_2 nanoribbon and all-CVD MoS_2 -graphene FETs

Semiconducting transition metal dichalcogenides (TMDCs) have attracted tremendous interest for high-performance and energy-efficient nanoscale field-effect transistors (FETs). In spite of recent progress on down-scaling the gate and channel lengths of TMDC FETs, the fabrication of sub-25 nm narrow channel width of TMDC FETs remained challenging. This chapter demonstrates the fabrication of tungsten disulfide (WS_2) nanoribbon down to sub-10 nm width using a controlled anisotropic wet chemical nanostructuring technique. Nanoribbon FETs exhibit good transistor performance, where the transport parameters such as on-current, mobility, and threshold voltage are predominantly governed by the narrow channel effects. In addition, scalable chemical vapour deposition (CVD)-grown MoS_2 and graphene FETs are very promising for future nanodevices, especially for flexible solar cells, memory devices and neuromorphic computing. This chapter also shows transport properties, memristive switching and Schottky barrier analysis in CVD-grown MoS_2 -graphene heterostructure FET devices. These findings open the door for the fabrication of future-generation nanometer-scale transistors, sensors, optoelectronic devices, and integrated circuits based on van der Waals semiconductors.

6.1 Ultra-narrow semiconductor WS_2 nanoribbon FETs

Semiconductor field-effect transistors (FETs) representing the basic building blocks of modern computers have revolutionized information technology due to successful miniaturization over several decades [16]. However, continued down-scaling of conventional silicon transistors has reached its physical limits and poses critical challenges for its high performance and energy efficiency [24]. To facilitate continued progress, two-dimensional (2D) semiconducting transition metal dichalcogenides (TMDCs) have attracted tremendous interest due to their atomically thin body and dangling-bond-free surface [17]. The ultimate miniaturization of TMDC-based FETs will allow sustainable progress in Moore's scaling law for high-density integration [131] and enhanced performance beyond silicon technologies [32, 180–182].

The design and control of semiconducting TMDC-based FETs and engineering

their properties at an atomic scale are challenging and of paramount importance for advances in basic science and technology [30, 43]. Recently, considerable efforts have been devoted to scale-down the channel length and width of the TMDC-based FETs [132, 134, 135]. Devices with planar and vertical TMDC FET structures with sub-10nm channel [134, 183] length and sub-nm gate dimensions with carbon nanotube [130] and graphene [131] were realized [183, 184]. However, the channel width of the state-of-the-art devices is mostly limited to be more than 25 nm [132, 135–137] due to limited resolution of lithography processes and physical etching techniques used so far. Importantly, controlling edge structures remains one of the main interests because electronic properties of the edge-states become increasingly relevant in such nanoscale transistors [50–52].

Here, we demonstrate the fabrication of ultra-narrow WS₂ nanoribbons down to 9 nm width with atomically sharp zig-zag edges using a wet-chemical anisotropic etching technique with atomic precision [50]. Transistor performance with good channel conductance could be measured down to 18 nm width of WS₂ nanoribbon. The nanoribbons FETs of different widths (18-70 nm) were systematically investigated, showing the transport properties in the extremely narrow channels to be governed by the narrow channel effects. The mobility in the narrowest channel FETs is found to be limited by the impurity scattering process in comparison to the wider channels. A bias and gate-induced metal-to-insulator transition is observed in the temperature dependence of FETs, elucidating the percolation transport mechanism in the nanoribbons. These findings can promote the scaling down of transistors for next-generation electronics.

6.1.1 Device architecture and fabrication processes of WS₂ nanoribbon FETs

Figure 6.1a. presents the schematic of ultra-narrow nanoribbon FETs with multilayer WS₂ channels having atomically controlled zig-zag edges along with the measurement geometry. The colored scanning electron microscopic (SEM) image of the fabricated nanoribbon FETs of various channel widths is shown in Fig. 6.1b. Figure 6.1c shows the crucial steps for the fabrication of nanoribbons, where WS₂ flakes were exfoliated on SiO₂/Si substrate and are patterned first by electron lithography and CHF₃ ion beam etching. This is followed by a final anisotropic wet chemical etching using hydrogen peroxide (H₂O₂) to fabricate nanoribbons down to 9 nm width. This anisotropic wet etching yields WS₂ edges to be exclusively zig-zag and atomically sharp [50]. Figure 6.1d shows a comparison of the nanofabricated TMDC nanoribbon channel width with the state-of-the-art results, where channel width is limited by the resolution of lithography processes and physical etching techniques. Electronic transport properties were investigated in WS₂ nanoribbons FETs of different channel widths $W=9\text{nm}$ to 70 nm , thickness of $t=35\text{ nm}$, channel length $L=600$ to 800 nm , with Ti/Au source and drain

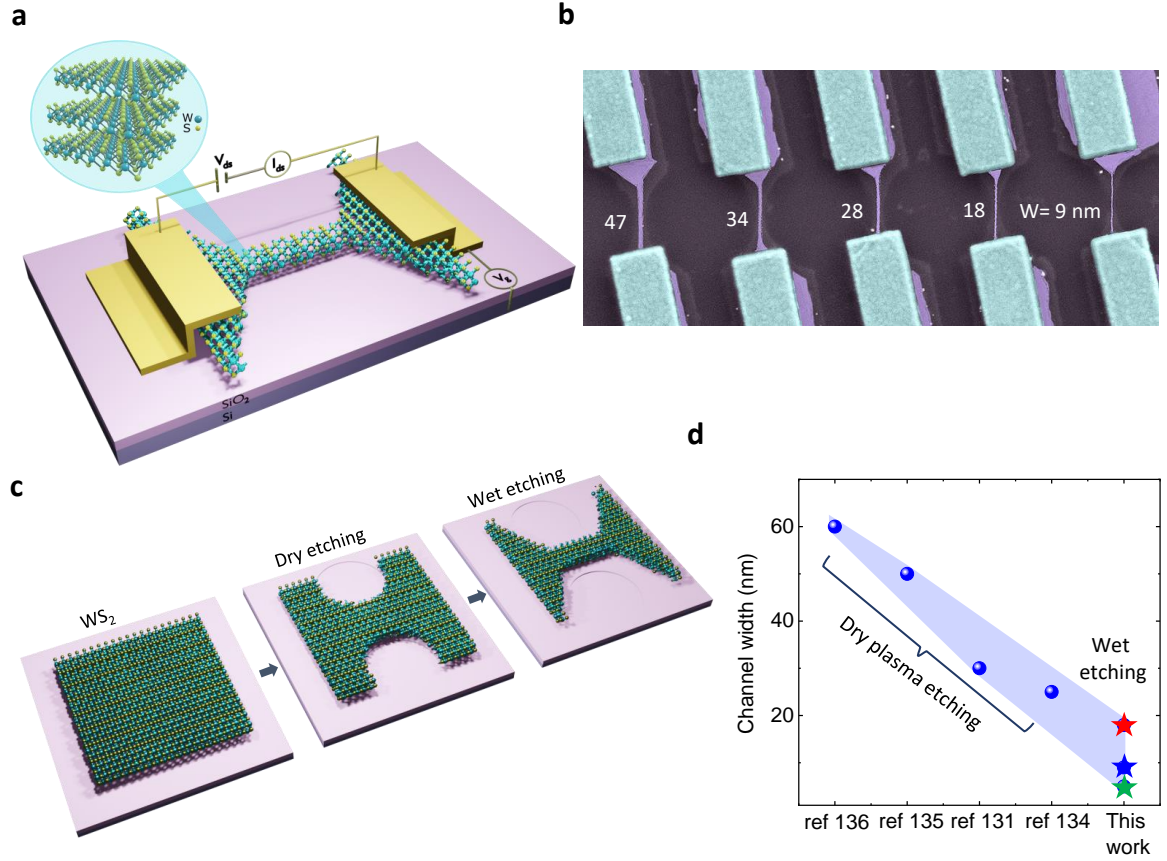


Figure 6.1: Ultra-narrow nanoribbon WS₂ field-effect transistors with zig-zag edges. (a, b) Schematics and scanning electron microscopic image of the fabricated WS₂ nanoribbon FETs on Si/SiO₂ substrate. (c) Key process steps for fabricating WS₂ nanoribbons with zig-zag edges by combining physical (CHF₃), wet-chemical (H₂O₂) etching and nano-patterning processes. (d) Comparison of our nanofabricated WS₂ nanoribbon channel-width with state-of-the-art results.

contacts and Si/SiO₂ substrate as back-gate.

6.1.2 Transport measurements of WS₂ nanoribbon FETs

First, electrical transport measurements were performed to investigate WS₂ nanoribbon properties at room temperature. Figure 6.2a shows the measured output characteristics with source-drain current (I_{ds}) as a function of applied source-drain voltage (V_{ds}) at various back-gate voltages, $V_g = -10$ to 80V. The nanoribbon channel conductance increases monotonically with increasing V_{ds} for a fixed applied gate voltage V_g . It is evident that with increasing V_g , the I_{ds} increase due to increasing carrier concentration in the WS₂ nanoribbon channel. Figure 6.2b shows transfer characteristics (I_{ds} vs. V_g) of the WS₂ nanoribbon at different V_{ds} on a linear scale. We observed an increase of I_{ds} with increasing positive V_g ,

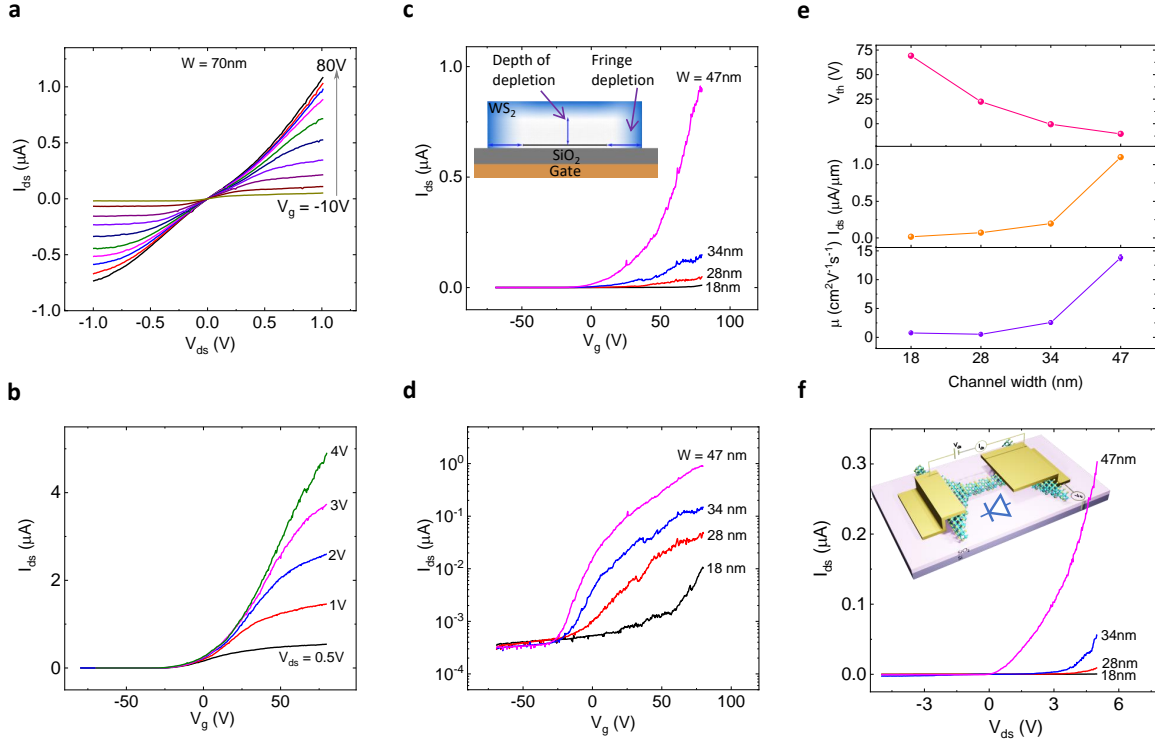


Figure 6.2: Field effect transistor properties of WS₂ nanoribbons. (a) Output characteristics showing I_{ds} vs. V_{ds} of WS₂ nanoribbon FET with a channel width of 70 nm at different gate voltages. (b) Transfer characteristics of WS₂ FET with 70 nm channel width at different bias voltages. (c) Transfer characteristics of WS₂ nanoribbons for different channel widths with $V_{ds} = 5V$. Inset schematic explains the narrow channel effect, where the fringe-depletion enhances the threshold voltage (V_{th}) in the channels. (d) Semilog plots of transfer characteristics for different widths of WS₂ nanoribbon to estimate the narrow channel effect. (e) The plots of threshold voltages V_{th} (top panel), on-state current level I_{ds} (middle panel) at $V_g = 80V$, and field-effect mobilities μ (bottom panel) for WS₂ nanoribbon FETs with different channel widths measured with $V_{ds} = 5V$. The error bars in estimating mobilities are calculated from the noise level in determining the transconductance. (f) I_{ds} vs. V_{ds} properties of nanoribbon FETs with various widths at $V_g = 80V$, mimicking a diode characteristic. Inset shows the actual device geometry with the source and drain contacts that are asymmetrically positioned on WS₂ nanoribbon and bulk regions.

which resembles typical n-type transport behavior, as expected for WS₂ [185]. From the transfer characteristics, the field-effect mobility ($\mu = \frac{L}{WC_g V_{ds}} \frac{dI_{ds}}{dV_g}$) is estimated to be $24 \text{ cm}^2\text{V}^{-1}\text{s}^{-1}$ with $V_{ds} = 1V$, where the gate capacitance per unit area, $C_g = \epsilon\epsilon_0/d_{ox} = 1.15 \times 10^{-8} \text{ Fcm}^{-2}$ ($d_{ox} = 285 \text{ nm}$ SiO₂ structure with relative dielectric constant $\epsilon = 3.9$), L and W are channel length and width, respectively, V_{ds} is the applied drain-source voltage and $\frac{dI_{ds}}{dV_g}$ is the transconductance (g_m). We estimated Schottky barrier height (SBH) of WS₂ nanoribbon with Ti/Au contact to be $\phi_b = 78 \pm 2.5 \text{ meV}$ using thermionic-emission model [91, 92, 186].

6.1.3 Narrow channel effects in WS₂ nanoribbon FETs

To study the evolution of electrical transport properties, we compared WS₂ nanoribbon FETs with different widths (18 to 47 nm) fabricated on the same flake. Figure 6.2c and 6.2d show the transfer characteristics of different channel widths of WS₂ nanoribbon FETs in linear and log scale, respectively. In the WS₂ nanoribbons, when the gate-induced depletion region is comparable to the channel width, the narrow channel effect should dominate the transport mechanism [187], as schematically presented in the inset of Fig. 6.2c. In narrow channels, the effect of the fringe depletion region should be significant in contrast to the wider channel, as the latter has enough space for strong inversion [187]. The origin of the fringe depletion most likely due to the surface absorbents (e.g., water, etchants) that results in carrier depletion [132]. The inversion region in the narrow channel requires it to act on both fringe depletion and field depletion via an applied gate voltage, which eventually enhances the threshold voltage (V_{th}) to accumulate charge carriers [132, 137].

As shown in Fig. 6.2e, we observe strong modulation in device parameters due to narrow channel effects in WS₂ nanoribbon FETs, such as on-state current (I_{ds}), threshold voltage (V_{th}), and field-effect mobility. It is conspicuous that with increasing channel width (W) of nanoribbon, the corresponding on-state current also increases because channel conductance ($G = I_{ds}/V_{ds} = \sigma Wt/L$) is directly proportional to the width of the channel. We also observe that the V_{th} increases with decreasing channel width due to the narrow channel effect, since the increase of threshold voltage can be written as, $\Delta V_{th} \propto (1 + \frac{\pi}{2} \frac{X_{depmax}}{W})$. Here, X_{depmax} and W are the maximum depth of depletion in WS₂ nanoribbon and the channel width, respectively. As long as $W \gg X_{depmax}$, ΔV_{th} does not scale much with W , but when $W \leq X_{depmax}$, then ΔV_{th} greatly scales with W [188]. Furthermore, relative channel current (I_{ds}/L , L is the channel length) decreases with decreasing channel width, and it can be understood by considering that the channel current would decrease since V_{th} increases in narrower channels. We could measure good transport properties in all WS₂ nanoribbon FETs down to 18 nm, except for the narrowest 9 nm channel width, which could be due to the shift of V_{th} to higher gate voltages and could not be measured with our Si/SiO₂ back-gated device. Furthermore, the extremely narrow channel should be more susceptible to the depletion width and edge-induced scattering mechanisms, which would limit the mobility in the channel. From the transfer characteristics, the field-effect mobility (μ) is estimated for different channel widths. The observed enhancement of μ with increasing channel width can be attributed to the relatively reduced edge/boundary induced scattering in wider channels in comparison to narrower channels [132, 136].

Figure 6.2f shows the I_{ds} vs. V_{ds} properties of nanoribbon FETs with various widths at $V_g = 80V$. Interestingly, the IV properties emulate diode characteristics, showing enhancement of current for positive V_{ds} (forward bias) and negligible

current for negative V_{ds} (reverse bias). It is conspicuous that the diode-like IV behavior is observed in nanoribbon FETs with widths 18-48nm, unlike to the symmetric IV in 70nm wide nanoribbon FET. The actual device geometry with the source and drain contacts that are asymmetrically positioned on WS₂ nanoribbon and bulk regions, as shown in the inset of Fig. 6.2f. A hypothesis to explain such diode properties is that etching pristine WS₂ depletes electrons due to relatively higher effects of surface absorbates and edge defects [132, 137] and transforms nanoribbon WS₂ a lesser n-type material, in other words, a p-type material in comparison to the bulk (lower etching effects). Thus, one can attribute the etched-nanoribbon part a p-type and the bulk part a n-type region, as a result it behaves like a pn junction diode. Furthermore, the asymmetric SB at the contacts between the nanoribbon and bulk regions can also give rise to such diode-like IV because relatively lesser n-type nanoribbon section should have higher SB with the contact compare to bulk WS₂ region.

6.1.4 Temperature dependence of transport properties in WS₂ nanoribbon

Next, we investigated the evolution of the transport properties in WS₂ nanoribbon FETs with temperature (T) for different channel widths. Figure 6.3 (a,b,c) presents the measured transfer properties in color contour plots at different T for WS₂ nanoribbon FETs having 18, 28, and 34 nm wide channels, respectively. We observed strong insulating behavior for the 18 nm wide nanoribbon channel. However, we observed a gate- and bias-voltage induced metal-to-insulator transition in wider nanoribbons (28 and 34 nm), which showed an insulating property at the low T range (<200K) and metallic behavior at higher T range (>200K) with a reduction in I_{ds} with increasing T.

The evolution of field-effect mobility (μ) with temperature T is presented in Fig. 6.3 (d,e,f) for WS₂ nanoribbon FETs of 18, 28 and 34 nm channel widths, respectively. The generic dependency of μ on T is fitted with $\mu \propto T^\gamma$, where the exponent (γ) depends on the scattering mechanism in the nanoribbons [185, 189]. For the 18 nm nanoribbon channel, we observe an increase of μ with an increase of T at low temperature and saturation for higher T (> 235K). We estimate $\gamma \approx 8.6$ due to mainly the boundary/edge or impurity scattering process in the 18 nm FET. Whereas for 28 nm FET, the $\gamma \approx 0.95$ at the low T limit (< 165K) and $\gamma \approx -7.8$ at the higher T limit were estimated. The limiting factor of μ at the low T range can be correlated to the edge or impurity scattering mechanisms, whereas μ is mainly dominated by phonon scattering at the higher T range (> 250K) [95, 185, 189]. Similarly, for nanoribbon of 34 nm wide, we estimate $\gamma \approx 1.94$ at a lower T range (< 150K), ascribing to the dominating edge/impurity scattering mechanism limiting the channel mobility. At the higher T range (>200K), $\gamma \approx -4.7$, consistent with the phonon scattering mechanisms

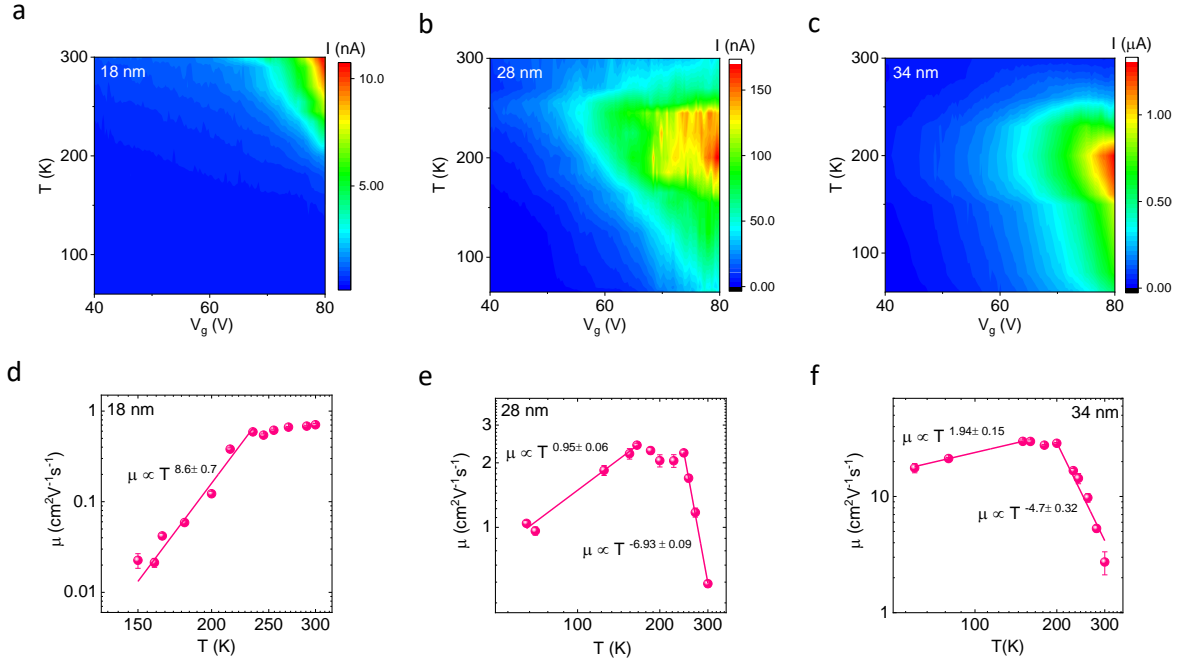


Figure 6.3: Temperature dependence of WS₂ nanoribbon FET device parameters. (a, b, c) Colour contour plots of the transfer characteristics within $V_g = 40\text{-}80\text{V}$ of the WS₂ FETs with 18, 28 and 34 nm channel widths at different temperatures. (d, e, f) Mobility μ as a function of temperature T of the WS₂ nanoribbon FETs with 18, 28 and 34 nm wide channels along with the power-law fitting to $\mu \propto T^\gamma$ (solid line) at different temperature ranges. The exponent (γ) depends on the scattering mechanism in the nanoribbons. Error bars are estimated based on uncertainties in determining the conductance across the channel.

limiting the channel mobility. Overall, in the wider channels, the dependencies of μ on T in the low-temperature regime are consistent with transport dominated by impurity scattering, whereas at $T > 200\text{K}$, it is limited by phonon scattering mechanism. The narrowest channel shows dominant edge or impurity scattering in comparison to wider channels, as expected because transport in narrow channels are more influenced by the WS₂ edges. Therefore, it is important to control the edge structures of TMDC nanoscale devices by controlled fabrication processes. The edge structures in our devices are sharp and zigzag-terminated [50] compared to the nano-ribbons that are fabricated via physical etching techniques.

6.1.5 Gate and bias induced metal to insulator transition in WS₂ nanoribbon

We further examined the bias-dependent transport properties with temperature to verify the influence of the edges or impurity states in our WS₂ nanoribbon devices. Figure 6.4a shows the transfer characteristics of WS₂ nanoribbon FET (W

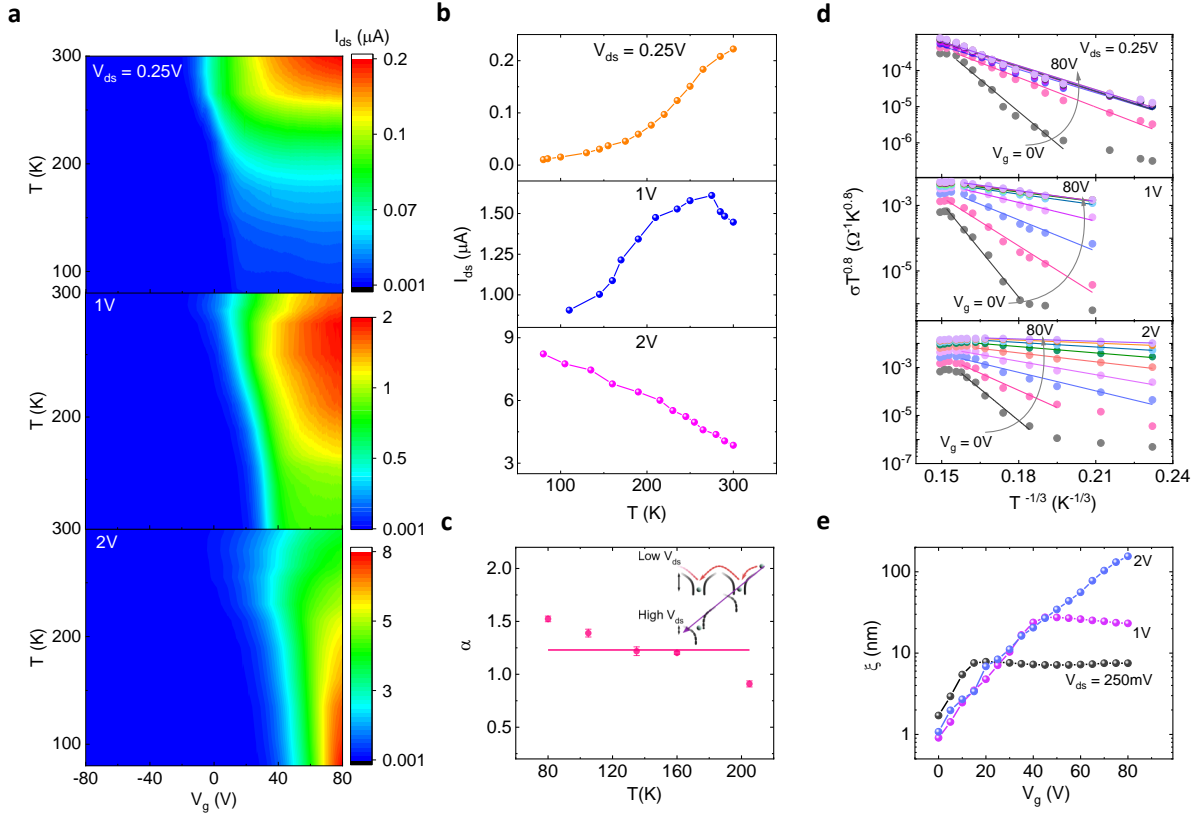


Figure 6.4: Gate and bias induced metal to insulator transition in WS₂ nanoribbon FET. (a) Colour contour plots of the temperature dependence of transfer characteristics in WS₂ nanoribbon transistor with a channel width of 70nm at $V_{ds} = 0.25\text{V}$ (top panel), 1V (middle panel), and 2V (bottom panel). (b) I_{ds} as a function of temperature in WS₂ nanoribbon transistor at $V_g = 80\text{V}$ with $V_{ds} = 0.25\text{V}$ (top panel), 1V (middle panel), and 2V (bottom panel). (c) Derived exponent (α) at different temperatures from the power-law fitting to verify the percolation transport mechanism in the WS₂ nanoribbon FET. Inset shows the deformation of the potential barrier with respect to the applied electric field in the conduction band. (d) Arrhenius plot of $\sigma T^{0.8}$ as a function of $T^{-\frac{1}{3}}$ along with the linear fitting to disseminate 2D VRH with $V_{ds} = 0.25\text{V}$ (top panel), 1V (middle panel) and 2V (bottom panel). (e) Localization length (ξ) at different V_g for $V_{ds} = 0.25\text{V}$ (black dots), 1V (red dots) and 2V (blue dots).

= 70nm) at different temperatures with $V_{ds} = 0.25\text{V}$, 1V, and 2V, respectively. The WS₂ nanoribbon FET demonstrates insulating properties at lower bias voltage ($V_{ds} = 0.25\text{V}$) within the 80-300 K temperature range. However, with applied $V_{ds} = 1\text{V}$, the transistor deviates from insulating behavior with temperature, especially at higher temperature limits ($T > 275\text{K}$), and remains metallic afterward at high V_g . Interestingly, a stronger gate-induced metal to insulating transition (MIT) is observed in the WS₂ nanoribbon FET for higher $V_{ds} = 2\text{V}$ with a transition at $V_g = 70\text{V}$. To clearly visualize the MIT, I_{ds} as a function of temperature is plotted in Fig. 6.4b for different V_{ds} and at $V_g = 80\text{V}$. Channel current I_{ds}

monotonically increase with T for $V_{ds} = 0.25\text{V}$, whereas for $V_{ds} = 1\text{V}$ the I_{ds} first increases with T but afterward decreases with increasing T ($T > 275\text{K}$), and $V_{ds} = 2\text{V}$ data shows a monotonic decrease of I_{ds} with increasing T resembling the metallic transport.

Gate and bias-induced MIT observed in WS_2 nanoribbons can be attributed to the percolation transport mechanism in TMDCs in a strongly interacting regime [82, 94, 95]. The strength of the Coulomb interaction of the carriers can be estimated by the Wigner-Seitz radius (r_s), which is the ratio between Coulomb potential, E_c , and kinetic (Fermi, E_F) energy of the carriers using the following equation [189, 190].

$$r_s = \frac{E_c}{E_F} = \frac{n_v}{\alpha_B^* \sqrt{\pi n_{2D}}} = \frac{n_v m^* e^2}{4\pi \epsilon \hbar^2 \sqrt{\pi n_{2D}}} \quad (6.1)$$

Here, $n_v = 2$ is degenerate valleys number, $\alpha_B^* = 4\pi\epsilon\hbar^2/m^*e^2$ is effective Bohr radius of the system, considering $\epsilon = 6.7$ for multilayer WS_2 , $m^* = 0.34m_e$ is the effective mass of the carriers in WS_2 [185, 191]. We obtain $r_s \sim 5.3$ in the nanoribbon FET at 80K near the MIT region with $V_{ds}=2\text{V}$ and a system with $r_s \gg 1$ is considered strongly interacting [189]. Next, MIT due to percolation driven transport and screening of the charge carriers depends on the applied gate voltage with the relationship $\sigma(I_{ds}) = A(n - n_c)^\alpha$, where A, n, n_c , and α are proportional constant, carrier density, percolation threshold carrier density, and critical percolation exponent, respectively [82, 94]. By considering $n \propto V_g$, we have $(n - n_c)^\alpha \propto (V_g - V_c)^\alpha$; where V_c is critical gate voltage for n_c . When $V_g < V_c$, carriers are strongly bound by the potential valleys and the WS_2 channel shows semiconducting transport properties. For $V_g > V_c$, carriers are weakly bounded by the potential valleys and the WS_2 channel depicts metallic properties. It is expected that in a 2D system, $\alpha = 1.33$ (4/3). The estimated α (near the transition region) in the WS_2 nanoribbon FET at $V_{ds} = 2\text{V}$ is about 1.23 ± 0.1 , shown in Fig. 6.4c. In a strongly interacting system considering the percolation transport model, the carriers in the channel transport via the tunneling and hopping across the potential valleys, as presented schematically in the inset of Fig. 6.4c. As the electric field in the channel increases, the tunneling and hopping probability increase because of distortion and decrease of barrier height, and WS_2 nanoribbon FET shows MIT with gate voltage, as reported in monolayer and multilayer pristine TMDCs [82, 94, 95].

Further, we analysed the bias- and gate-induced MIT transport in nanoribbon WS_2 FET in light of variable range hopping (VRH) model. In VRH transport, carriers hop through the traps states in the crystal structure, along the edges or at the WS_2 - SiO_2 interface [192]. The conductance (σ) in the VRH model can be expressed as

$$\sigma = AT^m e^{-\left(\frac{T_0}{T}\right)^\gamma} \quad (6.2)$$

where, A is constant, T_0 is a hopping parameter related to characteristics temperature, $\gamma = \frac{1}{3}$ for 2D system and m is between -1 and -0.8 [95, 192]. Figure 6.4d shows the Arrhenius plot of $\sigma T^{0.8}$ as a function of $T^{-\frac{1}{3}}$ along with the linear fitting to equation 6.2 for $V_{ds} = 0.25V, 1V$ and $2V$, respectively at various V_g . 2D VRH has been reported in various 2D materials, where the localization length (ξ) increases due to efficient screening of the potential of trap states at higher carrier density [82, 94, 95, 192, 193]. The estimated ξ at different gate voltages with $V_{ds} = 0.25V, 1V$, and $2V$ is depicted in Fig. 6.4e. It is conspicuous that at the lower $V_{ds} = 0.25V$ and $1V$ the ξ saturates around $8nm$ and $27nm$, respectively with V_g . On the contrary, for $V_{ds} = 2V$ the localization length exponentially increases with V_g and a strong MIT is observed. These findings support our presumptions of reducing the potential barrier of the trap states at the higher electric field in the percolation mediated transport, presented in Fig. 6.4c (inset). Here, higher V_{ds} (electric field) assists the gate voltage (V_g) to screen the trap sites (reducing the hopping mediated transport), thus transport takes place through unlocalized states.

6.2 All-CVD MoS₂-graphene heterostructure FET

Two-dimensional (2D) semiconductors and their van der Waals heterostructures have generated huge interests for sustainable electronics, optoelectronics, and energy harvesting devices [53, 84, 138]. Moreover, neuromorphic computations and non-volatile memory applications greatly desire memristive switching devices due to their ability to store data and locally perform computation by electrical means [142]. Conventional materials with metal-oxide-metal show memristive switching, but are limited by flexibility, scaling effects and high power consumption issues [141]. On the other hand, 2D semiconductors can overcome such challenges [14]. So far, memristive switching in semiconducting 2D material (MoS₂) is realized with conventional 3D contact materials (Au) [53, 54]. However, memristive switching in all CVD 2D materials is a highly sought-after phenomenon for large-area applications. In this section, we demonstrate the memristive switching and contact properties of FET device based on scalable molybdenum disulfide (MoS₂)-graphene heterostructures grown by chemical vapor deposition (CVD).

Figure 6.5a shows the sketch of a MoS₂ FET device with vdW graphene contacts on Si/SiO₂ substrate and electrical connections to measure basic transistor properties. Si/SiO₂ substrate is used to apply gate voltage (V_g). Graphene vdW contacts are very suitable for 2D materials since it does not exert pinning effect in the materials [89, 138]. The transfer properties (I_{ds} vs. V_g) are shown in Fig. 6.5b at various bias voltages, $V_{ds} = 1V-4V$. The mobility is estimated to be $4\text{ cm}^2\text{V}^{-1}\text{s}^{-1}$ and threshold voltage (V_{th}) is around $V_g = 0V$. It is to be noted that the transfer properties for $V_{ds} = 1V$ and $2V$ are almost similar, which is explained

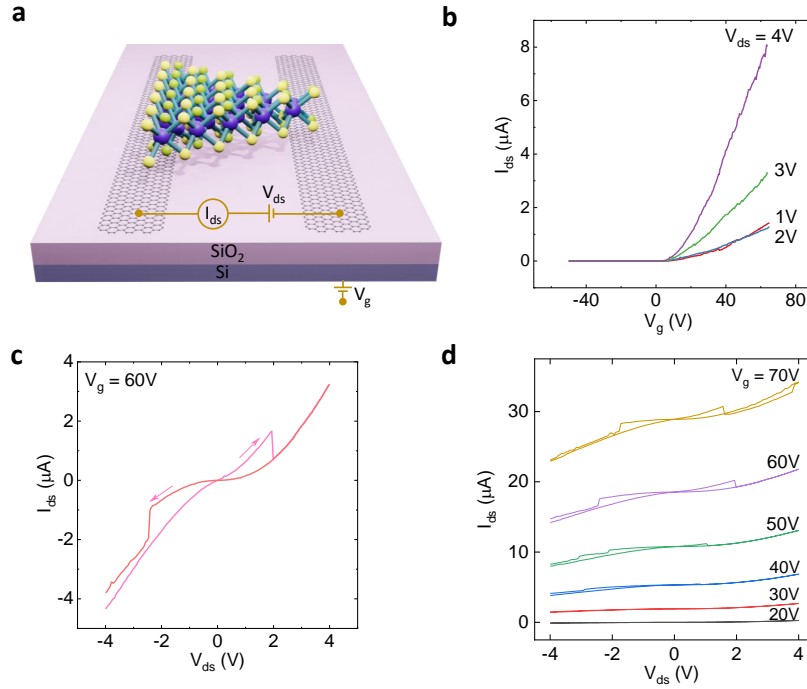


Figure 6.5: Gate-tunable memristive switching in all-CVD graphene and MoS₂ heterostructure. (a) Schematic of MoS₂ FET device with vdW graphene contacts on Si/SiO₂ substrate and electrical connections. (b) I_{ds} vs. V_g at different V_{ds} . (c) I_{ds} vs. V_{ds} at $V_g = 60V$, where memristive switching is observed. The arrows indicate the sweep directions. (d) Evolution of memristive switching with V_g .

in the next paragraph.

The I_{ds} vs. V_{ds} is shown in Fig. 6.5c and a switching behaviour of I_{ds} with V_{ds} emerges. When sweeping the V_{ds} up (toward positive values), I_{ds} sharply decrease from $1.65\mu A$ (low resistive state, LRS) to $0.75\mu A$ (high resistive state, HRS) at $V_{ds} \sim 2V$. This switching ($V_{ds} \sim 2V$) explains the similar transfer properties, shown in Fig. 6.5b for $V_{ds} = 1V$ and $2V$. The ratio of the memristive switching is about 2.2. Similar memristive switching is observed in CVD grown MoS₂ with vertical and lateral transistor transport with conventional metallic contacts [53, 54, 194]. To check the evolution of memristive switching in the MoS₂ FET with gate-voltage (V_g), I_{ds} vs. V_{ds} is measured at different V_g (Fig. 6.5d) by sweeping V_{ds} up and down. It can be observed that memristive switching emerges at $V_g \geq 50V$. The mechanisms that can give rise to such gate-tunable memristive switching are bias-mediated motion of defects in the MoS₂ crystal, dynamic change of Schottky barrier and migration of grain boundaries [53, 54, 195, 196]. This gate-tunable memristive switching functionality in three terminal transistor with atomically thin monolayer semiconducting TMDC and graphene vdW FETs have prospects to be used in all CVD 2D material-based in-memory-computation and data-storage devices.

6.2.1 Gate tunable Schottky barrier at the all-CVD MoS₂-graphene heterostructure

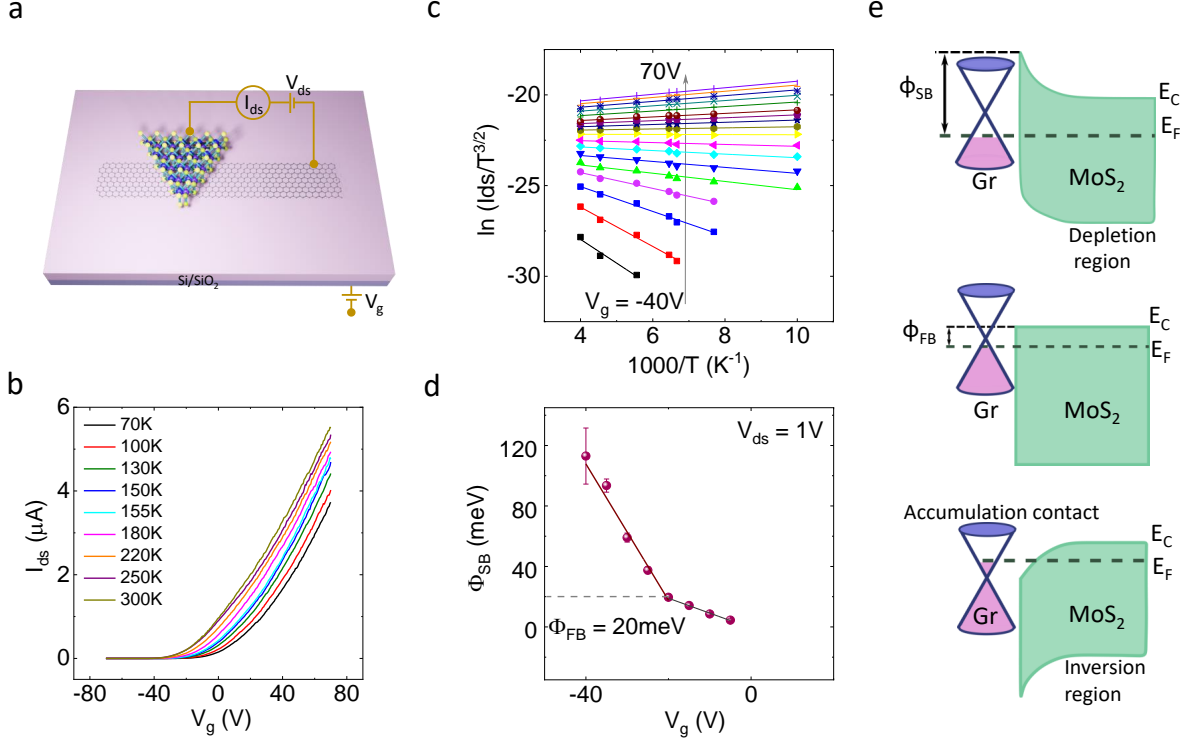


Figure 6.6: Charge transport and Schottky barrier (SB) at MoS₂-graphene van der Waals junction. (a) Schematic of vdW heterostructure device of MoS₂-graphene and measurement geometry. (b) I_{ds} vs. V_g with $V_{ds} = 1V$ at different temperatures. (c) Arrhenius plot of $\ln(I_{ds}/T^{3/2})$ with $1000/T$ at different V_g . (d) Estimated SB at different V_g . (e) A pictorial illustration of band structure to explain the reduction of SB at different V_g . Here, V_g changes the Fermi-level in graphene and MoS₂ simultaneously and modulates band structure accordingly.

The contact properties of CVD-grown graphene on MoS₂ in vdW heterostructure were investigated to understand device performance for scalable applications. Figure 6.6a demonstrates a schematic of vdW heterostructure device of MoS₂-graphene on Si-SiO₂ substrate and electrical connection to measure transport properties. The temperature dependent I_{ds} vs. V_g is shown in Fig. 6.6b from 70K-300K at $V_{ds} = 1V$. At this temperature range with this applied V_{ds} , the transfer properties show insulating behaviour, where with decreasing temperature, I_{ds} decreases. The thermionic emission model is used to estimate the Schottky barrier (SB) in this heterostructure junction and the Arrhenius plots of $\ln(I_{ds}/T^{3/2})$ with $1000/T$ at different V_g are shown in Fig. 6.6c [91, 92, 186, 197]. Figure 6.6d depicts the estimated SB at different gate voltages (V_g) at $V_{ds} = 1V$. The flat-band SB is found to be 20meV in CVD-grown MoS₂-graphene junction

at around $V_g = -20\text{V}$. The SB seems to be decreasing with increasing V_g , and at $V_g \geq -5\text{V}$, the calculation deviates from the thermionic emission model and limits further SB estimation. Here, applied V_g modulates the Fermi level of graphene and MoS_2 simultaneously.

Figure 6.6e shows the pictorial illustration of band alignment of graphene and MoS_2 to explain the gate modulation of SB. When V_g is negative $\leq -20\text{V}$, graphene is p-doped and MoS_2 channel is off, then the SB height is higher. With increasing V_g , the Fermi-level (E_F) in graphene moves toward the conduction band (CB) and in MoS_2 , it moves towards E_c . At $V_g = -20\text{V}$, the flat-band condition is reached (Fig. 6.6e, middle panel). Increasing V_g further moves the E_F in graphene into the CB and in MoS_2 , it moves nearer to E_c . At $V_g \geq -5\text{V}$, inversion in MoS_2 happens and graphene shows accumulation contact properties [138, 197].

In summary, the realization of ultra-narrow nanoscale semiconducting WS_2 FETs with atomically controlled zig-zag edges is extremely promising for future scaling down of semiconductor technology. The adapted nanostructuring process is compatible with the current semiconductor manufacturing using a top-down approach by anisotropic wet etching in conjunction with physical etching techniques. The charge transport properties in the extremely narrow channels are found to be governed by the narrow channel effects, where the ON current and mobility decrease and V_{th} increases with reducing the channel width. Besides, memristive switching and SB analysis in all-CVD MoS_2 and graphene vdW heterostructure have been presented. These all-CVD 2D vdW heterostructures have prospects to be used in large-area nanoelectronics, future data storage and in-memory-computation.

7 Conclusion and Outlook

The exploration of alternative device technology along with new materials is important for the near future computation and data storage processes. It is envisaged that the integration of memory and logic in compact device geometry will enable efficient computation by reducing the time required to transfer data between different components. Similarly, introducing neuromorphic computation will be beneficial for low-power and higher-efficient computation and data storage processes. Neuromorphic computation implements in-memory data processing techniques by mimicking the human brain, where data processing and storage are carried out using the neurons and synapses. Furthermore, scaling down conventional silicon-based FET to enhance its performance and energy efficiency becomes very complicated. Recent field effect transistors (FET) have evolved from planar to vertical “fins” (FINFET) device design to improve device performance. Moreover, gate-all-around (GAA) FETs based on nanosheets are already proposed to truncate the device size to further follow the Moore’s law. However, these schemes require complicated fabrication processes and inflict mobility degradation due to dangling bonds in ultrathin layers of conventional 3D bulk materials. Hence, new technologies are needed to continue increasing device performance to meet future demand.

Spintronic technology can be used in the next generation memory and logic devices. Spintronics exploits electron’s charge and spin quantum properties for faster and energy-efficient data storage and processes. Spintronic applications from 2D materials offer a plethora of opportunities for device applications and to realize fundamental physical phenomena. The main features of spintronic applications are spin-polarized current generation, detection and modulation in a channel. We utilized graphene as a spin transport channel and other 2D materials are used in vdW heterostructure device geometry.

In this thesis, we take the advantage of high SOC property of vdW topological insulator (TI) materials (BSTS) and combined it with graphene to explore its spintronics properties in the non-local lateral spin-valve device. We presented room temperature CSC and its inverse effect (ICSC) in BSTS and the detailed dependence on bias current, gate voltage, different geometries and magnetization orientations, proving the robustness of the CSC effects in the TI. We could conclude that both the CSC and the ICSC originate from the bulk SHE or REE, the

TSML of the TI surface states, or a combination of these effects. A study on the temperature dependence of (I)CSC measurements in TI-graphene heterostructure can help to isolate different contributions of spin polarization from the bulk (SHE, REE) and surface (TSML) states in the TI.

Next, we used semimetal TMDC (TaTe_2) as a spin-injector and detector in a lateral graphene spin-valve device at room temperature. Systematic bias and gate-dependent measurements of the spin injection signal indicate that the origin of spin polarization can mainly be because of the SHE or REE in TaTe_2 . The advantage of using such a material as spin source is that the spin polarization direction can be controlled by an electrical bias instead of the magnetic field as conventionally achieved with ferromagnetic materials. Furthermore, we demonstrated CSC in the normal metallic state of NbSe_2 up to room temperature. The engendered spin polarization is injected into the graphene channel and detected in non-local measurement geometry via spin-switch and Hanle spin precession measurements. A higher CSC signal in NbSe_2 is detected at a lower temperature, however, in its non-superconducting state. Systematic measurements of the spin-switch and Hanle signals reveal that the possible origins of the in-plane spin polarization are predominantly due to the SHE or REE in NbSe_2 considering different symmetry-permitted CSC processes. It would be a great leap of advancement in spintronics to observe the CSC effect in NbSe_2 in the superconducting state since superconducting quantum materials with high SOC can enhance the spintronic device performance by generating a larger spin current with a long spin lifetime [164, 167].

To modulate spin transport in the graphene spin channel, we used proximity-induced SOC effects of TMDCs. Graphene in proximatized to MoTe_2 acquires strong Rashba SOC and a spin-texture with spin-split conduction and valence bands, which allow tuning of spin-signal by a gate voltage. We observed gate-tunable SGE in graphene- MoTe_2 heterostructure that can be used for gate-controlled MRAM and spin-logic devices. Moreover, we measured spin-valley coupling and spin-relaxation anisotropy in all-CVD graphene- MoS_2 heterostructure devices, compatible with scalable devices. Spin precession and dynamics measurements reveal an enhanced SOC strength in the heterostructure compared to the pristine graphene at room temperature. Another exciting aspect is the observation of spin lifetime anisotropy in the graphene- MoS_2 heterostructure, which results in spin filtering functionalities due to the different spin relaxation times for in-plane and out-of-plane spins. Further study can shed some light to enhance imprinting SOC in graphene, for example, by improving the wet-transfer technique, integrating hBN substrate to get a clean homogeneous interface between the graphene and MoS_2 .

Interestingly, a memory unit is accompanied by a field-effect transistor (FET) to access a particular memory cell. Hence, all-2D memory applications will require 2D material-based FETs. Besides, in the post-silicon era, 2D TMDC semiconducting materials (MoS_2 , WS_2) have enormous potential for applications in next-generation (opto-) electronics and sensors. It is essential to investigate and engineer their electronic features by using an industrial-compatible etching method with atomic-scale control in the compact FET device structure to engineer their physical transport properties. In this thesis, we showed the fabrication of WS_2 FET with sub-10 nm width using a controlled anisotropic wet chemical technique. The adapted nanostructuring process is compatible with the current semiconductor manufacturing processes using a top-down approach of anisotropic wet etching in conjunction with physical etching techniques. The charge transport properties in the extremely narrow channels are found to be governed by the narrow channel effects, where the ON current and mobility decrease and V_{th} increase with reducing the channel width. Surprisingly, we observed diode-like IV behavior in the nanoribbon FETs with narrow channels (18-48nm) due to etching-dependent doping in the channels and such diode-like IV was not present in the FET with wider channels (70nm).

Temperature-dependent mobility in the nanoribbon FETs infers a competitive trend between phonon and defect-mediated scattering, where defect-mediated scattering is dominant in narrower channels. Gate and bias-induced MIT with temperature are observed and attributed to percolation-driven transport in the nanoribbons. In addition to the narrow channel TMDC FETs demonstrated here, the development of nanostructuring techniques for monolayer materials in a large area will enable a further leap in the miniaturization of transistors. Furthermore, the use of 2D materials heterostructures can enhance channel mobility and novel device architectures could help to reduce the channel length and gate dimensions to a sub-nm regime for cutting-edge nanoscale devices and electronic circuits. We also presented memristive switching and carried out Schottky barrier analysis in atomically thin all-CVD MoS_2 -graphene vdW heterostructure FETs. The CVD-grown materials have prospects to be used in large-area nanoelectronics, data storage and computation. Fabrication and characteristics of ultra-narrow WS_2 nanoribbon FETs and all-CVD vdW heterostructure open the platform for investigating electronic properties and the development of unique nanoscale devices with 2D materials.

References

- [1] C. D. Schuman, S. R. Kulkarni, M. Parsa, J. P. Mitchell, P. Date, and B. Kay, “Opportunities for neuromorphic computing algorithms and applications”, *Nature Computational Science* **2**, 10–19 (2022).
- [2] H. Haick and N. Tang, “Artificial Intelligence in Medical Sensors for Clinical Decisions”, *ACS Nano* **15**, 3557–3567 (2021).
- [3] A. Tzachor, M. Devare, B. King, S. Avin, and S. Ó hÉigeartaigh, “Responsible artificial intelligence in agriculture requires systemic understanding of risks and externalities”, *Nature Machine Intelligence* **4**, 104–109 (2022).
- [4] J. Grollier, D. Querlioz, K. Y. Camsari, K. Everschor-Sitte, S. Fukami, and M. D. Stiles, “Neuromorphic spintronics”, *Nature Electronics* **3**, 360–370 (2020).
- [5] D. Markovic[’], A. Mizrahi, D. Querlioz, and J. Grollier, “Physics for neuromorphic computing”, *Nature Reviews Physics* **2**, 499–510 (2020).
- [6] D. Ielmini and H. S. Wong, “In-memory computing with resistive switching devices”, *Nature Electronics* **1**, 333–343 (2018).
- [7] J. Zhou and J. Chen, “Prospect of Spintronics in Neuromorphic Computing”, *Advanced Electronic Materials* **7**, 2100465 (2021).
- [8] G. Lee, J.-H. Baek, F. Ren, S. J. Pearton, G.-H. Lee, J. Kim, G. Lee, J. Kim, J.-H. Baek, G.-H. Lee, F. Ren, and S. J. Pearton, “Artificial Neuron and Synapse Devices Based on 2D Materials”, *Small* **17**, 2100640 (2021).
- [9] M. C. Sahu, S. Sahoo, S. K. Mallik, A. K. Jena, and S. Sahoo, “Multifunctional 2D MoS₂ Optoelectronic Artificial Synapse with Integrated Arithmetic and Reconfigurable Logic Operations for In-Memory Neuromorphic Computing Applications”, *Advanced Materials Technologies*, 2201125 (2022).
- [10] W. Wan, R. Kubendran, C. Schaefer, S. B. Eryilmaz, W. Zhang, D. Wu, S. Deiss, P. Raina, H. Qian, B. Gao, S. Joshi, H. Wu, H. S. Wong, and G. Cauwenberghs, “A compute-in-memory chip based on resistive random-access memory”, *Nature* **608**, 504–512 (2022).
- [11] V. K. Sangwan and M. C. Hersam, “Neuromorphic nanoelectronic materials”, *Nature Nanotechnology* **15**, 517–528 (2020).

- [12] K. Roy, A. Jaiswal, and P. Panda, “Towards spike-based machine intelligence with neuromorphic computing”, *Nature* **575**, 607–617 (2019).
- [13] M. C. Lemme, D. Akinwande, C. Huyghebaert, and C. Stampfer, “2D materials for future heterogeneous electronics”, *Nature Communications* **13**, 1–5 (2022).
- [14] T. J. Ko, H. Li, S. A. Mofid, C. Yoo, E. Okogbue, S. S. Han, M. S. Shawkat, A. Krishnaprasad, M. M. Islam, D. Dev, Y. Shin, K. H. Oh, G. H. Lee, T. Roy, and Y. Jung, “Two-Dimensional Near-Atom-Thickness Materials for Emerging Neuromorphic Devices and Applications”, *iScience* **23**, 101676 (2020).
- [15] C. Liu, H. Chen, S. Wang, Q. Liu, Y. G. Jiang, D. W. Zhang, M. Liu, and P. Zhou, “Two-dimensional materials for next-generation computing technologies”, *Nature Nanotechnology* **15**, 545–557 (2020).
- [16] S. Salahuddin, K. Ni, and S. Datta, “The era of hyper-scaling in electronics”, *Nature Electronics* **1**, 442–450 (2018).
- [17] Y. Liu, X. Duan, H. J. Shin, S. Park, Y. Huang, and X. Duan, “Promises and prospects of two-dimensional transistors”, *Nature* **591**, 43–53 (2021).
- [18] S. Mahajan, “The role of materials science in the evolution of microelectronics”, *MRS Bulletin* **40**, 1079–1086 (2015).
- [19] M. Segal, “Material history: Learning from silicon”, *Nature* **483**, S43–S44 (2012).
- [20] A. I. Kingon, J. P. Maria, and S. K. Streiffer, “Alternative dielectrics to silicon dioxide for memory and logic devices”, *Nature* **406**, 1032–1038 (2000).
- [21] N. Anscombe, “Pushing the limits”, *Nature Photonics* **4**, 30–30 (2010).
- [22] I. Ferain, C. A. Colinge, and J. P. Colinge, “Multigate transistors as the future of classical metal-oxide-semiconductor field-effect transistors”, *Nature* **479**, 310–316 (2011).
- [23] R. H. Dennard and M. R. Wordeman, “Generalized Scaling Theory and Its Application to a 1/4 micrometer MOSFET Design”, *IEEE Transactions on Electron Devices* **31**, 452–462 (1984).
- [24] M. Lundstrom, “Applied physics: Moore’s law forever?”, *Science* **299**, 210–211 (2003).
- [25] E. Sicard, “Introducing 7-nm FinFET technology in Microwind”, hal-01558775 (2017).
- [26] *New Technology Features for 2024: RibbonFETs and PowerVias - Intel’s Process Roadmap to 2025: with 4nm, 3nm, 20A and 18A?!*, <https://www.anandtech.com>.
- [27] *What’s the Right Path For Scaling?*, <https://semiengineering.com/whats-the-right-path-for-scaling/>.

-
- [28] A. B. Sachid, M. Tosun, S. B. Desai, C. Y. Hsu, D. H. Lien, S. R. Madhva-pathy, Y. Z. Chen, M. Hettick, J. S. Kang, Y. Zeng, J. H. He, E. Y. Chang, Y. L. Chueh, A. Javey, and C. Hu, “Monolithic 3D CMOS Using Layered Semiconductors”, *Advanced Materials* **28**, 2547–2554 (2016).
 - [29] K. Nakamura, N. Nagamura, K. Ueno, T. Taniguchi, K. Watanabe, and K. Nagashio, “All 2D Heterostructure Tunnel Field-Effect Transistors: Impact of Band Alignment and Heterointerface Quality”, *ACS Applied Materials & Interfaces* **12**, 51598–51606 (2020).
 - [30] M. Chhowalla, D. Jena, and H. Zhang, “Two-dimensional semiconductors for transistors”, *Nature Reviews Materials* **1**, 16052 (2016).
 - [31] M. Shrivastava and V. Ramgopal Rao, “A Roadmap for Disruptive Applications and Heterogeneous Integration Using Two-Dimensional Materials: State-of-the-Art and Technological Challenges”, *Nano Letters* **21**, 6359–6381 (2021).
 - [32] S. Das, A. Sebastian, E. Pop, C. J. McClellan, A. D. Franklin, T. Grasser, T. Knobloch, Y. Illarionov, A. V. Penumatcha, J. Appenzeller, Z. Chen, W. Zhu, I. Asselberghs, L. J. Li, U. E. Avci, N. Bhat, T. D. Anthopoulos, and R. Singh, “Transistors based on two-dimensional materials for future integrated circuits”, *Nature Electronics* **4**, 786–799 (2021).
 - [33] I. Žutić, J. Fabian, and S. Das Sarma, “Spintronics: Fundamentals and applications”, *Reviews of Modern Physics* **76**, 323–410 (2004).
 - [34] P. J. Rajput, S. U. Bhandari, and G. Wadhwa, “A Review on-Spintronics an Emerging Technology”, *Silicon* **2021** **1**, 1–16 (2022).
 - [35] D. Sander, S. O. Valenzuela, D. Makarov, C. H. Marrows, E. E. Fullerton, P. Fischer, J. McCord, P. Vavassori, S. Mangin, P. Pirro, B. Hillebrands, A. D. Kent, T. Jungwirth, O. Gutfleisch, C. G. Kim, and A. Berger, “The 2017 Magnetism Roadmap”, *Journal of Physics D: Applied Physics* **50**, 363001 (2017).
 - [36] T. Miyazaki and N. Tezuka, “Spin polarized tunneling in ferromagnet/insulator/ferromagnet junctions”, *Journal of Magnetism and Magnetic Materials* **151**, 403–410 (1995).
 - [37] D. C. Ralph and M. D. Stiles, “Spin transfer torques”, *Journal of Magnetism and Magnetic Materials* **320**, 1190–1216 (2008).
 - [38] A. Manchon, J. Železný, I. M. Miron, T. Jungwirth, J. Sinova, A. Thiaville, K. Garello, and P. Gambardella, “Current-induced spin-orbit torques in ferromagnetic and antiferromagnetic systems”, *Reviews of Modern Physics* **91**, 035004 (2019).

- [39] K. Garelo, F. Yasin, S. Couet, L. Souriau, J. Swerts, S. Rao, S. Van Beek, W. Kim, E. Liu, S. Kundu, D. Tsvetanova, K. Croes, N. Jossart, E. Grimaldi, M. Baumgartner, D. Crotti, A. Fumemont, P. Gambardella, and G. Kar, “SOT-MRAM 300MM Integration for Low Power and Ultra-fast Embedded Memories”, 2018 IEEE Symposium on VLSI Circuits, 81–82 (2018).
- [40] H. Yang, S. O. Valenzuela, M. Chshiev, S. Couet, B. Dieny, B. Dlubak, A. Fert, K. Garelo, M. Jamet, D.-E. Jeong, K. Lee, T. Lee, M.-B. Martin, G. S. Kar, P. S  n  or, H.-J. Shin, and S. Roche, “Two-dimensional materials prospects for non-volatile spintronic memories”, *Nature* **606**, 663–673 (2022).
- [41] X. Lin, W. Yang, K. L. Wang, and W. Zhao, “Two-dimensional spintronics for low-power electronics”, *Nature Electronics* **2**, 274–283 (2019).
- [42] E. C. Ahn, “2D materials for spintronic devices”, *npj 2D Materials and Applications* **4**, 17 (2020).
- [43] D. Akinwande, C. Huyghebaert, C. H. Wang, M. I. Serna, S. Goossens, L. J. Li, H. S. Wong, and F. H. Koppens, “Graphene and two-dimensional materials for silicon technology”, *Nature* **573**, 507–518 (2019).
- [44] P. Ajayan, P. Kim, and K. Banerjee, “Two-dimensional van der Waals materials”, *Physics Today* **69**, 38 (2016).
- [45] J. F. Sierra, J. Fabian, R. K. Kawakami, S. Roche, and S. O. Valenzuela, “Van der Waals heterostructures for spintronics and opto-spintronics”, *Nature Nanotechnology* **16**, 856–868 (2021).
- [46] Y. Liu, N. O. Weiss, X. Duan, H. C. Cheng, Y. Huang, and X. Duan, “Van der Waals heterostructures and devices”, *Nature Reviews Materials* **1**, 1–17 (2016).
- [47] K. S. Novoselov, A. Mishchenko, A. Carvalho, and A. H. Castro Neto, “2D materials and van der Waals heterostructures”, *Science* **353**, aac9439 (2016).
- [48] Q. Shao, P. Li, L. Liu, H. Yang, S. Fukami, A. Razavi, H. Wu, K. Wang, F. Freimuth, Y. Mokrousov, M. D. Stiles, S. Emori, A. Hoffmann, J. Akerman, K. Roy, J. P. Wang, S. H. Yang, K. Garelo, and W. Zhang, “Roadmap of Spin-Orbit Torques”, *IEEE Transactions on Magnetism* **57**, 1–39 (2021).
- [49] W. Han, R. K. Kawakami, M. Gmitra, and J. Fabian, “Graphene spintronics”, *Nature Nanotechnology* **9**, 794–807 (2014).
- [50] B. Munkhbat, A. B. Yankovich, D. G. Baranov, R. Verre, E. Olsson, and T. O. Shegai, “Transition metal dichalcogenide metamaterials with atomic precision”, *Nature Communications* **11**, 1–8 (2020).

-
- [51] E. Ridolfi, L. R. Lima, E. R. Mucciolo, and C. H. Lewenkopf, “Electronic transport in disordered MoS₂ nanoribbons”, *Physical Review B* **95**, 035430 (2017).
 - [52] D. Koteekar-Patil, J. Deng, S. L. Wong, and K. E. J. Goh, “Coulomb Blockade in Etched Single- And Few-Layer MoS₂Nanoribbons”, *ACS Applied Electronic Materials* **1**, 2202–2207 (2019).
 - [53] V. K. Sangwan, D. Jariwala, I. S. Kim, K. S. Chen, T. J. Marks, L. J. Lauhon, and M. C. Hersam, “Gate-tunable memristive phenomena mediated by grain boundaries in single-layer MoS₂”, *Nature Nanotechnology* **10**, 403–406 (2015).
 - [54] V. K. Sangwan, H. S. Lee, H. Bergeron, I. Balla, M. E. Beck, K. S. Chen, and M. C. Hersam, “Multi-terminal memtransistors from polycrystalline monolayer molybdenum disulfide”, *Nature* **554**, 500–504 (2018).
 - [55] P. Boross, B. Dóra, A. Kiss, and F. Simon, “A unified theory of spin-relaxation due to spin-orbit coupling in metals and semiconductors”, *Scientific Reports* **3**, 1–5 (2013).
 - [56] F. G. Monzon and M. L. Roukes, “Spin injection and the local Hall effect in InAs quantum wells”, *Journal of Magnetism and Magnetic Materials* **198-199**, 632–635 (1999).
 - [57] C. Gould, C. Rüster, T. Jungwirth, E. Girgis, G. M. Schott, R. Giraud, K. Brunner, G. Schmidt, and L. W. Molenkamp, “Tunneling anisotropic magnetoresistance: A spin-valve-like tunnel magnetoresistance using a single magnetic layer”, *Physical Review Letters* **93**, 117203 (2004).
 - [58] J. H. Garcia, M. Vila, A. W. Cummings, and S. Roche, “Spin transport in graphene/transition metal dichalcogenide heterostructures”, *Chemical Society Reviews* **47**, 3359–3379 (2018).
 - [59] N. Tombros, C. Jozsa, M. Popinciuc, H. T. Jonkman, and B. J. Van Wees, “Electronic spin transport and spin precession in single graphene layers at room temperature”, *Nature* **448**, 571–574 (2007).
 - [60] D. Khokhriakov, A. W. Cummings, K. Song, M. Vila, B. Karpiak, A. Dankert, S. Roche, and S. P. Dash, “Tailoring emergent spin phenomena in Dirac material heterostructures”, *Science Advances* **4**, 9349 (2018).
 - [61] M. Drögeler, C. Franzen, F. Volmer, T. Pohlmann, L. Banszerus, M. Wolter, K. Watanabe, T. Taniguchi, C. Stampfer, and B. Beschoten, “Spin Lifetimes Exceeding 12 ns in Graphene Nonlocal Spin Valve Devices”, *Nano Letters* **16**, 3533–3539 (2016).
 - [62] D. Khokhriakov, B. Karpiak, A. M. Hoque, and S. P. Dash, “Two-dimensional spintronic circuit architectures on large scale graphene”, *Carbon* **161**, 892–899 (2020).

- [63] M. V. Kamalakar, J. Panda, M. Ramu, O. Karis, and T. Sarkar, “Ultimate spin currents in commercial chemical vapor deposited graphene”, *ACS Nano* **14**, 12771–12780 (2020).
- [64] D. Khokhriakov, S. Sayed, A. M. Hoque, B. Karpiak, B. Zhao, S. Datta, and S. P. Dash, “Multifunctional Spin Logic Gates In Graphene Spin Circuits”, *arXiv:2108.12259*, 1–20 (2021).
- [65] J. Chen, K. Wu, W. Hu, and J. Yang, “Spin–Orbit Coupling in 2D Semiconductors: A Theoretical Perspective”, *Journal of Physical Chemistry Letters* **12**, 12256–12268 (2021).
- [66] J. Sinova, S. O. Valenzuela, J. Wunderlich, C. H. Back, and T. Jungwirth, “Spin Hall effects”, *Reviews of Modern Physics* **87**, 1213–1260 (2015).
- [67] C. Mera Acosta, A. Fazzio, and G. M. Dalpian, “Zeeman-type spin splitting in nonmagnetic three-dimensional compounds”, *npj Quantum Materials* **4**, 1–6 (2019).
- [68] Z. Kovács-Krausz, A. M. Hoque, P. Makk, B. Szentpéteri, M. Kocsis, B. Fülöp, M. V. Yakushev, T. V. Kuznetsova, O. E. Tereshchenko, K. A. Kokh, I. E. Lukács, T. Taniguchi, K. Watanabe, S. P. Dash, and S. Csonka, “Electrically Controlled Spin Injection from Giant Rashba Spin-Orbit Conductor BiTeBr”, *Nano Letters* **20**, 4782–4791 (2020).
- [69] K. F. Mak, K. He, J. Shan, and T. F. Heinz, “Control of valley polarization in monolayer MoS₂ by optical helicity”, *Nature Nanotechnology* **7**, 494–498 (2012).
- [70] M. Mogi, K. Yasuda, R. Fujimura, R. Yoshimi, N. Ogawa, A. Tsukazaki, M. Kawamura, K. S. Takahashi, M. Kawasaki, and Y. Tokura, “Current-induced switching of proximity-induced ferromagnetic surface states in a topological insulator”, *Nature Communications* **12**, 1–6 (2021).
- [71] M. Gmitra, D. Kochan, P. Högl, and J. Fabian, “Trivial and inverted Dirac bands and the emergence of quantum spin Hall states in graphene on transition-metal dichalcogenides”, *Physical Review B* **93**, 155104 (2016).
- [72] M. Offidani, M. Milletari, R. Raimondi, and A. Ferreira, “Optimal Charge-to-Spin Conversion in Graphene on Transition-Metal Dichalcogenides”, *Physical Review Letters* **119**, 1–5 (2017).
- [73] B. Dieny et al., “Opportunities and challenges for spintronics in the microelectronics industry”, *Nature Electronics* **3**, 446–459 (2020).
- [74] J. Balakrishnan, G. K. W. Koon, A. Avsar, Y. Ho, J. H. Lee, M. Jaiswal, S.-J. Baeck, J.-H. Ahn, A. Ferreira, M. A. Cazalilla, A. H. C. Neto, and B. Özyilmaz, “Giant spin Hall effect in graphene grown by chemical vapour deposition”, *Nature Communications* **5**, 4748 (2014).

-
- [75] A. K. Geim and K. S. Novoselov, “The rise of graphene”, *Nature Materials* **6**, 183–191 (2007).
 - [76] M. Gmitra and J. Fabian, “Graphene on transition-metal dichalcogenides: A platform for proximity spin-orbit physics and optospintronics”, *Physical Review B* **92**, 155403 (2015).
 - [77] K. Song, D. Soriano, A. W. Cummings, R. Robles, P. Ordejón, and S. Roche, “Spin Proximity Effects in Graphene/Topological Insulator Heterostructures”, *Nano Letters* **18**, 2033–2039 (2018).
 - [78] Z. Wang, D. K. Ki, J. Y. Khoo, D. Mauro, H. Berger, L. S. Levitov, and A. F. Morpurgo, “Origin and magnitude of ‘designer’ spin-orbit interaction in graphene on semiconducting transition metal dichalcogenides”, *Physical Review X* **6**, 041020 (2016).
 - [79] J. O. Island, X. Cui, C. Lewandowski, J. Y. Khoo, E. M. Spanton, H. Zhou, D. Rhodes, J. C. Hone, T. Taniguchi, K. Watanabe, L. S. Levitov, M. P. Zaletel, and A. F. Young, “Spin-orbit-driven band inversion in bilayer graphene by the van der Waals proximity effect”, *Nature* **571**, 85–89 (2019).
 - [80] M. Gmitra, S. Konschuh, C. Ertler, C. Ambrosch-Draxl, and J. Fabian, “Band-structure topologies of graphene: Spin-orbit coupling effects from first principles”, *Physical Review B* **80**, 235431 (2009).
 - [81] G. Kwon, Y. H. Choi, H. Lee, H. S. Kim, J. Jeong, K. Jeong, M. Baik, H. Kwon, J. Ahn, E. Lee, and M. H. Cho, “Interaction- and defect-free van der Waals contacts between metals and two-dimensional semiconductors”, *Nature Electronics* **5**, 241–247 (2022).
 - [82] B. H. Moon, J. J. Bae, G. H. Han, H. Kim, H. Choi, and Y. H. Lee, “Anomalous conductance near percolative metal-insulator transition in monolayer MoS₂ at low voltage regime”, *ACS Nano* **13**, 6631–6637 (2019).
 - [83] D. Sarkar, X. Xie, W. Liu, W. Cao, J. Kang, Y. Gong, S. Kraemer, P. M. Ajayan, and K. Banerjee, “A subthermionic tunnel field-effect transistor with an atomically thin channel”, *Nature* **526**, 91–95 (2015).
 - [84] K. Nassiri Nazif, A. Daus, J. Hong, N. Lee, S. Vaziri, A. Kumar, F. Nitta, M. E. Chen, S. Kananian, R. Islam, K. H. Kim, J. H. Park, A. S. Poon, M. L. Brongersma, E. Pop, and K. C. Saraswat, “High-specific-power flexible transition metal dichalcogenide solar cells”, *Nature Communications* **12**, 1–9 (2021).
 - [85] X. Zhang, B. Liu, L. Gao, H. Yu, X. Liu, J. Du, J. Xiao, Y. Liu, L. Gu, Q. Liao, Z. Kang, Z. Zhang, and Y. Zhang, “Near-ideal van der Waals rectifiers based on all-two-dimensional Schottky junctions”, *Nature Communications* **12**, 1522 (2021).

- [86] T. Mueller and E. Malic, “Exciton physics and device application of two-dimensional transition metal dichalcogenide semiconductors”, *npj 2D Materials and Applications* **2**, 1–12 (2018).
- [87] A. Allain, J. Kang, K. Banerjee, and A. Kis, “Electrical contacts to two-dimensional semiconductors”, *Nature Materials* **14**, 1195–1205 (2015).
- [88] P. Zhang, Y. Zhang, Y. Wei, H. Jiang, X. Wang, and Y. Gong, “Contact engineering for two-dimensional semiconductors”, *Journal of Semiconductors* **41**, 071901 (2020).
- [89] T. Kim, S. Fan, S. Lee, M. K. Joo, and Y. H. Lee, “High-mobility junction field-effect transistor via graphene/MoS2 heterointerface”, *Scientific Reports* **10**, 1–8 (2020).
- [90] J. Hun Kim, J. Hwan Jeong, N. Kim, a. -, A. Kumar, M. A. Khan, M. Kumar -, S. Babu Mitta, M. Sup Choi, A. Nipane, F. Ali, C. Kim, J. T. Teherani, J. Hone, and W. Jong Yoo, “Electrical characterization of 2D materials-based field-effect transistors”, *2D Materials* **8**, 012002 (2020).
- [91] A. Dankert, L. Langouche, M. V. Kamalakar, and S. P. Dash, “High-performance molybdenum disulfide field-effect transistors with spin tunnel contacts”, *ACS Nano* **8**, 476–482 (2014).
- [92] S. Das, H. Y. Chen, A. V. Penumatcha, and J. Appenzeller, “High performance multilayer MoS2 transistors with scandium contacts”, *Nano Letters* **13**, 100–105 (2013).
- [93] P. C. Shen et al., “Ultralow contact resistance between semimetal and monolayer semiconductors”, *Nature* **593**, 211–217 (2021).
- [94] X. Chen, Z. Wu, S. Xu, L. Wang, R. Huang, Y. Han, W. Ye, W. Xiong, T. Han, G. Long, Y. Wang, Y. He, Y. Cai, P. Sheng, and N. Wang, “Probing the electron states and metal-insulator transition mechanisms in molybdenum disulphide vertical heterostructures”, *Nature Communications* **6**, 1–8 (2015).
- [95] P. D. Patil, S. Ghosh, M. Wasala, S. Lei, R. Vajtai, P. M. Ajayan, A. Ghosh, and S. Talapatra, “Gate-Induced Metal–Insulator Transition in 2D van der Waals Layers of Copper Indium Selenide Based Field-Effect Transistors”, *ACS Nano* **13**, 13413–13420 (2019).
- [96] B. H. Moon, “Metal-insulator transition in two-dimensional transition metal dichalcogenides”, *Emergent Materials* **4**, 989–998 (2021).
- [97] Y. Wu, Y. Xu, Z. Luo, Y. Yang, H. Xie, Q. Zhang, and X. Zhang, “Charge-spin interconversion and its applications in magnetic sensing”, *Journal of Applied Physics* **129**, 060902 (2021).

-
- [98] A. Dankert, J. Geurs, M. V. Kamalakar, S. Charpentier, and S. P. Dash, “Room temperature electrical detection of spin polarized currents in topological insulators”, *Nano Letters* **15**, 7976–7981 (2015).
 - [99] H. Wu, A. Chen, P. Zhang, H. He, J. Nance, C. Guo, J. Sasaki, T. Shirokura, P. N. Hai, B. Fang, S. A. Razavi, K. Wong, Y. Wen, Y. Ma, G. Yu, G. P. Carman, X. Han, X. Zhang, and K. L. Wang, “Magnetic memory driven by topological insulators”, *Nature Communications* **12**, 1–7 (2021).
 - [100] K. Vaklinova, A. Hoyer, M. Burghard, and K. Kern, “Current-Induced Spin Polarization in Topological Insulator-Graphene Heterostructures”, *Nano Letters* **16**, 2595–2602 (2016).
 - [101] C. H. Li, O. M. van’t Erve, J. T. Robinson, Y. Liu, L. Li, and B. T. Jonker, “Electrical detection of charge-current-induced spin polarization due to spin-momentum locking in Bi₂Se₃”, *Nature Nanotechnology* **9**, 218–224 (2014).
 - [102] Y. Ando, T. Hamasaki, T. Kurokawa, K. Ichiba, F. Yang, M. Novak, S. Sasaki, K. Segawa, Y. Ando, and M. Shiraishi, “Electrical Detection of the Spin Polarization Due to Charge Flow in the Surface State of the Topological Insulator Bi_{1.5}Sb_{0.5}Te_{1.7}Se_{1.3}”, *Nano Letters* **14**, 6226–6230 (2014).
 - [103] J. Tang, L.-t. Chang, X. Kou, K. Murata, E. S. Choi, M. Lang, Y. Fan, Y. Jiang, M. Montazeri, W. Jiang, Y. Wang, L. He, and K. L. Wang, “Electrical Detection of Spin-Polarized Conduction in (Bi_{0.53}Sb_{0.47})₂Te₃ Topological Insulator”, *Nano Letters* **14**, 5423–5429 (2014).
 - [104] L. Liu, A. Richardella, I. Garate, Y. Zhu, N. Samarth, and C. T. Chen, “Spin-polarized tunneling study of spin-momentum locking in topological insulators”, *Physical Review B* **91**, 235437 (2015).
 - [105] J. Tian, I. Miotkowski, S. Hong, and Y. P. Chen, “Electrical injection and detection of spin-polarized currents in topological insulator Bi₂Te₂Se”, *Scientific Reports* **5**, 1–8 (2015).
 - [106] C. H. Li, O. M. Vant Erve, S. Rajput, L. Li, and B. T. Jonker, “Direct comparison of current-induced spin polarization in topological insulator Bi₂Se₃ and InAs Rashba states”, *Nature Communications* **7**, 13518 (2016).
 - [107] B. Karpiak, A. Dankert, A. W. Cummings, S. R. Power, S. Roche, and S. P. Dash, “1D ferromagnetic edge contacts to 2D graphene/h-BN heterostructures”, *2D Materials* **5**, 014001 (2018).
 - [108] A. R. Mellnik, J. S. Lee, A. Richardella, J. L. Grab, P. J. Mintun, M. H. Fischer, A. Vaezi, A. Manchon, E. A. Kim, N. Samarth, and D. C. Ralph, “Spin-transfer torque generated by a topological insulator”, *Nature* **511**, 449–451 (2014).

- [109] A. Avsar, H. Ochoa, F. Guinea, B. Özyilmaz, B. J. van Wees, and I. J. Vera-Marun, “Colloquium : Spintronics in graphene and other two-dimensional materials”, *Reviews of Modern Physics* **92**, 021003 (2020).
- [110] D. MacNeill, G. M. Stiehl, M. H. D. Guimaraes, R. A. Buhrman, J. Park, and D. C. Ralph, “Control of spin-orbit torques through crystal symmetry in WTe₂/ferromagnet bilayers”, *Nature Physics* **13**, 300–305 (2017).
- [111] B. Zhao, D. Khokhriakov, Y. Zhang, H. Fu, B. Karpiak, A. M. Hoque, X. Xu, Y. Jiang, B. Yan, and S. P. Dash, “Observation of charge to spin conversion in Weyl semimetal WTe₂ at room temperature”, *Phys. Rev. Research* **2**, 013286 (2020).
- [112] B. Zhao, B. Karpiak, D. Khokhriakov, A. Johansson, A. M. Hoque, X. Xu, Y. Jiang, I. Mertig, and S. P. Dash, “Unconventional Chargeâ€“Spin Conversion in Weyl-Semimetal WTe₂”, *Advanced Materials* **32**, 2000818 (2020).
- [113] C. K. Safeer, N. Ontoso, J. Ingla-Aynés, F. Herling, V. T. Pham, A. Kurzmam, K. Ensslin, A. Chuvilin, I. Robredo, M. G. Vergniory, F. De Juan, L. E. Hueso, M. R. Calvo, and F. Casanova, “Large Multidirectional Spin-to-Charge Conversion in Low-Symmetry Semimetal MoTe₂ at Room Temperature”, *Nano Letters* **19**, 8758–8766 (2019).
- [114] G. M. Stiehl, R. Li, V. Gupta, I. E. Baggari, S. Jiang, H. Xie, L. F. Kourkoutis, K. F. Mak, J. Shan, R. A. Buhrman, and D. C. Ralph, “Layer-dependent spin-orbit torques generated by the centrosymmetric transition metal dichalcogenide β -MoTe₂”, *Physical Review B* **100**, 184402 (2019).
- [115] M. H. Guimarães, G. M. Stiehl, D. MacNeill, N. D. Reynolds, and D. C. Ralph, “Spin-Orbit Torques in NbSe₂/Permalloy Bilayers”, *Nano Letters* **18**, 1311–1316 (2018).
- [116] Q. Shao, G. Yu, Y. W. Lan, Y. Shi, M. Y. Li, C. Zheng, X. Zhu, L. J. Li, P. K. Amiri, and K. L. Wang, “Strong Rashba-Edelstein Effect-Induced Spin-Orbit Torques in Monolayer Transition Metal Dichalcogenide/Ferromagnet Bilayers”, *Nano Letters* **16**, 7514–7520 (2016).
- [117] G. M. Stiehl, D. MacNeill, N. Sivadas, I. El Baggari, M. H. Guimarães, N. D. Reynolds, L. F. Kourkoutis, C. J. Fennie, R. A. Buhrman, and D. C. Ralph, “Current-induced torques with dresselhaus symmetry due to resistance anisotropy in 2D materials”, *ACS Nano* **13**, 2599–2605 (2019).
- [118] H. Bangar, A. Kumar, N. Chowdhury, R. Mudgal, P. Gupta, R. S. Yadav, S. Das, and P. K. Muduli, “Large Spin-To-Charge Conversion at the Two-Dimensional Interface of Transition-Metal Dichalcogenides and Permalloy”, *ACS Applied Materials and Interfaces* **14**, 23 (2022).

-
- [119] J. Ingla-Aynés, I. Groen, F. Herling, N. Ontoso, C. K. Safeer, F. de Juan, L. E. Hueso, M. Gobbi, and F. Casanova, “Omnidirectional spin-to-charge conversion in graphene/NbSe₂ van der Waals heterostructures”, *2D Materials* **9**, 045001 (2022).
 - [120] L. A. Benítez, W. Savero Torres, J. F. Sierra, M. Timmermans, J. H. Garcia, S. Roche, M. V. Costache, and S. O. Valenzuela, “Tunable room-temperature spin galvanic and spin Hall effects in van der Waals heterostructures”, *Nature Materials* **19**, 170–175 (2020).
 - [121] C. K. Safeer, J. Ingla-Aynés, F. Herling, J. H. Garcia, M. Vila, N. Ontoso, M. R. Calvo, S. Roche, L. E. Hueso, and F. Casanova, “Room-Temperature Spin Hall Effect in Graphene/MoS₂ van der Waals Heterostructures”, *Nano Letters* **19**, 1074–1082 (2019).
 - [122] T. S. Ghiasi, A. A. Kaverzin, P. J. Blah, and B. J. Van Wees, “Charge-to-Spin Conversion by the Rashba-Edelstein Effect in Two-Dimensional van der Waals Heterostructures up to Room Temperature”, *Nano Letters* **19**, 5959–5966 (2019).
 - [123] D. Khokhriakov, A. M. Hoque, B. Karpiak, and S. P. Dash, “Gate-tunable spin-galvanic effect in graphene-topological insulator van der Waals heterostructures at room temperature”, *Nature Communications* **11**, 1–7 (2020).
 - [124] C. K. Safeer, F. Herling, W. Y. Choi, N. Ontoso, J. Ingla-Aynés, L. E. Hueso, and F. Casanova, “Reliability of spin-to-charge conversion measurements in graphene-based lateral spin valves”, *2D Materials* **9**, 015024 (2021).
 - [125] A. M. Hoque, D. Khokhriakov, K. Zollner, B. Zhao, B. Karpiak, J. Fabian, and S. P. Dash, “All-electrical creation and control of spin-galvanic signal in graphene and molybdenum ditelluride heterostructures at room temperature”, *Communications Physics* **4**, 1–9 (2021).
 - [126] L. A. Benítez, J. F. Sierra, W. Savero Torres, A. Arrighi, F. Bonell, M. V. Costache, and S. O. Valenzuela, “Strongly anisotropic spin relaxation in graphene–transition metal dichalcogenide heterostructures at room temperature”, *Nature Physics* **14**, 303–308 (2018).
 - [127] A. W. Cummings, J. H. Garcia, J. Fabian, and S. Roche, “Giant Spin Lifetime Anisotropy in Graphene Induced by Proximity Effects”, *Physical Review Letters* **119**, 206601 (2017).
 - [128] T. S. Ghiasi, J. Ingla-Aynés, A. A. Kaverzin, and B. J. Van Wees, “Large Proximity-Induced Spin Lifetime Anisotropy in Transition-Metal Dichalcogenide/Graphene Heterostructures”, *Nano Letters* **17**, 7528–7532 (2017).
 - [129] B. Radisavljevic, A. Radenovic, J. Brivio, V. Giacometti, and A. Kis, “Single-layer MoS₂ transistors”, *Nature Nanotechnology* **6**, 147–150 (2011).

-
- [130] S. B. Desai, S. R. Madhvapathy, A. B. Sachid, J. P. Llinas, Q. Wang, G. H. Ahn, G. Pitner, M. J. Kim, J. Bokor, C. Hu, H. S. Wong, and A. Javey, “MoS₂ transistors with 1-nanometer gate lengths”, *Science* **354**, 99–102 (2016).
- [131] F. Wu, H. Tian, Y. Shen, Z. Hou, J. Ren, G. Gou, Y. Sun, Y. Yang, and T.-L. Ren, “Vertical MoS₂ transistors with sub-1-nm gate lengths”, *Nature* **603**, 259–264 (2022).
- [132] S. Chen, S. Kim, W. Chen, J. Yuan, R. Bashir, J. Lou, A. M. Van Der Zande, and W. P. King, “Monolayer MoS₂ Nanoribbon Transistors Fabricated by Scanning Probe Lithography”, *Nano Letters* **19**, 2092–2098 (2019).
- [133] Y. Li, Z. Zhou, S. Zhang, and Z. Chen, “MoS₂ nanoribbons: High stability and unusual electronic and magnetic properties”, *Journal of the American Chemical Society* **130**, 16739–16744 (2008).
- [134] K. Xu, D. Chen, F. Yang, Z. Wang, L. Yin, F. Wang, R. Cheng, K. Liu, J. Xiong, Q. Liu, and J. He, “Sub-10 nm Nanopattern Architecture for 2D Material Field-Effect Transistors”, *Nano Letters* **17**, 1065–1070 (2017).
- [135] F. Zhang, C. H. Lee, J. A. Robinson, and J. Appenzeller, “Exploration of channel width scaling and edge states in transition metal dichalcogenides”, *Nano Research* **11**, 1768–1774 (2018).
- [136] D. Kotekar-Patil, J. Deng, S. L. Wong, C. S. Lau, and K. E. J. Goh, “Single layer MoS₂ nanoribbon field effect transistor”, *Applied Physics Letters* **114**, 013508 (2019).
- [137] H. Liu, J. Gu, and P. D. Ye, “MoS₂ nanoribbon transistors: Transition from depletion mode to enhancement mode by channel-width trimming”, *IEEE Electron Device Letters* **33**, 1273–1275 (2012).
- [138] L. Yu, Y. H. Lee, X. Ling, E. J. Santos, Y. C. Shin, Y. Lin, M. Dubey, E. Kaxiras, J. Kong, H. Wang, and T. Palacios, “Graphene/MoS₂ Hybrid technology for large-scale two-dimensional electronics”, *Nano Letters* **14**, 3055–3063 (2014).
- [139] G. Ciampalini, F. Fabbri, G. Menichetti, L. Buoni, S. Pace, V. Mišeikis, A. Pitanti, D. Pisignano, C. Coletti, A. Tredicucci, and S. Roddaro, “Unexpected Electron Transport Suppression in a Heterostructured Graphene-MoS₂ Multiple Field-Effect Transistor Architecture”, *ACS Nano* **16**, 1291–1300 (2022).
- [140] V. Mootheri, G. Arutchelvan, S. Banerjee, S. Sutar, A. Leonhardt, M. E. Boulon, C. Huyghebaert, M. Houssa, I. Asselberghs, I. Radu, M. Heyns, and D. Lin, “Graphene based Van der Waals contacts on MoS₂ field effect transistors”, *2D Materials* **8**, 015003 (2020).

-
- [141] D. B. Strukov, G. S. Snider, D. R. Stewart, and R. S. Williams, “The missing memristor found”, *Nature* **453**, 80–83 (2008).
 - [142] M. Lanza, A. Sebastian, W. D. Lu, M. Le Gallo, M.-F. Chang, D. Akinwande, F. M. Puglisi, H. N. Alshareef, M. Liu, and J. B. Roldan, “Memristive technologies for data storage, computation, encryption, and radio-frequency communication.”, *Science* **376**, eabj9979 (2022).
 - [143] D. Khokhriakov, B. Karpiak, A. M. Hoque, B. Zhao, S. Parui, and S. P. Dash, “Robust spin interconnect with isotropic spin dynamics in chemical vapor deposited graphene layers and boundaries”, *ACS Nano* **14**, 15864–15873 (2020).
 - [144] A. Fert and H. Jaffrès, “Conditions for efficient spin injection from a ferromagnetic metal into a semiconductor”, *Physical Review B - Condensed Matter and Materials Physics* **64**, 1–9 (2001).
 - [145] M. V. Kamalakar, A. Dankert, P. J. Kelly, and S. P. Dash, “Inversion of Spin Signal and Spin Filtering in Ferromagnet|Hexagonal Boron Nitride-Graphene van der Waals Heterostructures”, *Scientific Reports* **6**, 1–9 (2016).
 - [146] J. C. Toscano-Figueroa, N. Natera-Cordero, D. A. Bandurin, C. R. Anderson, V. H. Guarochico-Moreira, I. V. Grigorieva, and I. J. Vera-Marun, “Enhanced Spin Injection in Molecularly Functionalized Graphene via Ultrathin Oxide Barriers”, *Phys. Rev. Applied* **15**, 054018 (2021).
 - [147] R. Sun, S. Yang, X. Yang, E. Vetter, D. Sun, N. Li, L. Su, Y. Li, Y. Li, Z. Z. Gong, Z. K. Xie, K. Y. Hou, Q. Gul, W. He, X. Q. Zhang, and Z. H. Cheng, “Large Tunable Spin-to-Charge Conversion Induced by Hybrid Rashba and Dirac Surface States in Topological Insulator Heterostructures”, *Nano Letters* **19**, 4420–4426 (2019).
 - [148] A. Dankert, P. Bhaskar, D. Khokhriakov, I. H. Rodrigues, B. Karpiak, M. Venkata Kamalakar, S. Charpentier, I. Garate, and S. P. Dash, “Origin and evolution of surface spin current in topological insulators”, *Physical Review B* **97**, 125414 (2018).
 - [149] C. J. Lee, H. Park, J. Kang, J. Lee, M. Choi, and H. Park, “Extraction of intrinsic field-effect mobility of graphene considering effects of gate-bias-induced contact modulation”, *Journal of Applied Physics* **127**, 185105 (2020).
 - [150] A. M. Hoque, D. Khokhriakov, B. Karpiak, and S. P. Dash, “Charge-spin conversion in layered semimetal TaTe₂ and spin injection in van der Waals heterostructures”, *Physical Review Research* **2**, 033204 (2020).

- [151] L. Li, J. Zhang, G. Myeong, W. Shin, H. Lim, B. Kim, S. Kim, T. Jin, S. Cavill, B. S. Kim, C. Kim, J. Lischner, A. Ferreira, and S. Cho, “Gate-Tunable Reversible Rashba-Edelstein Effect in a Few-Layer Graphene/2H-TaS₂ Heterostructure at Room Temperature”, *ACS Nano* **14**, 5251–5259 (2020).
- [152] M. Kim, S. G. Xu, A. I. Berdyugin, A. Principi, S. Slizovskiy, N. Xin, P. Kumaravadivel, W. Kuang, M. Hamer, R. Krishna Kumar, R. V. Gorbachev, K. Watanabe, T. Taniguchi, I. V. Grigorieva, V. I. Fal’ko, M. Polini, and A. K. Geim, “Control of electron-electron interaction in graphene by proximity screenings”, *Nature Communications* **11**, 1–6 (2020).
- [153] W. Yan, E. Sagasta, M. Ribeiro, Y. Niimi, L. E. Hueso, and F. Casanova, “Large room temperature spin-to-charge conversion signals in a few-layer graphene/Pt lateral heterostructure”, *Nature Communications* **8**, 1–7 (2017).
- [154] W. Savero Torres, J. F. Sierra, L. A. Benítez, F. Bonell, M. V. Costache, and S. O. Valenzuela, “Spin precession and spin Hall effect in monolayer graphene/Pt nanostructures”, *2D Materials* **4**, 041008 (2017).
- [155] S. O. Valenzuela and M. Tinkham, “Direct electronic measurement of the spin Hall effect”, *Nature* **442**, 176–179 (2006).
- [156] X. He, Y. Wen, C. Zhang, Z. Lai, E. M. Chudnovsky, and X. Zhang, “Enhancement of critical current density in a superconducting NbSe₂ step junction”, *Nanoscale* **12**, 12076–12082 (2020).
- [157] D. Van Tuan, F. Ortmann, A. W. Cummings, D. Soriano, and S. Roche, “Spin dynamics and relaxation in graphene dictated by electron-hole puddles”, *Scientific Reports* **6**, 21046 (2016).
- [158] B. Zhao, A. M. Hoque, D. Khokhriakov, B. Karpiak, and S. P. Dash, “Charge-spin conversion signal in WTe₂ van der Waals hybrid devices with a geometrical design”, *Applied Physics Letters* **117**, 242401 (2020).
- [159] R. Habara and K. Wakabayashi, “Optically induced spin current in monolayer NbSe₂”, *Physical Review B* **103**, L161410 (2021).
- [160] F. Herling, C. K. Safeer, J. Ingla-Aynés, N. Ontoso, L. E. Hueso, and F. Casanova, “Gate tunability of highly efficient spin-to-charge conversion by spin Hall effect in graphene proximitized with WSe₂”, *APL Materials* **8**, 071103 (2020).
- [161] A. Manchon, H. C. Koo, J. Nitta, S. M. Frolov, and R. A. Duine, “New perspectives for Rashba spin-orbit coupling”, *Nature Materials* **14**, 871–882 (2015).
- [162] M. V. Kamalakar, C. Groenvelde, A. Dankert, and S. P. Dash, “Long distance spin communication in chemical vapour deposited graphene”, *Nature Communications* **6**, 6766 (2015).

-
- [163] G. Schmidt, D. Ferrand, L. Molenkamp, A. Filip, and B. van Wees, “Fundamental obstacle for electrical spin injection from a ferromagnetic metal into a diffusive semiconductor”, *Physical Review B* **62**, R4790 (2000).
 - [164] T. Wakamura, H. Akaike, Y. Omori, Y. Niimi, S. Takahashi, A. Fujimaki, S. Maekawa, and Y. Otani, “Quasiparticle-mediated spin Hall effect in a superconductor”, *Nature Materials* **14**, 675–679 (2015).
 - [165] K.-R. Jeon, K. Cho, A. Chakraborty, J.-C. Jeon, J. Yoon, H. Han, J.-K. Kim, and S. S. P. Parkin, “Role of Two-Dimensional Ising Superconductivity in the Nonequilibrium Quasiparticle Spin-to-Charge Conversion Efficiency”, *ACS Nano* **15**, 16819–16827 (2021).
 - [166] W. Han, Y. Otani, and S. Maekawa, “Quantum materials for spin and charge conversion”, *npj Quantum Materials* **3**, 27 (2018).
 - [167] J. Linder and J. W. Robinson, “Superconducting spintronics”, *Nature Physics* **11**, 307–315 (2015).
 - [168] J. Balakrishnan, G. Kok Wai Koon, M. Jaiswal, A. H. Castro Neto, and B. Özyilmaz, “Colossal enhancement of spin-orbit coupling in weakly hydrogenated graphene”, *Nature Physics* **9**, 284–287 (2013).
 - [169] K. Pi, W. Han, K. M. McCreary, A. G. Swartz, Y. Li, and R. K. Kawakami, “Manipulation of Spin Transport in Graphene by Surface Chemical Doping”, *Physical Review Letters* **104**, 187201 (2010).
 - [170] M. Z. Hasan and C. L. Kane, “Colloquium: Topological insulators”, *Reviews of Modern Physics* **82**, 3045–3067 (2010).
 - [171] P. Giannozzi et al., “QUANTUM ESPRESSO: a modular and open-source software project for quantum simulations of materials”, *Journal of Physics: Condensed Matter* **21**, 395502 (2009).
 - [172] P. Hohenberg and W. Kohn, “Inhomogeneous Electron Gas”, *Physical Review* **136**, B864–B871 (1964).
 - [173] S. Manipatruni, D. E. Nikonov, C.-c. Lin, t. A. Gosavi, H. Liu, B. Prasad, Y.-l. Huang, E. Bonturim, R. Ramesh, and i. A. Young, “Scalable energy-efficient magnetoelectric spin-orbit logic”, *Nature* **565**, 35–42 (2019).
 - [174] R. Mupparapu, T. Bucher, and I. Staude, “Integration of two-dimensional transition metal dichalcogenides with Mie-resonant dielectric nanostructures”, *Advances in Physics: X* **5**, 1734083 (2020).
 - [175] S.-S. Chee, D. Seo, H. Kim, H. Jang, S. Lee, S. P. Moon, K. H. Lee, S. W. Kim, H. Choi, and M.-H. Ham, “Lowering the Schottky Barrier Height by Graphene/Ag Electrodes for High-Mobility MoS₂ Field-Effect Transistors”, *Advanced Materials* **31**, 1804422 (2019).

- [176] X. Cui, G. H. Lee, Y. D. Kim, G. Arefe, P. Y. Huang, C. H. Lee, D. A. Chenet, X. Zhang, L. Wang, F. Ye, F. Pizzocchero, B. S. Jessen, K. Watanabe, T. Taniguchi, D. A. Muller, T. Low, P. Kim, and J. Hone, “Multi-terminal transport measurements of MoS₂ using a van der Waals heterostructure device platform”, *Nature Nanotechnology* **10**, 534–540 (2015).
- [177] B. Raes, J. E. Scheerder, M. V. Costache, F. Bonell, J. F. Sierra, J. Cuppens, J. Van De Vondel, and S. O. Valenzuela, “Determination of the spin-lifetime anisotropy in graphene using oblique spin precession”, *Nature Communications* **7**, 1–7 (2016).
- [178] L. A. Benítez, J. F. Sierra, W. Savero Torres, M. Timmermans, M. V. Costache, and S. O. Valenzuela, “Investigating the spin-orbit interaction in van der Waals heterostructures by means of the spin relaxation anisotropy”, *APL Materials* **7**, 120701 (2019).
- [179] A. David, P. Rakytá, A. Kormányos, and G. Burkard, “Induced spin-orbit coupling in twisted graphene-transition metal dichalcogenide heterobilayers: Twistronics meets spintronics”, *Physical Review B* **100**, 85412 (2019).
- [180] A. Sebastian, R. Pendurthi, T. H. Choudhury, J. M. Redwing, and S. Das, “Benchmarking monolayer MoS₂ and WS₂ field-effect transistors”, *Nature Communications* **12**, 693 (2021).
- [181] A. Daus, S. Vaziri, V. Chen, R. W. Koçroglu Grady, C. S. Bailey, H. R. Lee, K. Schauble, K. Brenner, and E. Pop, “High-performance flexible nanoscale transistors based on transition metal dichalcogenides”, *Nature Electronics* **4**, 495–501 (2021).
- [182] N. Li, Q. Wang, C. Shen, Z. Wei, H. Yu, J. Zhao, X. Lu, G. Wang, C. He, L. Xie, J. Zhu, L. Du, R. Yang, D. Shi, and G. Zhang, “Large-scale flexible and transparent electronics based on monolayer molybdenum disulfide field-effect transistors”, *Nature Electronics* **3**, 711–717 (2020).
- [183] J. Jiang, M. H. Doan, L. Sun, H. Kim, H. Yu, M. K. Joo, S. H. Park, H. Yang, D. L. Duong, and Y. H. Lee, “Ultrashort Vertical-Channel van der Waals Semiconductor Transistors”, *Advanced Science* **7**, 1902964 (2020).
- [184] M. L. Chen, X. Sun, H. Liu, H. Wang, Q. Zhu, S. Wang, H. Du, B. Dong, J. Zhang, Y. Sun, S. Qiu, T. Alava, S. Liu, D. M. Sun, and Z. Han, “A FinFET with one atomic layer channel”, *Nature Communications* **11**, 1–7 (2020).
- [185] J. Stankiewicz, J. Sesé, G. Balakrishnan, and Z. Fisk, “Electrical transport properties of WS₂”, *Physical Review B - Condensed Matter and Materials Physics* **90**, 8174–8181 (2014).

-
- [186] J. R. Chen, P. M. Odenthal, A. G. Swartz, G. C. Floyd, H. Wen, K. Y. Luo, and R. K. Kawakami, “Control of Schottky barriers in single layer MoS2 transistors with ferromagnetic contacts”, *Nano Letters* **13**, 3106–3110 (2013).
 - [187] K. E. Kroell and G. K. Ackermann, “Threshold voltage of narrow channel field effect transistors”, *Solid State Electronics* **19**, 77–81 (1976).
 - [188] K. Abbas, *Handbook of Digital CMOS Technology, Circuits, and Systems* (Springer International Publishing, Cham, 2020).
 - [189] B. Radisavljevic and A. Kis, “Mobility engineering and a metal–insulator transition in monolayer MoS2”, *Nature Materials* **12**, 815–820 (2013).
 - [190] L. H. Ho, A. P. Micolich, A. R. Hamilton, and O. P. Sushkov, “Ground-plane screening of Coulomb interactions in two-dimensional systems: How effectively can one two-dimensional system screen interactions in another”, *Physical Review B - Condensed Matter and Materials Physics* **80**, 155412 (2009).
 - [191] A. Laturia, M. L. Van De Put, and W. G. Vandenberghe, “Dielectric properties of hexagonal boron nitride and transition metal dichalcogenides: from monolayer to bulk”, *npj 2D Materials and Applications* **2**, 6 (2018).
 - [192] S. Ghatak, A. N. Pal, and A. Ghosh, “Nature of electronic states in atomically thin MoS2 field-effect transistors”, *ACS Nano* **5**, 7707–7712 (2011).
 - [193] B. Muchharla, T. N. Narayanan, K. Balakrishnan, P. M. Ajayan, and S. Talapatra, “Temperature dependent electrical transport of disordered reduced graphene oxide”, *2D Materials* **1**, 011008 (2014).
 - [194] M. Kim, R. Ge, X. Wu, X. Lan, J. Tice, J. C. Lee, and D. Akinwande, “Zero-static power radio-frequency switches based on MoS2 atomrystals”, *Nature Communications* **9**, 1–7 (2018).
 - [195] A. Azizi, X. Zou, P. Ercius, Z. Zhang, A. L. Elías, N. Perea-López, G. Stone, M. Terrones, B. I. Yakobson, and N. Alem, “Dislocation motion and grain boundary migration in two-dimensional tungsten disulphide”, *Nature Communications* **5**, 1–7 (2014).
 - [196] S. M. Hus, R. Ge, P. A. Chen, L. Liang, G. E. Donnelly, W. Ko, F. Huang, M. H. Chiang, A. P. Li, and D. Akinwande, “Observation of single-defect memristor in an MoS2 atomic sheet”, *Nature Nanotechnology* **16**, 58–62 (2020).
 - [197] D. Qiu and E. K. Kim, “Electrically Tunable and Negative Schottky Barriers in Multi-layered Graphene/MoS2 Heterostructured Transistors”, *Scientific Reports* **5**, 13743 (2015).

Appended Papers

Paper I

Room temperature nonlocal detection of charge-spin interconversion in a topological insulator

Anamul Md. Hoque,^{†,‡} Lars Sjöström,^{†,‡} Dmitrii Khokhriakov,[†] Bing Zhao,[†] and
Saroj P. Dash^{*,†}

[†]*Department of Microtechnology and Nanoscience, Chalmers University of Technology,
SE-41296, Göteborg, Sweden*

[‡]*These authors contributed equally to this work*

E-mail: saroj.dash@chalmers.se

Abstract

Topological insulators (TIs) are emerging materials for next-generation nanoelectronic devices, thanks to the non-trivial spin-momentum locking of their topological surface states. Although charge-spin conversion (CSC) has previously been reported in TIs by potentiometric measurements, reliable nonlocal detection has so far been observed only at cryogenic temperatures up to $T = 15$ K. Here, we report nonlocal detection of CSC and its inverse effect in a TI compound $\text{Bi}_{1.5}\text{Sb}_{0.5}\text{Te}_{1.7}\text{Se}_{1.3}$ at room temperature using a van der Waals heterostructure with a graphene spin valve device. The lateral nonlocal device design with graphene allows observation of both spin switch and Hanle spin precession signals for generation, injection and detection of spin currents by the TI. Detailed bias- and gate-dependent measurements in different geometries prove the robustness of the CSC effects in the TI. These findings demonstrate the possibility of using topological materials to make all-electrical room-temperature spintronic devices.

Keywords

topological insulator, charge-spin conversion, graphene spin-valve, Hanle spin precession, spin Hall effects, spin momentum locking, room temperature

Topological insulators (TIs) have attracted significant attention in condensed matter physics and information technology because of their unique nontrivial electronic band structure with topologically protected electronic states.^{1–3} Their inverted bulk bands for electronic excitations induced by strong spin-orbit coupling creates a gapless metallic Dirac state with helical spin textures.^{4–6}

The topological states are characterized by spin-momentum locking (SML), where the electron spin orientation is locked perpendicularly to its momentum. Such spin-polarized states have a great potential for spintronic technologies, as application of a charge current can create a significant non-equilibrium spin density, providing a large charge-spin conversion (CSC) efficiency.^{7–10} The spin polarization has been utilized to create energy-efficient magnetization dynamics and switching of an adjacent ferromagnet (FM) in a heterostructure via spin-orbit torque (SOT) phenomena.^{8,11–13} However, the origins of a large SOT are not well understood¹⁴ and the contributions of spin polarization from the topological surface states, quantum confinement at the surfaces and bulk bands can coexist at the Fermi level, and interfacial effects in TI/FM heterostructures^{15,16} cannot be ruled out.

The CSC effects in TIs have been investigated using ferromagnetic (FM) tunnel contacts in potentiometric measurements up to room temperature^{17–23} and the competition between the bulk and surface contribution has been evaluated.²⁴ However, the background voltage in local measurement geometries and TI/FM interfaces also raise concerns about the measured signals. It has been shown that nonlocal (NL) measurement geometries enable the measurement of pure spin currents without any charge current contribution.^{25,26} Graphene based hybrid spin valves have been employed in the sensing circuit to take advantage of graphene's excellent spin transport and precession capabilities.^{27–31} However, the measured NL spin signals were only detected at very low temperatures up to $T = 15$ K,³⁰ limiting its practical applications.

Here, we demonstrate room temperature CSC and its inverse effect in the TI $\text{Bi}_{1.5}\text{Sb}_{0.5}\text{Te}_{1.7}\text{Se}_{1.3}$ (BSTS) using a van der Waals (vdW) heterostructure with a graphene spin valve device. The generated spin current in the TI is injected into a chemical vapor deposition (CVD) graphene channel and subsequently detected using a FM contact in a hybrid NL spin valve device. We take advantage of the lateral NL spin valve device design with graphene to observe both spin switch and Hanle spin precession signals, reliably demonstrating generation, injection and detection of spin currents by the TI. Detailed measurements in different device geometries and bias- and gate-dependent studies at room temperature prove the robustness of the CSC effects in the TI.

Results and discussion

To detect CSC in the TI, we utilized BSTS and graphene heterostructure based spin valve devices, as shown in Figures 1a-b. We choose BSTS as a TI, which is part of the well-studied^{5,15,18,30,32–35} $\text{Bi}_{2-x}\text{Sb}_x\text{Te}_{3-y}\text{Se}_y$ family of TIs and has its Fermi level in the band gap, giving rise to a dominant surface contribution to maximize the CSC efficiency.^{24,36,37} On the other hand, we used CVD graphene as the spin channel material because it has been shown to exhibit a robust and long distance spin transport with multifunctional spin logic operation at room temperature,^{27–29} as well as being more suitable than exfoliated graphene for future

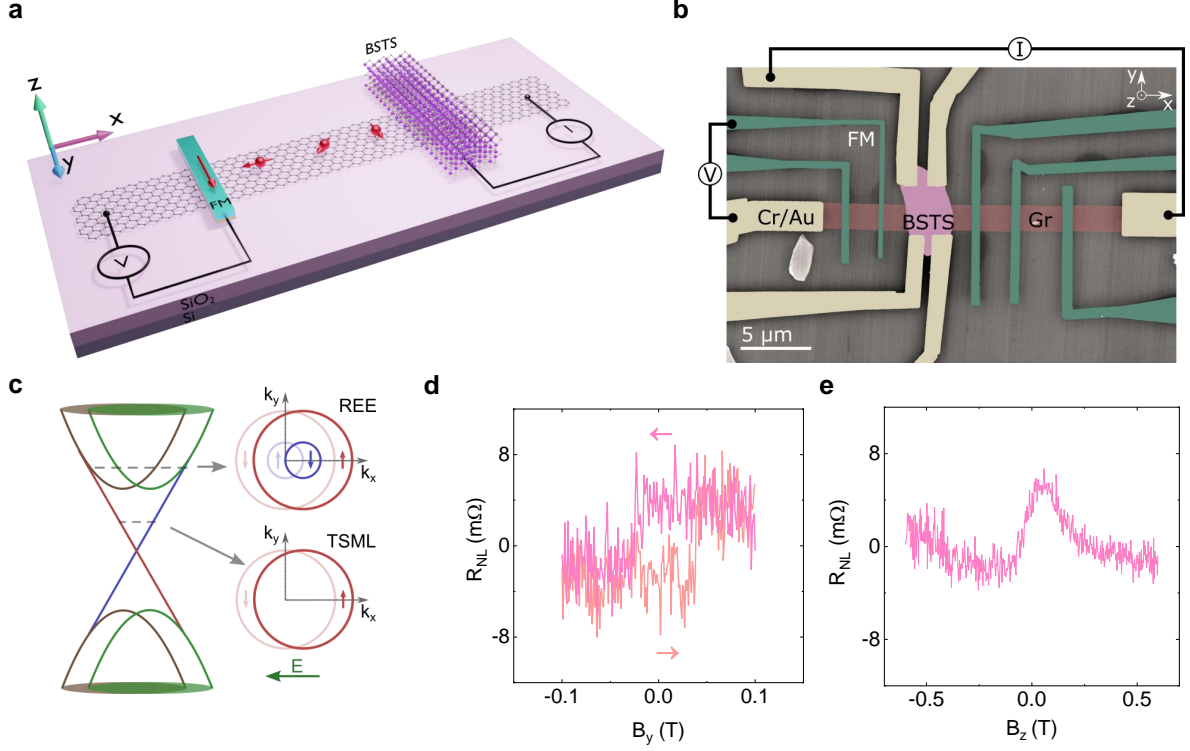


Figure 1: **Graphene/BSTS heterostructure device for nonlocal detection of charge-spin conversion at room temperature.** (a, b) Schematic and coloured SEM image of the graphene/BSTS heterostructure device with NL measurement geometry, with reference nonmagnetic (Cr/Au) and FM (TiO_2/Co) contacts. The scale bar shown is $5\ \mu\text{m}$. (c) Schematic of two CSC mechanisms: the Rashba-Edelstein effect (REE) and topological spin-momentum locking (TSML). (d) Spin switch signal ($R_{NL} = V_{NL}/I$) for spin injection from BSTS with B_y magnetic field sweep. (e) Hanle signal R_{NL} with B_z magnetic field sweep. The measurements were performed at $T = 295\ \text{K}$ for a bias current of $I = 150\ \mu\text{A}$ and a gate voltage of $V_g = -70\ \text{V}$. Linear backgrounds of $4\ \mu\text{V}$ and $5\ \mu\text{V}$ have been subtracted from the measured data in (d) and (e), respectively.

large-scale fabrication.^{25,27,38} We fabricated graphene/BSTS vdW heterostructures with reference non-magnetic (20 nm Cr/90 nm Au) and FM ($\sim 1\ \text{nm TiO}_2/90\ \text{nm Co}$) contacts for spin injection and detection in the graphene channel (see Supplementary information S1). Here, the TiO_2 oxide layer acts as a tunnel barrier to help mitigate issues with the graphene channel.^{39,40}

The CSC in TIs can arise due to the bulk spin Hall effect (SHE), the Rashba-Edelstein effect (REE) of the bulk states or the trivial surface states, and/or the topological spin-momentum locking (TSML) of the surface states.^{33,41} As shown in Figure 1c, the Fermi surface has a winding spin texture for both REE and TSML, which will be offset from the equilibrium position by the additional electron momentum that is caused by an applied electric field.^{35,42} Importantly, BSTS has been found to have dominant TI properties below $90\ \text{K}$,²⁴ which means that also the bulk SHE and the bulk REE can contribute to CSC at

room temperature, although the TSML may still be present.

We used a recently developed device geometry and measurement technique for detection of CSC in the TI, shown in Figure 1a.^{43–47} An applied charge current creates a spin density due to CSC in the TI, which is then injected into the graphene spin channel. The diffused spin polarization in the graphene channel is detected as a NL voltage by a remote FM electrode placed at a channel length of $L = 3.4\ \mu\text{m}$ (center-to-center distance) away from the TI flake. First, spin switch measurements were performed while sweeping an in-plane magnetic field along the y axis (B_y), which is the easy axis of the FM electrodes. The applied magnetic field results in switching of the magnetization orientation of the FM detector from parallel to antiparallel orientation with respect to the injected spin-polarized electrons from the TI into the graphene channel. This results in a change in NL resistance ($R_{NL} = V_{NL}/I$) as shown in Figure 1d, where V_{NL} is the measured voltage and I is the applied charge current across the graphene/TI structure. In order to prove the spin origin of the signal, Hanle spin precession measurements were conducted by sweeping the magnetic field out-of-plane along the z axis (B_z). This causes the in-plane spins to precess and dephase while diffusing along the graphene channel, and reach the FM detector electrode with a finite angle with respect to the contact magnetization direction.²⁶ As shown in Figure 1e, the measured Hanle signal R_{NL} depends on B_z , as it changes the projection of the spin polarization onto the FM contact magnetization direction. The observation of both spin switch and Hanle spin precession signals is a confirmation of the spin injection from the TI into the graphene channel due to an efficient CSC effect. By using data from the CSC signals and reference measurements (see below), the spin polarization of the BSTS flake could be estimated to about 0.1 % (see Supplementary information S2).

The Hanle signals were further investigated with the magnetization direction of the FM detector electrode in parallel and antiparallel orientations ($\pm y$), respectively, as shown in Figure 2a. Depending on the FM magnetization direction, the Hanle signal has either a minimum or a maximum around $B_z = 0$. The two curves for opposite magnetization were averaged to get rid of any non-spin-related background (see Supplementary information S3). As the observed signals are not symmetric, the averaged signal was then deconvoluted into its symmetric and antisymmetric components and subsequently fitted (see Supplementary information S3). From this, values for the spin lifetime τ_s and the spin diffusion length λ_s in the graphene were extracted as 75 ps and $1.5\ \mu\text{m}$, respectively. The relative contribution of the symmetric and antisymmetric components depends on the angle between the polarization of the spin current that is injected from the BSTS flake into the graphene and the magnetization direction of the FM detector contact,^{27,45,47} and this angle could here be estimated to $\varphi = 67 \pm 1^\circ$ (see Supplementary information S3). Simulated Hanle signals for different values of φ are illustrated in Figure 2b.^{45,47}

The asymmetric characteristic of the Hanle signals can have different origins, such as a combination of conventional and unconventional CSC mechanisms,^{48,49} however, the most likely one is the bias current distribution in the TI. Because of the positions of the two electrodes (one on TI and the other on graphene) that the bias current is applied between, the charge current through the BSTS flake has nonzero x , y and z components. Due to the mechanism of the CSC, the generated in-plane spin polarization (which is detected in the Hanle measurements) will be perpendicular to the charge current. The injected spin from the TI into the graphene channel will therefore have nonzero x and y components, corresponding

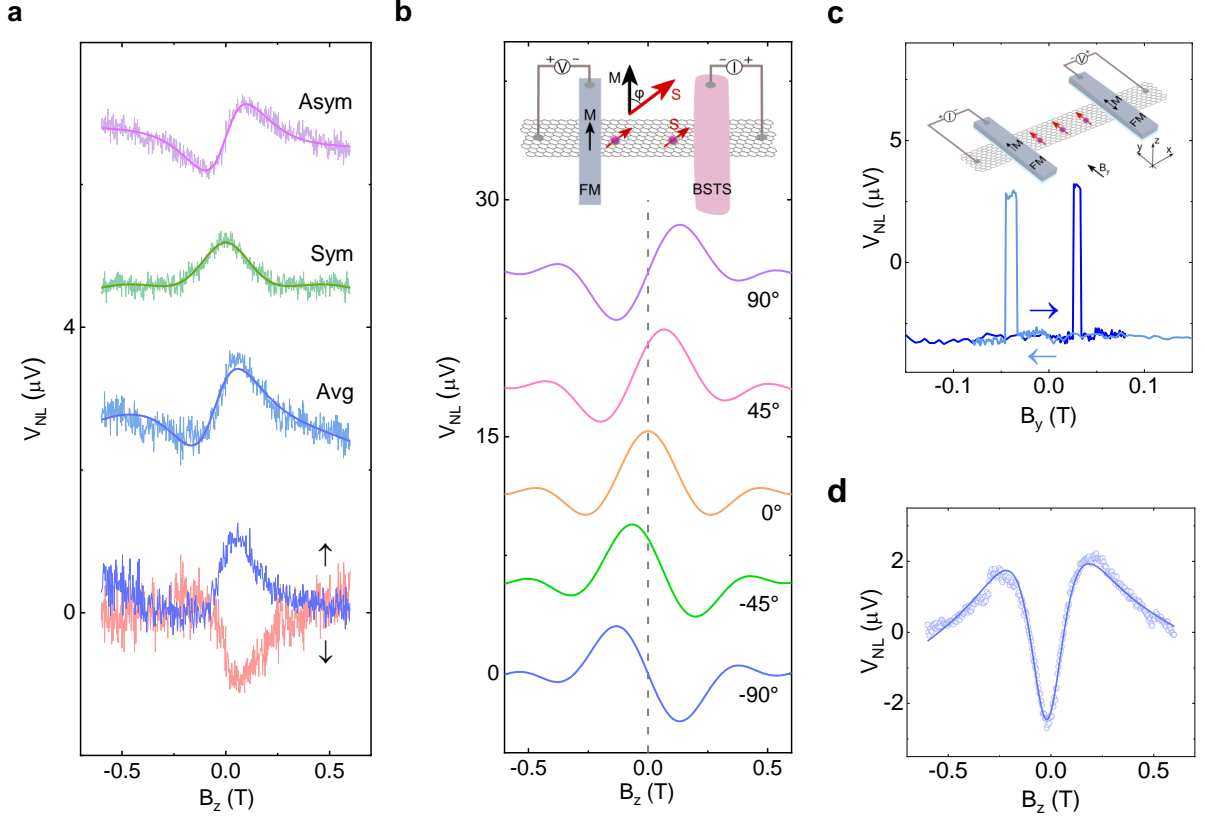


Figure 2: Asymmetric components of the charge-spin conversion Hanle signal. (a) Hanle spin precession signals with FM contact magnetization along the $+y$ (\uparrow) and the $-y$ (\downarrow) direction, respectively, as well as the averaged signal (Avg) and the symmetric (Sym) and the antisymmetric (Asym) components of the averaged signal. The green and purple solid lines are fits of the respective signal components, and the blue solid line is a guide to the eye for the averaged signal. The measurements were performed for $I = 150 \mu A$ and $V_g = -70 V$. The data are shifted vertically for clarity. (b) Simulation of the evolution of the CSC signal with the tilt angle of the injected spin polarization in the device. Inset: The top view of the CSC measurement geometry with the tilt angle (φ) of spins S injected from the BSTS with respect to the magnetic moment M of the FM spin injector. (c) A reference spin valve signal measured in pristine graphene with FM contacts used as both spin injector and spin detector. The measurement was performed for $I = -50 \mu A$ and $V_g = -70 V$. Inset: Schematic of the measurement setup with pristine graphene. (d) Hanle spin precession signal for measurement in pristine graphene. The solid line is a fit of the detected signal. The measurement was performed for $I = -100 \mu A$ and $V_g = -70 V$. Linear backgrounds of $5 \mu V$, $-1 \mu V$ and $-1 \mu V$ have been subtracted from the measured data in (a), (c) and (d), respectively.

to asymmetric Hanle signals.^{27,34,43,45,47,48}

For comparison, signals from spin valve and Hanle measurements in a pristine graphene region of the same device with FM electrodes as both spin injector and detector²⁸ are shown in Figures 2c-d. In contrast to the CSC-based measurements, the Hanle signal for pristine graphene is symmetric, because the injected spin and the detector contact magnetization

are always either parallel or antiparallel. The spin transport parameters that were extracted from Figure 2d are $\tau_s = 45$ ps and $\lambda_s = 0.85 \mu\text{m}$. Similar Hanle measurements for the graphene channel across the vdW heterostructure (see Supplementary information S4) give $\tau_s = 103$ ps and $\lambda_s = 1.0 \mu\text{m}$. The variation in transport parameters between the three different measurements is most likely because of differences in contact and channel properties. By comparing the results from the pristine graphene to those from the vdW heterostructure, we can conclude that there is little or no spin absorption by the TI flake, as discussed in Supplementary information S4.

Geometry and bias dependence of CSC in TI

In order to investigate the origin of the CSC, experiments were performed for the different measurement geometries shown in Figure 3a. In the first geometry, the bias current I_1 is applied on the $+x$ side of the BSTS flake and the NL voltage V_1 is detected on the $-x$ side of the flake. In the second setup, an opposite geometry is used with I_2 and V_2 . Both setups have similar channel lengths of $3.4 \mu\text{m}$ and $3.2 \mu\text{m}$, respectively. As shown in Figure 3b, there is a sign change for the spin switch signal between the two measurement geometries: setup 1 gives a high NL voltage when the contact magnetization of the detector is in the $+y$ direction and a low NL voltage for $-y$ contact magnetization, while setup 2 gives the opposite. The origin of the CSC must therefore be odd with the x component of the charge current, but may also depend on the y and z components. This behavior indicates that the origin of the spin current can be due to either of the conventional SHE, REE or TSML, since all of these effects depend on the in-plane charge current direction.^{33,34,41} These control experiments, however, rule out any such unconventional CSC mechanism in the TI as the one recently reported in the case of WTe_2 ,⁴³ where the latter showed a CSC which is independent of the x component of the charge current. It should be noted that differences in amplitude between the two signals in Figure 3b can arise from different detector FM contacts being used, which may have different polarizations and/or interface resistances with the graphene.

The bias current dependence of the spin signal was examined through both spin switch and Hanle measurements with an experimental setup as shown in Figure 3c. Both the spin switch (Figure 3d) and the Hanle (Figure 3e) signals show a sign change with reversed bias current. Furthermore, Figure 3f shows a linear bias dependence of the amplitude of both the spin switch and the Hanle signals. Here, the Hanle signal is larger than the spin switch signal. This is logical because the Hanle amplitude is the vector addition of the symmetric and the antisymmetric components, and therefore consists of both the x and the y components of the injected spin polarization from BSTS into graphene, due to the precession of spins in the xy plane. The spin switch signal, on the other hand, consists of only the y component of the spin, since there is no precession and the FM detector is only sensitive to spin components in the y direction.

Furthermore, considering that reversing the bias current means changing between injection and extraction of polarized spin, the observation of a sign change of the spin signal is as expected.⁴⁷ In principle, the linear bias dependence is also expected, since a larger charge current enables a larger spin polarization. The observation of linear bias dependence also rules out thermal effects (*e.g.* the Seebeck effect) in our data in the measured bias ranges.⁵⁰

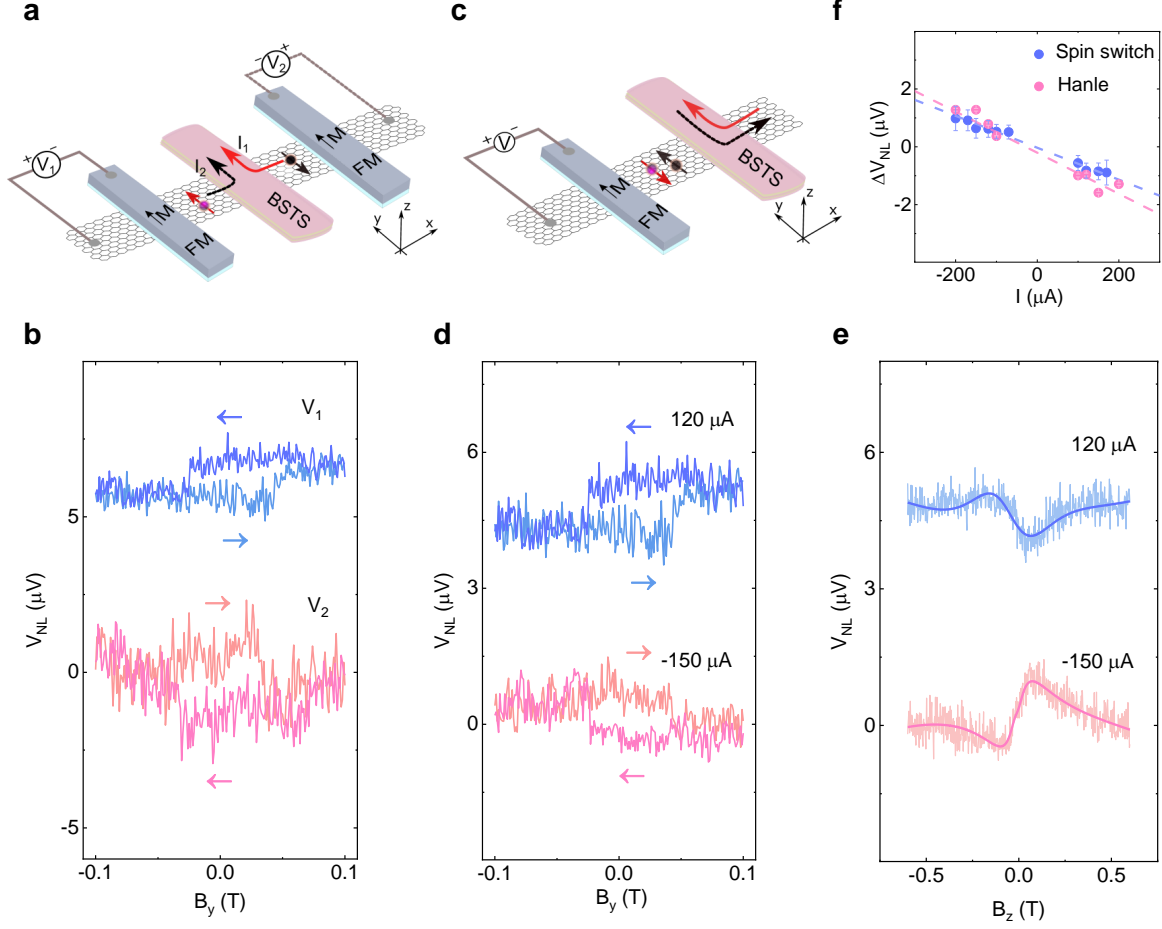


Figure 3: **Geometry and bias current dependence of charge-spin conversion signal in graphene/BSTS junction.** (a) Schematic of the device and the two different CSC measurement geometries. (b) Spin switch signals for each of the two measurement geometries. The measurements were performed at room temperature for $I = 120 \mu\text{A}$ and $V_g = -60 \text{ V}$ and for $I = 300 \mu\text{A}$ and $V_g = -75 \text{ V}$, respectively. (c) Schematic of the device and measurement geometry with arrows indicating the direction of positive and negative bias currents. (d, e) Spin switch and Hanle signals for $I = 120 \mu\text{A}$ and $I = -150 \mu\text{A}$. The Hanle signals are presented with corresponding guides to the eye. The measurements were performed at room temperature for $V_g = -60 \text{ V}$ and $V_g = -70 \text{ V}$, for spin switch and Hanle signals, respectively, and the data are shifted vertically for clarity. (f) The amplitude of the measured spin switch and Hanle signals as a function of bias current, and linear fits. Some error bars are smaller than the data points. Linear backgrounds of $-4 \mu\text{V}$ and $28 \mu\text{V}$ in (b), $-4 \mu\text{V}$ and $4 \mu\text{V}$ in (d) and $1 \mu\text{V}$ and $-3 \mu\text{V}$ in (e) have been subtracted from the respective measured data.

Gate dependence of CSC signal in TI

The gate dependence of the spin signal was investigated using the device geometry shown in Figure 4a, with use of the n++Si/SiO₂ substrate as the back gate. Figure 4b shows the Dirac curves of the graphene channel, both for pristine graphene and in the graphene/BSTS

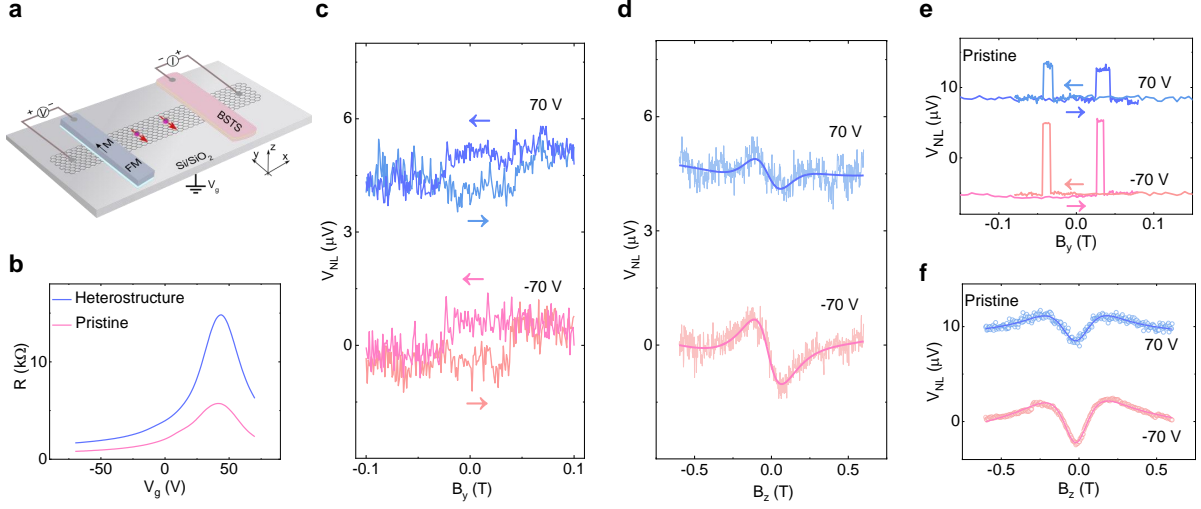


Figure 4: Gate voltage dependence of charge-spin conversion signal in graphene/BSTS junction. (a) Device geometry for gate dependence measurements with back gate. (b) The Dirac curve of heterostructure and pristine graphene regions of the device. (c, d) Spin switch and Hanle spin precession signals for electron and hole doped graphene regimes measured at $V_g = \pm 70$ V and $I = 150 \mu\text{A}$ at room temperature. The Hanle signals are presented with guides to the eye. The data are shifted vertically for clarity. (e, f) Spin valve and Hanle signals of the pristine graphene region at electron and hole doped graphene regimes, measured at $V_g = \pm 70$ V and $I = -100 \mu\text{A}$ at room temperature. Linear backgrounds of $-7 \mu\text{V}$ and $-3 \mu\text{V}$ in (c), $2 \mu\text{V}$ and $3 \mu\text{V}$ in (d), $4 \mu\text{V}$ and $0 \mu\text{V}$ in (e) and $-2 \mu\text{V}$ and $-1 \mu\text{V}$ in (f) have been subtracted from the respective measured data.

heterostructure region. The Dirac points at $V_g = 43$ V (for the heterostructure region) and $V_g = 41$ V (for pristine graphene) indicate negligible contribution from doping of graphene by the TI and band misalignment between the graphene and BSTS, which could have offset the charge carriers. The difference in the resistances comes from the longer channel for the graphene/BSTS heterostructure. The mobility of the charge carriers was calculated⁵¹ to be $\mu_{HS} = 1200 \text{ cm}^2/\text{Vs}$ for the heterostructure graphene and $\mu_{pr} = 1000 \text{ cm}^2/\text{Vs}$ for the pristine graphene, as reported in literature.^{34,46,52,53}

The gate dependence was measured for spin switch and Hanle spin precession, as shown in Figures 4c-d. As the TI is not very sensitive to gate voltage in our experiments (because of shielding by the graphene and the thickness of the TI flake itself, see Supplementary information S8), the modulation of the Fermi level in graphene from p- to n-doped regime for $V_g = \pm 70$ V causes only a small Fermi level tuning of BSTS and does not change the sign of the signal, proving the spin origin of the signal and ruling out any artifact arising from the stray magnetic field from the detector FM contacts on the graphene.⁵⁴ The absence of a sign change of the spin signal also indicates that the CSC does not originate from proximity-induced graphene in our device.³⁴ This is because both the proximity-induced SHE and the proximity-induced REE would have given rise to a sign change of the spin polarization with change in the carrier type in graphene.^{34,53,55,56} The possibility that the change of the

charge carrier type would be prevented by screening of the electric field in graphene due to the proximity to the TI⁵⁷ was deemed very unlikely because a sign-change of the proximity-induced REE signal has previously been observed with a change of the carrier type in similar CVD graphene/TI heterostructures.³⁴

In our device, the contribution from the bulk SHE and the bulk REE in the TI are, however, not expected to cause a sign change, since this would necessitate the Fermi level to be tuned across the TI band gap and would therefore require a very large applied gate voltage.^{34,52} The TSML does not give a sign change either, even when the Fermi level is tuned across the TI Dirac point, due to the opposite chirality of the TSML above and below the Dirac point, which counteracts the effect of the changed charge carrier types.^{24,34} It should furthermore be noted that our device geometry is not very suitable for seeing proximity-induced CSC, since these effects require the charge and spin currents to be perpendicular at the graphene/BSTS interface. While it is possible for some charge current to flow in the y direction at the interface, this is not the main contribution of the charge current direction. Additionally, the proximity-induced SHE further requires out-of-plane spin polarization,⁵⁸ which is not observed in the spin switch and Hanle measurements. However, because of the aforementioned similarities between the bulk SHE, the bulk REE and the TSML, it is not possible to further discern the exact contributions of the CSC in our device at room temperature.

For comparison, signals from spin valve and Hanle measurements in pristine graphene, with FM electrodes as both spin injector and detector, are shown in Figures 4e-f. Gate voltage modulation results in a behavior that is very similar to the case with CSC, with the main difference being the symmetry of the Hanle signals, as already discussed above. The detailed gate dependence of the Hanle spin signal and the extracted spin transport parameters are shown in Supplementary figure S3.

Inverse CSC effects

Inverse CSC (ICSC) experiments were also performed with the TI to verify the Onsager reciprocity of the system, by injecting spin current from the FM contact into the graphene channel. The spin current in graphene is absorbed by the TI and produces a NL voltage, as shown in Figure 5a for two different measurement geometries. The spin polarization causes the Fermi surface spin textures of the TI to shift from the equilibrium position in the way shown in the inset of Figure 5a, which should give rise to a charge current. Spin switch measurements indeed showed ICSC effects (Figure 5b), which was measured at room temperature. It can clearly be seen that the CSC (Figure 3d, bottom signal) and the ICSC (Figure 5b) obey the Onsager reciprocity by generating spin signals of opposite sign for similar bias current and the same geometry, due to the spin diffusion current having opposite directions in the two cases.

The spin polarization of BSTS in the ICSC measurement was determined to about 0.2 %, slightly higher than for the CSC counterpart. The reason for this slight difference could be due to different spin injection and detection efficiencies of the graphene/BSTS and the graphene/FM contacts with and without bias voltages. Moreover, it is important to mention that the electric field across the BSTS flake in the CSC measurement, which is different from the ICSC measurement, can also reduce the measured spin polarization.

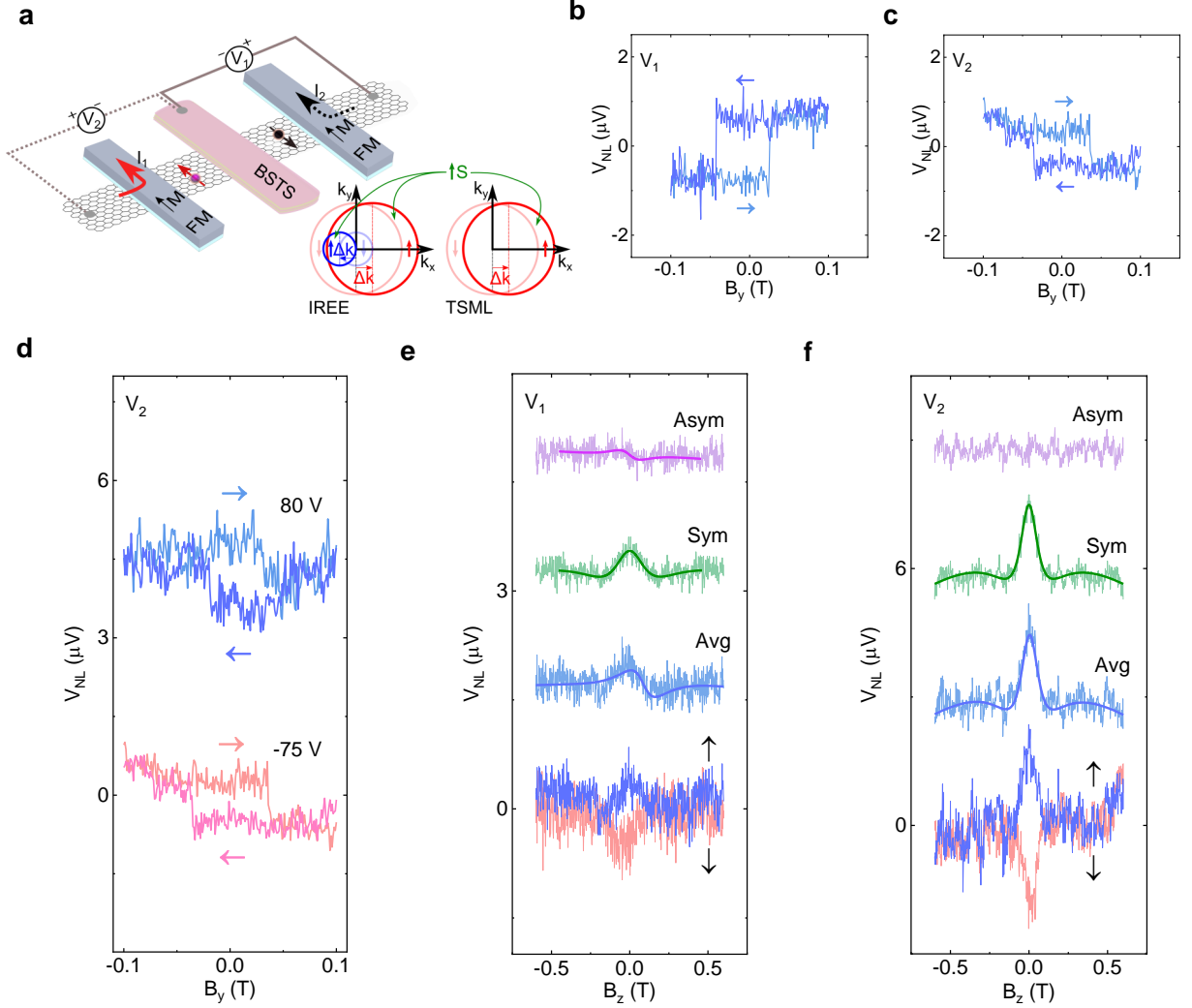


Figure 5: The inverse charge-spin conversion signal in graphene/BSTS junction. (a) Schematic of the device and the two different measurement setups for measuring ICSC. Inset: Schematic of ICSC through the inverse Rashba-Edelstein effect (IREE) and TSML. (b, c) Spin switch NL signals for each of the two measurement setups in (a). The measurements were performed for $I = -150 \mu A$ and $V_g = -70$ V and for $I = -100 \mu A$ and $V_g = -75$ V, respectively. (d) Spin switch NL signals for $V_g = 80$ V and $V_g = -75$ V at $I = -100 \mu A$ in measurement geometry 2. (e, f) Hanle spin precession signals for the two measurement setups with FM contact magnetization along the $+y$ (\uparrow) and the $-y$ (\downarrow) direction, respectively, as well as the averaged signal (Avg) and its symmetric (Sym) and antisymmetric (Asym) components. The green and purple solid lines are fits of the respective signal components, and the blue solid lines are guides to the eye for the averaged signals. The measurements were performed for $I = 130 \mu A$ and $V_g = -75$ V. The data are shifted vertically for clarity. Linear backgrounds of $-11 \mu V$ in (c), $-22 \mu V$ and $-11 \mu V$ in (d), $10 \mu V$ and $3 \mu V$ in (e) and $-7 \mu V$ and $-7 \mu V$ in (f) have been subtracted from the respective measured data.

Measurements in two geometries with opposite x components of the spin current showed a change in sign of NL voltage when the polarization of the injected spin current was reversed (Figures 5b-c). This means that the ICSC has a dependence on the x component of the spin current, similarly to the direct CSC. This, combined with the fact that no sign change of the ICSC signal was detected for reversal of the gate voltage in both n- and p-doped graphene regimes (Figure 5d), agrees with the results from the CSC experiments and indicates that the ICSC comes from the TI and not from proximitized graphene.

The Hanle spin precession measurements in the two geometries are shown in Figures 5e-f. The signals for opposite contact magnetization direction were averaged and subsequently deconvoluted into symmetric and antisymmetric components in the same way as described for the CSC signals. The angles between the polarization of the injected spins from the FM contact and the SML of the TI were calculated to be $\varphi = 24 \pm 8^\circ$ and $\varphi = 7.2 \pm 0.2^\circ$ for the two geometries, respectively. The most likely explanation for the difference in asymmetry between the CSC (Figure 2a) and the ICSC (Figures 5e-f) signals is that the charge current of the CSC effects has a distribution along different paths through the interface and/or the BSTS flake with and without the application of a bias (see Supplementary information S6).

The spin Hall angle was estimated^{46,48,59} to be $\theta_{SHE} \geq 2.8\%$ and the spin Hall length scale was subsequently calculated^{46,48} as $\lambda_{SHE} = \theta_{SHE} \lambda_s^{BSTS} \geq 0.55$ nm, where λ_s^{BSTS} is the spin diffusion length of the BSTS. Similarly, the REE efficiency parameter was calculated³⁴ to be $\alpha_{REE} = 2.8\%$ and the Rashba-Edelstein length scale was estimated³⁴ to $\lambda_{REE} \leq \alpha_{REE} \lambda_s = 16.7$ nm, where the spin diffusion length of graphene, λ_s , is chosen as an upper bound of the heterostructure spin diffusion length. However, these values are only to be regarded as rough estimates, due to the used models not being accurate for our measurement geometries. The calculations are shown in detail and the results are discussed in the Supplementary information S7.

Finally, some important differences should be emphasized between this work and a previous work by our group,³⁴ where the origin of the ICSC was found to be the proximity-induced IREE in graphene. First and foremost, the voltage signal was measured directly in the graphene Hall cross in the previous work, while this work utilizes contacts on top of the TI flake. In the first case, spins are more likely to only propagate through the graphene channel, leaving them mainly unaffected by the surface and bulk effects of the TI. Meanwhile, this work requires spins to be absorbed by the TI in order for a voltage to be detected. This difference in measurement geometry hence greatly influences the relative exposure of the polarized spins to the TI flake and the graphene in the heterostructure region, respectively. Second, the two different TIs that are used in the two works ($(\text{Bi}_{0.15}\text{Sb}_{0.85})_2\text{Te}_3$ and $\text{Bi}_{1.5}\text{Sb}_{0.5}\text{Te}_{1.7}\text{Se}_{1.3}$, respectively) are expected to have different electronic band structures and properties, which may also affect the relative contribution of the different possible ICSC mechanisms.

Conclusion

In summary, we demonstrated room temperature CSC and its inverse effect in the TI BSTS, using a hybrid device with a graphene spin valve. The lateral nonlocal spin switch and precession measurements, supported by the detailed dependence on bias current, gate voltage, different geometries and magnetization orientations, prove the robustness of the CSC effects in BSTS. We could conclude that both the CSC and the ICSC originate from the bulk SHE or REE, from the TSML of the TI surface states or from a combination of these effects. These results prove CSC effects in TIs at room temperature, which is considered a potential candidate for SOT-based memory, logic and neuromorphic computing technologies.^{3,60} With the recent progress in graphene spintronics,^{27–29} the attainment of TIs as spin injectors/detectors can also provide substantial advances in all-electrical spin-based devices and integrated circuits in 2D architectures.

Methods

Patterned graphene stripes were processed from 7 mm chips cut from a 4" wafer with CVD graphene (from Grolltex Inc.) through electron beam lithography and oxygen plasma etching. The $\text{Bi}_{1.5}\text{Sb}_{0.5}\text{Te}_{1.7}\text{Se}_{1.3}$ (BSTS) flakes were exfoliated mechanically on top of the graphene stripes inside a glovebox in N_2 atmosphere. Nonmagnetic reference contacts (20 nm Cr/90 nm Au) on BSTS and graphene were made using electron beam lithography, thin film deposition by electron beam evaporation and liftoff in acetone at 65 °C. Ferromagnetic tunnel contacts (~ 1 nm TiO_2 /90 nm Co) were subsequently made similarly using electron beam lithography, thin film deposition and liftoff processes. The TiO_2 tunnel barriers were prepared by electron beam evaporation of Ti in two steps, each followed by *in-situ* oxidation in a pure oxygen atmosphere. The bias current and gate voltage were applied using a Keithley 6221 current source and a Keithley 2400 source meter, respectively, and the nonlocal voltage was detected by a Keithley 2182A nanovoltmeter.

Acknowledgement

The authors acknowledge financial supports from EU Graphene Flagship (Core 3, No. 881603), Swedish Research Council VR project grants (No. 2021–04821), 2D TECH VINNOVA competence center (No. 2019-00068), FLAG-ERA project 2DSOTECH (VR No. 2021-05925), Graphene center, EI Nano, and AoA Materials program at Chalmers University of Technology. We acknowledge the help of staff at Quantum Device Physics and Nanofabrication laboratory in our department at Chalmers. Devices were fabricated at Nanofabrication laboratory, Myfab, MC2, Chalmers.

Author information

Contributions

A.M.H. and L.S. equally contributed to this manuscript. A.M.H. and L.S. fabricated and characterized the devices. D.K., B.Z., S.P.D. participated in discussions for device preparation and measurements. A.M.H., L.S. and S.P.D. conceived the idea and designed the experiments. A.M.H., L.S., and S.P.D. analyzed and interpreted the experimental data, compiled the figures, and wrote the manuscript with inputs from all co-authors. S.P.D. supervised the research project. These results are part of Lars Sjöström's master's thesis "Room Temperature Charge-Spin Interconversion in a Topological Insulator and Graphene Heterostructure", Chalmers Digital Repository (2021).

Supporting Information Available

Detailed fabrication and measurement methods and electrical properties of the device; calculation of the spin polarization of the BSTS flake; averaging of the Hanle signals for both detector contact magnetizations, deconvolution of the Hanle signal into symmetric and antisymmetric components, fitting of the components, extraction of spin transport parameters and calculation of the spin-to-magnetization angle; spin transport measurements in graphene across the van der Waals heterostructure; full gate dependence of the charge-spin conversion signal and the spin transport parameters, as well as the corresponding data for spin transport in pristine graphene; discussion about the difference in Hanle signal asymmetry and estimated tilt angle between the CSC and ICSC cases; calculations of the spin Hall angle, spin Hall length scale, Rashba-Edelstein efficiency parameter and Rashba-Edelstein length scale for the inverse charge-spin conversion effect; characterization measurements of BSTS

References

- (1) Tokura, Y.; Kawasaki, M.; Nagaosa, N. Emergent functions of quantum materials. *Nature Physics* **2017**, *13*, 1056–1068.
- (2) Qi, X.-L.; Zhang, S.-C. Topological insulators and superconductors. *Reviews of Modern Physics* **2011**, *83*, 1057–1110.
- (3) Sierra, J. F.; Fabian, J.; Kawakami, R. K.; Roche, S.; Valenzuela, S. O. Van der Waals heterostructures for spintronics and opto-spintronics. *Nature Nanotechnology* **2021**, *16*, 856–868.
- (4) Hasan, M. Z.; Kane, C. L. Colloquium: Topological insulators. *Reviews of Modern Physics* **2010**, *82*, 3045–3067.
- (5) Xia, Y.; Qian, D.; Hsieh, D.; Wray, L.; Pal, A.; Lin, H.; Bansil, A.; Grauer, D.; Hor, Y. S.; Cava, R. J.; Hasan, M. Z. Observation of a large-gap topological-insulator class with a single Dirac cone on the surface. *Nature Physics* **2009**, *5*, 398–402.

- (6) Hsieh, D. et al. A tunable topological insulator in the spin helical Dirac transport regime. *Nature* **2009**, *460*, 1101–1105.
- (7) Wu, H. et al. Magnetic memory driven by topological insulators. *Nature Communications* **2021**, *12*, 6251.
- (8) Mellnik, A. R.; Lee, J. S.; Richardella, A.; Grab, J. L.; Mintun, P. J.; Fischer, M. H.; Vaezi, A.; Manchon, A.; Kim, E. A.; Samarth, N.; Ralph, D. C. Spin-transfer torque generated by a topological insulator. *Nature* **2014**, *511*, 449–451.
- (9) Manchon, A.; Železný, J.; Miron, I. M.; Jungwirth, T.; Sinova, J.; Thiaville, A.; Garello, K.; Gambardella, P. Current-induced spin-orbit torques in ferromagnetic and antiferromagnetic systems. *Reviews of Modern Physics* **2019**, *91*, 035004.
- (10) DC, M. et al. Observation of anti-damping spin-orbit torques generated by in-plane and out-of-plane spin polarizations in MnPd3. *arXiv* **2020**,
- (11) Fan, Y. et al. Magnetization switching through giant spin-orbit torque in a magnetically doped topological insulator heterostructure. *Nature Materials* **2014**, *13*, 699–704.
- (12) Khang, N. H. D.; Ueda, Y.; Hai, P. N. A conductive topological insulator with large spin Hall effect for ultralow power spin-orbit torque switching. *Nature Materials* **2018**, *17*, 808–813.
- (13) Han, J.; Richardella, A.; Siddiqui, S. A.; Finley, J.; Samarth, N.; Liu, L. Room-Temperature Spin-Orbit Torque Switching Induced by a Topological Insulator. *Physical Review Letters* **2017**, *119*, 077702.
- (14) Valla, T.; Pan, Z. H.; Gardner, D.; Lee, Y. S.; Chu, S. Photoemission spectroscopy of magnetic and nonmagnetic impurities on the surface of the Bi₂Se₃ topological insulator. *Physical Review Letters* **2012**, *108*, 117601.
- (15) Bonell, F.; Goto, M.; Sauthier, G.; Sierra, J. F.; Figueroa, A. I.; Costache, M. V.; Miwa, S.; Suzuki, Y.; Valenzuela, S. O. Control of Spin-Orbit Torques by Interface Engineering in Topological Insulator Heterostructures. *Nano Letters* **2020**, *20*, 5893–5899.
- (16) Li, J.; Wang, Z. Y.; Tan, A.; Glans, P. A.; Arenholz, E.; Hwang, C.; Shi, J.; Qiu, Z. Q. Magnetic dead layer at the interface between a Co film and the topological insulator Bi₂Se₃. *Physical Review B - Condensed Matter and Materials Physics* **2012**, *86*, 054430.
- (17) Li, C. H.; van't Erve, O. M.; Robinson, J. T.; Liu, Y.; Li, L.; Jonker, B. T. Electrical detection of charge-current-induced spin polarization due to spin-momentum locking in Bi₂Se₃. *Nature Nanotechnology* **2014**, *9*, 218–224.
- (18) Dankert, A.; Geurs, J.; Kamalakar, M. V.; Charpentier, S.; Dash, S. P. Room temperature electrical detection of spin polarized currents in topological insulators. *Nano Letters* **2015**, *15*, 7976–7981.

- (19) Ando, Y.; Hamasaki, T.; Kurokawa, T.; Ichiba, K.; Yang, F.; Novak, M.; Sasaki, S.; Segawa, K.; Ando, Y.; Shiraishi, M. Electrical Detection of the Spin Polarization Due to Charge Flow in the Surface State of the Topological Insulator Bi_{1.5}Sb_{0.5}Te_{1.7}Se_{1.3}. *Nano Letters* **2014**, *14*, 6226–6230.
- (20) Tang, J.; Chang, L.-t.; Kou, X.; Murata, K.; Choi, E. S.; Lang, M.; Fan, Y.; Jiang, Y.; Montazeri, M.; Jiang, W.; Wang, Y.; He, L.; Wang, K. L. Electrical Detection of Spin-Polarized Conduction in (Bi_{0.53}Sb_{0.47})₂Te₃ Topological Insulator. *Nano Letters* **2014**, *14*, 5423–5429.
- (21) Liu, L.; Richardella, A.; Garate, I.; Zhu, Y.; Samarth, N.; Chen, C. T. Spin-polarized tunneling study of spin-momentum locking in topological insulators. *Physical Review B* **2015**, *91*, 235437.
- (22) Tian, J.; Miotkowski, I.; Hong, S.; Chen, Y. P. Electrical injection and detection of spin-polarized currents in topological insulator Bi₂Te₂Se. *Scientific Reports* **2015**, *5*, 1–8.
- (23) Li, C. H.; Vant Erve, O. M.; Rajput, S.; Li, L.; Jonker, B. T. Direct comparison of current-induced spin polarization in topological insulator Bi₂Se₃ and InAs Rashba states. *Nature Communications* **2016**, *7*, 13518.
- (24) Dankert, A.; Bhaskar, P.; Khokhriakov, D.; Rodrigues, I. H.; Karpiak, B.; Venkata Kamalakar, M.; Charpentier, S.; Garate, I.; Dash, S. P. Origin and evolution of surface spin current in topological insulators. *Physical Review B* **2018**, *97*, 125414.
- (25) Han, W.; Kawakami, R. K.; Gmitra, M.; Fabian, J. Graphene spintronics. *Nature Nanotechnology* **2014**, *9*, 794–807.
- (26) Avsar, A.; Ochoa, H.; Guinea, F.; Zyilmaz, B.; Van Wees, B. J.; Vera-Marun, I. J. Colloquium: Spintronics in graphene and other two-dimensional materials. *Reviews of Modern Physics* **2020**, *92*.
- (27) Khokhriakov, D.; Karpiak, B.; Hoque, A. M.; Dash, S. P. Two-dimensional spintronic circuit architectures on large scale graphene. *Carbon* **2020**, *161*, 892–899.
- (28) Khokhriakov, D.; Karpiak, B.; Hoque, A. M.; Zhao, B.; Parui, S.; Dash, S. P. Robust spin interconnect with isotropic spin dynamics in chemical vapor deposited graphene layers and boundaries. *ACS Nano* **2020**, *14*, 15864–15873.
- (29) Khokhriakov, D.; Sayed, S.; Hoque, A. M.; Karpiak, B.; Zhao, B.; Datta, S.; Dash, S. P. Multifunctional Spin Logic Gates In Graphene Spin Circuits. *arXiv* **2021**, 1–20.
- (30) Vaklinova, K.; Hoyer, A.; Burghard, M.; Kern, K. Current-Induced Spin Polarization in Topological Insulator-Graphene Heterostructures. *Nano Letters* **2016**, *16*, 2595–2602.
- (31) Voerman, J. A.; Li, C.; Huang, Y.; Brinkman, A. Spin-Momentum Locking in the Gate Tunable Topological Insulator BiSbTeSe₂ in Non-Local Transport Measurements. *Advanced Electronic Materials* **2019**, *5*, 1900334.



- (32) He, P.; Zhang, S. S.; Zhu, D.; Liu, Y.; Wang, Y.; Yu, J.; Vignale, G.; Yang, H. Bilinear magnetoelectric resistance as a probe of three-dimensional spin texture in topological surface states. *Nature Physics* **2018**, *14*, 495–499.
- (33) Sun, R. et al. Large Tunable Spin-to-Charge Conversion Induced by Hybrid Rashba and Dirac Surface States in Topological Insulator Heterostructures. *Nano Letters* **2019**, *19*, 4420–4426.
- (34) Khokhriakov, D.; Hoque, A. M.; Karpiak, B.; Dash, S. P. Gate-tunable spin-galvanic effect in graphene-topological insulator van der Waals heterostructures at room temperature. *Nature Communications* **2020**, *11*, 1–7.
- (35) Mogi, M.; Yasuda, K.; Fujimura, R.; Yoshimi, R.; Ogawa, N.; Tsukazaki, A.; Kawamura, M.; Takahashi, K. S.; Kawasaki, M.; Tokura, Y. Current-induced switching of proximity-induced ferromagnetic surface states in a topological insulator. *Nature Communications* **2021**, *12*, 1–6.
- (36) Ren, Z.; Taskin, A. A.; Sasaki, S.; Segawa, K.; Ando, Y. Optimizing Bi_{2-x}Sb_xTe_{3-y}Se_y solid solutions to approach the intrinsic topological insulator regime. *Physical Review B* **2011**, *84*, 165311.
- (37) Pan, Y.; Wu, D.; Angevaere, J. R.; Luijckes, H.; Frantzeskakis, E.; De Jong, N.; Van Heumen, E.; Bay, T. V.; Zwartsenberg, B.; Huang, Y. K.; Snelder, M.; Brinkman, A.; Golden, M. S.; de Visser, A. Low carrier concentration crystals of the topological insulator Bi_{2-x}Sb_xTe_{3-y}Se_y: A magnetotransport study. *New Journal of Physics* **2014**, *16*, 123035.
- (38) Bisswanger, T.; Winter, Z.; Schmidt, A.; Volmer, F.; Watanabe, K.; Taniguchi, T.; Stampfer, C.; Beschoten, B. CVD Bilayer Graphene Spin Valves with 26 μm Spin Diffusion Length at Room Temperature. *Nano Letters* **2022**,
- (39) Fert, A.; Jaffrès, H. Conditions for efficient spin injection from a ferromagnetic metal into a semiconductor. *Physical Review B - Condensed Matter and Materials Physics* **2001**, *64*, 1–9.
- (40) Kamalakar, M. V.; Dankert, A.; Kelly, P. J.; Dash, S. P. Inversion of Spin Signal and Spin Filtering in Ferromagnet—Hexagonal Boron Nitride-Graphene van der Waals Heterostructures. *Scientific Reports* **2016**, *6*, 1–9.
- (41) Sinova, J.; Valenzuela, S. O.; Wunderlich, J.; Back, C. H.; Jungwirth, T. Spin Hall effects. *Reviews of Modern Physics* **2015**, *87*, 1213–1260.
- (42) Ghiasi, T. S.; Kaverzin, A. A.; Blah, P. J.; Van Wees, B. J. Charge-to-Spin Conversion by the Rashba-Edelstein Effect in Two-Dimensional van der Waals Heterostructures up to Room Temperature. *Nano Letters* **2019**, *19*, 5959–5966.
- (43) Zhao, B.; Karpiak, B.; Khokhriakov, D.; Johansson, A.; Hoque, A. M.; Xu, X.; Jiang, Y.; Mertig, I.; Dash, S. P. Unconventional Charge-Spin Conversion in Weyl-Semimetal WTe₂. *Advanced Materials* **2020**, *32*.

- (44) Zhao, B.; Khokhriakov, D.; Zhang, Y.; Fu, H.; Karpiak, B.; Hoque, A. M.; Xu, X.; Jiang, Y.; Yan, B.; Dash, S. P. Observation of charge to spin conversion in Weyl semimetal WTe₂ at room temperature. *Physical Review Research* **2020**, *2*, 013286.
- (45) Zhao, B.; Hoque, A. M.; Khokhriakov, D.; Karpiak, B.; Dash, S. P. Charge-spin conversion signal in WTe₂ van der Waals hybrid devices with a geometrical design. *Applied Physics Letters* **2020**, *117*, 242401.
- (46) Hoque, A. M.; Khokhriakov, D.; Karpiak, B.; Dash, S. P. Charge-spin conversion in layered semimetal TaTe₂ and spin injection in van der Waals heterostructures. *Physical Review Research* **2020**, *2*, 033204.
- (47) Kovács-Krausz, Z.; Hoque, A. M.; Makk, P.; Szentpéteri, B.; Kocsis, M.; Fülöp, B.; Yakushev, M. V.; Kuznetsova, T. V.; Tereshchenko, O. E.; Kokh, K. A.; Lukács, I. E.; Taniguchi, T.; Watanabe, K.; Dash, S. P.; Csonka, S. Electrically Controlled Spin Injection from Giant Rashba Spin-Orbit Conductor BiTeBr. *Nano Letters* **2020**, *20*, 4782–4791.
- (48) Safeer, C. K.; Ontoso, N.; Ingla-Aynés, J.; Herling, F.; Pham, V. T.; Kurzmann, A.; Ensslin, K.; Chuvilin, A.; Robredo, I.; Vergniory, M. G.; De Juan, F.; Hueso, L. E.; Calvo, M. R.; Casanova, F. Large Multidirectional Spin-to-Charge Conversion in Low-Symmetry Semimetal MoTe₂ at Room Temperature. *Nano Letters* **2019**, *19*, 8758–8766.
- (49) Ingla-aynés, J.; Groen, I.; Herling, F.; Ontoso, N.; Safeer, C. K.; Juan, F. D.; Hueso, L. E.; Gobbi, M.; Casanova, F. Omnidirectional spin-to-charge conversion in graphene/NbSe₂ van der Waals heterostructures. *2D Materials* **2022**, *9*, 045001.
- (50) Sierra, J. F.; Neumann, I.; Cuppens, J.; Raes, B.; Costache, M. V.; Valenzuela, S. O. Thermoelectric spin voltage in graphene. *Nature Nanotechnology* **2018**, *13*, 107–111.
- (51) Lee, C. J.; Park, H.; Kang, J.; Lee, J.; Choi, M.; Park, H. Extraction of intrinsic field-effect mobility of graphene considering effects of gate-bias-induced contact modulation. *Journal of Applied Physics* **2020**, *127*.
- (52) Hoque, A. M.; Khokhriakov, D.; Zollner, K.; Zhao, B.; Karpiak, B.; Fabian, J.; Dash, S. P. All-electrical creation and control of spin-galvanic signal in graphene and molybdenum ditelluride heterostructures at room temperature. *Communications Physics* **2021**, *4*, 1–9.
- (53) Khokhriakov, D.; Cummings, A. W.; Song, K.; Vila, M.; Karpiak, B.; Dankert, A.; Roche, S.; Dash, S. P. Tailoring emergent spin phenomena in Dirac material heterostructures. *Science Advances* **2018**, *4*, 9349.
- (54) Karpiak, B.; Dankert, A.; Cummings, A. W.; Power, S. R.; Roche, S.; Dash, S. P. 1D ferromagnetic edge contacts to 2D graphene/h-BN heterostructures. *2D Materials* **2018**, *5*, 014001.

- (55) Herling, F.; Safeer, C. K.; Ingla-Aynés, J.; Ontoso, N.; Hueso, L. E.; Casanova, F. Gate tunability of highly efficient spin-to-charge conversion by spin Hall effect in graphene proximitized with WSe₂. *APL Materials* **2020**, *8*.
- (56) Li, L.; Zhang, J.; Myeong, G.; Shin, W.; Lim, H.; Kim, B.; Kim, S.; Jin, T.; Cavill, S.; Kim, B. S.; Kim, C.; Lischner, J.; Ferreira, A.; Cho, S. Gate-Tunable Reversible Rashba-Edelstein Effect in a Few-Layer Graphene/2H-TaS₂ Heterostructure at Room Temperature. *ACS Nano* **2020**, *14*, 5251–5259.
- (57) Kim, M. et al. Control of electron-electron interaction in graphene by proximity screenings. *Nature Communications* **2020**, *11*, 1–6.
- (58) Safeer, C. K.; Ingla-Aynés, J.; Herling, F.; Garcia, J. H.; Vila, M.; Ontoso, N.; Calvo, M. R.; Roche, S.; Hueso, L. E.; Casanova, F. Room-Temperature Spin Hall Effect in Graphene/MoS₂ van der Waals Heterostructures. *Nano Letters* **2019**,
- (59) Yan, W.; Sagasta, E.; Ribeiro, M.; Niimi, Y.; Hueso, L. E.; Casanova, F. Large room temperature spin-to-charge conversion signals in a few-layer graphene/Pt lateral heterostructure. *Nature Communications* **2017**, *8*, 1–7.
- (60) Dieny, B. et al. Opportunities and challenges for spintronics in the microelectronics industry. *Nature Electronics* **2020**, *3*, 446–459.

Paper II

Charge-spin conversion in layered semimetal TaTe₂ and spin injection in van der Waals heterostructures

Anamul Md. Hoque , Dmitrii Khokhriakov, Bogdan Karpiak, and Saroj P. Dash ^{*}

Department of Microtechnology and Nanoscience, Chalmers University of Technology, SE-41296, Göteborg, Sweden



(Received 5 December 2019; accepted 17 June 2020; published 6 August 2020)

A spin-polarized current source using nonmagnetic layered materials is promising for next-generation all-electrical spintronic science and technology. Here we electrically created spin polarization in a layered semimetal TaTe₂ via the charge-spin conversion process. Using a hybrid device of TaTe₂ in a van der Waals heterostructure with graphene, the spin polarization in TaTe₂ is efficiently injected and detected by nonlocal spin-switch, Hanle spin precession, and inverse spin Hall effect measurements. Systematic experiments at different bias currents and gate voltages in a vertical geometry prove the TaTe₂ as a nonmagnetic spin source at room temperature. These findings demonstrate the possibility of making an all-electrical spintronic device in a two-dimensional van der Waals heterostructure, which can be essential building blocks in energy-efficient spin-orbit technology.

DOI: [10.1103/PhysRevResearch.2.033204](https://doi.org/10.1103/PhysRevResearch.2.033204)

I. INTRODUCTION

Spintronic technology was mainly governed by the generation of spin-polarized currents by using the exchange interaction of conduction electrons in magnetic materials, which require a magnetic field to control their spin orientation [1–4]. However, the demand for faster and smaller spintronic technologies for memory, logic, and artificial intelligence requires efficient and spontaneous spin-polarized current sources using nonmagnetic materials, where all the device operations can be controlled by electrical means [5,6]. Recently, the electronic generation of spin-polarized currents was realized in nonmagnetic materials via the spin Hall effect (SHE), Rashba-Edelstein effect (REE), and spin momentum locking (SML) phenomenon [7–9].

Due to their potential for spintronic applications, the SHE and REE were extensively studied in heavy metals [10,11], semiconductors, oxide heterostructures [7], and more recently, on transition metal dichalcogenides (TMDs) [12], Weyl semimetals [12,13], Rashba spin-orbit materials [14], and their heterostructures with graphene [12,13,15–18]. Topological insulators (TIs) were shown to possess SML characteristics in the Dirac surface states, which could be detected using potentiometric measurements [19–21] and the charge-spin conversion process [22–24]. However, the spin injection from TIs into graphene is so far restricted to very low temperatures due to contributions from trivial bulk states [25,26]. Utilizing the SHE in Pt metal thin films, spin injection and detection has been realized in a graphene channel

[10,11]. However, the direct deposition of metallic layers on graphene can modify its electronic properties [27,28]. Recently discovered two-dimensional (2D) magnets can be potential candidates for spin injection into graphene; however, the low Curie temperature of the 2D magnets at this stage limits their room-temperature applications [29]. Therefore, finding a nonmagnetic layered material as a spin source in a van der Waals (vdW) heterostructure with graphene is necessary for newly emerging 2D spintronics science and technology [30].

Using our recently developed vertical measurement geometry [13], we demonstrate the electronic creation and injection of in-plane spin polarization using a layered semimetal tantalum ditelluride (TaTe₂) due to efficient charge-spin conversion processes. In a hybrid spintronic device, the spin polarization generated in TaTe₂ is efficiently injected into the graphene channel and subsequently detected by a ferromagnet using a sensitive nonlocal spin-valve and Hanle spin precession measurements. Detailed measurements using different bias currents and gate voltages provide insight into the current-induced spin polarization in TaTe₂ at room temperature.

II. RESULTS AND DISCUSSION

The choice of the layered monoclinic (1T') semimetal TaTe₂ is motivated by its high spin-orbit interaction (SOI) originating from 5d electrons along with the potential for use in charge-to-spin conversion technologies [7,31], and it can be exfoliated into thin 2D layers. Mainly, TaTe₂ is an excellent candidate for the generation of pure spin current due to SHE [7,32] and REE [9,33,34], as shown schematically in Fig. 1(a). Figure 1(b) shows the fabricated device picture, where a vdW heterostructure of TaTe₂ is prepared with a graphene channel to use its excellent spin transport properties [35,36] together with ferromagnetic Co/TiO₂ (FM) injector/detector tunnel contacts (see Appendix A for detailed fabrication processes). The characteristic Raman spectrum of a TaTe₂

^{*}Corresponding author: saroj.dash@chalmers.se

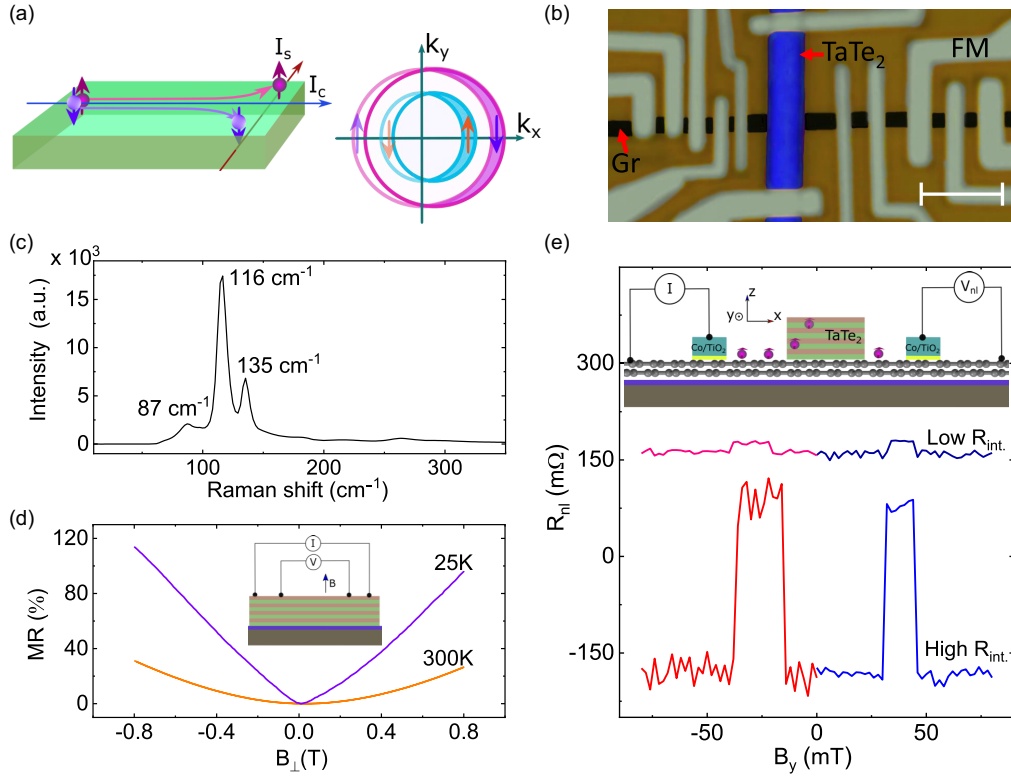


FIG. 1. Characterization of TaTe₂ and spin transport in the graphene-TaTe₂ heterostructure. (a) Schematic representation of the spin Hall effect in a symmetric system, where a spin current (I_s) is created due to transverse charge current (I_c). The adjacent diagram shows the current-induced spin polarization in Rashba spin-split bands near the Fermi level. (b) Optical micrograph with false colors of a device consisting of graphene (black), TaTe₂ (blue), and FM contacts (gray). The scale bar is 4 μm . (c) Raman spectrum of TaTe₂ at room temperature. (d) Magnetoresistance (MR%) of TaTe₂ at room temperature and 25 K. (e) Nonlocal spin-valve (NLSV) signal without and with spin absorption in the high- R_{int} and low- R_{int} conditions, respectively. The inset shows the NLSV measurement geometry.

flake is shown in Fig. 1(c) using a 638-nm laser, where three prominent peaks at 87, 116, and 135 cm^{-1} are visible [31]. In the transport measurements, TaTe₂ shows semimetallic properties (see Appendix B) and a large magnetoresistance ($\text{MR} \% = \frac{R_B - R_0}{R_0} \times 100$) [Fig. 1(d)], showing MR $\sim 30\%$ at room temperature and $\sim 120\%$ at 25 K at a magnetic field of -0.8 T [37].

Standard nonlocal (NL) spin-valve measurements were performed across the graphene-TaTe₂ heterostructure channel in different graphene-TaTe₂ interface resistance (R_{int}) conditions [Fig. 1(e)]. The spin-polarized electrons were injected and detected by FM contacts in the NL geometry while measuring a $\Delta R_{\text{nl}} = (\frac{\Delta V_{\text{nl}}}{I})$ as a function of magnetic field sweep (B_y) to achieve the parallel and antiparallel magnetization of FM electrodes. As shown in Fig. 1(e), while a large spin transport signal ΔR_{nl} of 272 m Ω was measured for high R_{int} of 16 k Ω , for very low R_{int} , tentatively $< 100 \Omega$ (see Appendix C), the ΔR_{nl} drastically reduced to 16 m Ω due to strong spin absorption in the low- R_{int} regime.

First, the spin-to-charge conversion experiments [measurement geometry in Fig. 2(a)] were performed in TaTe₂ via the inverse spin Hall effect (ISHE), when the R_{int} is $< 100 \Omega$ (see Appendix C). In this condition, the spin current injected from a FM into the graphene channel is strongly absorbed by TaTe₂, as shown in Fig. 1(e). The spin current in TaTe₂ subsequently gives rise to a transverse charge current due

to the efficient spin-charge conversion in TaTe₂, which is detected as a voltage signal (V_{nl}) across the TaTe₂ [Fig. 2(b)]. By sweeping an in-plane magnetic field along the x axis, B_x , the V_{nl} varies antisymmetrically at low field and saturates at ± 0.4 T as the magnetization of the injector FM rotates completely toward the x axis. The saturation field range of the FM contacts for the B_x field sweep has been verified from the spin precession x-Hall measurements in the graphene channel (see Appendix D). Considering the symmetry of the system with the spin current being absorbed from graphene into TaTe₂ along the z direction, spin polarization (≥ 0.4 T) in the x direction and manifested orthogonal charge current (I_s) in the y direction can be due to the ISHE or the Edelstein effect (EE) in TaTe₂ [12]. The V_{nl} signal has been measured at different spin injection bias currents, which scales linearly [Fig. 2(c)] at room temperature.

We observed a large spin-charge conversion (SCC) signal at room temperature in TaTe₂ with signal amplitude $\Delta R_{\text{SCC}} = \Delta V_{\text{nl}}/I_{\text{bias}} = -1.69 \mu\text{V}/-20 \mu\text{A} \sim 84 \text{ m}\Omega$, which is about few times larger than in WTe₂ [12], MoS₂, and Pt in heterostructure with graphene [10,11,17], one order of magnitude larger than in graphene-MoTe₂ heterostructure [38], and a few orders of magnitude higher than in Pt/Cu heterojunction [39] but comparable to the graphene-TaS₂ heterostructure system [15]. Recently, spin-orbit torque experiments using a TaTe₂-ferromagnet heterostructure reported a dominating

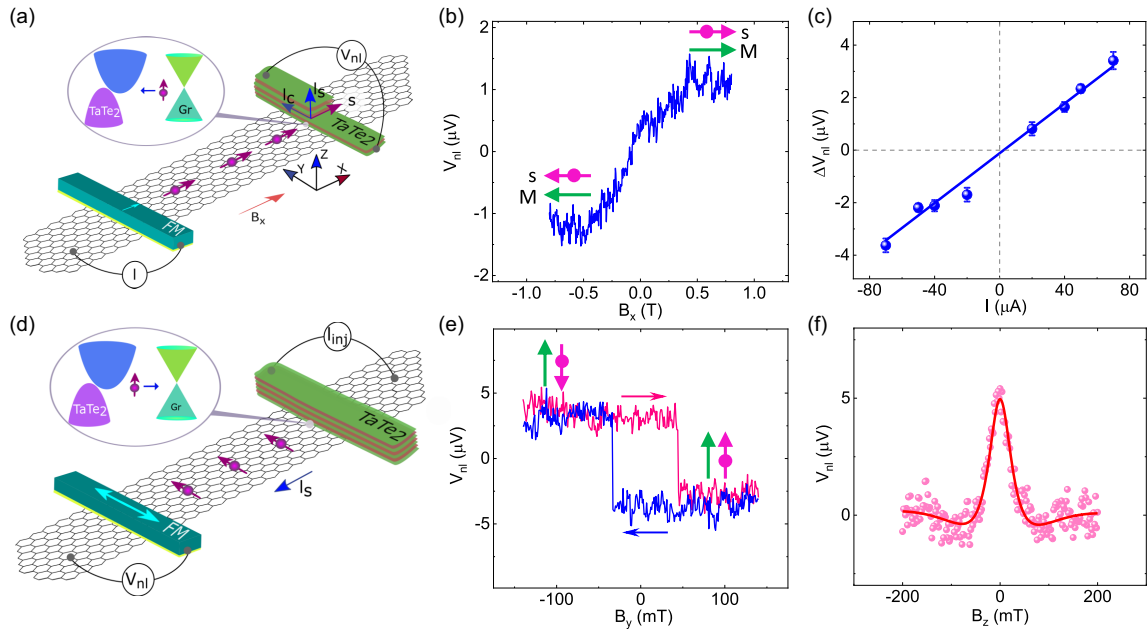


FIG. 2. Charge-spin conversion effects in TaTe₂ at room temperature. (a) Measurement geometry to detect the inverse spin Hall effect (ISHE) in TaTe₂ by injecting a spin current from the ferromagnet-graphene channel into TaTe₂ by spin absorption and detecting a voltage signal across the TaTe₂ in a NL geometry. (b) ISHE signal V_{nl} measured with an in-plane magnetic field (B_x) sweep for $I = 50 \mu\text{A}$ at $V_g = 40 \text{ V}$ at room temperature in device 1. (c) Bias current dependence of the ISHE signal amplitude ΔV_{nl} with a linear fit (solid line). (d) Measurement geometry where TaTe₂ is used as a spin-polarized current source for vertical injection of spins into the graphene channel, which is finally detected by a FM contact in a NL geometry. (e, f) The spin-switch and Hanle spin precession measurements for spin injection from TaTe₂ with a B_y and B_z sweep, respectively, with an application of an $I = -30 \mu\text{A}$ with $V_g = 40 \text{ V}$ at room temperature in device 2. The up and down magnetic field sweep directions are indicated by arrows in (e) for spin-switch experiments. The Hanle data is fitted using Eq. (2). A linear background is subtracted from the data.

Oersted field contribution by local measurements [40], which is avoided in our NL measurements. From our data, it is not possible to calculate the exact spin Hall angle (θ_{SH}) in TaTe₂, as the spin diffusion length λ_{TaTe_2} , is unknown. Furthermore, the larger width of a TaTe₂ flake ($2.6 \mu\text{m}$) compared to the spin diffusion length in graphene ($\sim 2.5 \mu\text{m}$) restrains the use of the available model [10–12]. An estimation of θ_{SH} was found to be in the range of 0.2–0.6 using a simple model and considering $\lambda_{\text{TaTe}_2} = 10\text{--}110 \text{ nm}$ and R_{int} of 10–100 Ω (see Appendix E). Moreover, we have also approximately calculated the inverse Edelstein effect (IEE) of TaTe₂ through IEE length $\lambda_{\text{IEE}} = \theta_{SH} * \lambda_{\text{TaTe}_2}$, and we found $\lambda_{\text{IEE}} \approx 6\text{--}60 \text{ nm}$ (see Appendix E for more discussion) as a function of λ_{TaTe_2} (10–110 nm).

Next, we focus on the observation of vertical spin injection (VSI) of in-plane spin polarization from TaTe₂ into a graphene channel at room temperature [see Fig. 2(d) for measurement geometry]. In the spin-switch experiment, we measured the spin signal V_{nl} as a function of an in-plane magnetic field B_y sweep, which switches the magnetization of the FM detector contact from parallel to antiparallel orientation with respect to the in-plane injected spin polarization from TaTe₂ [Fig. 2(e)]. The amplitude ($\Delta R_{nl} = \Delta V_{nl}/I_{\text{bias}}$) of the spin-to-charge conversion signal for vertical spin injection is about 240 m Ω . A confirmatory test of the in-plane spin polarization using a Hanle spin precession measurement was performed in the same NL geometry [Fig. 2(d)], where a perpendicular magnetic field (B_z) was swept while keeping the magnetization of

the detector FM contact in the in-plane orientation. The B_z field induces spin precession in addition to diffusion and dephasing, which results in a reduction of the spin signal as the detector probes only the projection of the spin orientation onto the FM contact. Figure 2(f) shows the Hanle data measured at room temperature while injecting spin from TaTe₂ into the graphene channel, and fitting with Eq. (F1), we estimate the spin lifetime $\tau_s = 195 \pm 26 \text{ ps}$ and spin diffusion length $\lambda_s = \sqrt{\tau_s D_s} = 1.98 \pm 0.3 \mu\text{m}$, considering the channel length between the TaTe₂ and detector FM electrode $L = 3.75 \mu\text{m}$ (distance between the center of the TaTe₂ flake to the center of the FM electrode). We found the spin polarization of the FM detector contact is about $P_{FM} \sim 6.13\%$ (Fig. 10). Subsequently, knowing the P_{FM} , the lower limit for the current-induced spin polarization of TaTe₂ is calculated to be about $P_{\text{TaTe}_2} = 1.34\% \pm 0.26\%$ (see Appendix F).

We further investigated the back-gate (V_g) dependence of the VSI spin-switch signal using TaTe₂ as the spin injector. Figure 3(a) shows a sketch of the graphene-TaTe₂ heterostructure and the change in the Fermi-level position in graphene with an application of V_g from electron- to hole-doped regimes, whereas no change is expected in TaTe₂ due to its metallic state. The measured spin-switch signals (V_{nl}) at various V_g in the range from -40 to 40 V are depicted in Fig. 3(b). The gate dependence of the magnitude of the spin signal ΔV_{nl} ($\Delta R_{nl} \approx 250\text{--}400 \text{ m}\Omega$) is presented in Fig. 3(c) (top panel), which shows that the spin-switch signal direction remains unchanged in the hole and electron transport regime.

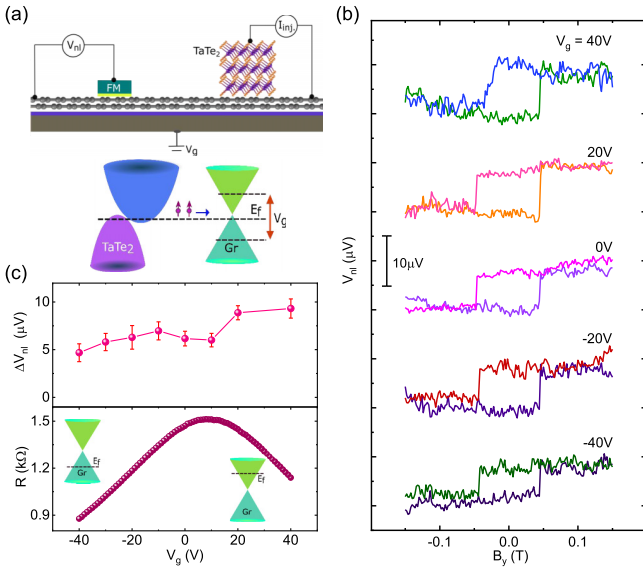


FIG. 3. Gate dependence of spin injection signal from TaTe₂. (a) Measurement setup and the band diagram of TaTe₂ and graphene with an application of a back-gate voltage (V_g) across the Si/SiO₂ substrate. (b) The measured NL spin-switch signals at various $V_g = -40$ – 40 V for both n - and p -doped graphene regime in device 3 with a bias current $I = -20$ μ A at room temperature. (c) The magnitude of the signal ΔV_{nl} as a function of V_g (top panel). The V_g dependence of the graphene-TaTe₂ heterostructure channel resistance (bottom panel) along with the Fermi-level position in the graphene band structure.

To compare ΔV_{nl} with the heterostructure channel properties, the gate dependence of the graphene-TaTe₂ heterostructure channel resistance is presented in the bottom panel of Fig. 3(c), where the charge neutrality point (V_{CNP}) is ~ 10 V with field-effect mobility of about 1074 $\text{cm}^2 \text{V}^{-1} \text{s}^{-1}$. Similar gate dependence of the spin-switch signal is observed for device 1 (see Appendix G). These results rule out any contribution of the local Hall effect produced by the local fringe field from the FM detector contact edges on the graphene, since this effect should change its sign with carrier types in graphene [41].

Next, the electrical-bias-controlled switching of the spin injection from TaTe₂ was measured. Figure 4(a) shows the spin-switch signal (V_{nl}) with injection bias currents of $I = +/ - 2$ μ A at $V_g = 20$ V. Reversing the current direction creates opposite spin polarization in TaTe₂ and hence accumulation of opposite spins in the graphene channel, which results in the opposite direction of the hysteretic behavior of the measured spin-switch signal. A full bias-dependent measurement was carried out at larger biases to understand the detailed energy dependence of the spin injection mechanism at the graphene-TaTe₂ junction [see Figs. 4(b) and 4(c)]. In the $-I$ range, we observed an increase of ΔV_{nl} with bias currents, where the amplitude of the spin-to-charge conversion signal is about $\Delta R_{nl} = 300 \text{ m}\Omega$. However, for the $+I$, the ΔV_{nl} increases linearly for low biases up to $I = 8$ μ A and disappears at larger bias within the measurement noise. One of the reasons for such bias dependence can be ascribed to the energy dependence of spin polarization in TaTe₂ or

the availability of spin-polarized density of states near the Fermi level in TaTe₂. In contrast to local detection of the spin signal [42,43], as the measurements were performed in the NL geometry without any bias across the detector FM contact, any effects originating from the detector can be ruled out. This asymmetric feature of the bias-dependent spin injection effect in graphene-TaTe₂ heterostructure can be correlated to an electronic diode, where instead of controlling the charge current with bias in the conventional diode we control the spin injection in the heterostructure. To further examine the asymmetry of the bias dependence, we also checked the bias dependence of the graphene-TaTe₂ injector interface resistance (R_{int} [see Fig. 4(d)]. Interestingly, R_{int} is observed to be asymmetric with bias, which can be the origin of the asymmetry in the spin injection signal due to a conductivity mismatch issue between the TaTe₂ spin source and the graphene channel [35,44].

We discuss the possible mechanisms that engender the generation of current-induced in-plane spin polarization in the TaTe₂ in VSI geometry. First, like the ISHE measurements, we can also explain the VSI signal in TaTe₂ using the symmetry principle [see Appendix H, Figs. 12(a)–12(d)], that the generated field or spin (s) is perpendicular to the applied charge current (I_c) and spin current (I_s). As the TaTe₂ crystals have a relatively smaller thickness (70 nm) compared to their lateral width (2.6 – 6 μ m), as well as a low resistance compared to the graphene and interface (R_{int}), this makes the electric field within TaTe₂ predominantly in plane. Moreover, considering the in-plane spin injection in graphene, the origin of spin polarization can be attributed to the bulk SHE of TaTe₂ due to an in-plane electric field in TaTe₂. Similarly, the surface or bulk states of TaTe₂, if present and spin polarized, can also inject in-plane spin into graphene due to the EE [13] (see Fig. 12). If we consider the lower symmetry of the TaTe₂ crystals [40], both SHE and EE can also give rise to in-plane spin polarization in the TaTe₂, as it does not have to follow the orthogonal rule between s , I_c , and I_s [45]. On the other hand, proximity-induced SHE in graphene can be excluded as an origin of the signals, as it is expected to align spin in the out-of-plane direction [16–18,46]. Moreover, with the lack of gate-dependent sign change behavior of the spin-switching signal for electron and hole transport regimes, the contribution of proximity-induced REE in graphene can be ruled out [15,16,47–49]. Any contribution of spin polarization from the Te layer can also be ruled out because equal and opposite contributions from both Te surfaces within a single TaTe₂ layer will be canceled out [50].

III. CONCLUSION

In summary, we demonstrated efficient charge-spin conversion in semimetal TaTe₂ as an efficient spin injector in graphene-based spintronic devices at room temperature by using a vertical spin injection geometry. The advantage of using such a spin source is that the spin polarization direction can be controlled by an electrical bias instead of the magnetic field as conventionally achieved with ferromagnetic materials. Systematic bias and gate-dependent measurements of the spin injection signal indicate that the origin of spin polarization can be mainly because of the SHE or EE in TaTe₂ considering symmetric or low-symmetric spin-charge

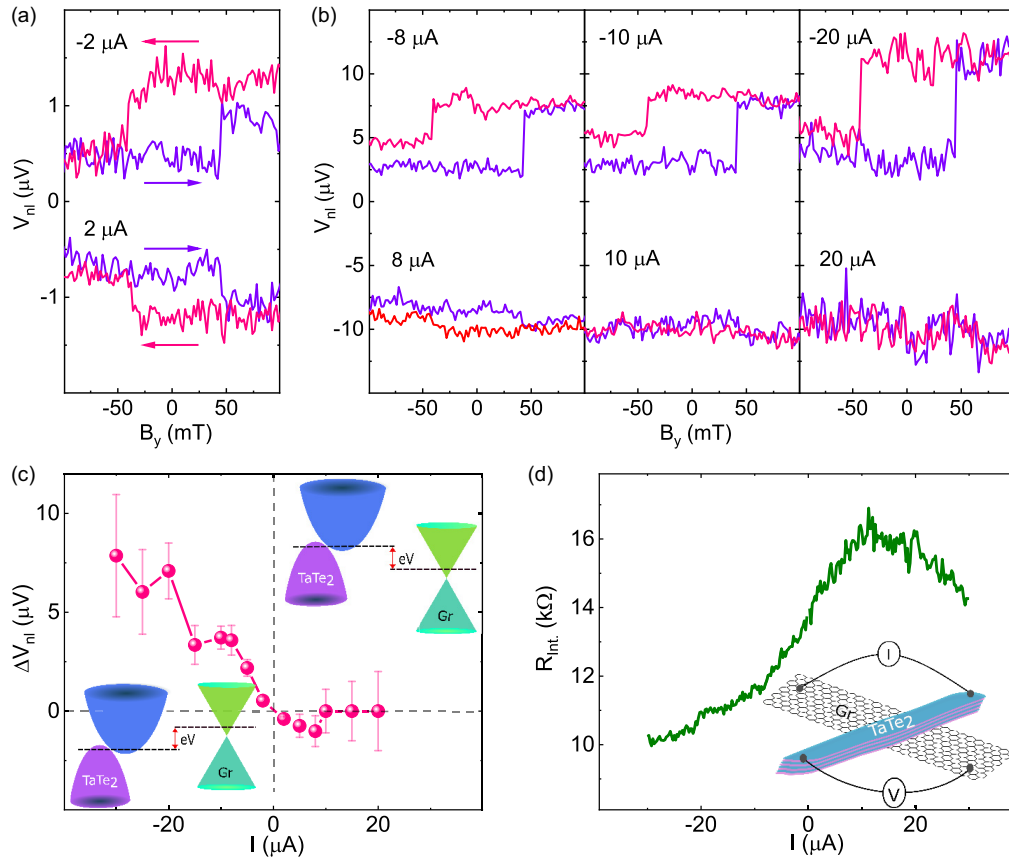


FIG. 4. Electrical control and bias dependence of spin injection signal from TaTe₂. (a) NL spin-switch signals (V_{nl}) with bias currents of $I = \pm 2 \mu\text{A}$ at $V_g = 20 \text{ V}$ at room temperature in device 3. (b) The V_{nl} at different bias currents, measured at room temperature at $V_g = 20 \text{ V}$. The data are vertically shifted for clarity. (c) Bias dependence of the magnitude of the signal ΔV_{nl} . Insets: Schematic of the nonequilibrium Fermi-level positions for positive and negative applied bias conditions. (d) Graphene-TaTe₂ interface resistance (R_{int}) characteristics with bias current (I) measured in four-terminal geometry (inset).

conversion processes. Such a nonmagnetic spin source based on the charge-spin conversion effect shows great potential to replace the ferromagnetic injector in all-electrical 2D spintronic circuits and is suitable for spin-orbit technologies.

ACKNOWLEDGMENTS

The authors acknowledge financial support from the European Union's Horizon 2020 Graphene Flagship Core 2 no. 785219 and Core3 no. 881603, 2DTech Vinnova Competence center at Chalmers, the EU FlagEra project (VR No. 2015-06813), and the Swedish Research Council VR project (Grant No. 2016-03658). We acknowledge the discussions and help of Bing Zhao in our research group.

APPENDIX A: FABRICATION AND CHARACTERIZATION OF GRAPHENE-TaTe₂ HETEROSTRUCTURE

To fabricate graphene-TaTe₂ heterostructure spintronic devices, first a few layer graphene were mechanically exfoliated from highly ordered pyrolytic graphite (HOPG) onto SiO₂ (300 nm)/*n*-doped Si substrate using the Scotch tape method. Later, TaTe₂ flakes were exfoliated from bulk crystal (from Hq Graphene) on polydimethylsiloxane (PDMS) film and dry transferred onto the few-layer graphene flake under a

microscope using a home-built micromanipulator-controlled transfer stage. Contacts to graphene and TaTe₂ were defined by electron-beam lithography, electron-beam evaporation, and a lift-off process. For the preparation of ferromagnetic tunnel contacts to graphene, a two-step deposition of 0.5 nm of Ti at less than 3×10^{-7} Torr and 30 min *in situ* oxidation at above 30 Torr was carried out, followed by 90 nm of Co deposition. The resistances of ferromagnetic tunnel contacts (TiO₂/Co) on the graphene channel were in the range of 5–20 kΩs at room temperature. The spin injection measurements were performed in a vacuum cryostat with a magnetic field up to 0.8 T. All the measurements were performed at room temperature using a Keithley 6221 current source, a Keithley 2182A nanovoltmeter, and Keithley 2612B source meter for application of gate voltages.

Figures 5(a) and 5(b) show the optical microscopic picture and atomic force microscopic image of device 1 consisting of exfoliated TaTe₂, graphene with Co/TiO₂ tunnel contacts. The widths of the TaTe₂ flake and graphene stripe are 2.6 μm and 1.8 μm, respectively. After bias-dependent measurements of the inverse spin Hall effect, the flake was damaged, presumably due to gate leakage. The thickness of the exfoliated TaTe₂ flake is about 70 nm, scanned along the dotted orange line in the atomic force microscopy image. Figures 5(c) and 5(d) present the optical micrographs of

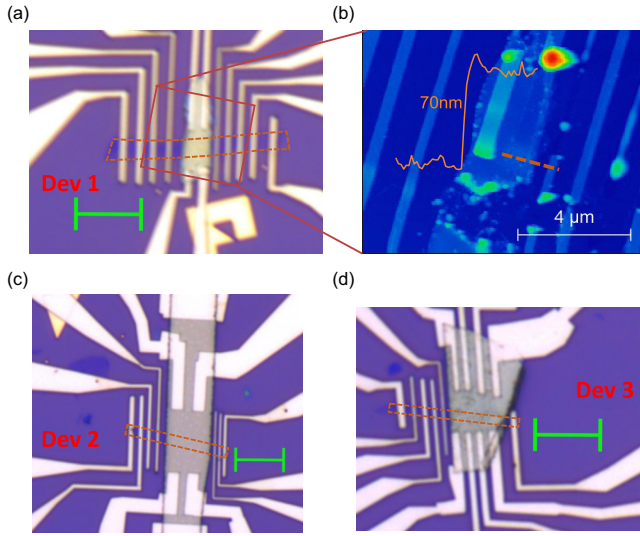


FIG. 5. (a, b) Optical microscopic picture and atomic force microscopic image of device 1 consisting of exfoliated 70 nm TaTe₂, graphene with Co/TiO₂ tunnel contacts. (c, d) Optical microscopic images of devices 2 and 3. The green color scale bar in the microscopic images is 6 μm .

devices 2 and 3, respectively, prepared by similar fabrication procedures. Dotted lines in the optical micrographs are to highlight the exfoliated multilayer graphene region below the TaTe₂ flake.

APPENDIX B: ELECTRIC AND MAGNETOTRANSPORT PROPERTIES OF TaTe₂

Figure 6(a) shows conventional four-terminal (4T) I - V characteristics of the TaTe₂ flake with channel resistance 120 Ω at room temperature (pink line) and 70 Ω at 25 K (green line). The resistivity ($\rho = R \frac{A}{L}$) of TaTe₂ is approximated to be $\sim 300 \times 10^{-8} \Omega\text{m}$ at room temperature and is $\sim 60 \times 10^{-8} \Omega\text{m}$ at 25 K. The TaTe₂ channel length (L) is 13 μm and the width (w) is 11 μm ; the thickness of TaTe₂ is about 30 nm.

We examined the magnetoresistance (MR%) of TaTe₂ with angle dependence measurements up to ± 0.8 T from the per-

pendicular (\perp) to in-plane field (\parallel) with respect to the device plane at 300 K with $I = -150 \mu\text{A}$, as shown in Fig. 6(b). Figure 6(c) presents a maximum MR% at different angles at 0.8 T with a cosine fit. It can be seen [from Figs. 6(b) and 6(c)] that MR% is maximum with the out-of-plane field (Angle = 0) but turns to a minimum with an in-plane field.

APPENDIX C: INTERFACIAL RESISTANCE OF GRAPHENE-TaTe₂ HETEROSTRUCTURE

The graphene-TaTe₂ interfacial resistance (R_{int}) is estimated by two-terminal (2T) measurement geometry in device 1 [Fig. 7(a)]. At the start of the measurements, the 2T resistance was 35 k Ω [Fig. 7(b)], and the 4T R_{int} was about 16 k Ω [Fig. 4(d)]. In such a high- R_{int} condition, the spin transport in graphene is not much affected (without spin absorption). Such high resistance, in the beginning, can be due to the larger van der Waals gap between graphene and TaTe₂. After a few hours of measurement, we observed the 2T resistance to decrease and stabilize at ~ 5 k Ω [Fig. 7(b)]. The 4T measurements could not be performed in the low-interface condition due to a lack of working contacts on both sides of the TaTe₂ flake. By considering the graphene channel and contact resistances, the low R_{int} is estimated to be less than 100 Ω . In this low- R_{int} condition, we observed a drastic reduction of the spin transport signal in graphene due to spin absorption by TaTe₂ [presented in Fig. 1(e)]. The inverse spin Hall effect measurements were performed in low- R_{int} and vertical spin injection measurements that were performed in high- R_{int} conditions.

APPENDIX D: x -FIELD HANLE IN GRAPHENE-TaTe₂ HETEROSTRUCTURE

Figure 8(a) shows a schematic of the measurement setup for nonlocal xHanle, where the magnetic field is applied in the planner perpendicular direction (x axis) to the magnetic easy axis (y axis) of the FM contacts [51]. Figure 8(b) shows the measured xHanle spin signal in a condition where TaTe₂ does not absorb the spin significantly. It can be seen that the magnetization of the FM becomes saturated at ± 0.4 T along the x axis.

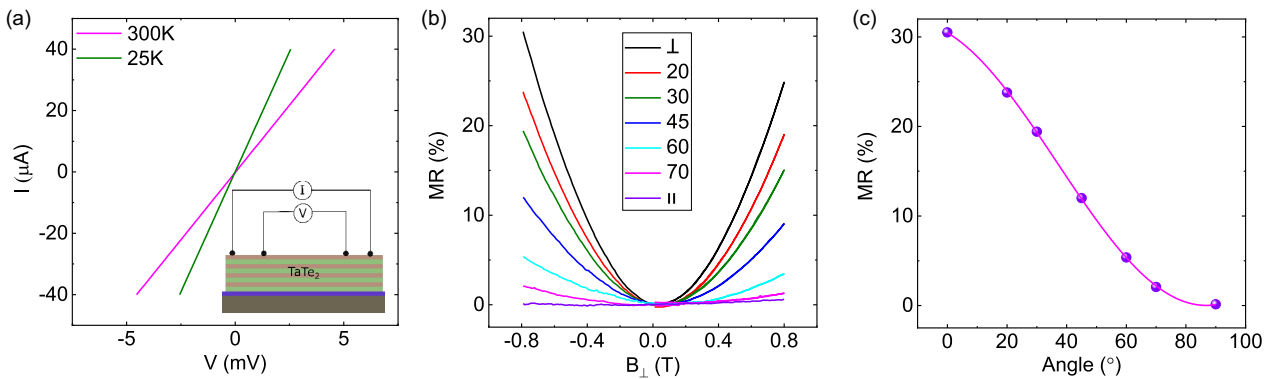


FIG. 6. Transport properties of TaTe₂. (a) Four-terminal (4T) I - V characteristics of TaTe₂ along with the measurement geometry. (b) Angle-dependent measurements of MR% in TaTe₂ from perpendicular (\perp) to the in-plane field (\parallel) at room temperature. (c) Maximum MR% at different angles at 0.8 T with cosine fit.

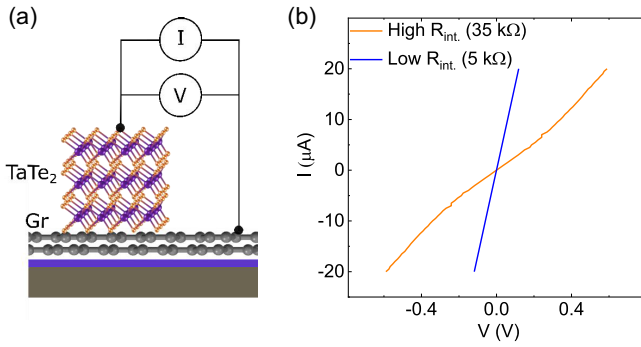


FIG. 7. Interfacial resistance in the graphene-TaTe₂ heterostructure. (a) Schematic of the 2T measurement geometry to measure I - V characteristics of the graphene-TaTe₂ heterostructure. (b) 2T I - V properties of the graphene-TaTe₂ heterostructure, where high resistance, 35 kΩ (orange line), and low resistance, 5 kΩ (blue line), stages are shown.

APPENDIX E: ESTIMATION OF SPIN HALL ANGLE

We have estimated the spin Hall angle (θ_{SH}) in TaTe₂ by using the spin diffusion model [10–12]. The manifested inverse spin Hall effect (ISHE) signal can be represented using the following equation:

$$\Delta R_{ISHE} = \frac{2\theta_{SH}\rho_{TaTe_2}X}{w_{TaTe_2}} \left(\frac{\hat{I}_s}{I_c} \right). \quad (E1)$$

$$\frac{\hat{I}_s}{I_c} \equiv \frac{\int_0^{t_M} I_s(z) dz}{I_c t_{TaTe_2}}$$

$$= \frac{\lambda_{TaTe_2}}{t_{TaTe_2}} \frac{(1 - e^{-\frac{t_{TaTe_2}}{\lambda_{TaTe_2}}})^2}{1 - e^{-2\frac{t_{TaTe_2}}{\lambda_{TaTe_2}}}} \frac{I_s(z=0)}{I_c}$$

$$= \frac{\lambda_{TaTe_2}}{t_{TaTe_2}} \frac{(1 - e^{-\frac{t_{TaTe_2}}{\lambda_{TaTe_2}}})^2}{1 - e^{-2\frac{t_{TaTe_2}}{\lambda_{TaTe_2}}}}$$

$$\times \frac{2p_i Q_{IF1} \left[(2Q_{IF2} + 1)(1 - Q_{IM})e^{-\frac{-L_{SH}}{\lambda_{gr}}} - (1 + Q_{IM})e^{-\frac{-3L_{SH}}{2\lambda_{gr}}} \right]}{(2Q_{IF1} + 1)(2Q_{IF2} + 1)(1 + Q_{IM}) - (2Q_{IF1} + 1)(1 + Q_{IM})e^{-\frac{-3L_{SH}}{2\lambda_{gr}}} - (2Q_{IF2} + 1)(1 - Q_{IM})e^{-\frac{-L_{SH}}{\lambda_{gr}}} - (Q_{IM} - 1)e^{-\frac{-2L_{SH}}{\lambda_{gr}}}}.$$

Here, $R_{gr} = \frac{R_{gr}\lambda_{gr}}{w_{gr}}$, $Q_{IFi} = \frac{1}{1-p^2} \frac{R_{ci}}{R_{gr}}$, with $i = 1, 2$, R_{ci} corresponding to injector and detector contact resistances, respectively. $Q_{IM} = \frac{w_{gr}R_{int.}}{R_{gr}\lambda_{gr}}$, $R_{int.}$, w_{gr} , R_{gr} are the TaTe₂-

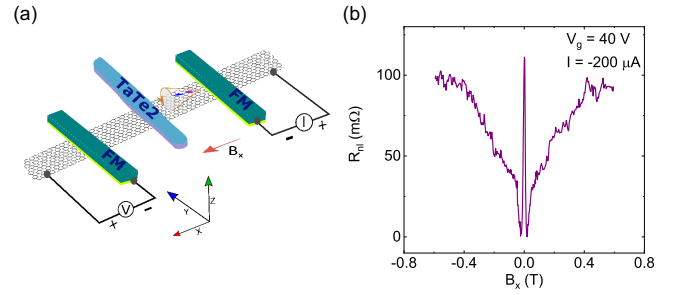


FIG. 8. x -field Hanle in graphene-TaTe₂ channel. (a) Schematic representation of the measurement setup to measure nonlocal x Hanle, where the magnetic field is applied in the planner perpendicular direction (x axis) to the magnetic easy axis (y axis) of the FM electrodes. (b) Measured x Hanle spin signal at $I = -200 \mu A$ and $V_g = 40 V$ at room temperature.

Here, ΔR_{ISHE} , θ_{SH} , ρ_{TaTe_2} , X , and w_{TaTe_2} are the ISHE signal amplitude ($\Delta R_{ISHE} = \Delta V_{ISHE}/I_{50\mu A} = 43 m\Omega$), spin Hall angle, resistivity of TaTe₂ (300 $\mu\Omega$ cm), shunting factor (0.94), and width of TaTe₂ (2.6 μm). \hat{I}_s and I_c are the effective spin current absorbed by TaTe₂ from the graphene channel due to the shunting effect and converted charge current due to ISHE in TaTe₂. The shunt factor (X) is estimated by considering the spin signal is in the linear regime with bias current, and from the spin signal presented in Fig. 1(e), $X = 1 - \frac{16}{272} = 0.94$, which alludes to 94% spin absorption by TaTe₂.

$\frac{\hat{I}_s}{I_c}$ can be written as below.

graphene interface resistance, graphene channel width, and square resistance, respectively, and are presented in Table I. As the spin diffusion length in TaTe₂ is an unknown parameter, we estimated spin Hall angle (θ_{SH}) as a function of spin

TABLE I. Parameters of graphene-TaTe₂ for device 3 to estimate the spin Hall angle in TaTe₂ to solve Eq. (E1).

	D_s (m ² /s)	τ_s (ps)	λ_{Gr} (μm)	w_{Gr} (μm)	L_{SH} (μm)	t_{TaTe_2} (nm)	w_{TaTe_2} (μm)	$R_{sq,Gr}$ (Ω)	ρ_{TaTe_2} ($\mu\Omega$ cm)	R_{c1} (k Ω)	R_{c2} (k Ω)
Device 1	0.021	311	2.56	1.8	2.5	70	2.6	339	300	20	15

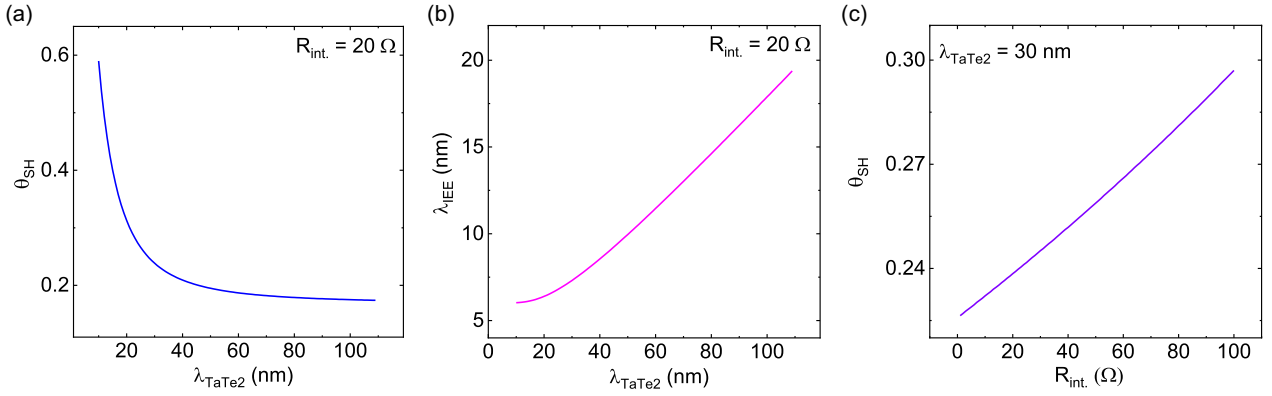


FIG. 9. Estimation of the spin Hall angle (θ_{SH}) in TaTe₂. (a) Spin Hall angle (θ_{SH}) as a function of spin diffusion length in TaTe₂ (λ_{TaTe_2}) considering $R_{int} = 20 \Omega$. (b) IEE length (λ_{IEE}) as a function of λ_{TaTe_2} . (c) Spin Hall angle (θ_{SH}) as a function of R_{int} considering spin diffusion length $\lambda_{TaTe_2} = 30$ nm.

diffusion length (λ_{TaTe_2}) in TaTe₂ by assuming $R_{int} = 20 \Omega$ [shown in Fig. 9(a)]. The spin Hall angle θ_{SH} decays exponentially with increasing λ_{TaTe_2} according to Eq. (E1) and its simplified solution. We found θ_{SH} is 0.59 at $\lambda_{TaTe_2} = 10$ nm; 0.23 at $\lambda_{TaTe_2} = 30$ nm, and becomes saturated with 0.20. We can also approximately calculate the inverse Edelstein effect (IEE) of TaTe₂ through IEE length $\lambda_{IEE} = \theta_{SH} * \lambda_{TaTe_2}$, and we found $\lambda_{IEE} \approx 6$ –60 nm [see Fig. 9(b)] as a function of λ_{TaTe_2} (10–110 nm) by considering $R_{int} = 20 \Omega$.

Overall, the calculated range of θ_{SH} for TaTe₂ seems to be consistent with Pt ($\theta_{SH,Pt} \approx 0.23$) [10,11], and other TMDs such as MoTe₂ ($\theta_{SH,MoTe_2} \approx 0.2$) [38], MoS₂ ($\theta_{SH,MoS_2} \approx 0.1$) [17], but one order of magnitude higher compared to the lower limit of the θ_{SH,WTe_2} for WTe₂ ($\theta_{SH,WTe_2} = 0.01$) [12]. Interestingly, the estimated values of λ_{IEE} are comparable to topological insulators [52] (2.1 nm), oxide interfaces [53] (6.4 nm), but it seems to be one order of magnitude higher than in heavy metals (0.1–0.4 nm) and other Rashba systems [33,54]. Figure 9(c) depicts θ_{SH} as a function of R_{int} by considering spin diffusion length in TaTe₂, $\lambda_{TaTe_2} = 30$ nm at room temperature. The spin Hall angle, θ_{SH} , shows a linear dependence on R_{int} and ranges from 0.22 to 0.29 for $R_{int} = 1$ –100 Ω .

APPENDIX F: SPIN TRANSPORT AND SPIN POLARIZATION IN GRAPHENE-TaTe₂ HETEROSTRUCTURE

We characterized the spin transport properties in the graphene-TaTe₂ channel (without spin absorption) to estimate the spin polarization of the detector FM contact. Figure 10 (a) shows the sketch of the measurement geometry for NL Hanle measurement, where the magnetic field is applied in the out-of-plane direction. The measured spin precession signal is fitted with the following Hanle precession Eq. (F1) to approximate the spin diffusion constant (D_s), spin diffusion length (λ_s), and lifetime (τ_s):

$$\Delta R_{NL} \propto \int_0^\infty \frac{1}{\sqrt{4\pi Dt}} e^{-\frac{L^2}{4Dt}} \cos(\omega_L t) e^{-\frac{t}{\tau_s}} dt. \quad (F1)$$

Furthermore, the measured Hanle spin signal (purple circles) along with its fit (magenta line) to Eq. (F2) is shown in Fig. 10(b) to extract TiO₂/Co contact polarization:

$$\Delta R_{NL} = \pm \frac{P_i P_d R_{sq} D_s}{W} \text{Re} \left\{ \frac{1}{2D_s} \frac{e^{-L\sqrt{\lambda_s^{-2} - i\frac{\omega}{D_s}}}}{\sqrt{\tau_s^{-1} - i\omega}} \right\}. \quad (F2)$$

Here, ω depends on the frequency of spin flips and Larmor precession, $\omega_L = \frac{g\mu_B}{\hbar} B_\perp$ is the Larmor frequency, where B_\perp is an applied perpendicular magnetic field to the easy axis of the FM contacts, $g = 2$ is assumed. In equation (F1) and (F2), D_s is the spin diffusion constant, and λ_s ($2.56 \pm 0.14 \mu\text{m}$) and τ_s (311 ± 16 ps) are the spin diffusion length and spin lifetime, respectively. In device 1, $R_{sq} = 339 \Omega$ for multilayer exfoliated graphene at $V_g = 40$ V on Si/SiO₂ substrate. The distance between spin injection and spin detection electrodes is $L = 4.5 \mu\text{m}$, graphene width, $w = 1.8 \mu\text{m}$. Considering the spin polarization of the injector and detector to be equal ($P_i = P_d$), P_{Co/TiO_2} is estimated to be about $6.13\% \pm 0.9\%$.

To estimate the current-induced spin polarization in TaTe₂ in device 2, we have also used the same equation, Eq. (F2), to fit the Hanle signal, as shown in Fig. 2(f). In device 2, using the graphene channel resistance, $R_{sq} = 1425 \Omega$, width

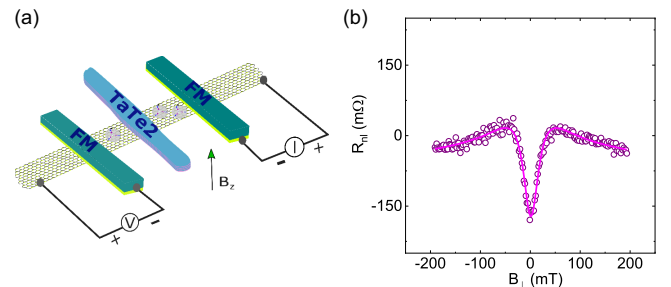


FIG. 10. Spin transport in the graphene-TaTe₂ heterostructure. (a) Sketch of the measurement setup for nonlocal Hanle measurement. (b) Hanle spin precession signal (purple circles) without spin absorption by TaTe₂ at back-gate voltage $V_g = 40$ V with bias current $I = -30 \mu\text{A}$ along with the fitted line (magenta line) to Eq. (F2) to estimate the spin polarization of FM contacts.

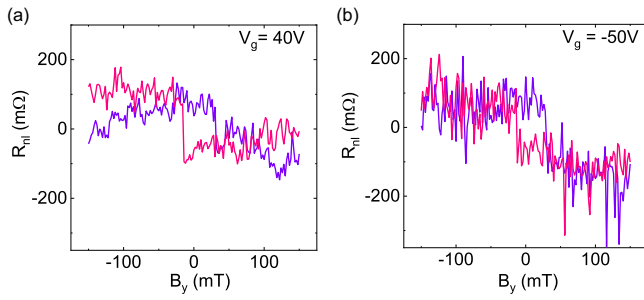


FIG. 11. Spin injection from TaTe₂ into graphene and spin-switch signal in device 1. (a, b) Spin injection from TaTe₂ into graphene for the electron- and hole-doped regimes at gate voltages $V_g = 40$ and -50 V with $I = -40$ and -30 μ A, respectively.

$w = 1.2$ μ m, we found that

$$\begin{aligned} \sqrt{P_{\text{TaTe}_2} P_{\text{Co/TiO}_2}} &= 0.0287 \pm 0.0127 \\ P_{\text{TaTe}_2} &= \frac{0.0287^2}{P_{\text{Co/TiO}_2}} \pm \frac{0.0127^2}{P_{\text{Co/TiO}_2}} \\ &= 0.0134 \pm 0.0026. \end{aligned}$$

Now, using previously obtained $P_{\text{Co/TiO}_2} = 6.13\%$, the spin polarization of TaTe₂ is approximated to be $P_{\text{TaTe}_2} = 1.34\% \pm 0.26\%$.

APPENDIX G: SPIN INJECTION FROM TaTe₂ INTO GRAPHENE IN DEVICE 1

The vertical spin injection results were reproducibly observed at room temperature in three different devices fabricated with similar methods, as presented in this manuscript. Figure 11 shows the spin injection from TaTe₂ into graphene and spinswitch signal in device 1. The possibility of spin

transport contribution from the reference FM electrodes on the graphene channel in the injector and detector circuit can be ruled out, as it would have resulted in multiple switches in the measured signal (see Fig. 1(e), where both FM injector and detector contacts are involved in the conventional spin-valve measurements).

APPENDIX H: CURRENT-INDUCED SPIN POLARIZATION IN SYMMETRIC AND LOW-SYMMETRIC CRYSTALS

Here we discuss possible origins of in-plane spin polarization in TaTe₂ considering the crystal structure of TaTe₂. 1T'-TaTe₂ is a centrosymmetric layered material at room temperature where spin current (I_s), charge current (I_c), and spin polarization (s) are perpendicular to each other for symmetric measurements of the spin Hall effect (SHE) or Edelstein effect (EE). To facilitate our discussion, three-dimensional (3D) axis directions are presented in Fig. 12(a), similar to the schematics shown in Figs. 2(a) and 2(d). Conventional ISHE in the symmetric 3D crystal of TaTe₂ is shown in Fig. 12(b), where I_s , I_c , and s are perpendicular to each other in the z , y , and x directions, respectively, and can explain the measurements depicted in Figs. 2(a)–2(c).

Interestingly, in-plane spin polarization along the y axis in TaTe₂, presented in Figs. 2(d)–2(f), is possible while injecting charge current (I_c) can be along the z axis [Fig. 12(c)] and x axis [Fig. 12(d)], which needs to be perpendicular to the corresponding spin current (I_s) to maintain symmetry. These symmetries allow bulk and surface states to inject spin from bulk (via SHE) or surface states (via Edelstein effect) of TaTe₂. While charge current (I_c) and spin current (I_s) are along the z axis and x axis, respectively, the spins are accumulated at the edges of TaTe₂ [Fig. 12(c)]. However, the TaTe₂ crystals have a relatively smaller thickness (70–100 nm) and

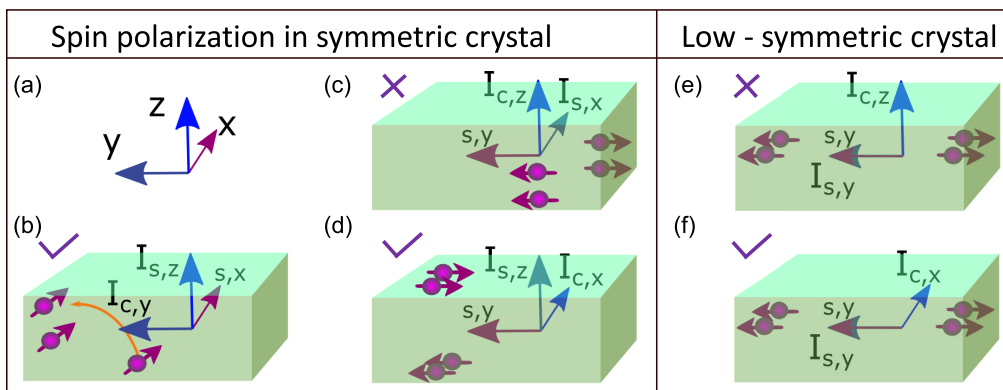


FIG. 12. (a) The x , y , and z -axis directions similar to the schematics shown in Figs. 2(a) and 2(d) to explain three-dimensional crystal symmetry. (b) Spin to charge conversion due to inverse spin Hall effect (ISHE), shown in Figs. 2(a)–2(c) in the high-symmetry crystal structure, where spin absorption in TaTe₂ renders z -direction spin current ($I_{s,z}$) with the spin direction along the x axis (s_x) and measured charge current in the y axis ($I_{c,y}$). (c) Spin polarization in symmetric TaTe₂ to explain the spin-switch measurements shown in Figs. 2(d)–2(f). In this case, injected spin current in graphene is along the y direction, and keeping this in mind, we have two possible scenarios. First, charge current and spin current are out of plane (along the z axis) and in plane (along the x axis), respectively, and spins are accumulated at the edges of TaTe₂. In the second scenario, shown in (d), where spin along the y direction is accumulated at the top and bottom surface of TaTe₂ and charge current and spin current are in x and z direction. (e, f) Spin polarization and spin current are parallel and along the y axis in lower symmetry situations but perpendicular to the charge current, which can be in the z or x axis, respectively.

negligible edge area in contact with graphene compared to the bottom surface area. Hence, in-plane (y -axis) spin injection into graphene from the accumulated spins at the TaTe₂ edges is improbable. On the other hand, considering charge current (I_c) and spin current (I_s) are along the x and z axis [Fig. 12(d)], where spin along the y axis can accumulate at the top and bottom surface of TaTe₂, this can explain our measurements of spin polarization in symmetric TaTe₂ crystal with lateral widths of 2.6–6 μm in contact with graphene and nanometer-range thickness.

However, in-plane spin polarization can also emerge in unconventional and lower symmetric TaTe₂ crystal [see Figs. 12(e) and 12(f)], where spin current and spin orientation can be parallel to each other and along the y axis ($s \parallel I_s$) but are perpendicular to the charge current (I_c), which could be in either z or x direction in our measurement geometry [45]. Again, considering k -dependent spin polarization and the lateral width of TaTe₂, which is considerably higher than the thickness, the latter situation is more likely to emanate in such a lower symmetric crystal because of SHE or EE.

- [1] W. Han, R. K. Kawakami, M. Gmitra, and J. Fabian, Graphene spintronics, *Nat. Nanotechnol.* **9**, 794 (2014).
- [2] I. Žutić, J. Fabian, and S. Das Sarma, Spintronics: Fundamentals and applications, *Rev. Mod. Phys.* **76**, 323 (2004).
- [3] D. D. Awschalom and M. E. Flatté, Challenges for semiconductor spintronics, *Nat. Phys.* **3**, 153 (2007).
- [4] A. Fert, Origin, development, and future of spintronics (Nobel lecture), *Angew Chemie Int. Ed.* **47**, 5956 (2008).
- [5] A. Manchon, J. Železný, I. M. Miron, T. Jungwirth, J. Sinova, A. Thiaville, K. Garello, and P. Gambardella, Current-induced spin-orbit torques in ferromagnetic and antiferromagnetic systems, *Rev. Mod. Phys.* **91**, 035004 (2019).
- [6] K. Garello, F. Yasin, H. Hody, S. Couet, L. Souriau, S. H. Sharifi, J. Swerts, R. Carpenter, S. Rao, W. Kim *et al.*, Manufacturable 300 mm platform solution for Field-Free Switching SOT-MRAM, 2019 *Symposium on VLSI Technology* (Kyoto, Japan, 2019), pp. T194-T195.
- [7] J. Sinova, S. O. Valenzuela, J. Wunderlich, C. H. Back, and T. Jungwirth, Spin Hall effects, *Rev. Mod. Phys.* **87**, 1213 (2015).
- [8] A. Manchon, H. C. Koo, J. Nitta, S. M. Frolov, and R. A. Duine, New perspectives for Rashba spin-orbit coupling, *Nat. Mater.* **14**, 871 (2015).
- [9] J. C. Rojas-Sánchez and A. Fert, Compared Efficiencies of Conversions between Charge and Spin Current by Spin-Orbit Interactions in Two- and Three-Dimensional Systems, *Phys. Rev. Appl.* **11**, 054049 (2019).
- [10] W. S. Torres, J. F. Sierra, L. A. Benítez, F. Bonell, M. V. Costache, and S. O. Valenzuela, Spin precession and spin Hall effect in monolayer graphene/Pt nanostructures, *2D Mater.* **4**, 041008 (2017).
- [11] W. Yan, E. Sagasta, M. Ribeiro, Y. Niimi, L. E. Hueso, and F. Casanova, Large room temperature spin-to-charge conversion signals in a few-layer graphene/Pt lateral heterostructure, *Nat. Commun.* **8**, 661 (2017).
- [12] B. Zhao, D. Khokhriakov, Y. Zhang, H. Fu, B. Karpiak, A. Md. Hoque, X. Xu, Y. Jiang, B. Yan, and S. P. Dash, Observation of charge to spin conversion in Weyl semimetal WTe₂ at room temperature, *Phys. Rev. Res.* **2**, 013286 (2020).
- [13] B. Zhao, B. Karpiak, D. Khokhriakov, A. M. Hoque, X. Xu, Y. Jiang, and S. P. Dash, Edelstein effect in type-II Weyl semimetal WTe₂ up to room temperature, *arXiv:1910.06225*.
- [14] Z. Kovács-Krausz, A. M. Hoque, P. Makk, B. Szentpéteri, M. Kocsis, B. Fülöp, M. V. Yakushev, T. V. Kuznetsova, O. E. Tereshchenko, K. A. Kokh *et al.*, Electrically controlled spin injection from giant Rashba spin-orbit conductor BiTeBr, *Nano Lett.* **20**, 4782 (2020).
- [15] L. Li, J. Zhang, G. Myeong, W. Shin, H. Lim, B. Kim, S. Kim, T. Jin, S. Cavill, B. S. Kim *et al.*, Gate-tunable reversible Rashba-Edelstein effect in a few-layer graphene/2H-TaS₂ heterostructure at room temperature, *ACS Nano* **14**, 5251 (2020).
- [16] T. S. Ghiasi, A. A. Kaverzin, P. J. Blah, and B. J. van Wees, Charge-to-spin conversion by the Rashba-Edelstein effect in two-dimensional van der Waals heterostructures up to room temperature, *Nano Lett.* **19**, 5959 (2019).
- [17] C. K. Safeer, J. Ingla-Aynés, F. Herling, J. H. Garcia, M. Vila, N. Ontoso, M. R. Calvo, S. Roche, L. E. Hueso, and F. Casanova, Room-temperature spin Hall effect in graphene/MoS₂ van der Waals heterostructures, *Nano Lett.* **19**, 1074 (2019).
- [18] D. Khokhriakov, A. W. Cummings, K. Song, M. Vila, B. Karpiak, A. Dankert, S. Roche, and S. P. Dash, Tailoring emergent spin phenomena in Dirac material heterostructures, *Sci. Adv.* **4**, eaat9349 (2018).
- [19] C. H. Li, O. M. J. van't Erve, J. T. Robinson, Y. Liu, L. Li, and B. T. Jonker, Electrical detection of charge-current-induced spin polarization due to spin-momentum locking in Bi₂Se₃, *Nat. Nanotechnol.* **9**, 218 (2014).
- [20] A. Dankert, J. Geurs, M. V. Kamalakar, S. Charpentier, and S. P. Dash, Room temperature electrical detection of spin polarized currents in topological insulators, *Nano Lett.* **15**, 7976 (2015).
- [21] A. Dankert, P. Bhaskar, D. Khokhriakov, I. H. Rodrigues, B. Karpiak, M. V. Kamalakar, S. Charpentier, I. Garate, and S. P. Dash, Origin and evolution of surface spin current in topological insulators, *Phys. Rev. B* **97**, 125414 (2018).
- [22] N. H. D. Khang, Y. Ueda, and P. N. Hai, A conductive topological insulator with large spin Hall effect for ultralow power spin-orbit torque switching, *Nat. Mater.* **17**, 808 (2018).
- [23] A. R. Mellnik, J. S. Lee, A. Richardella, J. L. Grab, P. J. Mintun, M. H. Fischer, A. Vaezi, A. Manchon, E. A. Kim, N. Samarth, and D. C. Ralph, Spin-transfer torque generated by a topological insulator, *Nature (London)* **511**, 449 (2014).
- [24] D. C. Manendra, R. Grassi, J.-Y. Chen, M. Jamali, D. R. Hickey, D. Zhang, Z. Zhao, H. Li, P. Quartermann, Y. Lv, M. Li, A. Manchon, K. A. Mkhoyan, T. Low, and J.-P. Wang, Room-temperature high spin-orbit torque due to quantum confinement in sputtered Bi_xSe_(1-x) films, *Nat. Mater.* **17**, 800 (2018).
- [25] J. A. Voerman, C. Li, Y. Huang, and A. Brinkman, Spin-momentum locking in the gate tunable topological insulator BiSbTeSe₂ in non-local transport measurements, *Adv. Electron. Mater.* **5**, 1900334 (2019).
- [26] K. Vaklinova, A. Hoyer, M. Burghard, and K. Kern, Current-induced spin polarization in topological insulator-graphene heterostructures, *Nano Lett.* **16**, 2595 (2016).

- [27] B. Zhao, D. Khokhriakov, B. Karpiak, A. M. Hoque, L. Xu, L. Shen, Y. P. Feng, X. Xu, Y. Jiang, and S. P. Dash, Electrically controlled spin-switch and evolution of Hanle spin precession in graphene, *2D Mater.* **6**, 035042 (2019).
- [28] A. H. Castro Neto and F. Guinea, Impurity-Induced Spin-Orbit Coupling in Graphene, *Phys. Rev. Lett.* **103**, 026804 (2009).
- [29] B. Karpiak, A. W. Cummings, K. Zollner, M. Vila, D. Khokhriakov, A. M. Hoque, A. Dankert, P. Svedlindh, J. Fabian, S. Roche, and S. P. Dash, Magnetic proximity in a van der Waals heterostructure of magnetic insulator and graphene, *2D Mater.* **7**, 015026 (2020).
- [30] S. Manipatruni, D. E. Nikonov, C.-C. Lin, T. A. Gosavi, H. Liu, B. Prasad, Y.-L. Huang, E. Bonturim, R. Ramesh, and I. A. Young, Scalable energy-efficient magnetoelectric spin-orbit logic, *Nature (London)* **565**, 35 (2019).
- [31] J. J. Gao, J. G. Si, X. Luo, J. Yan, F. C. Chen, G. T. Lin, L. Hu, R. R. Zhang, P. Tong, W. H. Song, X. B. Zhu, W. J. Lu, and Y. P. Sun, Origin of the structural phase transition in single-crystal TaTe₂, *Phys. Rev. B* **98**, 224104 (2018).
- [32] M. Milletari, M. Offidani, A. Ferreira, and R. Raimondi, Covariant Conservation Laws and the Spin Hall Effect in Dirac-Rashba Systems, *Phys. Rev. Lett.* **119**, 246801 (2017).
- [33] J. C. R. Sánchez, L. Vila, G. Desfonds, S. Gambarelli, J. P. Attané, J. M. De Teresa, C. Magén, and A. Fert, Spin-to-charge conversion using Rashba coupling at the interface between non-magnetic materials, *Nat. Commun.* **4**, 2944 (2013).
- [34] M. Offidani, M. Milletari, R. Raimondi, and A. Ferreira, Optimal Charge-to-Spin Conversion in Graphene on Transition-Metal Dichalcogenides, *Phys. Rev. Lett.* **119**, 196801 (2017).
- [35] M. V. Kamalakar, A. Dankert, P. J. Kelly, and S. P. Dash, Inversion of spin signal and spin filtering in ferromagnet/hexagonal boron nitride-graphene van der Waals heterostructures, *Sci. Rep.* **6**, 21168 (2016).
- [36] D. Khokhriakov, B. Karpiak, A. M. Hoque, and S. P. Dash, Two-dimensional spintronic circuit architectures on large scale graphene, *Carbon* **161**, 892 (2020).
- [37] J. Zhang, B. Yang, H. Zheng, X. Han, and Y. Yan, Large magnetic anisotropy and strain induced enhancement of magnetic anisotropy in monolayer TaTe₂, *Phys. Chem. Chem. Phys.* **19**, 24341 (2017).
- [38] C. K. Safeer, N. Ontoso, J. Ingla-Aynés, F. Herling, V. T. Pham, A. Kurzman, K. Ensslin, A. Chuvilin, I. Robredo, M. G. Vergniory *et al.*, Large multidirectional spin-to-charge conversion in low-symmetry semimetal MoTe₂ at room temperature, *Nano Lett.* **19**, 8758 (2019).
- [39] S. O. Valenzuela and M. Tinkham, Direct electronic measurement of the spin Hall effect, *Nature (London)* **442**, 176 (2006).
- [40] G. M. Stiehl, D. MacNeill, N. Sivadas, I. El Baggari, M. H. Guimarães, N. D. Reynolds, L. F. Kourkoutis, C. J. Fennie, R. A. Buhrman, and D. C. Ralph, Current-induced torques with Dresselhaus symmetry due to resistance anisotropy in 2D materials, *ACS nano* **13**, 2599 (2019).
- [41] B. Karpiak, A. Dankert, A. W. Cummings, S. R. Power, S. Roche, and S. P. Dash, 1D ferromagnetic edge contacts to 2D graphene/h-BN heterostructures, *2D Mater.* **5**, 014001 (2018).
- [42] R. S. Patel, S. P. Dash, M. P. De Jong, and R. Jansen, Magnetic tunnel contacts to silicon with low-work-function ytterbium nanolayers, *J. Appl. Phys.* **106**, 016107 (2009).
- [43] S. Sharma, S. P. Dash, H. Saito, S. Yuasa, B. J. van Wees, and R. Jansen, Anisotropy of spin polarization and spin accumulation in Si/Al₂O₃/ferromagnet tunnel devices, *Phys. Rev. B* **86**, 165308 (2012).
- [44] A. Fert and H. Jaffrès, Conditions for efficient spin injection from a ferromagnetic metal into a semiconductor, *Phys. Rev. B* **64**, 184420 (2001).
- [45] D. Culcer and R. Winkler, Generation of Spin Currents and Spin Densities in Systems with Reduced Symmetry, *Phys. Rev. Lett.* **99**, 226601 (2007).
- [46] A. Dankert and S. P. Dash, Electrical gate control of spin current in van der Waals heterostructures at room temperature, *Nat. Commun.* **8**, 16093 (2017).
- [47] D. Khokhriakov, A. M. Hoque, B. Karpiak, and S. P. Dash, Gate-tunable spin-galvanic effect in graphene-topological insulator van der Waals heterostructures at room temperature, *Nature Commun.* **11**, 1 (2020).
- [48] A. M. Hoque, D. Khokhriakov, B. Karpiak, and S. P. Dash, All-electrical creation and control of giant spin-galvanic effect in 1T-MoTe₂/graphene heterostructures at room temperature, *arXiv:1908.09367v2*.
- [49] L. A. Benítez, W. S. Torres, J. F. Sierra, M. Timmermans, J. H. Garcia, S. Roche, M. V. Costache, and S. O. Valenzuela, Tunable room-temperature spin galvanic and spin Hall effects in van der Waals heterostructures, *Nat. Mater.* **19**, 170 (2020).
- [50] X. Zhang, Q. Liu, J.-W. Luo, A. J. Freeman, and A. Zunger, Hidden spin polarization in inversion-symmetric bulk crystals, *Nat. Phys.* **10**, 387 (2014).
- [51] J.-C. Rojas Sánchez, P. Laczkowski, W. F. Savero Torres, M. Cubukcu, V. D. Nguyen, L. Notin, C. Beigné, C. Vergnaud, A. Marty, M. Jamet, L. Vila, and J. P. Attané, In-plane and out-of-plane spin precession in lateral spin-valves, *Appl. Phys. Lett.* **102**, 132408 (2013).
- [52] J.-C. Rojas-Sánchez, S. Oyarzún, Y. Fu, A. Marty, C. Vergnaud, S. Gambarelli, L. Vila, M. Jamet, Y. Ohtsubo, A. Taleb-Ibrahimi *et al.*, Spin to Charge Conversion at Room Temperature by Spin Pumping into a New Type of Topological Insulator: α -Sn Films, *Phys. Rev. Lett.* **116**, 096602 (2016).
- [53] E. Lesne, Y. Fu, S. Oyarzun, J. C. Rojas-Sánchez, D. C. Vaz, H. Naganuma, G. Sicoli, J.-P. Attané, M. Jamet, E. Jacquet *et al.*, Highly efficient and tunable spin-to-charge conversion through Rashba coupling at oxide interfaces, *Nat. Mater.* **15**, 1261 (2016).
- [54] A. Nomura, T. Tashiro, H. Nakayama, and K. Ando, Temperature dependence of inverse Rashba-Edelstein effect at metallic interface, *Appl. Phys. Lett.* **106**, 212403 (2015).

Paper III

Charge to Spin Conversion in van der Waals Metal NbSe₂

Anamul Md. Hoque¹, Bing Zhao¹, Dmitrii Khokhriakov¹, Prasanta Muduli², Saroj P. Dash^{1,3*}

¹*Department of Microtechnology and Nanoscience, Chalmers University of Technology, SE-41296, Göteborg, Sweden*

²*Department of Physics, Indian Institute of Technology Madras, Chennai 600036, India*

³*Graphene Center, Chalmers University of Technology, SE-41296, Göteborg, Sweden*

Abstract:

Quantum materials with a large charge current-induced spin polarization are promising for next-generation all-electrical spintronic science and technology. Van der Waals metals with high spin-orbit coupling and spin textures have attracted significant attention for an efficient charge-to-spin conversion process. Here, we demonstrate the electrical generation of spin polarization in NbSe₂ up to room temperature. Characterization of NbSe₂ shows superconducting transition temperature, $T_c \sim 7\text{K}$. To probe the current-induced spin polarization in NbSe₂, we used a graphene-based non-local spin-valve device, where the spin-polarization in NbSe₂ is efficiently injected and detected using non-local spin-switch and Hanle spin precession measurements. A significantly higher charge-spin conversion in NbSe₂ is observed at a lower temperature. Systematic measurements provide the possible origins of the spin polarization to be predominantly due to the spin Hall effect or Rashba-Edelstein effect in NbSe₂, considering different symmetry-allowed charge-spin conversion processes.

Keywords: Nonmagnetic spin source, current-induced spin polarization, NbSe₂, graphene, spin Hall effect, Rashba Edelstein effect, spintronics, spin-valve, Hanle

Corresponding author: saroj.dash@chalmers.se

Two-dimensional (2D) materials and their van der Waals (vdW) heterostructures have become attractive platforms to explore numerous physical phenomena, primarily associated with spin-orbit coupling (SOC), exotic superconductivity, and magnetism for next-generation electronic devices^{1,2}. 2D transition metal dichalcogenides (TMDCs) are ideal hosts for realizing spin-polarized electronic states due to the high SOC accompanied with broken symmetries in the crystal structure^{3,4}. Recently, vdW materials have paved the way for utilizing various charge-to-spin interconversion (CSC) processes^{3,5,6}. For example, charge-to-spin interconversion and spin-orbit torque (SOT) effects are observed in semimetals such as WTe₂, MoTe₂, and NbSe₂ up to room temperature^{7–12}. Furthermore, the 2D materials can be fabricated in vdW heterostructures with atomically clean interfaces without adulterating their distinctive electronic properties that provide routes for band structure engineering and proximity-induced SOC¹³. For instance, heterostructures of graphene with 2D materials have shown unprecedented gate-tunable CSC processes and spin textures^{11,14–19}.

It is known that 2H NbSe₂ is a vdW layered metallic TMDC with superconducting (SC) behaviour below a critical temperature $T_c \approx 7\text{K}$ ²⁰. It is expected that the CSC effects can be enhanced in the SC state mediated by quasiparticles with higher spin lifetimes^{2,21}. Interestingly, NbSe₂ in the normal state also has enormous prospects in the CSC process, triggered by high SOC of the Nb 4*d* orbital and breaking of symmetries with higher electrical conductivities than semiconductive and semimetallic TMDCs⁷. NbSe₂ also exhibits Ising-type SOC similar to the intrinsic Zeeman field, which results in unconventional spin textures²². Recently NbSe₂/Permalloy structures demonstrated a large anti-damping torque, which is attributed to strain-induced symmetry breaking⁷. Furthermore, spin- and angle-resolved photoemission spectroscopy (ARPES) also reveals that the electronic band structure of NbSe₂ in the normal state hosts a strong momentum-dependent spin polarization at Fermi level²³. Such fascinating spin-dependent electronic properties in NbSe₂ are highly desirable to create current-induced spin polarization.

Here, we demonstrate the electronic generation of spin polarization in NbSe₂ up to room temperature owing to the efficient CSC process. The engendered spin polarization in NbSe₂ is efficiently injected into the graphene spin-channel in the vdW heterostructure spin-valve device and detected by a ferromagnet (FM) using non-local (NL) spin-switch and Hanle spin-precession measurements. A significantly higher CSC signal in NbSe₂ is observed at a lower temperature in the non-superconducting regime. These findings demonstrate NbSe₂ to be a metallic spin source up to room, which can be pivotal for future energy-efficient all-electric spin-based technologies^{6,24}.

To detect the CSC properties in NbSe₂, we fabricated NbSe₂-graphene vdW heterostructure devices. We used chemical vapor deposited (CVD) graphene as a spin channel material, due to its excellent spin transport property arising from low SOC and hyperfine interactions^{25,26}. Most interestingly, it was demonstrated that graphene can make a very good vdW heterostructure with other 2D materials²⁷. Figure 1(a) presents the schematic of the NbSe₂-graphene vdW heterostructure device along with ferromagnetic (FM) contacts to characterize the spin transport properties in the heterostructure (see the Methods in the Supplementary for details). A scanning electron microscopic (SEM) image of a fabricated device consisting of CVD graphene, multilayer NbSe₂ flake, and multiple FM contacts is shown in Fig.1(b). An optical micrograph and atomic force microscopic (AFM) image of the corresponding device has been shown in Supplementary Fig. S1. The interface resistance between NbSe₂-graphene is found to be 50 Ω , the FM contact resistance is 12k Ω and the field-effect mobility (μ) of the graphene channel is $\approx 2000\text{cm}^2\text{V}^{-1}\text{s}^{-1}$ (see Supplementary Fig. S2).

As a high SOC material, NbSe₂ can give rise to current-induced in-plane (y-axis) spin polarization via conventional spin Hall effect (shown in Fig. 1(c)), where charge current (I_c) along the x-axis creates a transverse spin current (I_s) along the z-axis^{10,12}. Furthermore, high SOC in NbSe₂ crystal along with structure inversion asymmetry (SIA) in the layered NbSe₂-graphene interface can result in Rashba spin splitting in the band structure with helical spin texture with opposite spin-subbands, as shown in Fig. 1(d).

Upon application of an electric field (E), hence the charge current can shift the helical Fermi surface in the k -space and create net spin polarization via the Rashba-Edelstein effect. The created spin polarization in NbSe_2 can be injected into a graphene spin channel in vdW heterostructure and detected by NL measurement geometry to realize a pure spin signal.

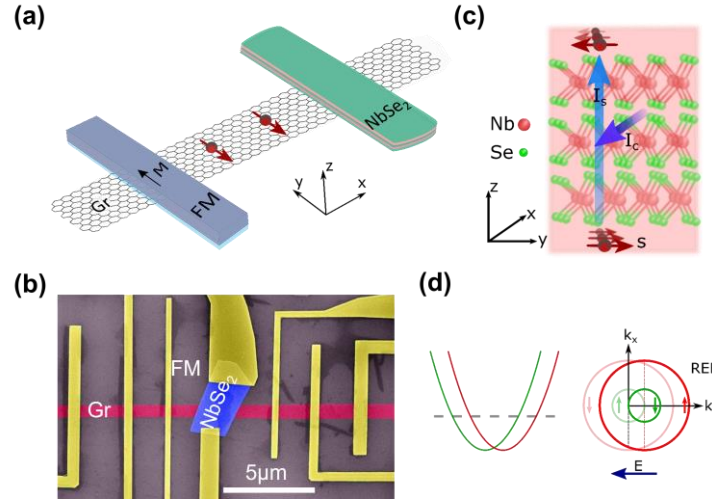


Figure 1. The device design of NbSe_2 -graphene heterostructure. (a) Schematic of NbSe_2 -graphene heterostructure, where NbSe_2 creates non-equilibrium spin polarization and injects spin-polarized electrons into graphene spin-channel, which is detected by an FM (TiO_2/Co) contacts in non-local measurement geometry. (b) Colored scanning electron microscopic (SEM) image of a fabricated device consisting of CVD graphene, multilayer NbSe_2 flake (blue), and multiple FM contacts (yellow) to characterize spin transport properties. The scale bar is 5 μm . (c) Schematic illustration of charge to spin conversion process due to conventional spin Hall effect in NbSe_2 , where charge current (I_c) engenders a transverse spin current (I_s). (d) Charge current from the applied electric field (E) induced spin polarization due to the Rashba-Edelstein effect (REE) at the Fermi surface in spin-split bands of a high spin-orbit coupling interface.

At first, high-quality crystal structures of the materials were ensured by Raman spectroscopy. The Raman spectrum of single-layer CVD graphene (top panel) and exfoliated multilayer NbSe_2 (bottom panel) using 638 nm LASER have been presented in Fig. 2(a). The Raman spectra of graphene confirm high-quality graphene crystal since almost no defect-induced D peak is observed. Furthermore, the higher intensity of the 2D peak at 2645 cm^{-1} than that of the G peak at 1590 cm^{-1} indicates the growth of single-layer graphene²⁸. In the case of NbSe_2 , the characteristic A1g peak for multilayer 2H NbSe_2 is observed at 230 cm^{-1} ²⁹.

We started with investigating the superconducting properties of exfoliated multilayer NbSe_2 flake by measuring the temperature dependence of longitudinal resistance, as shown in Fig. 2(b). The device picture and measurement geometry are shown in the insets of Fig. 2(b). We used $1 \mu\text{A}$ of DC bias current and the superconducting critical temperature (T_c) in this flake is found to be 6.8K. The IV measurement with DC bias current and corresponding differential resistance (dV/dI) as a function of the bias current at 3K for the NbSe_2 flake are shown in Fig. 2(c) and 2(d), respectively. The nonlinear IV is due to superconductive properties in NbSe_2 and from the dV/dI plot, we can estimate the critical current density, $J_{c, \text{NbSe}_2} = 0.7 \times 10^6 \text{ A/cm}^2$ for the multilayer NbSe_2 at 3K, consistent with the recent study³⁰. The room temperature IV measurement (Supplementary Fig. S3(b), (c)) is in agreement with the metallic properties of NbSe_2 . Raman spectroscopies, together with the presence of superconducting transition in NbSe_2 confirm good-quality materials are used in the heterostructure.

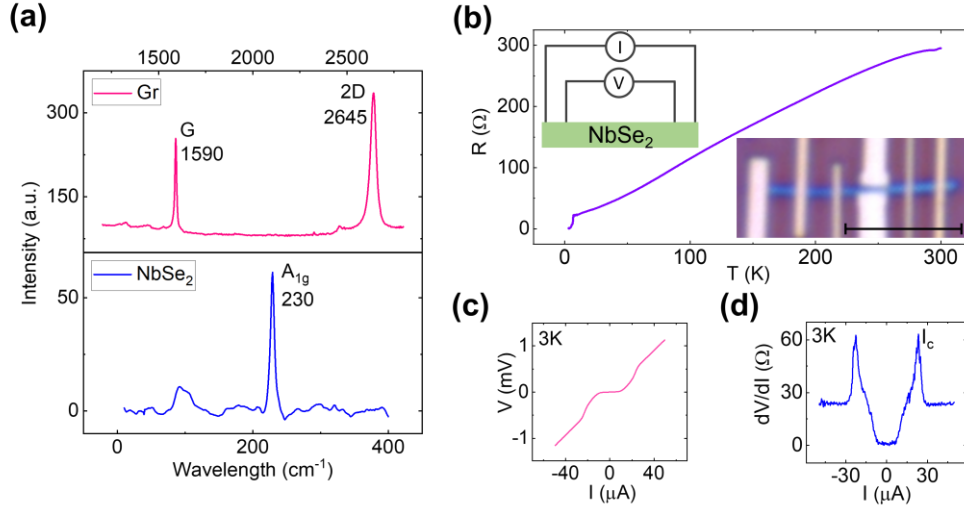


Figure 2. Materials characteristics of NbSe₂ and graphene. (a) Raman spectrum of single-layer CVD graphene (top panel) and exfoliated multilayer NbSe₂ (bottom panel) using 638 nm LASER. (b) Temperature dependence of the longitudinal resistance of multilayer NbSe₂ flake, where superconducting critical temperature (T_c) is around 6.8K is evident. Insets are the four-terminal measurement geometry (top) and device picture (bottom) along with scale bar of 5μm. (c), (d) The four-probe IV measurements and corresponding differential resistance as a function of the bias current in the multilayer NbSe₂ flake at 3K.

To investigate the charge-spin conversion (CSC) effect in NbSe₂, a charge current is applied in a multilayer NbSe₂ flake to create a non-equilibrium spin polarization on its surface. The spins are injected into the graphene channel and finally detected by an FM contact in NL measurement geometry. Figure 3(a) shows a schematic illustration of the measurement geometry used to detect the CSC effect in NbSe₂ along with the axis orientation and corresponding spin (s), charge current (I_c) and spin components (I_s). According to our measurement geometry in Fig. 3(a) by considering conventional SHE in NbSe₂, a charge current along x-axis can create an out-of-plane (z-axis) spin current, which renders spin polarization along y-axis. It is worth mentioning that the spin diffusion current in graphene spin channel is along x-axis in our measurement geometry with spin orientation towards y-axis after spin polarization is created in NbSe₂ and injected into graphene. In our experiments, we measure the NL voltage at the FM contact (left nearest contact to the NbSe₂ flake, shown in Fig. 1(b) by applying varying magnetic fields along with the B_y and B_z directions, respectively. A varying magnetic field along the magnetic easy axis (y-axis) switches the magnetization of the FM contact and renders a switching signal which detects non-equilibrium in-plane spin in graphene injected from the NbSe₂ flake. The spin-switch signal presented in Fig. 3(b) is measured with $I = 400 \mu A$ at $V_g = -40 V$. The amplitude of the signal estimated from the change in NL resistance corresponding to the opposite magnetization of the FM contact is about $\Delta R_{NL} = 1.77 \pm 0.6 m\Omega$.

Furthermore, an out-of-plane varying magnetic field (B_z) in our measurement geometry should render a Hanle spin precession signal, which unequivocally confirms the CSC process in the NbSe₂ and spin transport in the graphene spin channel. Figure 3(c) shows the manifested Hanle spin signal measured with $I = +420 \mu A$ and $V_g = -40 V$ while injecting spin from NbSe₂ into the graphene channel along with the fitting to equation S1. We have estimated the spin lifetime, $\tau_s = 23 \pm 6 ps$ and spin diffusion length, $\lambda_s = \sqrt{\tau_s D_s} = 0.65 \pm 0.05 \mu m$, considering the channel length $L = 2.4 \mu m$ (distance between the center of the NbSe₂ flake to the center of the detector's FM electrode). Moreover, the spin transport in the pristine CVD graphene is shown in Supplementary Fig. S4, where spin lifetime is estimated to be around 150 ps. To mention, we observe variations in spin lifetime in different CVD graphene channels in the range of 100 - 400 ps. In NbSe₂-graphene heterostructure, the lower τ_s in graphene spin channel after spin is injected from NbSe₂ can be attributed to the influence of long-range disorders, lattice deformation, and extrinsic interstitials in the graphene crystal that acts as spin-defect centers. These imperfections might be

introduced during processing CVD graphene, NbSe₂ transfer, and device fabrication processes. Additionally, spin absorption by NbSe₂ can also give rise to lower τ_s because of the transparent NbSe₂-graphene interface³¹. Interestingly, we observe only symmetric Hanle component, although the NbSe₂ flake in our device is at an angle to the graphene spin channel³². Furthermore, any contribution of the spin injection from the FM contact on NbSe₂ can be eliminated from the spin switch signal, because the influence of the FM magnetization would have manifested a typical spin valve signal (as presented in Fig. S4(a)) with double spin-valve switching while sweeping B_y . If any other substantial amount of spin component other than the y-axis were present, the Hanle measurement would have rendered an anti-symmetric component, which was not observed, presumably due to the small efficiency of SHE in other directions. Besides, Hanle measurement rules out any effect of stray fields from the detector FM contacts on the manifested CSC signals since the stray Hall effect would have rendered a linear Hall signal for an out-of-plane field (B_{\perp})³³.

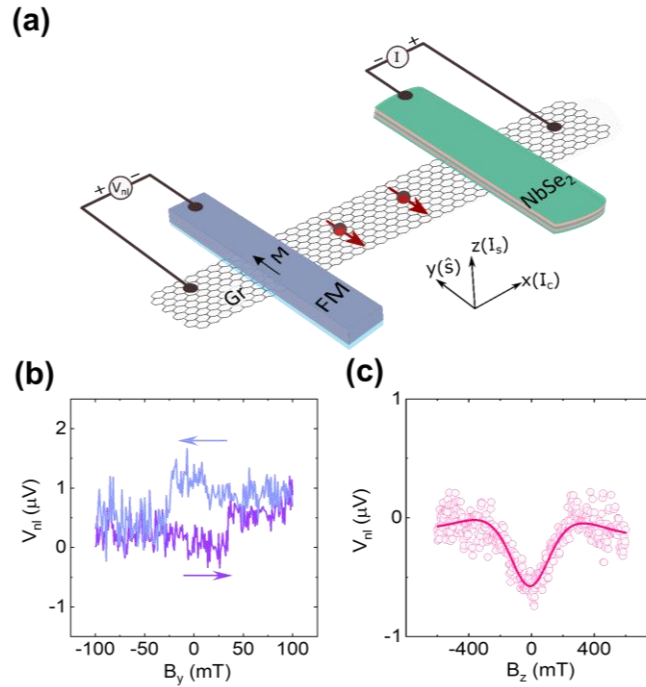


Figure 3. Charge-spin conversion in NbSe₂ at room temperature. (a) Schematic illustration of non-local measurement geometry to detect the charge-spin conversion effect in NbSe₂ by injecting spin current into the graphene spin channel. (b), (c) The spin-switch and Hanle spin precession measurements for spin injection from NbSe₂ with a B_y and B_z sweep, respectively. For spin-switch experiments, the up and down magnetic sweep directions are indicated by arrows. The Hanle data is fitted using equation S1. A linear background is subtracted from the data.

Next, we estimated the spin polarization of NbSe₂ is about $P_{\text{NbSe}_2} = 1 \pm 0.3\%$, assuming the spin polarization of FM contact on bare CVD graphene is $P_{\text{Co}} = 1.5 \pm 0.6\%$ (see Supplementary Note 1). This estimated spin-polarization accounts for the creation of spin polarized carriers in NbSe₂ along the y-axis and injected into the graphene channel through the vdW gap. The efficiency of the CSC process due to spin Hall effect in NbSe₂ can be characterized by the spin Hall angle ($\theta_{\text{SH}} \propto J_s/J_c$) and by using a simple model (as discussed in Supplementary Note 1), we found the θ_{SH} of NbSe₂ varies approximately from 0.68 ± 0.15 to 0.30 ± 0.06 by assuming the variation of spin diffusion length in NbSe₂, $\lambda_{\text{NbSe}_2} = 5 - 40$ nm (see Fig. S5(a) and Supplementary Note 2)^{10,12,34,35}. This estimation of θ_{SH} is consistent with the recently reported theoretical study, where θ_{SH} in NbSe₂ is predicted to be ≈ 0.5 by light irradiation³⁶. Note that the spin diffusion length (λ_{NbSe_2}) in NbSe₂ is not experimentally reported yet. We also analytically calculated the length scale, $\theta_{\text{SH}} \cdot \lambda_{\text{NbSe}_2}$ (nm), associated with the CSC in NbSe₂ (5-13nm) (Supplementary Fig. S5(b)), which is comparable to the recently reported length scale in layered TMDCs, e.g. 1.15nm in MoTe₂¹⁰. We

restrict our calculation by assuming $\lambda_{NbSe_2} = 5 - 40\text{nm}$ to be in the comparable spin diffusion length of other TMDCs, e.g., $WTe_2 = 8\text{nm}$ and to get reasonable θ_{SH}^{12} . Another plausible origin of the measured CSC signal could be the Rashba-Edelstein effect (REE) due to Rashba spin-split bands in $NbSe_2$ and its proximity effect in the $NbSe_2$ -graphene heterostructure region⁴. The characteristic efficiency parameter (α_{RE}) of the REE is calculated (Supplementary Note 2) to be $5.3 \pm 1.8\%$, which is consistent with the recent studies on 2D material heterostructures^{10,15,16,37,38}. It is to be noted that the models that are used to quantify the spin Hall angle and the Rashba-Edelstein efficiency parameter are not fully compatible with our measurement geometry. However, these approaches helped us to evaluate these parameters roughly, enabling us to compare with other materials on an order-of-magnitude scale.

We measured the temperature dependence of the CSC process in $NbSe_2$ to observe the evolution of spin polarization in $NbSe_2$ with temperature in Dev2 (Fig. S1(d)). Figure 4(a) shows the NL spin-switch signal arising due to the CSC effect in $NbSe_2$ and subsequent spin injection into graphene at 3K. The magnitude of the CSC signal is found to be $\Delta R_{nl} \approx 106 \pm 27\text{ m}\Omega$. Next, we measured the Hanle spin precession signal above and below T_c of $NbSe_2$ to validate the manifested spin-switch signal is a spin-related phenomenon. Figure 4(b) shows the Hanle signals along with the fitting to equation S1. The magnitude of the Hanle spin signal, ΔR_{nl} , and extracted spin lifetime τ_s at different temperatures (3K to 30K) have been shown in Fig. 4(c). Interestingly we found that the ΔR_{nl} increases drastically below T_c , but τ_s remains unchanged around 150 ps, below and above T_c , because spin transport parameters of graphene are known to be weakly dependent on temperature^{9,26}. We would like to note that, as τ_s remains unchanged, the larger ΔR_{nl} can be attributed to more efficient CSC conversion effect below T_c . However, the increase in CSC signal with decreasing temperature could also be due to the decrease of $NbSe_2$ resistivity (ρ_{NbSe_2}) and conductivity mismatch between $NbSe_2$ and graphene interface.

It is expected that quasiparticle mediated CSC process to be enhanced near the superconducting state of the corresponding material²¹. Although we manifested CSC signal in $NbSe_2$ at 3K (below $T_c \sim 7\text{K}$), but we would also like to mention that the $NbSe_2$ flake is not in the superconducting state in our CSC experiments as the applied bias current density ($\sim 4 \times 10^6\text{ A/cm}^2$) is much higher than the critical current density ($\sim 0.7 \times 10^6\text{ A/cm}^2$ at 3K). We optimized the bias current magnitude to maximize the CSC signal at different temperatures that surmount the noise level of the signals, which vary due to the conductivity mismatch of the $NbSe_2$ and detector FM contact with the graphene spin channel.

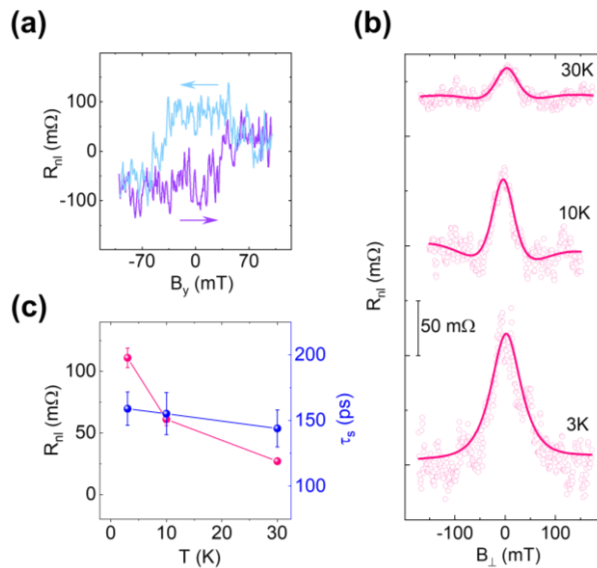


Figure 4. Temperature dependence of charge-spin conversion effect in $NbSe_2$. (a) Spin-switch signal for charge-spin conversion effect in $NbSe_2$ (Dev. 2) resulting in spin injection from $NbSe_2$ into graphene at 3K. (b) Hanle spin precession measurements along with the fitting to equation S1 (solid line). Measurements were performed in Dev 2 in a bias current range of 200 - 500 μA and at $V_g = -40\text{ V}$. A linear background is subtracted from the data and shifted

along the y-axis for clear visualization. **(c)** The magnitude of the Hanle spin signal ΔR_{nl} and extracted spin lifetime (τ_s) at different temperatures.

Here, we discuss possible origins that can give rise to the manifested CSC signal in NbSe₂. First and foremost, the NL spin-switch with varying in-plane B_y field and Hanle spin-precession measurements with changing out-of-plane field B_z confirm that the detected signals are due to the in-plane (y-axis) spin-polarized current that is created in NbSe₂ and injected into graphene. We can rule out the spin polarization generation via proximity-induced spin Hall effect (SHE) because this effect would have resulted in an out-of-plane spin polarization (s_z) in the heterostructure region, which is not observed³⁹. In addition, the proximity-induced Rashba-Edelstein (REE) effect in graphene from NbSe₂ should have rendered the opposite sign of the measured CSC signal for the p- and n-doped regimes^{14,16,37}. However, we observed CSC signal only in the p-doped regime of graphene with higher negative gate voltage, most likely due to the conductivity mismatch issues of the graphene channel with NbSe₂ and FM contacts in the n-doped regime of graphene^{17,19,40}. Hence, proximity-induced REE cannot be ruled out or nor be claimed to be the origin of the observed CSC signal with our measurements. Furthermore, the unconventional CSC process, which is recently reported in multilayer TMDCs (WTe₂ and MoTe₂), cannot also be disregarded in NbSe₂ since it is a layered material with structural inversion asymmetry in the crystal structure that can be further enhanced by the induced strain at the vdW heterostructure device geometry^{9,10}. Finally, considering the symmetry principle¹⁰, spin polarization direction (s) is set perpendicular to the applied charge current (I_c) and spin current (I_s) direction; the SHE and REE in NbSe₂ most likely merge or independently produce the observed CSC signal in NbSe₂. In future, the measurements of the CSC and inverse CSC in NbSe₂ with different device configurations and measurement geometries with different thicknesses and their correlation with properties in the superconducting state can be interesting. To be noted, during the review process of our manuscript, multidirectional spin-to-charge conversion in graphene/NbSe₂ van der Waals heterostructures has been reported⁴¹.

In summary, we demonstrated CSC in the normal metallic state of NbSe₂ up to room temperature. The engendered spin polarization can be injected into the graphene channel and detected in non-local measurement geometry via spin-switch and Hanle spin precession measurements. A higher CSC signal in NbSe₂ is detected at a lower temperature, however, in its non-superconducting state because of the requirement of a higher bias current than the critical current of NbSe₂ for observation of spin signals. Systematic measurements of the spin-switch and Hanle signals reveal that the possible origins of the in-plane spin polarization are predominantly due to the spin Hall effect or Rashba-Edelstein effect in NbSe₂ considering different symmetry-permitted CSC processes. Such features of current-induced spin polarization in NbSe₂ have promising potentials to be used as a non-magnetic spin source in future all-electric spintronic devices and spin-orbit technologies. Furthermore, the realization of CSC in superconducting quantum materials with high SOC strength can enhance the spintronic device performance by generating a larger spin current with a longer spin lifetime².

Supplementary Material

Details about the device fabrication, characterization, and estimation of charge-spin conversion.

Acknowledgments

The authors acknowledge financial support from EU Graphene Flagship (Core 3, No. 881603), Swedish Research Council VR project grants (No. 2021-04821), 2D TECH VINNOVA competence center (No. 2019-00068), FLAG-ERA project 2DSOTECH (VR No. 2021-05925), Graphene center, El Nano, and AoA Materials program at Chalmers University of Technology. We acknowledge the help of staff at Quantum Device Physics and Nanofabrication laboratory in our MC2 department at Chalmers. Devices were fabricated at the Nanofabrication Laboratory, Myfab, MC2, Chalmers.

References

- ¹ A.K. Geim and I. V. Grigorieva, *Nature* **499**, 419 (2013).
- ² J. Linder and J.W.A. Robinson, *Nat. Phys.* **11**, 307 (2015).
- ³ J. Sinova, S.O. Valenzuela, J. Wunderlich, C.H. Back, and T. Jungwirth, *Rev. Mod. Phys.* **87**, 1213 (2015).
- ⁴ A. Manchon, H.C. Koo, J. Nitta, S.M. Frolov, and R.A. Duine, *Nat. Mater.* **14**, 871 (2015).
- ⁵ D. Khokhriakov, B. Karpiak, A.M. Hoque, and S.P. Dash, *Carbon N. Y.* **161**, 892 (2020).
- ⁶ X. Lin, W. Yang, K.L. Wang, and W. Zhao, *Nat. Electron.* **2**, 274 (2019).
- ⁷ M.H.D. Guimarães, G.M. Stiehl, D. MacNeill, N.D. Reynolds, and D.C. Ralph, *Nano Lett.* **18**, 1311 (2018).
- ⁸ D. MacNeill, G.M. Stiehl, M.H.D. Guimaraes, R.A. Buhrman, J. Park, and D.C. Ralph, *Nat. Phys.* **13**, 300 (2017).
- ⁹ B. Zhao, B. Karpiak, D. Khokhriakov, A. Johansson, A.M. Hoque, X. Xu, Y. Jiang, I. Mertig, and S.P. Dash, *Adv. Mater.* **32**, 2000818 (2020).
- ¹⁰ C.K. Safeer, N. Ontoso, J. Ingla-Aynés, F. Herling, V.T. Pham, A. Kurzmann, K. Ensslin, A. Chuvilin, I. Robredo, M.G. Vergniory, F. De Juan, L.E. Hueso, M.R. Calvo, and F. Casanova, *Nano Lett.* **19**, 8758 (2019).
- ¹¹ T.S. Ghiasi, A.A. Kaverzin, P.J. Blah, and B.J. Van Wees, *Nano Lett.* **19**, 5959 (2019).
- ¹² B. Zhao, D. Khokhriakov, Y. Zhang, H. Fu, B. Karpiak, A.M. Hoque, X. Xu, Y. Jiang, B. Yan, and S.P. Dash, *Phys. Rev. Res.* **2**, 013286 (2020).
- ¹³ J.F. Sierra, J. Fabian, R.K. Kawakami, S. Roche, and S.O. Valenzuela, *Nat. Nanotechnol.* **16**, 856 (2021).
- ¹⁴ L.A. Benítez, W. Saverio Torres, J.F. Sierra, M. Timmermans, J.H. Garcia, S. Roche, M. V. Costache, and S.O. Valenzuela, *Nat. Mater.* **19**, 170 (2020).
- ¹⁵ A.M. Hoque, D. Khokhriakov, K. Zollner, B. Zhao, B. Karpiak, J. Fabian, and S.P. Dash, *Commun. Phys.* **4**, 1 (2021).
- ¹⁶ D. Khokhriakov, A.M. Hoque, B. Karpiak, and S.P. Dash, *Nat. Commun.* **11**, 1 (2020).
- ¹⁷ D. Khokhriakov, A.W. Cummings, K. Song, M. Vila, B. Karpiak, A. Dankert, S. Roche, and S.P. Dash, *Sci. Adv.* **4**, eaat9349 (2018).
- ¹⁸ Z. Kovács-Krausz, A.M. Hoque, P. Makk, B. Szentpéteri, M. Kocsis, B. Fülöp, M.V. Yakushev, T.V. Kuznetsova, O.E. Tereshchenko, K.A. Kokh, I.E. Lukács, T. Taniguchi, K. Watanabe, S.P. Dash, and S. Csonka, *Nano Lett.* **20**, 4782 (2020).
- ¹⁹ A.M. Hoque, D. Khokhriakov, B. Karpiak, and S.P. Dash, *Phys. Rev. Res.* **2**, 033204 (2020).
- ²⁰ T. Dvir, F. Massee, L. Attias, M. Khodas, M. Aprili, C.H.L. Quay, and H. Steinberg, *Nat. Commun.* **9**, 1 (2018).
- ²¹ T. Wakamura, H. Akaike, Y. Omori, Y. Niimi, S. Takahashi, A. Fujimaki, S. Maekawa, and Y. Otani, *Nat. Mater.* **14**, 675 (2015).
- ²² X. Xi, Z. Wang, W. Zhao, J.H. Park, K.T. Law, H. Berger, L. Forró, J. Shan, and K.F. Mak, *Nat. Phys.* **12**, 139 (2016).
- ²³ L. Bawden, S.P. Cooil, F. Mazzola, J.M. Riley, L.J. Collins-Mcintyre, V. Sunko, K.W.B. Hunvik, M. Leandersson, C.M. Polley, T. Balasubramanian, T.K. Kim, M. Hoesch, J.W. Wells, G. Balakrishnan, M.S. Bahramy, and P.D.C. King, *Nat. Commun.* **7**, 1 (2016).
- ²⁴ S. Manipatruni, D.E. Nikonov, C.C. Lin, T.A. Gosavi, H. Liu, B. Prasad, Y.L. Huang, E. Bonturim, R. Ramesh, and I.A. Young, *Nature* **565**, 35 (2019).
- ²⁵ D. Khokhriakov, B. Karpiak, A.M. Hoque, and S.P. Dash, *Carbon N. Y.* **161**, 892 (2020).
- ²⁶ M.V. Kamalakar, C. Groenvelde, A. Dankert, and S.P. Dash, *Nat. Commun.* **6**, 6766 (2015).
- ²⁷ Z. Wang, D.K. Ki, J.Y. Khoo, D. Mauro, H. Berger, L.S. Levitov, and A.F. Morpurgo, *Phys. Rev. X* **6**, 041020 (2016).
- ²⁸ L.M. Malard, M.A. Pimenta, G. Dresselhaus, and M.S. Dresselhaus, *Phys. Rep.* **473**, 51 (2009).
- ²⁹ Y. Wu, M. An, R. Xiong, J. Shi, and Q.M. Zhang, *J. Phys. D: Appl. Phys.* **41**, 175408 (2008).

- ³⁰ X. He, Y. Wen, C. Zhang, Z. Lai, E.M. Chudnovsky, and X. Zhang, *Nanoscale* **12**, 12076 (2020).
- ³¹ A. Dankert and S.P. Dash, *Nat. Commun.* **8**, 16093 (2017).
- ³² B. Zhao, A.M. Hoque, D. Khokhriakov, B. Karpiak, and S.P. Dash, *Appl. Phys. Lett.* **117**, 242401 (2020).
- ³³ B. Karpiak, A. Dankert, A.W. Cummings, S.R. Power, S. Roche, and S.P. Dash, *2D Mater.* **5**, 014001 (2017).
- ³⁴ W. Yan, E. Sagasta, M. Ribeiro, Y. Niimi, L.E. Hueso, and F. Casanova, *Nat. Commun.* **8**, 1 (2017).
- ³⁵ W. Saverio Torres, J.F. Sierra, L.A. Benitez, F. Bonell, M. V Costache, and S.O. Valenzuela, *2D Mater.* **4**, 041008 (2017).
- ³⁶ R. Habara and K. Wakabayashi, *Phys. Rev. B* **103**, L161410 (2021).
- ³⁷ L. Li, J. Zhang, G. Myeong, W. Shin, H. Lim, B. Kim, S. Kim, T. Jin, S. Cavill, B.S. Kim, C. Kim, J. Lischner, A. Ferreira, and S. Cho, *ACS Nano* **14**, 5251 (2020).
- ³⁸ T.S. Ghiasi, A.A. Kaverzin, P.J. Blah, and B.J. van Wees, *Nano Lett.* **19**, 5959 (2019).
- ³⁹ C.K. Safeer, J. Ingla-Aynés, F. Herling, J.H. Garcia, M. Vila, N. Ontoso, M.R. Calvo, S. Roche, L.E. Hueso, and F. Casanova, *Nano Lett.* **19**, 1074 (2019).
- ⁴⁰ A. Fert and H. Jaffrès, *Phys. Rev. B - Condens. Matter Phys.* **64**, 184420 (2001).
- ⁴¹ J. Ingla-Aynés, I. Groen, F. Herling, N. Ontoso, C.K. Safeer, F. de Juan, L.E. Hueso, M. Gobbi, and F. Casanova, *2D Mater.* **9**, 045001 (2022).

Paper IV

All-electrical creation and control of spin-galvanic signal in graphene and molybdenum ditelluride heterostructures at room temperature

Anamul Md. Hoque¹ , Dmitrii Khokhriakov¹ , Klaus Zollner², Bing Zhao¹, Bogdan Karpiak¹, Jaroslav Fabian²  & Saroj P. Dash^{1,3} ✉

The ability to engineer new states of matter and control their spintronic properties by electric fields is at the heart of future information technology. Here, we report a gate-tunable spin-galvanic effect in van der Waals heterostructures of graphene with a semimetal of molybdenum ditelluride at room temperature due to an efficient spin-charge conversion process. Measurements in different device geometries with control over the spin orientations exhibit spin-switch and Hanle spin precession behavior, confirming the spin origin of the signal. The control experiments with the pristine graphene channels do not show any such signals. We explain the experimental spin-galvanic signals by theoretical calculations considering the spin-orbit induced spin-splitting in the bands of the graphene in the heterostructure. The calculations also reveal an unusual spin texture in graphene heterostructure with an anisotropic out-of-plane and in-plane spin polarization. These findings open opportunities to utilize graphene-based heterostructures for gate-controlled spintronic devices.

¹Department of Microtechnology and Nanoscience, Chalmers University of Technology, Göteborg, Sweden. ²Institute for Theoretical Physics, University of Regensburg, Regensburg, Germany. ³Graphene center, Chalmers University of Technology, Göteborg, Sweden. ✉email: saroj.dash@chalmers.se

The spin-orbit interaction (SOI) is the fundamental physical phenomenon and pivotal for state-of-the-art spintronics and quantum technologies^{1–4}. Specifically, the SOI is the origin of fascinating effects like current-induced transverse spin polarization in non-magnetic materials, known as spin Hall effect (SHE) in bulk, Rashba-Edelstein effect (REE) at the heterostructure interfaces, and spin-momentum locking (SML) in topological materials⁵. Recent experiments utilizing the charge-to-spin conversion (CSC) and its inverse effects have been performed on metallic multilayers⁶, semiconductors², oxide heterostructures^{7,8}, two-dimensional (2D) materials^{9,10}, van der Waals (vdW) heterostructures with graphene (Gr)^{11–17}, and the topological insulators^{18,19}. Such SOI-induced charge-spin conversion features are promising for all-electrical spin-orbit torque-based technology^{1–4}.

Recently discovered topological Weyl semimetals (WSMs) were predicted to provide a much larger CSC efficiency, giant REE²⁰ and SHE²¹, due to their non-trivial band structure in both bulk and surface states. The type-II WSMs, such as tungsten ditelluride (WTe₂) and molybdenum ditelluride (MoTe₂) possess strong SOI and band structure with a large Berry curvature and spin-polarized bulk and surface states up to room temperature^{22,23}. Furthermore, the CSC in WSMs is of great interest in its own^{9,15,24–28}, but their true potential lies in forming vdW heterostructures with graphene. It has been predicted that the addition of a graphene layer on topological materials can even enhance the REE by orders of magnitude^{29–32}, which can be due to different proximity-induced interactions in the heterostructures, such as Kane-Mele SOI, spin-valley coupling, and Bychkov-Rashba interaction^{30,33}. Recently, charge-spin conversion effects are also reported in Gr-TMD heterostructure^{34,35} and also in low-symmetry semimetal WTe₂^{15,26}, with both conventional and unconventional nature. Moreover, an interesting energy-dependent spin texture and giant CSC efficiency are also expected to be present in semimetal-graphene heterostructures. The much-needed experimental proof of such gate tunable charge-spin conversion effect in graphene-semimetal vdW heterostructure would considerably boost the chance of its utilization in emerging spintronic technologies.

Here, we report the creation of proximity-induced spin-galvanic effect (SGE) in vdW heterostructures of semimetal MoTe₂ and graphene. This article demonstrates a proximity-driven SOI mechanism, the Rashba-Edelstein effect (REE), in the vdW heterostructure-based spintronic device to achieve spin-to-charge conversion (SCC) with high efficiency. The magnitude and the sign of the spin-galvanic signal can be controlled by applying gate voltage near the charge neutrality point, which is understood based on our density functional theory (DFT) calculations showing SOI-induced spin-split electronic band structure of the graphene in the heterostructure. We also performed measurements in geometries where the injector ferromagnet is placed perpendicularly to the Gr-MoTe₂ heterostructures, showing the REE-induced spin-switch and Hanle spin precession signals. These results highlight the unique possibility of achieving efficient gate tunability of the SGE in vdW heterostructure.

Results

We have chosen semimetal MoTe₂ as the high SOI material, which has gained growing interest regarding its topological properties in the T_d phase. The MoTe₂ is verified as the first type-II WSM, where tilted Weyl cones exist in pairs as the contact point between electron and hole pockets, which are connected by a spin-polarized Fermi arc surface states^{23,36,37}. Our basic measurements of temperature dependence (Supplementary Fig. S1) together with the Raman spectrum (Supplementary Fig. S2) of MoTe₂ show the metallic 1 T'

phase of the material at room temperature³⁸. Because of the ability to create designer heterostructure of various layered materials^{39,40}, we prepare the heterostructure of multilayer MoTe₂ of thickness 43 nm (Supplementary Fig. S3) and monolayer chemical vapor deposited (CVD) graphene^{41,42} by dry transfer method inside a glovebox.

The hybrid spintronic devices were nanofabricated in Hall-bar-shaped geometry with multiple contacts to detect the SGE. Measurements were performed in various device geometries such as magnetization rotation, spin switch, and Hanle spin precession methods. First, we present results from magnetization rotation experiments in a device where the ferromagnetic contact is placed parallel to the graphene-MoTe₂ heterostructures, as shown in the schematics and the device picture (Fig. 1a and b). The device consists of Hall-bar shaped Gr-MoTe₂ heterostructure region for spin-to-charge conversion, graphene channel for spin transport, Co/TiO₂ ferromagnetic contacts (FM) on graphene for spin injection (contact 1 in Fig. 1b), and Ti/Au contacts (contact 3 & 4 in Fig. 1b) on graphene for detection of the voltage signal and also as reference electrodes (contact 2 in Fig. 1b), and Si/SiO₂ substrate acts as a global back gate. To be noted, the contacts (3 & 4) are made explicitly on graphene to detect the proximity-induced effects. This is in contrast to the devices used in Zhao, B. et al.^{12,15,26}, where the contacts are made on WTe₂ flake to measure spin Hall effects (SHE) in WTe₂, and no proximity effect could be detected. The contact resistances of FMs on graphene are about 5–8 kΩ and the channel mobility of Gr-MoTe₂ heterostructure is estimated to be about 2200 cm²V⁻¹s⁻¹ at room temperature.

The basic spin transport measurements were carried out at room temperature using FM injector and detector tunnel contacts in the pristine graphene ($L_{\text{ch}} = 5.7 \mu\text{m}$) and Gr-MoTe₂ heterostructure regions ($L_{\text{ch}} = 6.7 \mu\text{m}$), as depicted in Supplementary Fig. S4. The spin transport in pristine graphene shows 200 mΩ of spin-valve signal and corresponding Hanle measurements provide an estimated spin lifetime of ~ 185 ps; on the other hand, no spin transport signal could be observed through the Gr-MoTe₂ heterostructure region. This disappearance of the spin signal across the heterostructure can be either due to spin absorption by MoTe₂ or the creation of a strong SOI and band structure hybridization in the Gr-MoTe₂ heterostructure. Although the spin absorption effect by MoTe₂ cannot be ruled out, the measured gate tunable spin galvanic signal presented below does not indicate the contribution of charge-spin conversion from only MoTe₂, but to be originating from the proximitized graphene. As predicted for graphene-transition metal dichalcogenides (TMD) heterostructure³³, graphene in proximity to MoTe₂ can also acquire strong SOI and a spin texture with a Rashba spin-split in conduction and valence bands with the same spin chirality (Fig. 1c), which can be probed by tuning the Fermi level (E_F) using a gate voltage.

Proximity-induced spin-galvanic effect. The charge-spin conversion due to the proximity-induced SOI in Gr-MoTe₂ heterostructure can be measured by employing a direct REE or its inverse phenomenon (IREE) based methods⁵. The charge current-induced REE can be detected by a FM contact due to charge-to-spin conversion. In contrast, for the IREE measurements, a spin current is injected from a FM into a heterostructure region and, consequently, a voltage signal is measured due to a spin-to-charge conversion. Figure 1a shows the schematics of the NL measurement geometry used for the detection of SGE in the IREE measurement geometry. In this hybrid spintronic device, the spin current is injected from a FM contact into the graphene channel and diffused into the Gr-MoTe₂ heterostructure, and

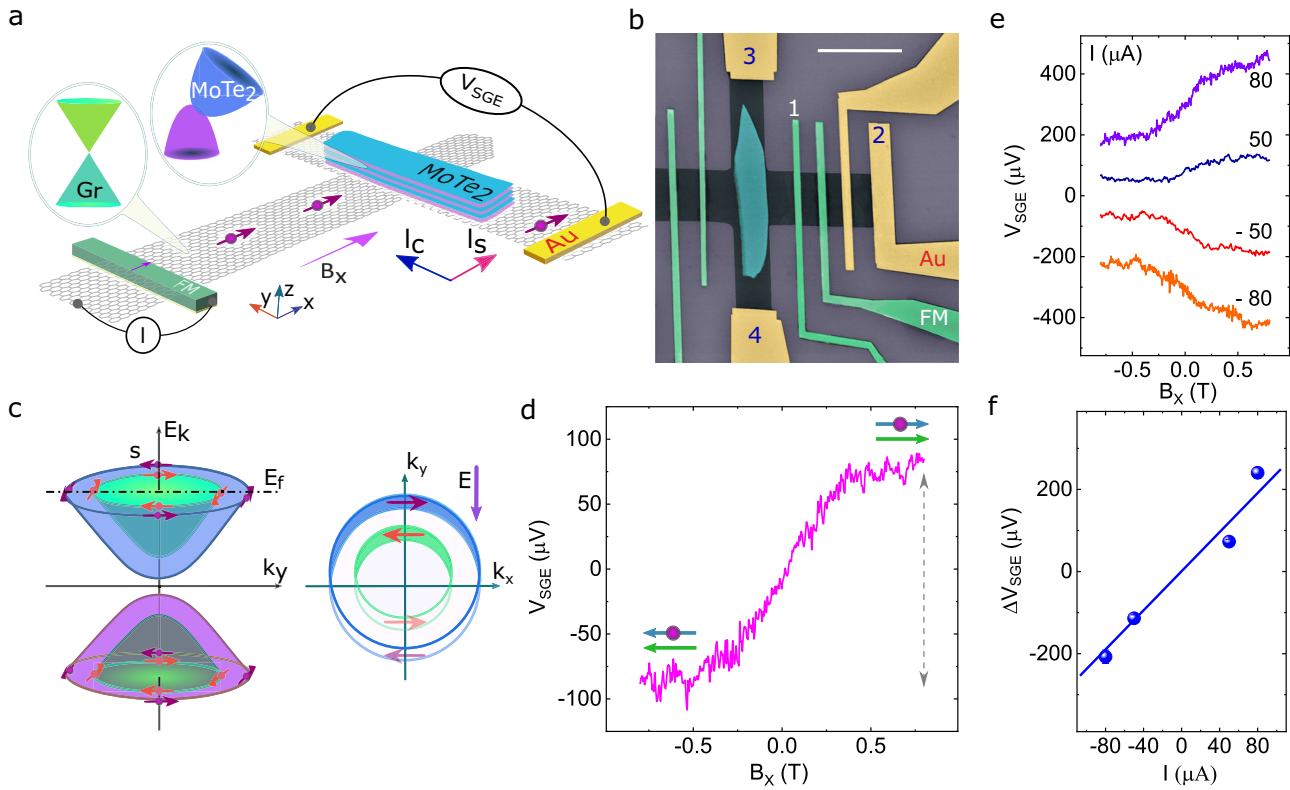


Fig. 1 Proximity-induced spin-galvanic effect in graphene-MoTe₂ van der Waals heterostructure at room temperature. **a, b** The spintronic device schematics with the measurement scheme and colored scanning electron microscopic (SEM) image consisting of graphene (gray)/MoTe₂ (blue) heterostructure on Si/SiO₂ substrate, ferromagnetic (FM) and non-magnetic (Ti/Au) contacts on graphene. The scale bar in the SEM image is 6 μm. **c** A schematic band diagram of modified graphene in a heterostructure with MoTe₂, showing Rashba spin-split conduction and valence bands in accordance with the energy in momentum space (E_k), where Fermi energy (E_F) is in the conduction band. Application of an electric field with such spin texture is expected to create a spin accumulation due to the Rashba-Edelstein effect (REE), and inversely, a spin accumulation can be converted to a charge voltage via inverse Rashba-Edelstein effect (IREE). **d** Measured spin-galvanic effect as a non-local voltage (V_{SGE}) signal due to IREE by injecting a spin current (I_s) from a FM into the graphene-MoTe₂ heterostructure region. A change in V_{SGE} is measured by sweeping a magnetic field along the x-axis (B_x) with an application of $I = 80 \mu A$, the gate voltage $V_g = -10V$ in Dev 1 at room temperature. The green and blue arrows denote the FM magnetization and direction of the diffused spin into the graphene-MoTe₂ heterostructure, respectively. **e, f** Measured bias dependence of V_{SGE} signal and its magnitude ΔV_{SGE} as a function of bias current in Dev 1. A linear background is subtracted from the data and shifted in the y-axis for clarity. The line is the linear fit to the data in **f**. The error bars are calculated from the noise level of the manifested signals and not clearly visible because error bars are smaller than the data points.

finally detected as a voltage signal (V_{SGE}) across the Hall-bar structure with non-magnetic Ti/Au contacts on graphene. Due to the IREE in the Gr-MoTe₂ heterostructure region with a possibility of spin-split bands (Fig. 1c), the diffused spin-polarized carriers create a non-equilibrium spin density across the heterostructure with a net momentum along the $\pm y$ -axis depending on the spin direction ($\pm s$). This is detected as a voltage signal, V_{SGE} ($I_c \propto z \times n_s$); here, I_c , z and n_s are the induced charge current, out-of-plane direction non-equilibrium spin density accumulated via spin current I_s , respectively. The direction of the injected spin (in $\pm x$ -direction) and hence the V_{SGE} is controlled by sweeping a magnetic field in the x-direction ($\pm B_x$), which induces spin precession together with rotation and saturates the magnetization of the injector FM (Fig. 1d). The spin precession due to the applied x-field ($\pm B_x$) will be in the y - z plane, and the projection of spin polarization along the x -axis will be the same during the spin precession. Nevertheless, the accumulated non-equilibrium spin density (n_s) depends on the spin direction towards the x -axis ($\pm x$) in our measurement system of IREE. Due to the unchanged spin projection along the x -axis during the spin precession, together with changing magnetization of the injector FM contact, the resulting IREE signal increases with B_x until the saturation of FM magnetization (0.4 T) without any contribution of spin precession. Accordingly, the measured V_{SGE} increases in the low field

range and saturates at magnetic fields above $B \approx \pm 0.4$ T (see Supplementary Fig. S5, where a x-Hall measurement shows the saturation field of the FM contact). A giant spin-galvanic signal has been obtained at room temperature with an amplitude up to $\Delta R_{SGE} = \Delta V_{SGE}/I \sim 4.96 \Omega$ (with $I = -80 \mu A$ at $V_g = 40$ V) and lower bound of the efficiency (α_{RE}) of IREE is estimated to be 7.6% by using the Eq. (1)^{17,34}.

$$\alpha_{RE} = \frac{\Delta R_{SGE}}{2\rho_G} \frac{w_{MoTe_2}}{P\lambda_G \left(e^{-\frac{L}{\lambda_G}} - e^{-\frac{L+w_{MoTe_2}}{\lambda_G}} \right)} \quad (1)$$

Here, ΔR_{SGE} , P , w_{MoTe_2} (2.3 μm), λ_G (2.65 μm), ρ_G (1.6 kΩ), and L (3.37 μm) are the signal amplitude, the spin polarization of Co/TiO₂ contact (considering 10%, see Supplementary Fig. S6), the width of the MoTe₂ flake, spin diffusion length, channel resistivity, and channel length, respectively. Here, we consider the spin diffusion length of the pristine graphene region since no spin precession signal is observed in the Gr-MoTe₂ heterostructure region. However, we would like to mention that the estimated α_{RE} is the lower limit as the spin diffusion length in Gr-MoTe₂ heterostructure is smaller due to the enhanced SOI. This magnitude of the observed R_{SGE} and α_{RE} is found to be larger than the previous results on 2D materials heterostructures^{16,17}.

We can also electrically tune the magnitude and sign of the SGE signal with the spin injection bias current I . In our measurement configuration, changing the bias current on the FM spin injector contact changes the direction of accumulated spin polarization in the graphene channel. Hence, with a change in the non-equilibrium spin density, the direction of the measured V_{SGE} that is induced by IREE also changes (Fig. 1e). To be noted, the bias current $+I$ corresponds to spin injection from the FM into the graphene channel, and $-I$ correspond to the spin extraction condition. The bias dependence of measured V_{SGE} signal amplitude in the range of $I = -80 \mu\text{A}$ to $80 \mu\text{A}$ has been depicted in Fig. 1f, along with a linear fit to the data points. We also observed inverse SGE (ISGE), following the reciprocity relation, where charge current is applied with Ti/Au contacts across Gr-MoTe₂ heterostructure Hall-cross and non-local voltage (V_{nl}) is measured in graphene channel with FM detector contact (Supplementary Fig. S7).

Angle dependence of the spin-galvanic signal. Next, the angular dependence of the measured NL voltage signal was performed at room temperature. The measurements were manifested by varying the angle (θ) of the applied in-plane (x - y plane) magnetic field (B) direction with respect to the x -axis, illustrated by the schematics and measurement geometry in Fig. 2a. The measured V_{SGE} changes with the effective component of B in the x -direction as depicted in Fig. 2b in Dev 2 ($L_{\text{ch}} = 5 \mu\text{m}$) with an injection bias current of $I = 60 \mu\text{A}$. No spin-galvanic signal is detected when the

B is aligned with the y -axis ($\theta = 90^\circ$) because at this stage, the injected spins remain parallel to the B field and no spin precession is taking place in the measurement geometry. The sign of the V_{SGE} reverses gradually in between $\theta = 0^\circ$ to 180° (π) due to changing the FM magnetization direction along ($\pm x$ -axis) and associated reversal of the injected spin orientation.

In contrast to the Gr-MoTe₂ heterostructure, no such features have been observed in control samples of only graphene Hall-cross, with measurement geometry shown in the inset of Fig. 2c. Figure 2c shows the null non-local signal (V_{nl}) measured in pristine graphene Hall-cross at room temperature with $I = 100 \mu\text{A}$, $V_g = -50 \text{ V}$ for different measurement angles. The magnitude of the measured SGE signals (ΔV_{SGE}) in the Gr-MoTe₂ heterostructure and non-local signal in the only graphene (ΔV_{nl}) as a function of the measurement angle θ are shown in Fig. 2d, following the expected behavior, where the induced voltage V_{SGE} ($I_c \propto z \times n_s(I_s)$)^{15,43}. The angle dependence data of the ΔV_{SGE} is found to follow the $\cos(\theta)$ function, which establishes the relation between the direction of the injected spin-current and the induced SGE in the Gr-MoTe₂ heterostructure. On the other hand, the ΔV_{nl} in only graphene Hall-cross renders the null signal with the applied magnetic field direction, which rules out the effect of the stray field from the FM electrodes to be the origin of the manifested SGE signal in the Gr-MoTe₂ heterostructure.

Gate-controlled switching of spin-galvanic signal. In order to demonstrate the electric field-controlled switching of the SGE, we

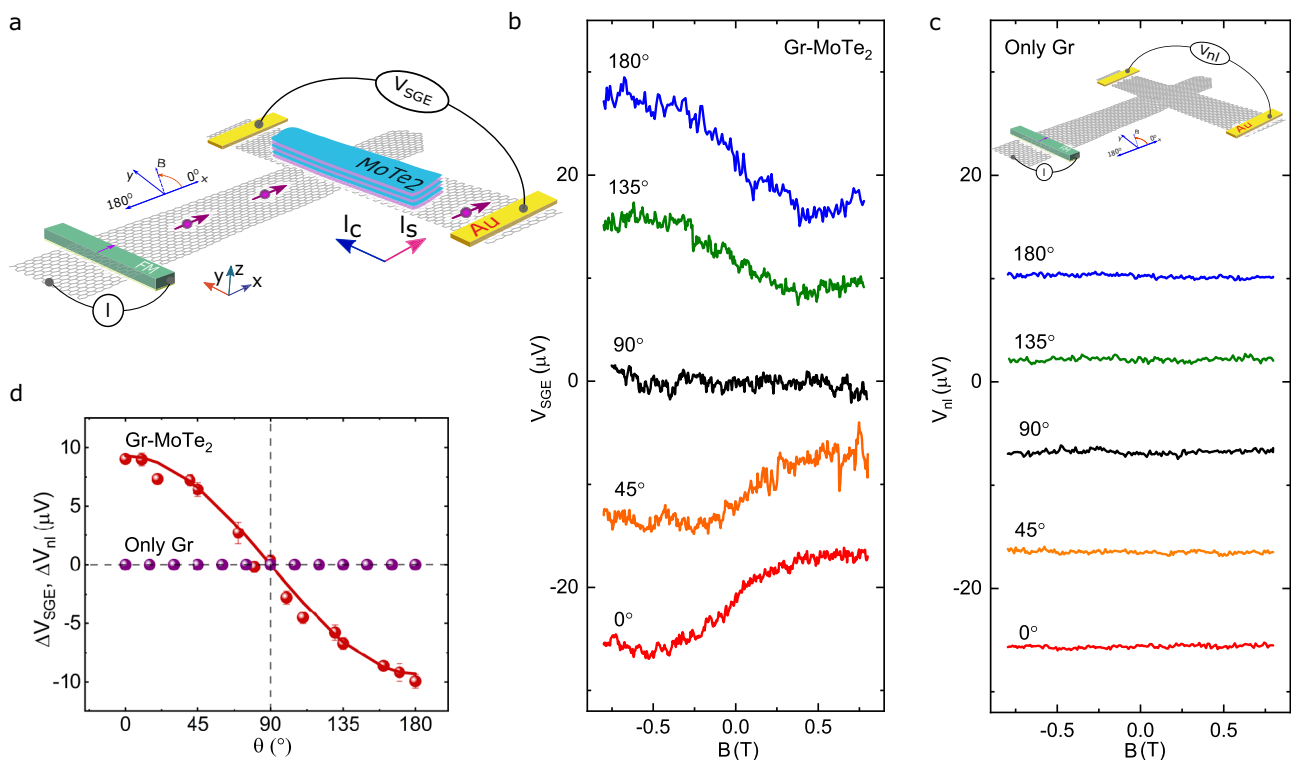


Fig. 2 Angle dependence of spin-galvanic signal in the graphene-MoTe₂ heterostructure. **a** A schematic illustration of the spin-galvanic signal measurement geometry with directions of an applied magnetic field (B), the injector ferromagnet magnetization (M), the spin current (I_s), and external magnetic field angle (θ) in x - y plane. **b** The manifested spin-galvanic signal (V_{SGE}) as a function of the magnetic field (B) sweep for various measurement angle (θ) orientations in the x - y plane, with an application of $I = 60 \mu\text{A}$ in Dev 2 at room temperature. A linear background is subtracted from the data and shifted in the y -axis for clarity (see Supplementary Fig. S8). **c** As a control experiment, the non-local signal as a function of magnetic field sweep (B) for various in-plane (x - y plane) measurement angle (θ) orientations in only graphene Hall cross at room temperature with $I = 100 \mu\text{A}$ and $V_g = -50 \text{ V}$ along with the measurement geometry in the inset. The signals are shifted in the y -axis for clarity. **d** The magnitude of spin-galvanic signals (ΔV_{SGE}) in graphene-MoTe₂ heterostructure and non-local signal (V_{nl}) in the only graphene as a function of the applied magnetic field angle (θ). The solid line is the $\cos(\theta)$ function. The error bars are calculated from the noise level of the manifested signals and not clearly visible because error bars are smaller than the data points.

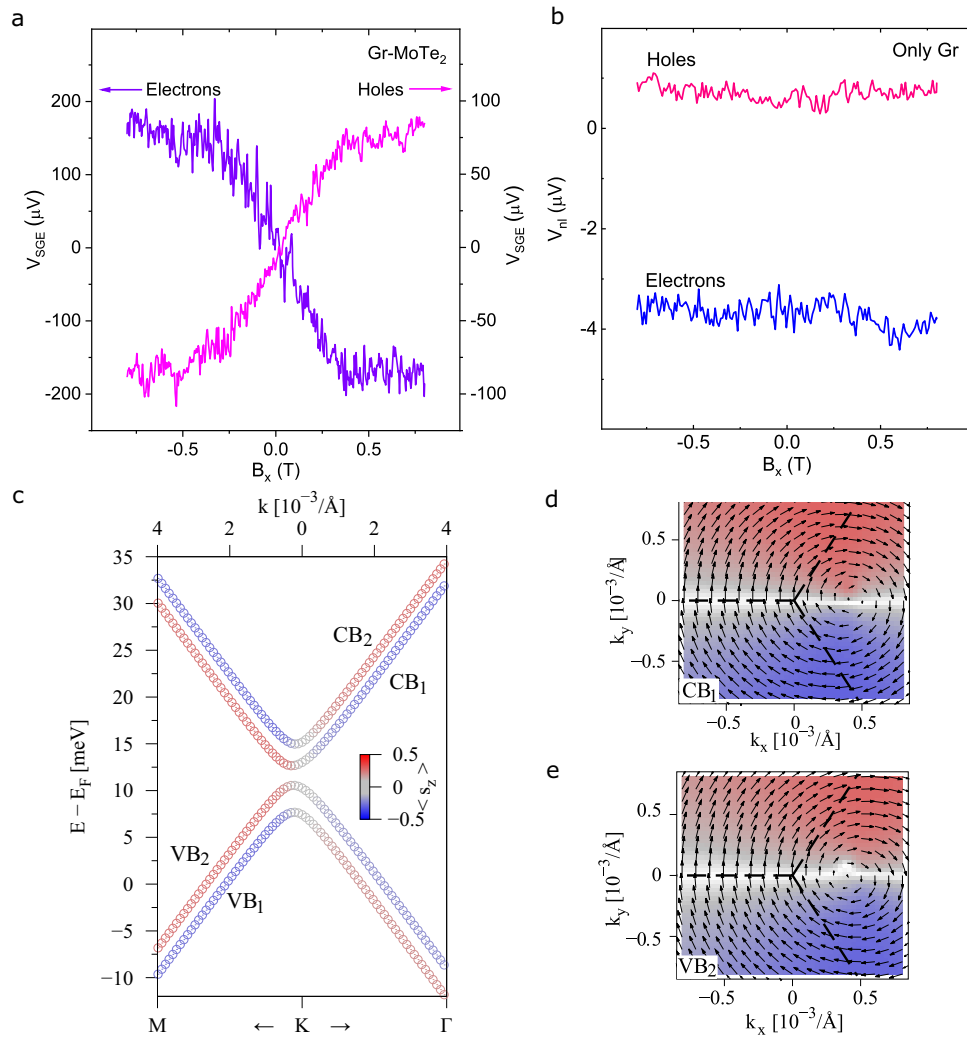


Fig. 3 Gate-controlled switching of spin-galvanic signal in graphene-MoTe₂ heterostructure at room temperature. **a** Measured spin-galvanic signal (V_{SGE}) by sweeping a magnetic field along the x -axis (B_x) at room temperature in graphene-MoTe₂ heterostructure (Dev 1) with $I = 80 \mu A$ and applied gate voltages of $V_g = 20$ V and -10 V to position the Fermi level (E_F) in the electron and hole doping regimes, respectively. A linear background is subtracted from the data (see Supplementary Fig. S9). **b** Measured non-local signals (V_{nl}) in pristine graphene Hall cross by sweeping a magnetic field in the x -direction (B_x) for electron- and hole-doped regions with $I = 100 \mu A$, $V_g = 70$ V and -50 V, respectively. **c** The low energy band structure of graphene in proximitized to MoTe₂ from density functional theory calculations. The color is the expected value of the spins polarized along with the z -direction (s_z). **d, e** Density functional theory calculations for similar clockwise spin texture in the outermost conduction (e_1^{CB}) and valence band (e_2^{VB}) in graphene-MoTe₂ heterostructure.

measured SGE for the electron (n) and hole (p) doped regimes of the Gr-MoTe₂ heterostructure. The applied gate voltage modulates the Fermi level (E_F) position in the Gr-MoTe₂ hybrid bands for probing the spin-split REE-induced non-equilibrium spin accumulation (n_s) with different charge carrier types. Figure 3a shows the opposite signs of V_{SGE} signals for two different doping regimes, electrons (violet) at $V_g = 20$ V and holes (magenta) at $V_g = -10$ V at room temperature. Control experiments with gate dependence of standard Hanle spin precession signals (Supplementary Fig. S6) confirm that the sign change in SGE is not due to a change in the sign of spin polarization of the injector FM contacts. The proximity-induced REE effect in graphene is predicted to be dependent on the conduction charge carrier type, i.e., electrons and holes, since spin polarity in Rashba contour remains unchanged in valence and conduction bands, unlike the spin-momentum locking in topological insulators^{33,44}. The observed IREE produces a charge current ($I_c \propto z \times n_s$) perpendicular to the injected spin densities (n_s), which changes its

direction because of a unidirectional accumulation of electron and holes ($-q$ for electrons and $+q$ for holes) in the heterostructure with specific spin orientations. So, it can be concluded that the measured SGE signal and the sign change of the V_{SGE} is inherently due to induced IREE in Gr-MoTe₂ heterostructure. Similar gate-dependent sign change behavior of SGE is also observed in Dev 2 (see Supplementary Fig. S10). To compare the induced SGE in Gr-MoTe₂ with pristine graphene, NL signals (V_{nl}) are measured for electron- and hole-doped regions, depicted in Fig. 3b, with $I = 100 \mu A$ at $V_g = 70$ V and -50 V, respectively. The resultant signals can be considered as null noise-signals because of the absence of REE in pristine graphene.

To understand our experimental findings of SGE, we have performed a DFT calculation of the electronic band structure of Gr-MoTe₂ heterostructure to identify the Rashba spin texture and to verify the enhanced SOI strength in the heterostructure (Supplementary Note 1 for details)^{45,46}. A side and top view of the geometry used for band structure calculations are shown in

Supplementary Fig. S13. The low energy band structure of the graphene and 1 T'-MoTe₂ heterostructure is presented in Fig. 3c and we found four states ($\epsilon_{1/2}^{VB/CB}$) of Rashba spin-splitting with SOI strength of around 2.5 meV (see Supplementary Fig. S15). We also noticed that the bands display a clear signature of Rashba SOI, as the spin in the outermost conduction (ϵ_1^{CB}) and valence band (ϵ_2^{VB}) is aligned clockwise (Fig. 3d, e), while the corresponding spin-orbit split partner bands (for example, ϵ_1^{CB} and ϵ_2^{CB}) show a counter-clockwise sense of spin-alignment (Supplementary Fig. S16). The calculations have also revealed an unusual proximity-induced spin texture in graphene: the out-of-plane spin polarization is highly anisotropic around K, and the in-plane spin polarization (Rashba) vortex is shifted from K'. Such a spin texture in the graphene valence and conduction band in the heterostructure can explain our measured SGE signal, where the sign of the SGE signal is efficiently controlled by the application of a gate voltage.

Interestingly, the gate electric field is changing simultaneously the spin properties (SOI and Rashba effect) and carrier concentration and type in the Gr-MoTe₂ heterostructure. To estimate the overall effect of SOI, we have theoretically calculated the splitting of low energy band due to SOI (ΔE_{so}) in Gr-MoTe₂ heterostructure at various electric fields (see Supplementary Fig. S18 in the Supplementary Note 2 for details). We found that the splitting of the low energy bands in the Gr-MoTe₂ interface and the doping can be tuned by the electric field. Theoretically, we found that for the negative field (−2 V/nm), where graphene is electron-doped, the splitting (i.e., Rashba SOI) is larger than for the positive field (2 V/nm), where graphene is hole-doped. Our measurements also show that the signal amplitude (ΔV_{SGE}) is higher for electrons compared to holes, which is in agreement with the theoretical analysis. However, experimentally we only applied about ± 0.50 V/nm and a very negligible modulation of Rashba SOI is expected within this applied electric field range. In addition to a small change of Rashba SOI with the electric field, the gate voltage also changes the Fermi level in Gr-MoTe₂ heterostructure significantly (hence, the charge of carrier type), which gives rise to the sign change of the SGE signal.

Systematic gate dependence of V_{SGE} is measured at different gate voltages (V_g) in the range from −40 to +40 V for two different spin injection bias currents $I = \pm 80 \mu A$ at room temperature (Fig. 4a). It can be observed that the SGE signal changes sign with gate voltage and spin injection bias currents. To correlate the sign change behavior of the SGE signal with the carrier type of the Gr-MoTe₂ heterostructure, the gate dependence of graphene channel resistance (R_{Gr}) is plotted together with ΔV_{SGE} and ΔR_{SGE} . To be noted, the R_{Gr} is measured for the channel length of 6.7 μm (Fig. 4b inset), which includes part of the graphene region that is not contributing to the SGE signal. Therefore, the charge neutrality point (CNP) for the only Gr-MoTe₂ heterostructure region can be between 10–20 V. Interestingly, the gate dependence of SGE signal ΔV_{SGE} and ΔR_{SGE} change sign around the charge neutrality point, which is between 10–20 V. Opposite signs of the SGE signals are consistently observed for carriers in the electron- and hole-doped regimes of the heterostructure, i.e. for the conduction and valence bands of the hybrid structure. The signal amplitudes ΔV_{SGE} , ΔR_{SGE} , and corresponding α_{RE} (Supplementary Fig. S11) are also found to be asymmetric, higher for an electron-doped regime compared to the hole-doped regime. Such behavior can be due to the different doping regimes and spin-charge conversion efficiency.

Spin-galvanic signal detection via spin switch and spin precession. To substantiate the proximity-induced SGE in Gr-MoTe₂ heterostructure via spin-switch and Hanle spin precession

measurements¹¹, a different device is fabricated (Supplementary Fig. S12a) where an injector FM is placed perpendicular (x-axis) to the heterostructure. At first, the spin transport properties in graphene across the Gr-MoTe₂ heterostructure have been verified. Figure 5a depicts the schematic of the device and measurement geometry to measure the non-local spin signal with a FM detector in graphene across the Gr-MoTe₂ heterostructure. The non-local spin valve (V_{nl}) in graphene is depicted in Fig. 5b with $I = -300 \mu A$ at $V_g = -50 V$, where the magnetic field is applied along the easy axis of the injector's magnetization (x-axis). The Hanle spin precession signal in graphene is presented in Fig. 5c with $I = -50 \mu A$ at $V_g = -50 V$. The characteristic switching in spin-valve and antisymmetric Hanle are due to the perpendicular magnetization of the injector (x-axis) and detector (y-axis) FM contacts. Next, the non-local SGE signal in the Gr-MoTe₂ has been investigated. Figure 5d shows the schematic of the device and measurement geometry to measure non-local SGE signal (V_{SGE}) with Ti/Au contacts along the Hall-cross of Gr-MoTe₂ heterostructure. In this measurement geometry, it is expected that applying a changing magnetic field along the easy axis (x-axis) of the FM injector should have manifested a spin switch signal across the Hall-cross due to proximity-induced SGE. The SGE signal with varying in-plane magnetic field (B_x) at room temperature is presented in Fig. 5e with $I = -100 \mu A$ at $V_g = -50 V$. As the graphene channel was highly doped in this device, a complete gate-dependent measurement could not be performed, as the signal became noisy at positive gate voltages. The full bias dependence of SGE signals is presented in Supplementary Fig. S12. As a confirmation of the spin-related origin of the observed SGE, Hanle spin precession with out-of-plane field B_z is measured and shown in Fig. 5f along with fitting for $I = -100 \mu A$ at $V_g = -50 V$. The spin lifetime and spin diffusion length in Gr-MoTe₂ heterostructure are extracted to be around $\tau_s = 20 ps \pm 1 ps$ and $\lambda_s = 155 nm \pm 5 nm$.

Discussion

The observed SGE in Gr-MoTe₂ heterostructure can have interesting microscopic origins. Although topologically non-trivial Weyl states in MoTe₂ are found to exist at low temperature²⁷, the trivial spin-polarized surface and bulk states are also shown to exist in these materials even at room temperature²³. Additionally, the existence of polar instability near the surface is also observed even when the MoTe₂ bulk is in a centrosymmetric phase^{23,36}. Therefore, the surface states of MoTe₂ can have a strong influence on the band hybridization and proximity-induced spin-charge conversion properties of Gr-MoTe₂ heterostructure. Additionally, our calculations show the presence of a very strong SOI with band splitting of a few meV in graphene in proximity with MoTe₂, similar to the predictions on graphene-semiconducting TMD heterostructure^{30,47}. Interestingly, the induced Rashba spin-split bands in graphene should have opposite spin polarization with a helical spin texture due to the lack of inversion symmetry at the interface, which is protected by time-reversal symmetry^{4,33}. Moreover, this proximity-induced band splitting in graphene is predicted to emanate along the energy axis with an in-plane spin polarization, which is the cardinal aspect for a novel spin-to-charge conversion effects⁴⁷. The in-plane spin accumulation in our measured Gr-MoTe₂ heterostructures renders this SGE signal to be due to proximity-induced IREE in graphene. It can be affirmed that the polarization of the accumulated spins is in-plane; otherwise, a signal would have been observed when the applied magnetic field direction is aligned with the y-axis ($\theta = 90^\circ$) in our angle dependence measurements^{16,17}.

In our measurements, we do not observe the contribution of SHE and REE from only MoTe₂ to the manifested gate-tunable

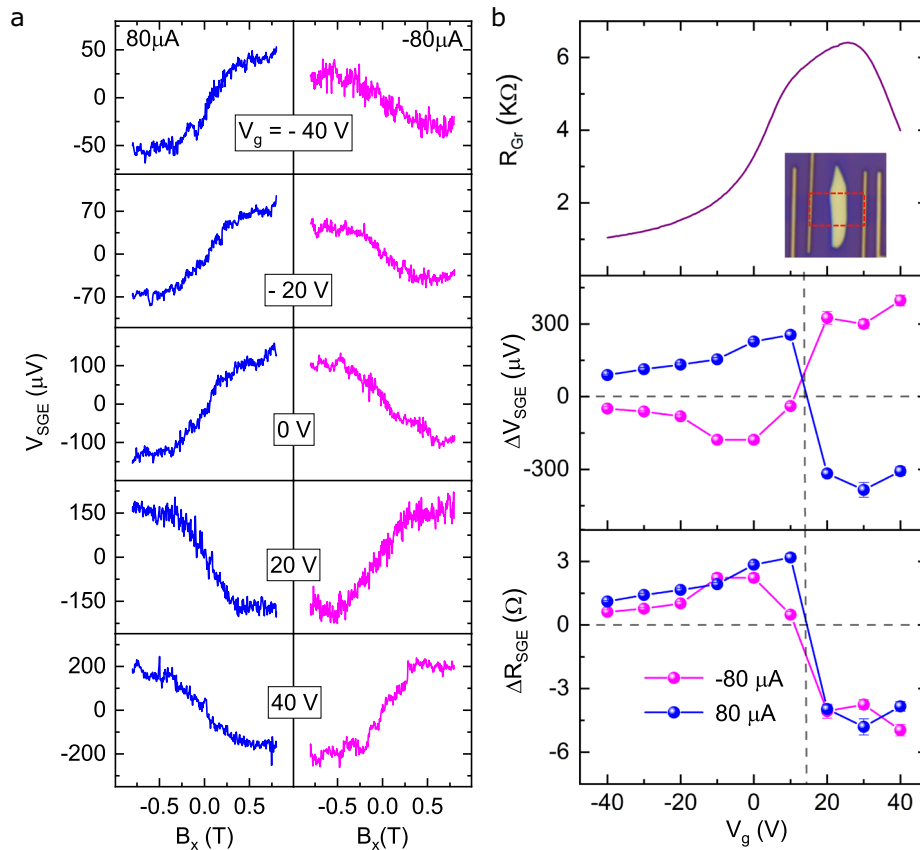


Fig. 4 Gate dependence of spin-galvanic signal in graphene-MoTe₂ heterostructure at room temperature. **a** Evolution of measured spin-galvanic signal (V_{SGE}) by sweeping magnetic field along the x-axis (B_x) at different gate voltages in the range of +40 to −40 V, with $I = \pm 80 \mu A$ in Dev 1 at room temperature. The sign of the spin-galvanic signal changes with gate voltage V_g and spin injection bias current I . **b** Gate dependence of graphene channel resistance (R_{Gr}) and spin-galvanic signals (ΔV_{SGE} and $\Delta R_{SGE} = \Delta V_{SGE}/I$) at $I = \pm 80 \mu A$ at room temperature. The sign change of the spin-galvanic signal is observed close to the charge neutrality point of graphene and the signals are of opposite sign for n and p-type regimes of the graphene-MoTe₂ heterostructure. The error bars are calculated from the noise level of the manifested signals and not clearly visible because error bars are smaller than the data points.

SGE signals, as the charge carriers in metallic MoTe₂ are not tunable by a gate voltage. We can also rule out proximity-induced SHE in graphene in a heterostructure with MoTe₂ since that would have polarized the spins in the z-direction, which would have resulted in a spin precession Hanle peaks near $B = 0$ T field, which are not observed¹⁶. We can exclude the thermal-related spin effects as the origin of the observed SGE signal for the reason that the sign of the SGE signal changes with the DC bias current direction, as depicted in Fig. 1e, as the temperature gradient in the heterostructure should not change with the bias direction. Moreover, we manifested the linear bias dependence of the SGE signal (Fig. 1f), while the thermal-related effect should be proportional to I^2 . In addition, we observe a gate dependence tuning of the SGE signal magnitude with a sign change for the electron- and hole-doped regimes of the Gr-MoTe₂ heterostructure. The effect of stray Hall effect in our SGE signal can be disregarded because of the larger channel length between the injector and detector, and higher magnitude of the obtained SGE signal, which is in the range of few Ohms where the magnitude of the stray Hall effect is estimated to be in the range of few milli-Ohms in a similar kind of device structure^{16,48}. The controlled experiments with only graphene channels show a null signal, further supporting the measurements. Moreover, spin-switch and Hanle spin precession measurements have been observed while injecting spin current by a FM injector perpendicular (x-axis) to the Gr-MoTe₂

heterostructure. So, the observed SGE is inevitably due to IREE in proximitized graphene because of proximity-induced SOI from MoTe₂.

In conclusion, we demonstrated the electrical detection and control of proximity-induced Rashba spin-orbit interaction in vdW heterostructures at room temperature. The observed SGE in the heterostructure of semi-metallic MoTe₂ and large-area CVD graphene can offer unique advantages for faster and low-power spin-charge conversion-based spintronic devices. Specifically, vdW heterostructure provides entirely new mechanisms for tuning emergent spin functionalities by an electric field, resulting from interfacial proximity interactions between the stacked layered materials. Due to the proximity effect, graphene acquires strong SOI and a spin texture with spin-split conduction and valence bands, which is ideal for tuning by a gate voltage. Controlling the magnitude and sign of the spin voltage by an external electric field at room temperature can be efficiently used for gate tunable spin-orbit torque (SOT) based magnetic random-access memory (MRAM)³ and logic technologies⁵. The strong Rashba SOI in vdW heterostructures can further enable new energy-dependent spin textures by tuning their proximity-induced interactions and expected to provide a new playground for the creation of unique topological states of matter, for example, in heterostructures with layered ferromagnetic⁴⁹ and superconducting materials^{1,4}.

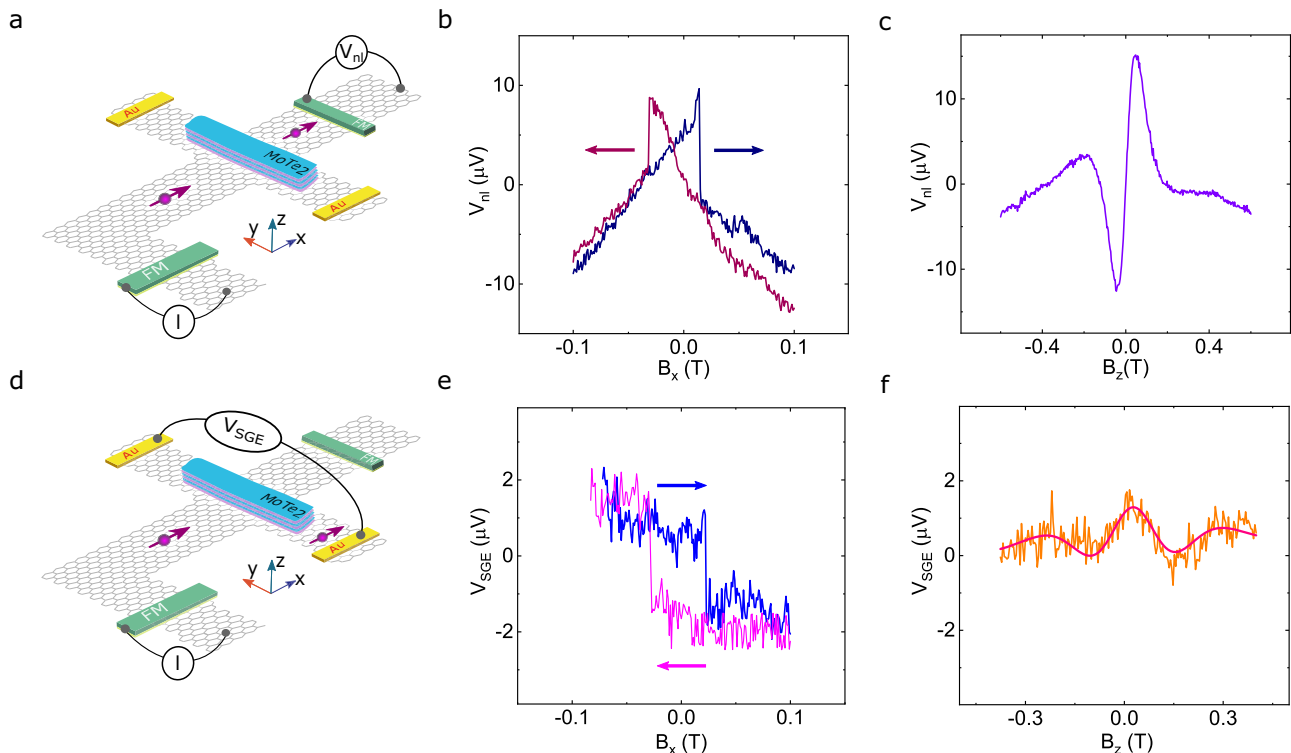


Fig. 5 Spin-galvanic signal with an injector ferromagnet (FM) perpendicular to the graphene-MoTe₂ heterostructure. **a** A schematic of the device and measurement geometry to measure the non-local spin signal with a ferromagnetic detector in graphene across the graphene-MoTe₂ heterostructure. **b, c** Spin valve and Hanle spin precession measurements, respectively. **d** A schematic of the device and measurement geometry to measure the non-local spin-galvanic signal (V_{SGE}) with non-ferromagnetic detectors (Ti/Au) along the Hall-cross of graphene-MoTe₂ heterostructure. **e** The spin-galvanic signal, V_{SGE} , is measured with varying in-plane magnetic field (B_x) at room temperature. **f** The spin-galvanic signal was detected via Hanle spin precession with varying out-of-plane magnetic field (B_z) along with Hanle fitting.

Methods

Device fabrication and measurements. The vdW heterostructures of Gr-MoTe₂ were fabricated by dry transfer of 1 T' MoTe₂ (from HQ Graphene) flakes on CVD graphene (from Groltex), onto SiO₂ (285 nm)/n-doped Si substrate using scotch tape method inside a glovebox in an inert atmosphere. The graphene and the Gr-MoTe₂ channels were patterned into Hall-bar-shaped structures by electron beam lithography and oxygen plasma etching. Both non-magnetic and ferromagnetic contacts to graphene were defined by two-step electron beam lithography and lift-off process. The non-magnetic contacts were prepared by deposition of 10 nm Ti and 60 nm Au by electron beam evaporation and lift-off process. For the preparation of ferromagnetic contacts to graphene, we used a two-step electron beam evaporation of 0.6 nm of Ti and in-situ oxidation, followed by a 90 nm of Cobalt (Co) deposition. The lift-off was performed in warm acetone and IPA. The spin-galvanic measurements were performed in a vacuum system with a magnetic field up to 0.8 Tesla and a sample rotation stage. All the electrical measurements were performed at room temperature using a current source Keithley 6221, a nano voltmeter Keithley 2182 A and Keithley 2612B source meter for application of gate voltages.

Density functional theory calculations. The electronic structure calculations and structural relaxation of our heterostructures are performed by means of density functional theory⁴⁶ within Quantum ESPRESSO⁴⁵. Self-consistent calculations are performed with the k -point sampling of $18 \times 18 \times 1$. We use an energy cutoff for charge density of $550 R_p$, and the kinetic energy cutoff for wavefunctions is $65 R_p$ for the fully relativistic pseudopotential with the projector augmented wave method⁵⁰ with the Perdew-Burke-Ernzerhof exchange-correlation functional⁵¹. For the relaxation of the heterostructures, we add van der Waals corrections^{52,53} and use a quasi-newton algorithm based on the trust radius procedure. In order to simulate quasi-2D systems, a vacuum of at least 18 \AA is used to avoid interactions between periodic images in our slab geometry. We choose a 5×5 supercell for graphene, a 2×3 supercell of 1 T' MoTe₂, and we end up with 86 atoms in the hexagonal heterostructure unit cell. Structural relaxations are performed until all components of all forces were reduced below $10^{-3} [R_p/a_0]$, where a_0 is the Bohr radius.

Data availability

The data that support the findings of this study are available from the corresponding authors on reasonable request.

Received: 23 November 2020; Accepted: 6 April 2021;

Published online: 08 June 2021

References

1. Soumyanarayanan, A., Reyren, N., Fert, A. & Panagopoulos, C. Emergent phenomena induced by spin-orbit coupling at surfaces and interfaces. *Nature* **539**, 509–517 (2016).
2. Manipatruni, S. et al. Scalable energy-efficient magnetoelectric spin-orbit logic. *Nature* **565**, 35–42 (2019).
3. Garelo, K. et al. SOT-MRAM 300MM integration for low power and ultrafast embedded memories. In *2018 IEEE Symposium on VLSI Circuits* 81–82 (IEEE, 2018). <https://doi.org/10.1109/VLSIC.2018.8502269>
4. Manchon, A., Koo, H. C., Nitta, J., Frolov, S. M. & Duine, R. A. New perspectives for Rashba spin-orbit coupling. *Nat. Mater.* **14**, 871–882 (2015).
5. Sinova, J., Valenzuela, S. O., Wunderlich, J., Back, C. H. & Jungwirth, T. Spin Hall effects. *Rev. Mod. Phys.* **87**, 1213–1260 (2015).
6. Sánchez, J. C. R. et al. Spin-to-charge conversion using Rashba coupling at the interface between non-magnetic materials. *Nat. Commun.* **4**, 2944 (2013).
7. Song, Q. et al. Observation of inverse Edelstein effect in Rashba-split 2DEG between SrTiO₃ and LaAlO₃ at room temperature. *Sci. Adv.* **3**, e1602312 (2017).
8. Lesne, E. et al. Highly efficient and tunable spin-to-charge conversion through Rashba coupling at oxide interfaces. *Nat. Mater.* **15**, 1261–1266 (2016).
9. MacNeill, D. et al. Control of spin-orbit torques through crystal symmetry in WTe₂/ferromagnet bilayers. *Nat. Phys.* **13**, 300–305 (2017).
10. Shao, Q. et al. Strong Rashba-Edelstein effect-induced spin-orbit torques in monolayer transition metal dichalcogenide/ferromagnet bilayers. *Nano Lett.* **16**, 7514–7520 (2016).
11. Khokhriakov, D., Hoque, A. M., Karpiak, B. & Dash, S. P. Gate-tunable spin-galvanic effect in graphene-topological insulator van der Waals heterostructures at room temperature. *Nat. Commun.* **11**, 3657 (2020).
12. Zhao, B., Hoque, A. M., Khokhriakov, D., Karpiak, B. & Dash, S. P. Charge-spin conversion signal in WTe₂ van der Waals hybrid devices with a geometrical design. *Appl. Phys. Lett.* **117**, 242401 (2020).

13. Hoque, A. M., Khokhriakov, D., Karpiak, B. & Dash, S. P. Charge-spin conversion in layered semimetal TaTe₂ and spin injection in van der Waals heterostructures. *Phys. Rev. Res.* **2**, 033204 (2020).
14. Kovács-Krausz, Z. et al. Electrically controlled spin injection from giant Rashba spin-orbit conductor BiTeBr. *Nano Lett.* **20**, 4782–4791 (2020).
15. Zhao, B. et al. Observation of charge to spin conversion in Weyl semimetal WTe₂ at room temperature. *Phys. Rev. Res.* **2**, 013286 (2020).
16. Ghiasi, T. S., Kaverzin, A. A., Blah, P. J. & van Wees, B. J. Charge-to-spin conversion by the Rashba–Edelstein effect in two-dimensional van der Waals heterostructures up to room temperature. *Nano Lett.* **19**, 5959–5966 (2019).
17. Safeer, C. K. et al. Room-temperature spin Hall effect in graphene/MoS₂ van der Waals heterostructures. *Nano Lett.* **19**, 1074–1082 (2019).
18. Dankert, A., Geurs, J., Kamalakar, M. V., Charpentier, S. & Dash, S. P. Room temperature electrical detection of spin polarized currents in topological insulators. *Nano Lett.* **15**, 7976–7981 (2015).
19. Mellnik, A. R. et al. Spin-transfer torque generated by a topological insulator. *Nature* **511**, 449–451 (2014).
20. Johansson, A., Henk, J. & Mertig, I. Edelstein effect in Weyl semimetals. *Phys. Rev. B* **97**, 085417 (2018).
21. Sun, Y., Zhang, Y., Felser, C. & Yan, B. Strong intrinsic spin Hall effect in the TaAs family of Weyl semimetals. *Phys. Rev. Lett.* **117**, 146403 (2016).
22. Das, P. K. et al. Layer-dependent quantum cooperation of electron and hole states in the anomalous semimetal WTe₂. *Nat. Commun.* **7**, 10847 (2016).
23. Weber, A. P. et al. Spin-resolved electronic response to the phase transition in MoTe₂. *Phys. Rev. Lett.* **121**, 156401 (2018).
24. Shi, S. et al. All-electric magnetization switching and Dzyaloshinskii–Moriya interaction in WTe₂/ferromagnet heterostructures. *Nat. Nanotechnol.* **14**, 945–949 (2019).
25. Stiehl, G. M. et al. Layer-dependent spin-orbit torques generated by the centrosymmetric transition metal dichalcogenide β-MoTe₂. *Phys. Rev. B* **100**, 184402 (2019).
26. Zhao, B. et al. Unconventional charge–spin conversion in Weyl-semimetal WTe₂. *Adv. Mater.* <https://doi.org/10.1002/adma.202000818>
27. Safeer, C. K. et al. Large multidirectional spin-to-charge conversion in low-symmetry semimetal MoTe₂ at room temperature. *Nano Lett.* **19**, 8758–8766 (2019).
28. Vila, M. et al. Charge-to-spin interconversion in low-symmetry topological materials. (2020). Preprint at <https://doi.org/10.21203/rs.3.rs-124172/v1> (2020)
29. Khokhriakov, D. et al. Tailoring emergent spin phenomena in Dirac material heterostructures. *Sci. Adv.* **4**, eaat9349 (2018).
30. Cummings, A. W., Garcia, J. H., Fabian, J. & Roche, S. Giant spin lifetime anisotropy in graphene induced by proximity effects. *Phys. Rev. Lett.* **119**, 206601 (2017).
31. Zhang, J., Triola, C. & Rossi, E. Proximity effect in graphene–topological-insulator heterostructures. *Phys. Rev. Lett.* **112**, 096802 (2014).
32. Song, K. et al. Spin proximity effects in graphene/topological insulator heterostructures. *Nano Lett.* **18**, 2033–2039 (2018).
33. Offidani, M., Milletari, M., Raimondi, R. & Ferreira, A. Optimal charge-to-spin conversion in graphene on transition-metal dichalcogenides. *Phys. Rev. Lett.* **119**, 196801 (2017).
34. Li, L. et al. Gate-tunable reversible Rashba–Edelstein effect in a few-layer graphene/2H-TaS₂ heterostructure at room temperature. *ACS Nano* **14**, 5251–5259 (2020).
35. Benítez, L. A. et al. Tunable room-temperature spin galvanic and spin Hall effects in van der Waals heterostructures. *Nat. Mater.* **19**, 170–175 (2020).
36. Jiang, J. et al. Signature of type-II Weyl semimetal phase in MoTe₂. *Nat. Commun.* **8**, 13973 (2017).
37. Deng, K. et al. Experimental observation of topological Fermi arcs in type-II Weyl semimetal MoTe₂. *Nat. Phys.* **12**, 1105–1110 (2016).
38. Grzeszczyk, M. et al. Raman scattering of few-layers MoTe₂. *2D Mater.* **3**, 025010 (2016).
39. Gmitra, M. & Fabian, J. Graphene on transition-metal dichalcogenides: a platform for proximity spin-orbit physics and optospintronics. *Phys. Rev. B* **92**, 155403 (2015).
40. Wang, Z. et al. Origin and magnitude of ‘Designer’ spin-orbit interaction in graphene on semiconducting transition metal dichalcogenides. *Phys. Rev. X* **6**, 041020 (2016).
41. Khokhriakov, D., Karpiak, B., Hoque, A. M. & Dash, S. P. Two-dimensional spintronic circuit architectures on large scale graphene. *Carbon N. Y.* **161**, 892–899 (2019).
42. Khokhriakov, D. et al. Robust spin interconnect with isotropic spin dynamics in chemical vapor deposited graphene layers and boundaries. *ACS Nano* (2020). <https://doi.org/10.1021/acsnano.0c07163>
43. Kimura, T., Otani, Y., Sato, T., Takahashi, S. & Maekawa, S. Room-temperature reversible spin Hall effect. *Phys. Rev. Lett.* **98**, 156601 (2007).
44. Hasan, M. Z. & Kane, C. L. Colloquium: topological insulators. *Rev. Mod. Phys.* **82**, 3045–3067 (2010).
45. Giannozzi, P. et al. Quantum ESPRESSO: a modular and open-source software project for quantum simulations of materials. *J. Phys. Condens. Matter* **21**, 395502 (2009).
46. Hohenberg, P. & Kohn, W. Inhomogeneous electron gas. *Phys. Rev.* **136**, B864–B871 (1964).
47. Milletari, M., Offidani, M., Ferreira, A. & Raimondi, R. Covariant conservation laws and the spin Hall effect in Dirac-Rashba systems. *Phys. Rev. Lett.* **119**, 246801 (2017).
48. Karpiak, B. et al. 1D ferromagnetic edge contacts to 2D graphene/h-BN heterostructures. *2D Mater.* **5**, 014001 (2017).
49. Karpiak, B. et al. Magnetic proximity in a van der Waals heterostructure of magnetic insulator and graphene. *2D Mater.* **7**, 015026 (2020).
50. Kresse, G. & Joubert, D. From ultrasoft pseudopotentials to the projector augmented-wave method. *Phys. Rev. B* **59**, 1758–1775 (1999).
51. Perdew, J. P., Burke, K. & Ernzerhof, M. Generalized gradient approximation made simple. *Phys. Rev. Lett.* **77**, 3865–3868 (1996).
52. Barone, V. et al. Role and effective treatment of dispersive forces in materials: polyethylene and graphite crystals as test cases. *J. Comput. Chem.* **30**, 934–939 (2009).
53. Grimme, S. Semiempirical GGA-type density functional constructed with a long-range dispersion correction. *J. Comput. Chem.* **27**, 1787–1799 (2006).

Acknowledgements

The authors acknowledge financial support from the European Union Graphene Flagship (Core 2 No. 785219 and Core 3 No. 881603), EU FlagEra project (from Swedish Research Council VR No. 2015-06813), Swedish Research Council VR project grants (No. 2016-03658), 2D Tech VINNOVA center, Graphene center, and the EI Nano and AoA Materials program at Chalmers University of Technology. KZ and JF also acknowledge support by the Deutsche Forschungsgemeinschaft (DFG, German Research Foundation) SFB 1277 (Project-ID 314695032). We acknowledge the staff at Quantum Device Physics and Nanofabrication laboratory in our department at the Chalmers University of Technology.

Author contributions

S.P.D. and A.M.H. conceived the idea and designed the experiments. A.M.H. fabricated and measured the devices. D.K., B.K., B.Z. and S.P.D. contributed to some device fabrication and measurements. A.M.H. and S.P.D. analyzed the experimental data and wrote the manuscript. DFT calculations were carried out by K.Z. and J.F. All authors participated in the discussions and manuscript preparation. S.P.D. supervised the research and managed the research project.

Funding

Open access funding provided by Chalmers University of Technology.

Competing interests

The authors declare no competing interests.

Additional information

Supplementary information The online version contains supplementary material available at <https://doi.org/10.1038/s42005-021-00611-6>.

Correspondence and requests for materials should be addressed to S.P.D.

Reprints and permission information is available at <http://www.nature.com/reprints>

Publisher's note Springer Nature remains neutral with regard to jurisdictional claims in published maps and institutional affiliations.



Open Access This article is licensed under a Creative Commons Attribution 4.0 International License, which permits use, sharing, adaptation, distribution and reproduction in any medium or format, as long as you give appropriate credit to the original author(s) and the source, provide a link to the Creative Commons license, and indicate if changes were made. The images or other third party material in this article are included in the article's Creative Commons license, unless indicated otherwise in a credit line to the material. If material is not included in the article's Creative Commons license and your intended use is not permitted by statutory regulation or exceeds the permitted use, you will need to obtain permission directly from the copyright holder. To view a copy of this license, visit <http://creativecommons.org/licenses/by/4.0/>.

© The Author(s) 2021

Paper V

Spin–valley coupling and spin-relaxation anisotropy in all-CVD Graphene-MoS₂ van der Waals heterostructure

Anamul Md. Hoque¹, Vasudev Ramachandra¹, Antony George², Emad Najafidehaghani²,
Ziyang Gan², Richa Mitra¹, Bing Zhao¹, Dmitrii Khokhriakov¹,
Andrey Turchanin², Samuel Lara-Avila¹, Sergey Kubatkin¹, Saroj P. Dash^{1*}

¹*Department of Microtechnology and Nanoscience, Chalmers University of Technology, SE-41296, Göteborg, Sweden.*

²*Friedrich Schiller University Jena, Institute of Physical Chemistry, 07743, Jena, Germany*

Abstract

Two-dimensional (2D) van der Waals heterostructures fabricated by combining 2D materials with unique properties in one ultimate unit can offer a plethora of fundamental phenomena and practical applications. Recently, proximity-induced quantum and spintronic effects have been realized in heterostructures of graphene with 2D semiconductors and their twisted systems. However, these studies are so far limited to exfoliated flake-based devices, limiting their potential for scalable practical applications. Here, we report spin–valley coupling and spin-relaxation anisotropy in graphene-MoS₂ heterostructure devices prepared from scalable chemical vapor deposited (CVD) 2D materials. Spin precession and dynamics measurements reveal an enhanced spin-orbit coupling (SOC) strength in the heterostructure in comparison to the pristine graphene at room temperature. Consequently, a large spin relaxation anisotropy is observed in the heterostructure, providing a method for spin filtering due to spin-valley coupling. These findings open a scalable platform for all-CVD 2D van der Waals heterostructures design and their novel device applications.

**Corresponding author: Saroj P. Dash, Email: saroj.dash@chalmers.se*

Keywords: Graphene, MoS₂, CVD growth, 2D materials heterostructures, Spin transport, Spin lifetime anisotropy, Spintronics, Spin-orbit coupling, proximity effect, spin valley coupling.

Introduction

Two-dimensional (2D) materials host unique charge, spin, and orbital degrees of freedom that can be uniquely manipulated in van der Waals (vdW) heterostructures for quantum and spintronic applications^{1–4}. Graphene (Gr) is well-known for Dirac fermions and high carrier mobility along with long-distance spin transport due to its low spin-orbit coupling (SOC)^{5–9}. However, significant efforts have been made to enhance SOC in Gr to realize gate tunable spintronic functionalities¹⁰. One way to achieve sizable SOC in Gr is by employing chemically-adsorbed heavy adatoms,^{11,12}; however, doping can introduce defects in Gr and compromise the fascinating electronic properties¹³. Alternatively, the vdW heterostructures of Gr with high-SOC 2D materials, such as transition metal dichalcogenides (TMDCs) and topological insulators (TI), have emerged as a promising platform for proximity-induced SOC,^{14,15} while preserving their electronic properties^{16–19}. Moreover, introducing SOC in twisted Gr heterostructures can yield new correlated electronic phases and novel quantum phenomena^{20,21}.

The signatures of the increased SOC demonstrated the potential of Gr-TMDCs heterostructures in quantum and spintronic devices^{15,22}. First, an increase in SOC strength in Gr-TMDC and its gate modulation and hydrostatic pressure dependence are demonstrated at low temperature^{23–27}. The spin transport in Gr-MoS₂ heterostructures revealed spin field-effect modulation functionality up to room temperature, where the spin signal could be controlled by a gate electric field^{28,29}. Moreover, valley-polarized spin injection and proximity-induced spin Hall and Rashba Edelstein effects have been realized in the Gr-TMDC heterostructures^{30–35}. Another exciting aspect of proximity-induced SOC in Gr is the spin lifetime anisotropy, which results in spin filtering functionalities due to the different spin relaxation times for spins polarized in different orientations³⁶. However, experimental reports on spin–valley coupling are so far limited to exfoliated flakes, and realization in scalable Gr-TMDCs heterostructure is still missing and challenging as well due to the complex fabrication process.

Here, we report spin transport and dynamics in scalable graphene-MoS₂ vdW heterostructure spintronic devices grown by the chemical vapor deposition (CVD) methods. The CVD-grown materials and their vdW heterostructure devices show excellent charge transport properties. Spin transport and precession properties were investigated in the heterostructure channel using a nonlocal spin valve and Hanle spin precession measurements at room temperature. Detailed oblique field dependence of spin precession measurements are performed to estimate spin–valley coupling and spin-relaxation anisotropy. These studies open a scalable platform for all-CVD 2D heterostructure-based devices.

Results and Discussion

All-CVD graphene-MoS₂ heterostructure device fabrication and electrical characterization

Figure 1a shows the schematic of a device structure consisting of CVD grown graphene-MoS₂ heterostructure on Si/SiO₂ substrate, which allows to apply back-gate voltage (V_g). The bottom panel in Fig. 1a illustrates the band diagram of graphene and MoS₂ with spin-split bands for up and down spins^{37,38}. The graphene-MoS₂ vdW heterostructure region can induce spin–valley SOC

in graphene via proximity effect and modify the band structure and spin transport in the channel^{17,39}. An optical micrograph of a fabricated device is presented in Fig. 1b, where the monolayer CVD graphene channel is covered with a monolayer CVD MoS₂, which was transferred by wet transfer technique⁴⁰. Subsequently, e-beam lithography was performed to make ferromagnetic (FM) tunnel contacts of TiO₂ (~ 1 nm)/Co (~ 80 nm) suitable for studying charge and spin transport properties in the devices (see the Methods for details).

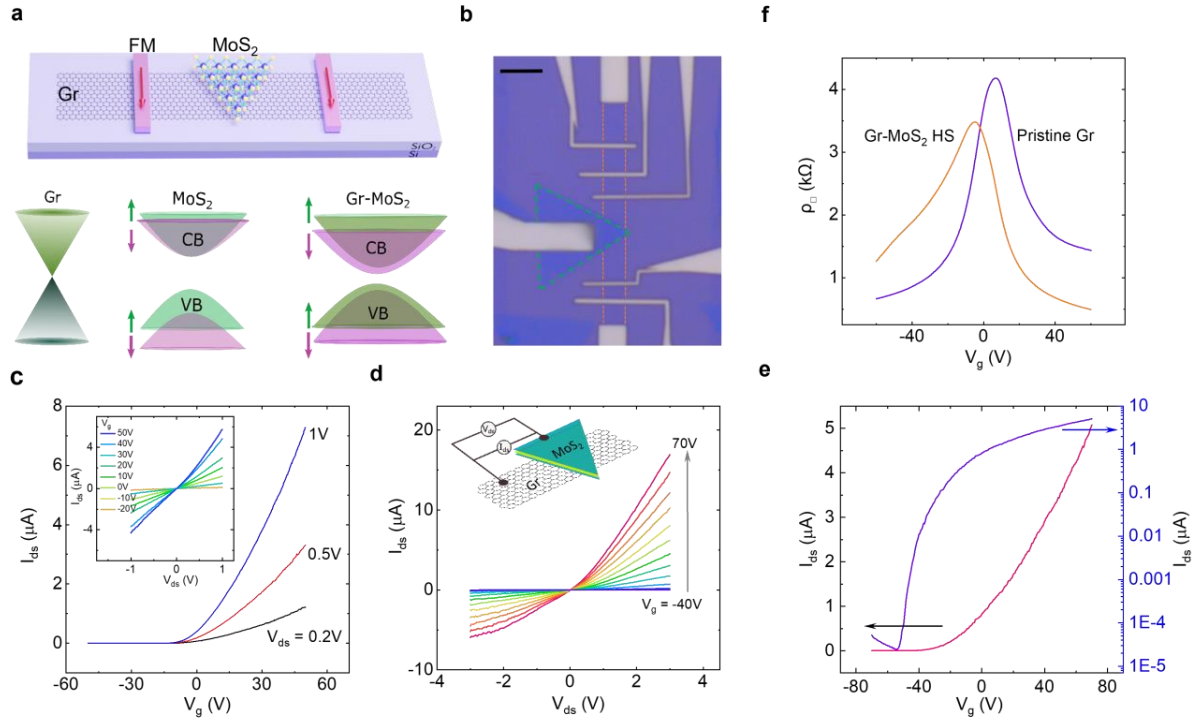


Figure 1. All-CVD graphene-MoS₂ heterostructure spintronic device and electrical properties. (a) Schematic representation of the Gr and MoS₂ vdW heterostructure device on Si/SiO₂ substrate along with the FM contacts. Pictorial depiction of the band diagram of graphene, MoS₂, and their heterostructure with spin-split bands. (b) Optical image of CVD Gr (orange dotted line) and CVD MoS₂ (green dotted line) vdW heterostructure along with the different FM (Co/TiO₂) contacts. The scale bar is 5 μm. The width and the shapes of the FM contacts are designed on Gr to facilitate spin injection and detection. (c) Source-drain current I_{ds} as a function of the applied back-gate voltage (V_g) of single-layer of CVD MoS₂ field-effect transistor with different source-drain bias voltages V_{ds} . Inset shows I_{ds} vs. V_{ds} at different V_g . (d) I_{ds} vs. V_{ds} plots at different gate voltages between Gr-MoS₂ along with the measurement geometry in the inset. (e) Transfer properties (I_{ds} vs. V_g) between Gr-MoS₂ at $V_{ds} = 1V$ in linear (pink) and log (violet) scale. (f) Gate-dependent resistivity of Gr channels in pristine and heterostructure regions probed in four-terminal measurement geometry.

First, we describe the characterization of the individual CVD-grown monolayer materials to inspect their electrical properties. The transport properties (source-drain current I_{ds} vs. gate voltage V_g) of MoS₂ are depicted in Fig. 1c for different bias voltages V_{ds} , along with I_{ds} vs. V_{ds} at different V_g in the inset. The I_{ds} increase monotonically with increasing V_{ds} , and the I_{ds} increase with increasing V_g for fixed V_{ds} due to increasing carrier concentration in the MoS₂, which corresponds to n-type

transport properties⁴¹. We estimated the field-effect mobility by $\mu = \frac{Lg_m}{WC_gV_{ds}} = 1.21 \text{ cm}^2\text{V}^{-1}\text{s}^{-1}$; where L , W , C_g and g_m are the channel length, width, gate capacitance per area ($1.15 \times 10^{-8} \text{ Fcm}^{-2}$ for 285nm SiO_2) and transconductance, respectively.

Next, charge transport properties are measured for Gr-MoS₂ vdW junction. Figure 1d shows the measured I_{ds} as a function of applied V_{ds} at various V_g along with the measurement geometry. The asymmetric I_{ds} - V_{ds} properties with diode-like behavior could be attributed to work function mismatch between the electrodes and the materials^{42,43}. The transfer characteristic (I_{ds} vs. V_g) of the Gr-MoS₂ heterostructure for $V_{ds} = 1\text{V}$ is depicted in Fig. 1e. We found an increase of I_{ds} with increasing positive V_g that is derived mainly from the transport properties of MoS₂, where graphene acts as vdW contact. The field-effect mobility μ is estimated to be $12.4 \text{ cm}^2\text{V}^{-1}\text{s}^{-1}$ in the Gr-MoS₂ heterostructure, which is one order of magnitude higher than the pristine MoS₂ with metallic contacts. This enhancement of mobility of MoS₂ with graphene contact can be attributed to reduced defect states in the MoS₂ contact region and smaller Schottky barrier at the Gr-MoS₂ vdW interface⁴³⁻⁴⁵. Figure 1f presents the gate-dependent Gr resistivity ($\rho_{\square} = \frac{R_4TW}{L}$) in the pristine and Gr-MoS₂ heterostructure region, with Dirac point at 6.8V and -5V, respectively. We estimate the maximum μ to be $2340 \text{ cm}^2\text{V}^{-1}\text{s}^{-1}$ for pristine Gr and $3000 \text{ cm}^2\text{V}^{-1}\text{s}^{-1}$ for the Gr-MoS₂ heterostructure regions. The electrical properties of the heterostructure region indicate the excellent quality of materials, even wet transfer of CVD MoS₂ on CVD Gr does not have a detrimental effect on its phenomenal electrical transport properties^{7,46}.

Spin transport and precession across the all-CVD graphene-MoS₂ van der Waals heterostructure

To investigate the spin dynamics in the all-CVD Gr-MoS₂ heterostructure, nonlocal (NL) spin transport measurements (Fig. 2a) were carried out with varying magnetic field (B) along different directions. We adopted NL measurements geometry, where the injected current and detected voltage circuits are secluded to detect pure spin-polarized current. Spin-valve (SV) measurements are performed to detect in-plane spin transport in the Gr-MoS₂ heterostructure channel, where B_y field is applied along the magnetic easy axis of the FM contacts to switch their magnetization. The switching of the FM contacts renders a spin valve (SV) signal between parallel and antiparallel magnetization states of the injector and detector FM contacts. Figure 2b shows the NLSV signal ($\Delta R_{nl} = \Delta V_{nl}/I$) in the Dev1 of Gr-MoS₂ heterostructure with channel length $L = 9.6 \mu\text{m}$.

Next, we measured the Hanle spin precession signal by applying a perpendicular magnetic field (B_z) to the Gr-MoS₂ plane. In this measurement geometry, the magnetic field dephases the diffusing spins in the channel and renders a cosine-dependent Hanle spin precession signal that diminishes with increasing the magnetic field. Figure 2c shows the measured Hanle signals for parallel and antiparallel FM magnetizations along with the fitting with equation 1.

$$\Delta R_{NL} \propto \int_0^\infty \frac{1}{\sqrt{4\pi Dt}} e^{-\frac{L^2}{4Ds t}} \cos(\omega_L t) e^{-\frac{t}{\tau_s}} dt \quad (1)$$

Here, $\omega_L = \frac{g\mu_B}{\hbar} B_L$ is Larmor frequency with B_L is applied a perpendicular magnetic field to the easy axis of the FM contacts, $g = 2$ is assumed, D_s is the spin diffusion constant, λ_s and τ_s are

the transverse spin diffusion length and lifetime in graphene, respectively. The fitting parameters provide spin transport parameters in the xy plane. We found that the in-plane spin lifetime in the Gr-MoS₂ heterostructure channel is about $\tau_{||} = 125 \pm 6$ ps, and spin diffusion length, $\lambda_{||} = 2.2 \pm 0.13$ μm .

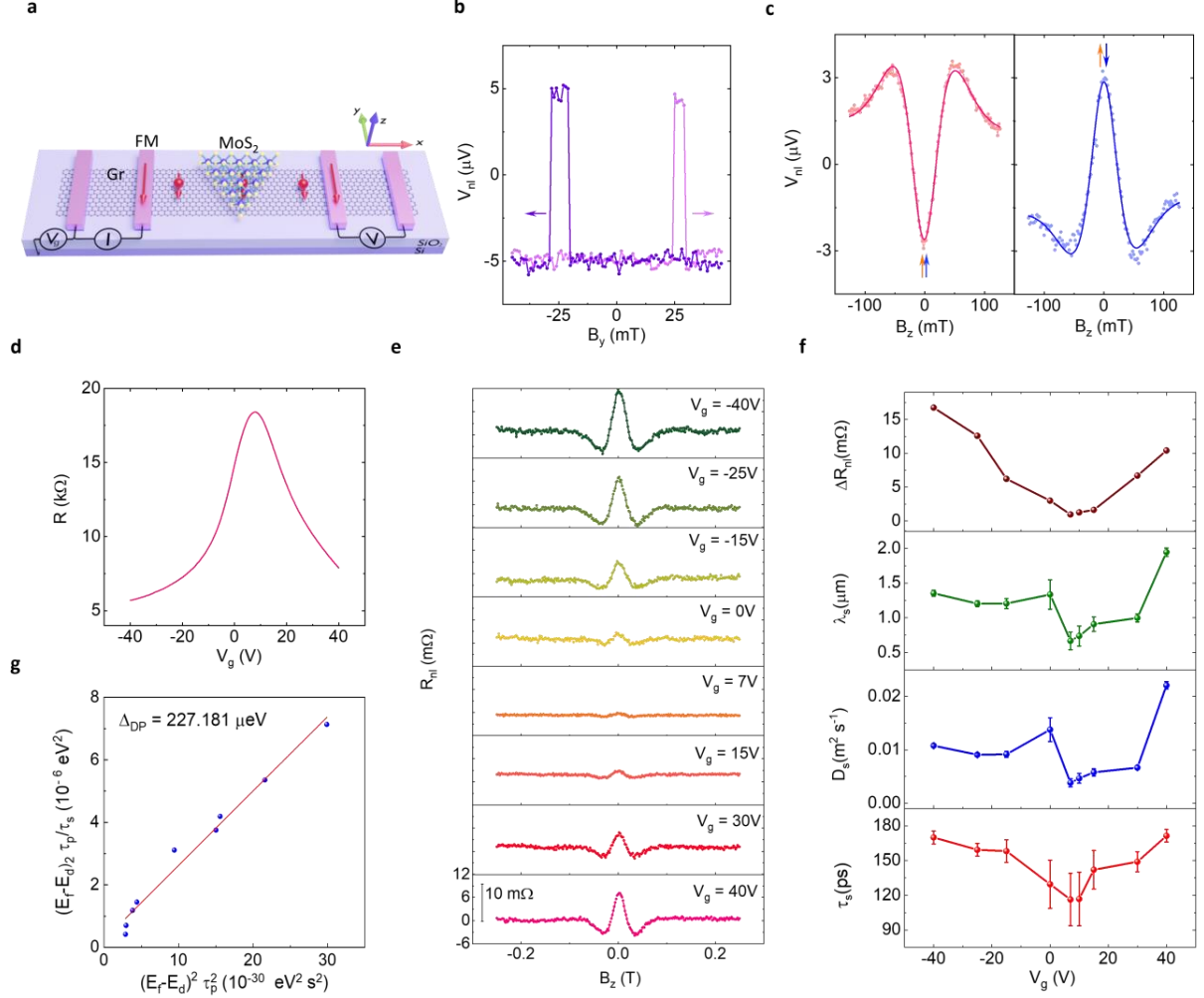


Figure 2. Spin transport and precession across the all-CVD graphene-MoS₂ heterostructure at room temperature. (a) Schematic of the NL geometry to measure spin transport and precession in Gr-MoS₂ heterostructure region. (b) NLSV signal with changing magnetic field along the y-axis. Up and down magnetic field sweep directions are indicated by the arrows. (c) Hanle spin precession signals with out-of-field magnetic field sweep and the data fittings (solid lines) to estimate spin parameters in the heterostructure region for parallel and antiparallel magnetization of the FM electrodes. Measurements were performed in Dev1 with $I = -250$ μA and $V_g = 60\text{V}$, and a small linear background is subtracted from the data. (d) Gate-dependent heterostructure channel resistance of Gr-MoS₂ heterostructure. The Dirac point in this Gr-MoS₂ heterostructure channel is 7V. (e) Evolution of Hanle precession signal in Gr-MoS₂ heterostructure measured at different gate voltages V_g in Dev 2 with $I = -400$ μA . The scale bar for the magnitude of NLSV signal R_{nl} is 10 mΩ. (f) Gate dependence of the Hanle spin precession signal amplitude (ΔR_{nl}), spin diffusion length (λ_s), diffusion constant (D_s), and spin lifetime (τ_s). (g) Estimation of SOC strength in Gr-MoS₂ heterostructure along with fitting (solid line) to equation 2.

Next, we investigated the influence of the gate electric field on the Hanle spin precession signal in the Gr-MoS₂ heterostructure (Dev2) with a channel length of 10.6 μm. The Dirac curve of the heterostructure region is presented in Fig. 2d, where the Dirac point of Gr is $V_g \sim 7V$ and mobility is estimated to be about $2700 \text{ cm}^2\text{V}^{-1}\text{s}^{-1}$. Figure 2e shows the evolution of Hanle spin precession signal measured with different V_g at room temperature. The amplitude (ΔR_{nl}) and extracted spin parameters from the Hanle spin precession measurements at different V_g are shown in the panels in Fig. 2f. It is noticeable that λ_s , D_s , and τ_s are steady at about $1.35 \mu\text{m}$, $0.01 \text{ m}^2\text{s}^{-1}$, and 160 ps , respectively, in the higher V_g range. However, near the Dirac point, reduction of all spin parameters are observed, which can be originated from conductivity mismatch between FM injector and detector contacts with graphene channel^{47,48}. Contrary to the studies in exfoliated Gr-TMDC samples, where the gate-dependent spin transport showed the disappearance of the spin signals at the higher positive gate voltages^{28,29,39}, all-CVD samples exhibited the spin signals to be present also at higher gate voltages. The observation of spin signals at higher V_g in all-CVD samples indicates the absence of tunable spin absorption effect by CVD MoS₂ on the CVD Gr channel. Moreover, an abiding spin absorption by CVD MoS₂ on CVD graphene in our devices might be effective in all gate voltages^{49,50}. Such behavior can be understood from the very low Schottky barrier estimated in our all-CVD MoS₂/Gr interfaces with $\Phi_B \sim 20 \text{ meV}$ (to be reported) in comparison to $\sim 100 \text{ meV}$ obtained in previous exfoliated samples^{28,29,39} in the flat band conditions^{42,43}.

First, we evaluated spin scattering in the all-CVD Gr-MoS₂ channel by considering two main spin relaxation mechanisms, i.e., the Elliott-Yafet (EY) and D'yakonov-Perel' (DP). Here, EY includes the spin-flip events that are due to momentum scattering (τ_p), where τ_s is proportional to τ_p . On the other hand, DP accounts for the spin scattering events due to an effective magnetic field between the momentum scattering events, where τ_s is inversely proportional to τ_p . The SOC can be correlated to these scattering mechanisms, which can be expressed as $\tau_{s,DP}^{-1} = 4 \left(\frac{\Delta_{DP}}{\hbar} \right)^2 \tau_p$ and $\tau_{s,EY} = \left(\frac{E_F}{\Delta_{EY}} \right)^2 \tau_p$. Here, E_F is the relative Fermi energy with respect to the Dirac point, Δ_{EY} and Δ_{DP} are energy scales due to EY and DP mechanisms, respectively. The total spin lifetime in the channel can be expressed as $\tau_s = (\tau_{s,DP}^{-1} + \tau_{s,EY}^{-1})^{-1}$, which yields

$$E_F^2 \frac{\tau_p}{\tau_s} = \Delta_{EY}^2 + 4 \left(\frac{\Delta_{DP} E_F \tau_p}{\hbar} \right)^2 \quad (2)$$

Figure 2g shows the estimated data points along with the fitting to equation (2) and we found $\Delta_{EY} = 488 \mu\text{eV}$ and $\Delta_{DP} = 227 \mu\text{eV}$. The estimated DP strength mostly incorporates the SOC due to broken inversion symmetry⁵¹, which resembles Rashba SOC that turns the spin orientation towards the graphene plane. In addition to the Rashba SOC, MoS₂ can imprint spin-valley coupling due to Zeeman effect that turns the spin orientation towards out-of-plane (z-axis) direction and the associated strength is discussed in latter section.

Spin transport and precession in pristine CVD graphene

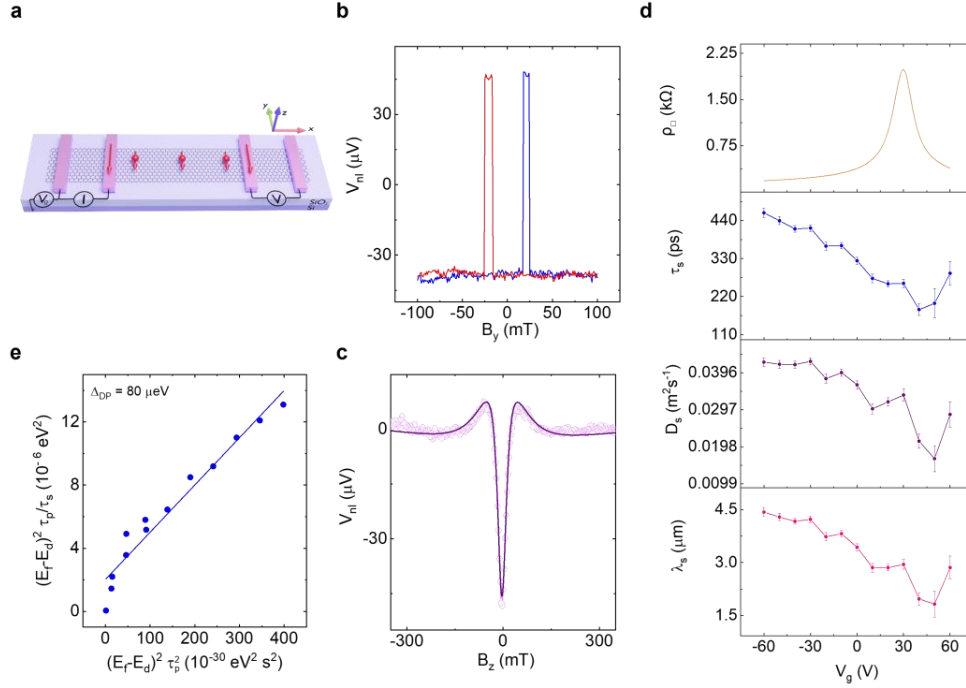


Figure 3: Spin transport parameters in pristine CVD graphene at room temperature. (a) A schematic representation of the device with a pristine graphene channel and the measurement geometry with injector and detector FM contacts. (b) Nonlocal spin-valve measurement with changing magnetic field along the y-axis (magnetic easy axis). (c) Nonlocal Hanle spin precession signal with changing magnetic field along out of plane direction (z-axis). (d) Gate-dependent channel resistivity along with extracted spin diffusion length (λ_s), diffusion constant (D_s), and spin lifetime (τ_s) from the Hanle signals. (e) Estimation of SOC strength in pristine graphene channel along with fitting (solid line) to Eq. 2. Measurements were performed with bias current $I = -100\mu A$ at room temperature.

We measured spin transport in a pristine CVD Gr channel (Fig. 3a) to compare with the heterostructure. Nonlocal spin valve and Hanle spin precession signals are presented in Fig. 3b and 3c, respectively. The gate dependence of pristine Gr channel resistivity is shown in the top panel of Fig. 3d, where the channel length is about 6 μm and the field-effect mobility is calculated to be about 3000 $cm^2 V^{-1} s^{-1}$ and the Dirac point voltage is $V_d = 30V$. The extracted spin parameters λ_s , D_s , and τ_s from the Hanle signals as a function of V_g are presented sequentially in Fig. 3d. At higher gate voltages, away from the Dirac point, the spin parameters in the Gr remain unchanged. For instance, τ_s , D_s , and λ_s are about 420 ps, 0.03m²s⁻¹ and 4.21 μm , respectively at $V_g \leq -30V$. However, near the Dirac point of the Gr channel, the lowest values of all parameters are observed. The spin transport parameters start to increase again at $V_g \geq 60V$ due to the reduction of Gr channel resistivity, ameliorating the conductivity mismatch issue between Gr and injector and detector FM contacts^{47,48}. The extracted SOC strength in pristine Gr due to EY and DP spin relaxation mechanisms (using eq 2) are $\Delta_{EY} = 1.43meV$ and $\Delta_{DP} = 80\mu eV$ (Fig. 3e). Similar Δ_{EY} strength ($\approx 0.5 - 1.5 meV$) is reported on pristine Gr on SiO₂ and hBN, which can be attributed to the non-proximity induced SOC scattering mechanisms^{52,53}. We observed significantly higher Δ_{DP}

in the Gr-MoS₂ heterostructure region due to the strong proximity effect, which is about three times higher than what is manifested in pristine Gr.

Spin–valley coupling and spin-lifetime anisotropy in all-CVD graphene-MoS₂ heterostructure

It is predicted that graphene in proximity to high SOC materials can give rise to large spin lifetime anisotropy ($\xi = \frac{\tau_{\perp}}{\tau_{\parallel}}$), mainly by means of induced Rashba SOC or spin-valley coupling⁵⁴. The SOC associated with Rashba spin-split bands gives rise to a higher in-plane spin lifetime ($\tau_{\parallel} > \tau_{\perp}$) and anisotropy of less than unity ($\xi < 1$). On the other hand, induced spin-valley coupling in the heterostructure renders higher out-of-plane spin polarization ($\tau_{\parallel} < \tau_{\perp}$) and results in $\xi > 1$ because of dominant out-of-plane spin polarization in different valleys (K and K') of the TMDC^{22,39,51}. To verify the SOC mechanisms in all-CVD Gr-MoS₂ heterostructure, we estimated anisotropy (ξ) by employing oblique magnetic field-dependent evolution of Hanle spin precession signals⁵⁵ in all-CVD Gr-MoS₂ heterostructure. In this measurement scheme (Fig. 4a), the changing magnetic field (B) is applied at an angle (β) to the FM contact in the yz-plane and let the spins perpendicular to the external magnetic to dephase. Hence, the manifested NL spin signal only measures the projection of the dephased spin onto that applied field direction. Figure 4b shows measured Hanle spin precession signals for different magnetic field directions.

Figure 4c shows the normalized value of the nonlocal resistances ($R_{nl,\beta} / R_{nl,0}$) as a function of $\cos^2(\beta^*)$ for the respective applied field (B) direction in the dephased regime, which is highlighted by the shaded region in Fig. 4b. Here, β^* is the angle with a smaller correction of the out-of-plane tilting angle of the FM contacts due to the external magnetic field⁵⁵. The average value of data points is accounted to reduce the effect of the measurement noise in the analysis. We fitted the data points with the following equation 3 (Fig. 4c).

$$\frac{R_{NL}^{\beta}}{R_{NL}^0} = \sqrt{\cos^2(\beta) + \frac{1}{\xi} \sin^2(\beta)}^{-1} \exp \left[-\frac{L}{\lambda_{\parallel}} \left(\sqrt{\cos^2(\beta) + \frac{1}{\xi} \sin^2(\beta)} - 1 \right) \right] \cos^2(\beta^*) \quad (3)$$

Here, L represents the heterostructure channel length, and λ_{\parallel} is the in-plane spin diffusion length. We found anisotropy, $\xi \approx 1.6 \pm 0.13$ at in the Gr-MoS₂ heterostructure channel. We estimated the spin-valley coupling in the Gr-MoS₂ heterostructure by using the following equation:

$$\xi = \left(\frac{\lambda_{VZ}}{\lambda_R} \right)^2 \frac{\tau_{iv}}{\tau_p} + \frac{1}{2} \quad (4)$$

Here, λ_{VZ} and λ_R are the valley Zeeman and Rashba SOC constants; τ_{iv} and τ_p are the intervalley and momentum scattering lifetimes. We found $\lambda_{VZ} \sim 238 \mu\text{eV}$ by considering $\tau_{iv} \approx \tau_p$ and $\lambda_R = 227 \mu\text{eV}$. The exact ratio of $\frac{\tau_{iv}}{\tau_p}$ is difficult to estimate; however, the relatively lower ξ must be compatible with our assumption, whereas the theoretical study report an anisotropy of $\xi \approx 20$, considering $\tau_{iv} \approx 5\tau_p$ ⁵⁴. We also compared the estimated anisotropy in pristine graphene by measuring oblique Hanle spin signals in different magnetic field directions, as shown in Fig 4d. Figure 4e shows the normalized value of the nonlocal resistances ($R_{nl,\beta} / R_{nl,0}$) as a function of $\cos^2(\beta^*)$ for the respective B direction in the fully dephased regime, which is highlighted by the

shaded region in Fig 4d. The fit to equation 3 with the data points provides an estimation of anisotropy close to unity, $\xi \approx 0.91 \pm 0.12$, shown in Fig. 4e. It is expected that graphene on SiO_2 substrate with a lower SOC should render isotropic spin lifetime^{46,54}.

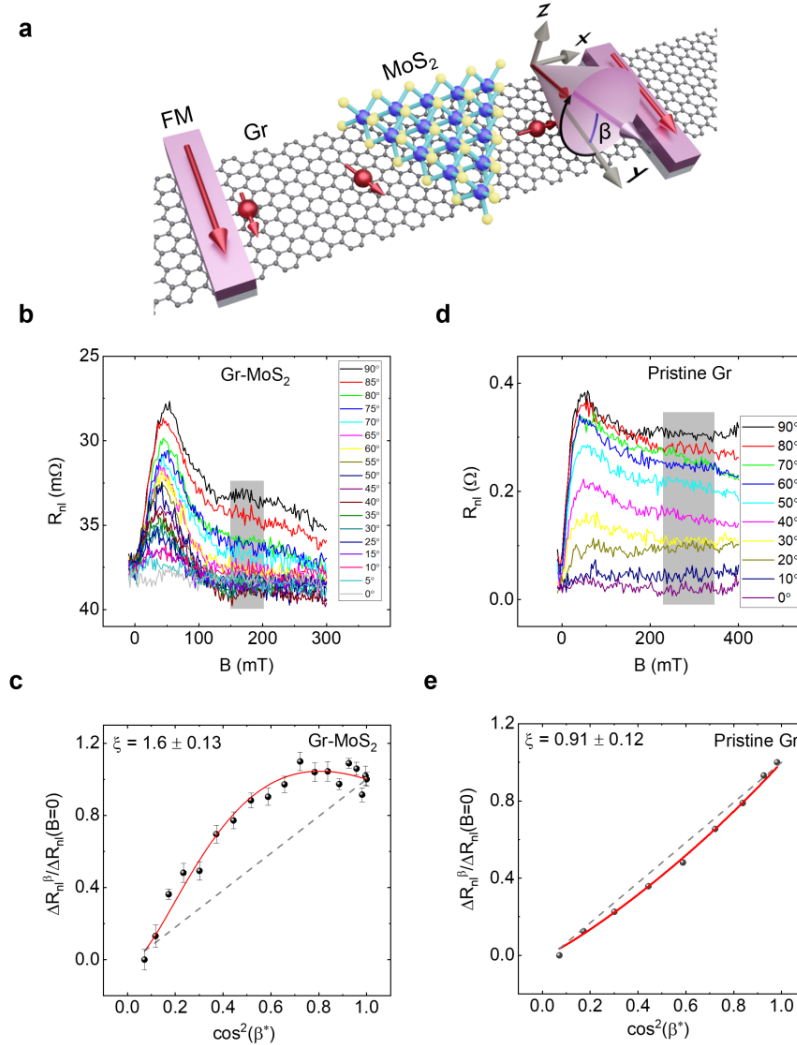


Figure 4: Spin-lifetime anisotropy in all-CVD graphene-MoS₂ heterostructure at room temperature. (a) Schematic illustration of the device and measurement scheme for spin precession in Gr-MoS₂ heterostructure with an oblique magnetic field. The applied magnetic field is at an angle β along the magnetic easy axis of the FM contacts (y-axis) in the yz-plane. (b) Spin precession signals as a function of changing B field at different angles in Dev1 with $I = -350 \mu\text{A}$ at $V_g = 40\text{V}$ at room temperature. (c) Data points denote normalized nonlocal resistances ($R_{nl,\beta}/R_{nl,0}$) as a function of $\cos^2(\beta^*)$ along with the fitting (red line) to equation 3 to estimate anisotropy. (d) Spin precession signals as a function of changing B field at different angles with $I = -100\mu\text{A}$ at $V_g = 20\text{V}$ in pristine graphene. (e) Data points denote normalized nonlocal resistances ($R_{nl,\beta}/R_{nl,0}$) as a function of $\cos^2(\beta^*)$ along with the fitting (solid line) to equation 3 to estimate anisotropy in pristine graphene. The dashed lines in c and e visualize the isotropic case.

According to the theoretical calculations and recent experiments in exfoliated Gr-TMDC heterostructures, the anisotropy ξ can be in the range of 1 to 10^{36,39,51,54}. For instance, exfoliated

Gr-MoSe₂ and Gr-WSe₂ heterostructures show $\xi > 10$ at 75K, whereas Gr-WS₂ heterostructure shows $\xi \approx 10$ at room temperature^{39,51}. Furthermore, the anisotropy in exfoliated Gr-MoS₂ heterostructure is estimated to be higher than unity ($\xi > 1$) at room temperature³⁹. We estimated spin lifetime anisotropy of $\xi = 1.6$ in the all-CVD Gr-MoS₂ heterostructure using oblique Hanle measurements, which can be due to proximity induced spin-valley locking in graphene from MoS₂. Interestingly, the anisotropy in the Gr-TMDC heterostructure significantly depends on the intervalley (τ_{iv}) and momentum scattering (τ_p) lifetimes, which also depend on the charge scatterers (n) in the spin transport channel⁵⁴. The proximity SOC strength and anisotropy can also be influenced by the interfacial interstitials, twist-angle and band alignment in the all-CVD Gr-TMDC heterostructure channels^{40,56}.

Summary

We demonstrated spin–valley coupling and spin-relaxation anisotropy in scalable all-CVD grown Gr-MoS₂ vdW heterostructure devices at room temperature. The CVD-grown materials and their heterostructures showed excellent charge and spin transport properties, showing the good quality of the hybrid devices and interfaces. The spin transport and Hanle precession in the heterostructure channel showed increased SOC strength in the proximitized graphene, which is three times higher than that in pristine graphene. The spin relaxation anisotropy properties evaluated using oblique Hanle spin precession measurements revealed an anisotropic spin dynamic of $\xi \sim 1.6$ in the proximitized graphene, compared to $\xi \sim 1$ in the pristine graphene channel. The associated spin-valley coupling strength of 238 μeV is estimated in the all-CVD Gr-MoS₂ heterostructure. The observation of increased SOC strength and spin relaxation anisotropy between the in-plane and perpendicular spin polarization in all-CVD Gr-MoS₂ heterostructures have enormous prospects for making spin filtering devices in scalable all-2D materials. These advances will open opportunities to utilize all-CVD vdW heterostructure devices for the development of next-generation scalable spintronic and quantum devices.

Methods

The devices were fabricated using all-CVD grown monolayer graphene and MoS₂ heterostructures. The four-inch wafer-scale CVD graphene was obtained from Graphenea on a highly doped Si/SiO₂ substrate (with a thermally grown 285-nm-thick SiO₂ layer). First, graphene stripes were patterned by electron beam lithography and oxygen plasma etching and cleaned afterwards by acetone and IPA. The CVD monolayer MoS₂ layers of triangular shape with a typical size of about 50–100 μm were grown by the CVD process as described in ref^{57,58} on a SiO₂ (300 nm)/Si substrate. A wet-transferred technique was employed to transfer CVD MoS₂ on top of patterned CVD graphene stripes⁴⁰. Appropriate heterostructure regions were identified by an optical microscope for device fabrication. We used electron-beam lithography (EBL) to define the contacts and e-beam evaporation for depositing the contacts. We prepare ~ 1 nm of TiO₂ tunnel barrier with deposition of Ti and followed by in situ oxidation for 30 minutes. We deposited Co contacts of 80nm thickness without breaking the vacuum, followed by the lift-off process in warm acetone at 65°C. The Co/TiO₂ contacts serve as injector and detector for spin-polarized carriers and the highly doped Si/SiO₂ is used as a back gate. We found the FM contact resistances with

three-terminal measurement geometry around 3-8k Ω . We used Keithley 6221 current source to apply bias current, Keithley 2182A nanovoltmeter to detect voltage and Keithley 2450 sourcemeter to apply back gate. The transport measurements were conducted in a vacuum cryostat at room temperature with the sample stage rotation facilities and a variable magnetic field.

Acknowledgements

The authors acknowledge financial support from FlagEra project H2O (funded by VR), 2D TECH VINNOVA competence center (No. 2019-00068), EU Graphene Flagship (Core 3, No. 881603), 2D TECH VINNOVA competence center (No. 2019-00068), Swedish Research Council VR project grants (No. 2021-04821), FLAG-ERA project 2DSOTECH (VR No. 2021-05925), Graphene center, Ei Nano, and AoA Materials program at Chalmers University of Technology. We acknowledge the help of staff at the Quantum Device Physics laboratory and Nanofabrication laboratory in our Department of Microtechnology and Nanoscience at the Chalmers University of Technology.

Data availability

The data that support the findings of this study are available from the corresponding authors on a reasonable request.

Competing interests

The authors declare no competing interests.

Reference

1. Dieny, B. *et al.* Opportunities and challenges for spintronics in the microelectronics industry. *Nat. Electron.* **3**, 446–459 (2020).
2. Žutić, I., Fabian, J. & Das Sarma, S. Spintronics: Fundamentals and applications. *Rev. Mod. Phys.* **76**, 323–410 (2004).
3. Lin, X., Yang, W., Wang, K. L. & Zhao, W. Two-dimensional spintronics for low-power electronics. *Nat. Electron.* **2**, 274–283 (2019).
4. Behin-Aein, B., Datta, D., Salahuddin, S. & Datta, S. Proposal for an all-spin logic device with built-in memory. *Nat. Nanotechnol.* **5**, 266–270 (2010).
5. Geim, A. K. & Novoselov, K. S. The rise of graphene. *Nat. Mater.* **6**, 183–191 (2007).
6. Khokhriakov, D. *et al.* Multifunctional Spin Logic Gates In Graphene Spin Circuits. *arXiv Prepr.* (2021). doi:10.48550/arxiv.2108.12259.
7. Khokhriakov, D., Karpiak, B., Hoque, A. M. & Dash, S. P. Two-dimensional spintronic circuit architectures on large scale graphene. *Carbon N. Y.* **161**, 892–899 (2020).
8. Kamalakar, M. V., Groenveld, C., Dankert, A. & Dash, S. P. Long distance spin communication in chemical vapour deposited graphene. *Nat. Commun.* **6**, 6766 (2015).
9. Gmitra, M., Konschuh, S., Ertler, C., Ambrosch-Draxl, C. & Fabian, J. Band-structure topologies of graphene: Spin-orbit coupling effects from first principles. *Phys. Rev. B* **80**, 235431 (2009).
10. Sierra, J. F., Fabian, J., Kawakami, R. K., Roche, S. & Valenzuela, S. O. Van der Waals heterostructures for spintronics and opto-spintronics. *Nat. Nanotechnol.* **16**, 856–868 (2021).
11. Balakrishnan, J. *et al.* Giant spin Hall effect in graphene grown by chemical vapour deposition. *Nat. Commun.* **5**, 4748 (2014).

12. Balakrishnan, J., Kok Wai Koon, G., Jaiswal, M., Castro Neto, A. H. & Özyilmaz, B. Colossal enhancement of spin–orbit coupling in weakly hydrogenated graphene. *Nat. Phys.* **9**, 284–287 (2013).
13. Pi, K. *et al.* Manipulation of Spin Transport in Graphene by Surface Chemical Doping. *Phys. Rev. Lett.* **104**, 187201 (2010).
14. Avsar, A. *et al.* Colloquium : Spintronics in graphene and other two-dimensional materials. *Rev. Mod. Phys.* **92**, 021003 (2020).
15. Ahn, E. C. 2D materials for spintronic devices. *npj 2D Mater. Appl.* **4**, 17 (2020).
16. Gmitra, M. & Fabian, J. Graphene on transition-metal dichalcogenides: A platform for proximity spin-orbit physics and optospintronics. *Phys. Rev. B* **92**, 155403 (2015).
17. Gmitra, M., Kochan, D., Högl, P. & Fabian, J. Trivial and inverted Dirac bands and the emergence of quantum spin Hall states in graphene on transition-metal dichalcogenides. *Phys. Rev. B* **93**, 155104 (2016).
18. Song, K. *et al.* Spin Proximity Effects in Graphene/Topological Insulator Heterostructures. *Nano Lett.* **18**, 2033–2039 (2018).
19. Khokhriakov, D., Hoque, A. M., Karpiak, B. & Dash, S. P. Gate-tunable spin-galvanic effect in graphene-topological insulator van der Waals heterostructures at room temperature. *Nat. Commun.* **11**, 3657 (2020).
20. Cao, Y. *et al.* Correlated insulator behaviour at half-filling in magic-angle graphene superlattices. *Nature* **556**, 80–84 (2018).
21. Cao, Y. *et al.* Unconventional superconductivity in magic-angle graphene superlattices. *Nature* **556**, 43–50 (2018).
22. Garcia, J. H., Vila, M., Cummings, A. W. & Roche, S. Spin transport in graphene/transition metal dichalcogenide heterostructures. *Chem. Soc. Rev.* **47**, 3359–3379 (2018).
23. Szentpéteri, B. *et al.* Tailoring the Band Structure of Twisted Double Bilayer Graphene with Pressure. *Nano Lett.* **21**, 8777–8784 (2021).
24. Island, J. O. *et al.* Spin–orbit-driven band inversion in bilayer graphene by the van der Waals proximity effect. *Nature* **571**, 85–89 (2019).
25. Fülöp, B. *et al.* Boosting proximity spin–orbit coupling in graphene/WSe₂ heterostructures via hydrostatic pressure. *npj 2D Mater. Appl.* **5**, 82 (2021).
26. Wang, Z. *et al.* Strong interface-induced spin-orbit interaction in graphene on WS₂. *Nat. Commun.* **6**, (2015).
27. Wang, Z. *et al.* Origin and magnitude of “designer” spin-orbit interaction in graphene on semiconducting transition metal dichalcogenides. *Phys. Rev. X* **6**, 041020 (2016).
28. Dankert, A. & Dash, S. P. Electrical gate control of spin current in van der Waals heterostructures at room temperature. *Nat. Commun.* **8**, 16093 (2017).
29. Yan, W. *et al.* A two-dimensional spin field-effect switch. *Nat. Commun.* **7**, 13372 (2016).
30. Luo, Y. K. *et al.* Opto-Valleytronic Spin Injection in Monolayer MoS₂/Few-Layer Graphene Hybrid Spin Valves. *Nano Lett.* **17**, 3877–3883 (2017).
31. Safeer, C. K. *et al.* Room-Temperature Spin Hall Effect in Graphene/MoS₂ van der Waals Heterostructures. *Nano Lett.* **19**, 1074–1082 (2019).
32. Benítez, L. A. *et al.* Tunable room-temperature spin galvanic and spin Hall effects in van der Waals heterostructures. *Nat. Mater.* **19**, 170–175 (2020).
33. Ghiasi, T. S., Kaverzin, A. A., Blah, P. J. & van Wees, B. J. Charge-to-Spin Conversion by the Rashba–Edelstein Effect in Two-Dimensional van der Waals Heterostructures up to Room Temperature. *Nano Lett.* **19**, 5959–5966 (2019).
34. Avsar, A. *et al.* Optospintronics in Graphene via Proximity Coupling. *ACS Nano* **11**, 11678–11686 (2017).
35. Luo, Y. K. *et al.* Opto-Valleytronic Spin Injection in Monolayer MoS₂/Few-Layer Graphene Hybrid Spin Valves. *Nano Lett.* **17**, 3877–3883 (2017).
36. Benítez, L. A. *et al.* Investigating the spin-orbit interaction in van der Waals heterostructures by means of the spin relaxation anisotropy. *APL Mater.* **7**, 120701 (2019).
37. Schaibley, J. R. *et al.* Valleytronics in 2D materials. *Nat. Rev. Mater.* **1**, 16055 (2016).
38. Mak, K. F., He, K., Shan, J. & Heinz, T. F. Control of valley polarization in monolayer MoS₂ by optical helicity. *Nat. Nanotechnol.* **7**, 494–498 (2012).
39. Benítez, L. A. *et al.* Strongly anisotropic spin relaxation in graphene–transition metal

- dichalcogenide heterostructures at room temperature. *Nat. Phys.* **14**, 303–308 (2018).
40. Mupparapu, R., Bucher, T. & Staude, I. Integration of two-dimensional transition metal dichalcogenides with Mie-resonant dielectric nanostructures. *Adv. Phys. X* **5**, 1734083 (2020).
 41. Radisavljevic, B., Radenovic, A., Brivio, J., Giacometti, V. & Kis, A. Single-layer MoS₂ transistors. *Nat. Nanotechnol.* **6**, 147–150 (2011).
 42. Allain, A., Kang, J., Banerjee, K. & Kis, A. Electrical contacts to two-dimensional semiconductors. *Nature Materials* **14**, 1195–1205 (2015).
 43. Kim, T., Fan, S., Lee, S., Joo, M.-K. & Lee, Y. H. High-mobility junction field-effect transistor via graphene/MoS₂ heterointerface. *Sci. Rep.* **10**, 13101 (2020).
 44. Chee, S. S. *et al.* Lowering the Schottky Barrier Height by Graphene/Ag Electrodes for High-Mobility MoS₂ Field-Effect Transistors. *Adv. Mater.* **31**, 1804422 (2019).
 45. Cui, X. *et al.* Multi-terminal transport measurements of MoS₂ using a van der Waals heterostructure device platform. *Nat. Nanotechnol.* **10**, 534–540 (2015).
 46. Khokhriakov, D. *et al.* Robust Spin Interconnect with Isotropic Spin Dynamics in Chemical Vapor Deposited Graphene Layers and Boundaries. *ACS Nano* **14**, 15864–15873 (2020).
 47. Rashba, E. I. Theory of electrical spin injection: Tunnel contacts as a solution of the conductivity mismatch problem. *Phys. Rev. B - Condens. Matter Mater. Phys.* **62**, (2000).
 48. Fert, A. & Jaffrès, H. Conditions for efficient spin injection from a ferromagnetic metal into a semiconductor. *Phys. Rev. B - Condens. Matter Mater. Phys.* **64**, 184420 (2001).
 49. Herling, F. *et al.* Gate tunability of highly efficient spin-to-charge conversion by spin Hall effect in graphene proximitized with WSe₂. *APL Mater.* **8**, 071103 (2020).
 50. Omar, S. & Van Wees, B. J. Spin transport in high-mobility graphene on WS₂ substrate with electric-field tunable proximity spin-orbit interaction. *Phys. Rev. B* **97**, 045414 (2018).
 51. Ghiasi, T. S., Ingla-Aynés, J., Kaverzin, A. A. & van Wees, B. J. Large Proximity-Induced Spin Lifetime Anisotropy in Transition-Metal Dichalcogenide/Graphene Heterostructures. *Nano Lett.* **17**, 7528–7532 (2017).
 52. Khokhriakov, D. *et al.* Tailoring emergent spin phenomena in Dirac material heterostructures. *Sci. Adv.* **4**, eaat9349 (2018).
 53. Gurram, M., Omar, S. & van Wees, B. J. Electrical spin injection, transport, and detection in graphene-hexagonal boron nitride van der Waals heterostructures: progress and perspectives. *2D Mater.* **5**, 032004 (2018).
 54. Cummings, A. W., Garcia, J. H., Fabian, J. & Roche, S. Giant Spin Lifetime Anisotropy in Graphene Induced by Proximity Effects. *Phys. Rev. Lett.* **119**, 206601 (2017).
 55. Raes, B. *et al.* Determination of the spin-lifetime anisotropy in graphene using oblique spin precession. *Nat. Commun.* **7**, 11444 (2016).
 56. David, A., Rakyta, P., Kormányos, A. & Burkard, G. Induced spin-orbit coupling in twisted graphene-transition metal dichalcogenide heterobilayers: Twistronics meets spintronics. *Phys. Rev. B* **100**, 85412 (2019).
 57. van der Zande, A. M. *et al.* Grains and grain boundaries in highly crystalline monolayer molybdenum disulphide. *Nat. Mater.* **12**, 554–561 (2013).
 58. George, A. *et al.* Controlled growth of transition metal dichalcogenide monolayers using Knudsen-type effusion cells for the precursors. *JPhys Mater.* **2**, 016001 (2019).

Paper VI

Ultra-narrow Semiconductor WS₂ Nanoribbon Field-effect Transistors with Atomically Designed Zig-zag Edges

Anamul Md. Hoque, Aleksandr Poliakov, Battulga Munkhbat, Abhay V. Agrawal, Bing Zhao, Richa Mitra, Sergey Kubatkin, Samuel Lara Avila, Timur O. Shegai*, Saroj P. Dash*

Department of Microtechnology and Nanoscience, Chalmers University of Technology, SE-41296, Göteborg, Sweden

Department of Physics, Chalmers University of Technology, SE-41296, Göteborg, Sweden

Abstract

Semiconducting transition metal dichalcogenides (TMDs) have attracted tremendous interest for high-performance, energy-efficient, and nanoscale field-effect transistors (FETs). In spite of recent progress on down-scaling the gate and channel lengths of TMD FETs, the fabrication of sub-25 nm narrow channel remained challenging and devices with atomic-scale control over the edges are so far lacking. Here, we demonstrate the fabrication of ultra-narrow tungsten disulfide (WS₂) nanoribbon down to sub-10 nm width with atomically sharp zig-zag edges using a controlled anisotropic wet chemical nanostructuring technique. Nanoribbon FETs measured down to 18 nm exhibit good transistor performance, where the transport parameters such as on-current, mobility, and the threshold voltage are predominantly governed by the narrow channel effects. The mobility in the narrow channels are found to be limited by the impurity scattering in comparison to the wider channels. The observation of a bias and gate-induced metal-insulator transition with temperature can be attributed to the percolation transport mechanism in the channels. These findings open the door for the fabrication of future-generation nanometer-scale van der Waals semiconductor based devices.

Keywords: 2D semiconductors, WS₂, Nanoribbon, transition metal dichalcogenides, TMDs, zig-zag edge, nanotransistor, 2D field-effect transistor.

Corresponding authors: Timur O. Shegai*, Saroj P. Dash*

Introduction

Semiconductor field-effect transistors (FETs) representing the basic building blocks of modern computers, have revolutionized information technology due to successful miniaturization over several decades¹. However, continued down-scaling of conventional silicon transistors has reached its physical limits and poses critical challenges for its high-performance and energy efficiency². To facilitate continued progress, two-dimensional (2D) semiconducting transition metal dichalcogenides (TMDs) have attracted tremendous interest due to their atomically thin body and dangling-bond-free surface³. The ultimate miniaturization of TMD-based FETs will allow sustainable progress in Moore's scaling law for high-density integration⁴ and enhanced performance beyond silicon technologies^{5–8}.

The design and control of semiconducting TMD-based FETs and engineering their properties at an atomic scale are challenging and of paramount importance for advances in basic science and technology^{9,10}. Recently, considerable efforts have been devoted to scale-down the channel length and width of the TMD-based FETs^{11–13}. Devices with planar and vertical TMD FET structures of sub-10nm channel length¹⁴ and sub-nm gate dimensions with carbon nanotube¹⁵ and graphene⁴ are realized^{4,14–16}. However, the channel width of the state-of-the-art devices is mostly limited to be more than 25 nm^{11,13,17,18} due to limited resolution of lithography processes and physical etching techniques used so far. Importantly, controlling edge structures remains one of the main interests because electronic properties of the edge-states become increasingly relevant in such nanoscale transistors^{19–21}.

Here, we demonstrate the fabrication of ultra-narrow WS₂ nanoribbons down to 5 nm width with atomically sharp zig-zag edges using a wet-chemical anisotropic etching technique with atomic precision¹⁹. Transistor performance with good channel conductance could be measured down to 18 nm width of WS₂. The nanoribbons FETs of different widths (18 - 70 nm) are systematically investigated, showing the transport properties in the extremely narrow channels to be governed by the narrow channel effects. The mobility in the channel FETs is found to be limited by the impurity scattering process in comparison to the wider channels. A bias and gate-induced metal-to-insulator transition (MIT) is observed in the temperature dependence of FETs, elucidating the percolation transport mechanism in the nanoribbons. These findings can promote the scaling down of transistors for next-generation electronics.

Results and Discussion

Device architecture and fabrication processes of WS₂ nanoribbon FETs

Figure 1a. presents the schematic of ultra-narrow nanoribbon FETs with multilayer WS₂ channels having atomically controlled zig-zag edges along with the measurement geometry. The colored scanning electron microscopic (SEM) image of the fabricated nanoribbon FETs of various channel widths is shown in Fig. 1b. Figure 1c shows the crucial steps for the fabrication of nanoribbons, where WS₂ flakes were exfoliated on SiO₂/n-Si substrate and are patterned first by electron lithography and CHF₃ ion beam etching. This is followed by a final anisotropic wet chemical etching in hydrogen peroxide (H₂O₂) to fabricate WS₂ nanoribbons down to 5 nm width with zig-zag and

atomically sharp edges¹⁹ (see the Methods for details). Figure 1d shows a comparison of our nanofabricated TMD nanoribbon channel width with the state-of-the-art results, where channel width is limited by the resolution of lithography processes and physical etching techniques. Electronic transport properties are investigated in WS₂ nanoribbons FETs of different channel widths $W = 9$ nm to 47 nm in the same flake, thickness of $t \sim 35$ nm, channel length $L = 600$ to 800 nm, with Ti/Au source and drain contacts and n⁺⁺Si/SiO₂ substrate as back-gate.

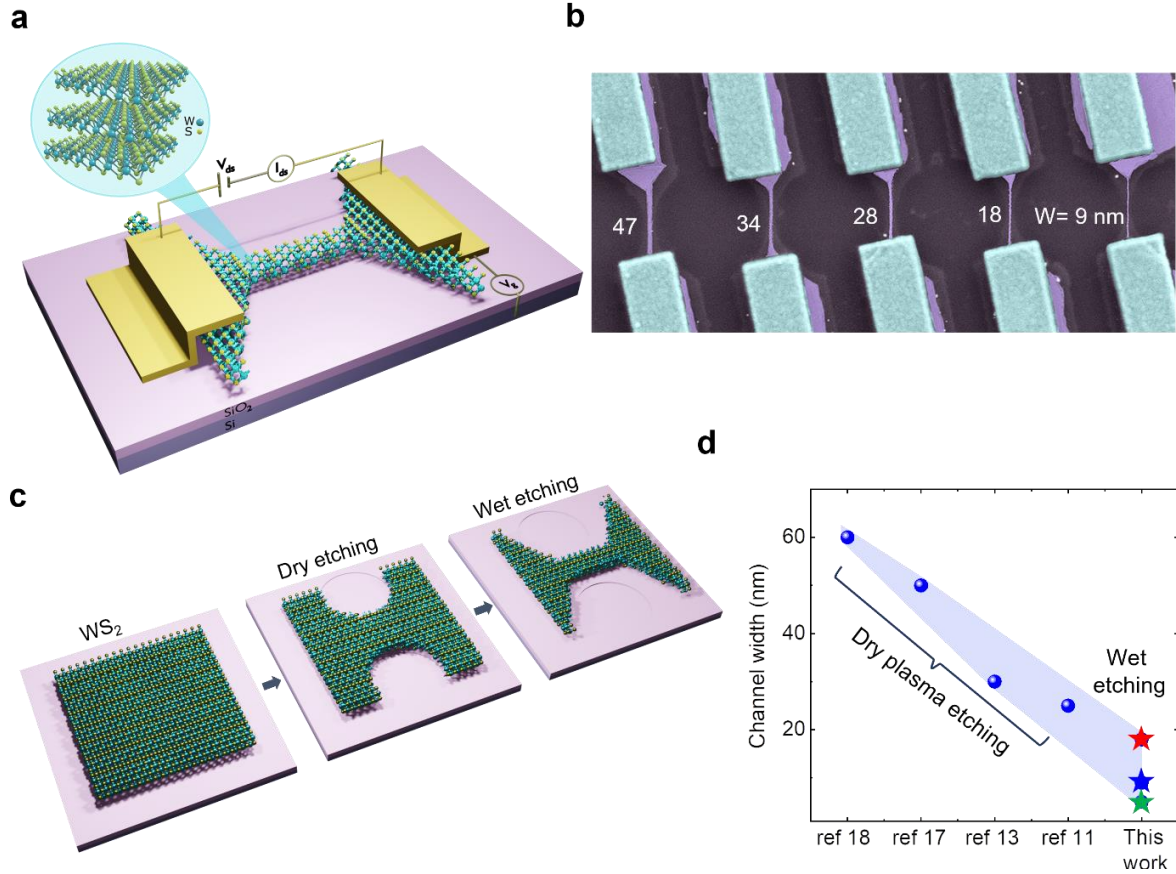


Figure 1. Ultra-narrow nanoribbon WS₂ field-effect transistors with zig-zag edges. **a,b.** Schematics and colored scanning electron microscopic image of the fabricated multilayer WS₂ nanoribbon FETs on Si/SiO₂ substrate. **c.** Key process steps for fabricating WS₂ nanoribbons with zig-zag edges by combining dry-plasma (CHF₃) and wet-chemical (H₂O₂) etching and nano-patterning processes. **d.** Comparison of our nanofabricated WS₂ nanoribbon channel-width with state-of-the-art results.

Transport measurements of WS₂ nanoribbon FETs

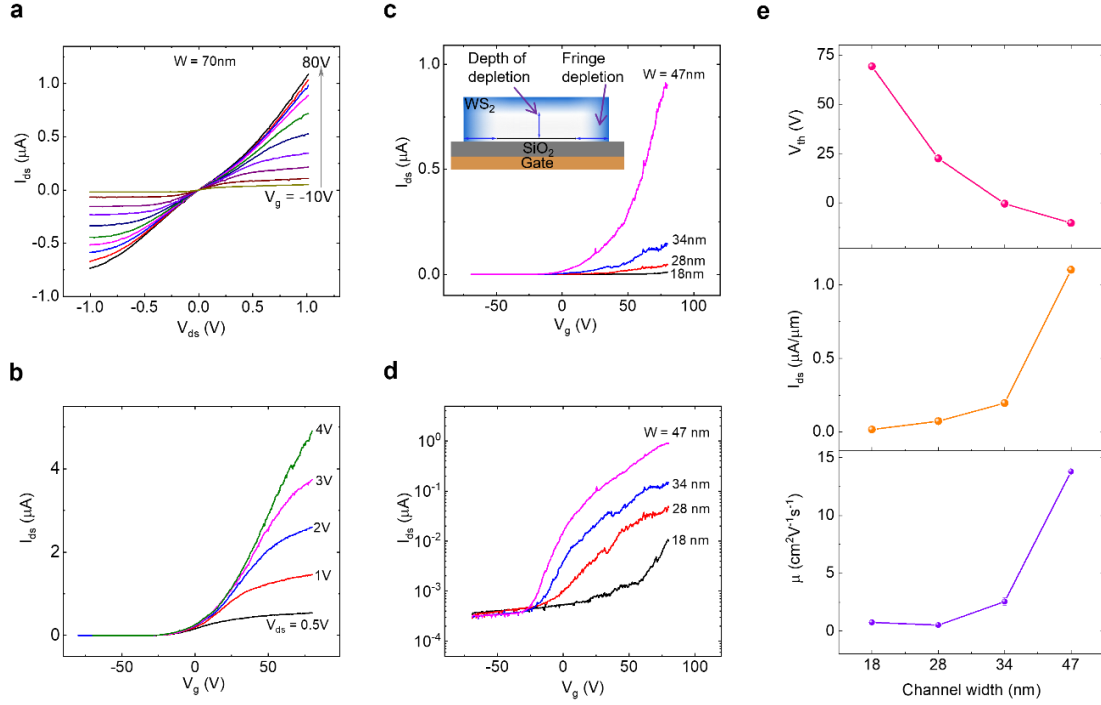


Figure 2: Field effect transistor properties of WS₂ nanoribbons. (a) Output characteristics are showing I_{ds} vs. V_{ds} of WS₂ nanoribbon FET with a channel width of 70 nm at different gate voltages. (b) Transfer characteristics of WS₂ FET with 70 nm channel width at different bias voltages. (c) Transfer characteristics of WS₂ nanoribbons for different channel widths with $V_{ds} = 5V$. Inset schematic explains the narrow channel effect, where the fringe-depletion enhances the threshold voltage (V_{th}) in the channels. (d) Semilog plots of transfer characteristics for different widths of WS₂ nanoribbon. (e) The plots of threshold voltages V_{th} (top panel), on-state current level I_{ds} (middle panel) at $V_g = 80V$, and field-effect mobilities μ (bottom panel) for WS₂ nanoribbon FETs with different channel widths measured with $V_{ds} = 5V$. The error bars in estimating mobilities are calculated from the noise level in determining the transconductance.

First, electrical transport measurements were performed to investigate WS₂ nanoribbon properties at room temperature. Figure 2a shows the measured output characteristics of a WS₂ nanoribbon ($W \sim 70nm$) with source-drain current (I_{ds}) as a function of applied source-drain voltage (V_{ds}) at various back-gate voltages, $V_g = -10$ to $80V$. The nanoribbon channel conductance increases monotonically with increasing V_{ds} for a fixed applied gate voltage V_g . It is evident that with increasing V_g , the I_{ds} increase due to increasing carrier concentration in the WS₂ nanoribbon channel. Figure 2b shows transfer characteristics (I_{ds} vs. V_g) of the WS₂ nanoribbon at different V_{ds} on a linear scale. We observed an increase of I_{ds} with increasing positive V_g , which resembles typical n-type transport behavior, as expected for WS₂²². From the transfer characteristics, the field effect mobility ($\mu = \frac{L}{WC_g V_{ds}} \cdot \frac{dI_{ds}}{dV_g}$) is estimated to be $24 \text{ cm}^2\text{V}^{-1}\text{s}^{-1}$ with $V_{ds} = 1V$, where the gate capacitance per unit area, $C_g = \epsilon\epsilon_0/d_{ox} = 1.15 \times 10^{-8} \text{ Fcm}^{-2}$ ($d_{ox} = 285 \text{ nm}$ SiO₂ structure with relative dielectric constant $\epsilon = 4.9$), L and W are channel length and width, respectively, V_{ds} is the applied drain-source voltage

and $\frac{dI_{ds}}{dV_g}$ is the transconductance (g_m). We estimated Schottky barrier height (SBH) of WS₂ nanoribbon with Ti/Au contact to be $\Phi_b = 78 \pm 2.5$ meV at $V_g = 80$ V using thermionic-emission model^{23–26} (see details in Supplementary Fig. S1).

Narrow channel effects in WS₂ nanoribbon FETs

To observe the evolution of electrical transport properties, we compared WS₂ nanoribbon FETs with different widths (18 to 47 nm) fabricated on the same flake. Figure 2c and 2d show the transfer characteristics of different channel widths of WS₂ nanoribbon FETs in linear and log scale, respectively. In the WS₂ nanoribbons, when the gate-induced depletion region is comparable to the channel width, the narrow channel effect should emerge in the transport measurements²⁷, as schematically presented in the inset of Fig. 2c. In narrow channels, the effect of the fringe depletion region should be significant in contrast to the wider channel, as the latter has enough space for strong inversion²⁷. The origin of the fringe depletion most likely due to the surface adsorbents (e.g., water, etchants) that results in carrier depletion¹³. The inversion region in the narrow channel requires it to act on both fringe depletion and field depletion via an applied gate voltage, which eventually enhances the threshold voltage (V_{th}) to accumulate charge carriers^{13,18}.

As shown in Fig. 2e, we observe strong modulation in device parameters due to narrow channel effects in WS₂ nanoribbon FETs, such as on-state current (I_{ds}), threshold voltages (V_{th}), and field-effect mobilities. It is conspicuous that with increasing channel width (W) of nanoribbon, the corresponding on-state current also increases because channel conductance ($G = \frac{I_{ds}}{V_{ds}} = \frac{\sigma W t}{L}$) is directly proportional to the width of the channel. We also observe that the V_{th} increases with decreasing channel width due to the narrow channel effect, since $\Delta V_{th} \propto \left(1 + \frac{\pi X_{depmax}}{2W}\right)$ ²⁸. Here, X_{depmax} and W are the maximum depth of depletion in WS₂ nanoribbon and W is the channel width, respectively. As long as $W \gg X_{depmax}$, ΔV_{th} does not scale much with W , but when $W \leq X_{depmax}$, then ΔV_{th} greatly scales with W . Furthermore, relative channel current (I_{ds}/L , L is the channel length) decreases with decreasing channel width, and it can be understood by considering that the channel current would decrease since V_{th} increases in narrower channels. We could also measure the FETs with 9 nm and 5 nm channel width that show further shift of V_{th} to higher gate voltages due to carrier depletion (see Fig. S2). The extremely narrow channel should be more susceptible to the depletion width and edge-induced scattering mechanisms, which would limit the mobility in the channel. From the transfer characteristics, the field-effect mobility (μ) is estimated for different channel widths. The observed enhancement of μ with increasing channel width can be attributed to the relatively less edge/boundary induced scattering in wider channels in comparison to narrow channels^{13,17}.

Temperature dependence of transport properties in WS₂ nanoribbon

Next, we investigated the evolution of the transport properties in WS₂ nanoribbon FETs with temperature (T) for different channel widths. Figure 3 (a,b,c) presents the measured transfer properties in color contour plots at different T for WS₂ nanoribbon FETs of 18, 28, and 34 nm wide channels, respectively. We observed an insulating behavior in 18 nm wide WS₂ nanoribbon channel. However, we observed a gate- and bias-voltage induced metal-to-insulator transition in wider

nanoribbons (28 and 34 nm), which showed an insulating property at the low T range (<200K) and metallic behavior at higher T range (>200K).

The evolution of field-effect mobility (μ) with temperature T is presented in Fig. 3 d,e,f for WS₂ nanoribbon FETs of 18, 28 and 34 nm channel widths, respectively. The generic dependency of μ on T is fitted with $\mu \propto T^\gamma$, where the exponent γ depends on the scattering mechanism in the nanoribbons^{22,29}. For the 18 nm nanoribbon channel, we observe an increase of μ with an increase with T at low temperature and saturation for higher T (> 235 K). We estimate $\gamma \approx 8.6$ due to mainly the boundary/edge or impurity scattering process in the 18 nm FET. Whereas for 28 nm FET, the $\gamma \approx 0.95$ at the low T limit (< 165 K) and $\gamma \approx -7.8$ at the higher T limit are estimated. The limiting factor of μ at the low T range can be correlated to the edge or impurity scattering mechanisms, whereas μ is mainly dominated by phonon scattering at the higher T range (>250 K)^{22,29,30}. Similarly, for nanoribbon of 34 nm, we estimate $\gamma \approx 1.94$ at a lower T range (<150 K), ascribing to the dominating edge/impurity scattering mechanism for limiting channel mobility. At the higher T range (>200 K), $\gamma \approx -4.7$, consistent with the phonon scattering mechanisms limiting the channel mobility. Overall, in the wider channels, the dependencies of μ on T in the low-temperature regime are consistent with transport dominated by impurity scattering, whereas above ~ 200 K is limited by phonon scattering. The narrowest channel shows dominant edge or impurity scattering in comparison to wider channels, as expected because transport in narrow channels are more influenced by the WS₂ edges. Therefore, it is important to control the edge structures of TMD nanoscale devices by controlled fabrication processes. The edge structures in our devices are sharp and zigzag-terminated¹⁹ compared to the nano-ribbons that are fabricated via physical etching techniques.

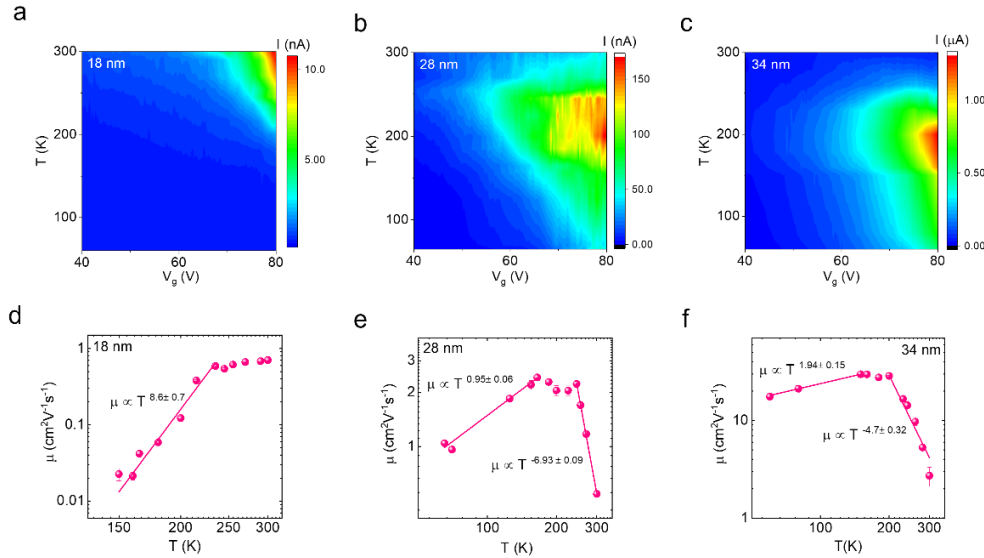


Figure 3: Temperature dependence of WS₂ nanoribbon FET device parameters. (a,b,c) Colour contour plots of the transfer characteristics within $V_g = 40\text{-}80\text{V}$ of the WS₂ FETs with 18, 28 and 34 nm channel widths at different temperatures. (d,e,f) Mobility μ as a function of the temperature T of the WS₂ nanoribbon FETs with 18, 28 and 34 nm channel widths along with the power-law fitting with $\mu \propto T^\gamma$ (solid line) in different temperature ranges. The exponent γ depends on the scattering mechanism in the nanoribbons. Error bars are estimated based on uncertainties in determining the conductance across the channel.

Gate and bias induced of metal to insulator transition in WS₂ nanoribbon

We further examined the bias-dependent transport properties with temperature to verify the influence of the edges or impurity states in our WS₂ nanoribbon devices. Figure 4a shows the transfer characteristics of WS₂ nanoribbon FET ($w = 70\text{nm}$) at different temperatures with $V_{ds} = 0.25\text{V}$, 1V , and 2V , respectively. The WS₂ nanoribbon FET demonstrates insulating properties at lower bias voltage ($V_{ds} = 0.25\text{V}$) within the $80\text{--}300\text{K}$ temperature range. However, with applied $V_{ds} = 1\text{V}$, the transistor deviates from insulating behavior with temperature, especially at higher temperature limits ($T > 275\text{K}$), and remains metallic afterward at high V_g . Interestingly, a stronger gate-induced MIT is observed in the WS₂ nanoribbon FET for higher $V_{ds} = 2\text{V}$ with a transition at $V_g = 70\text{V}$. To clearly visualize the MIT, I_{ds} as a function of temperature is plotted in Fig. 4b for different V_{ds} at $V_g = 80\text{V}$. Channel current I_{ds} monotonically increase with T for $V_{ds} = 0.25\text{V}$, whereas for $V_{ds} = 1\text{V}$ the I_{ds} first increases with T but afterward decrease with increasing T ($T > 275\text{K}$), and $V_{ds} = 2\text{V}$ data shows a monotonic decrease of I_{ds} with increasing T resembling the metallic transport.

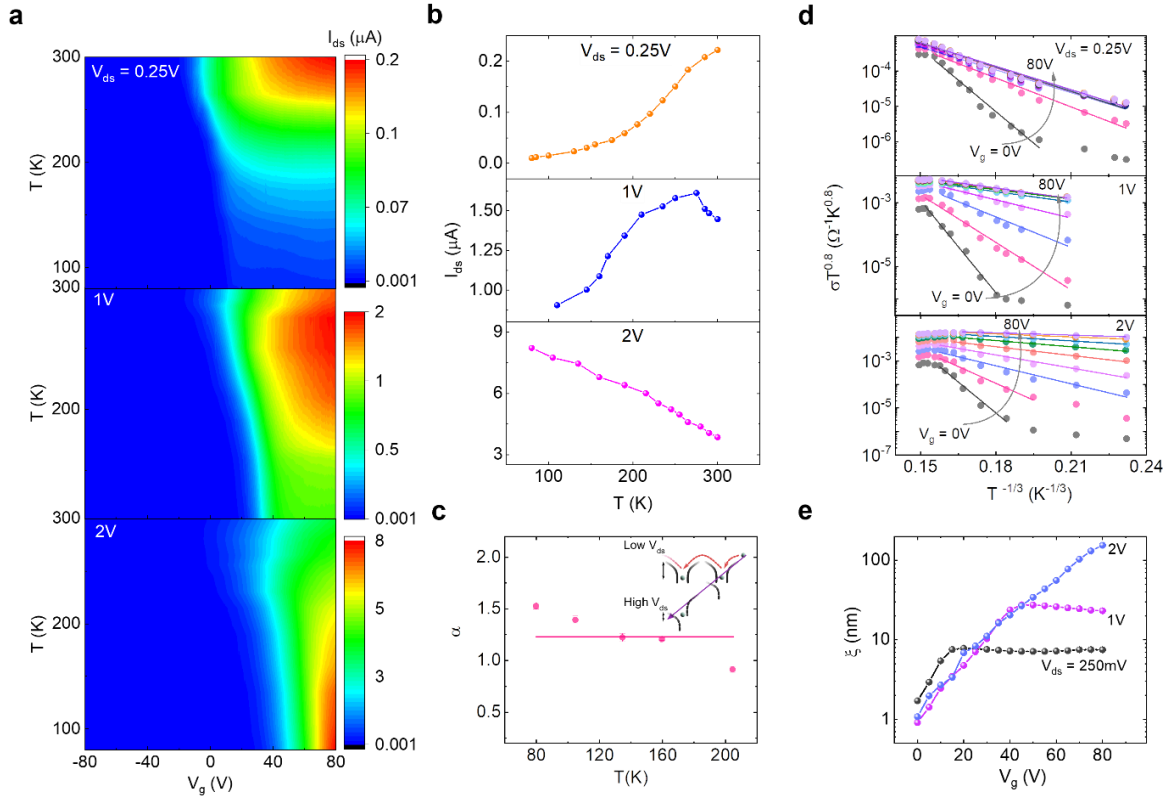


Figure 4: Gate and bias induced metal to insulator transition in WS₂ nanoribbon FET. (a) Colour contour plots of the temperature dependence of transfer characteristics in WS₂ nanoribbon transistor with a channel width of 70nm at $V_{ds} = 0.25\text{V}$ (top panel), 1V (middle panel), and 2V (bottom panel). (b) I_{ds} as a function of temperature in WS₂ nanoribbon transistor at $V_g = 80\text{V}$ with $V_{ds} = 0.25\text{V}$ (top panel), 1V (middle panel), and 2V (bottom panel). (c) Derived exponent (α) at different temperatures from the power-law fitting to verify the percolation transport mechanism in the WS₂ nanoribbon FET. Inset shows the deformation of the potential barrier with respect to the applied electric field in the conduction band. (d) Arrhenius plot of $\sigma T^{0.8}$ as a function

of $T^{-1/3}$ along with the linear fitting to demonstrate 2D VRH with $V_{ds} = 0.25V$ (top panel), $1V$ (middle panel) and $2V$ (bottom panel). **(e)** localization length (ξ) at different V_g for $V_{ds} = 0.25V$ (black dots), $1V$ (red dots) and $2V$ (blue dots).

Gate and bias-induced MIT observed in WS_2 nanoribbons can be attributed to the percolation transport mechanism in TMDs in a strongly correlated regime^{30–32}. The strength of the Coulomb interaction of the carriers can be estimated by the Wigner-Seitz radius (r_s), which is the ratio between Coulomb potential, E_c , and kinetic (Fermi, E_F) energy of the carriers using the following equation^{29,33}.

$$r_s = \frac{E_c}{E_F} = \frac{n_v}{\alpha_B^* \sqrt{\pi n_{2D}}} = \frac{n_v m^* e^2}{4\pi \epsilon \hbar^2 \sqrt{\pi n_{2D}}} \quad (1)$$

Here, $n_v = 2$ is degenerate valleys number, $\alpha_B^* = 4\pi\epsilon\hbar^2/m^*e^2$ is effective Bohr radius of the system, $\epsilon = 6.7$ for multilayer WS_2 , $m^* = 0.34m_e$ is the effective mass of the carriers in WS_2 ^{22,34}. We obtain $r_s \sim 5.3$ in the nanoribbon FET at 80K near the MIT region with $V_{ds}=2V$ and a system with $r_s \gg 1$ is considered highly interactive²⁹. Next, MIT due to percolation driven transport and screening of the charge carriers depends on the applied gate voltage with the relationship $\sigma(I_{ds}) = A(n-n_c)^\alpha$, where A , n , n_c , and α are proportional constant, carrier density, percolation threshold carrier density, and critical percolation exponent, respectively^{31,32}. By considering $n \propto V_g$, we have $(n-n_c)^\alpha \propto (V_g - V_c)^\alpha$; where V_c is critical gate voltage for n_c . When $V_g < V_c$, carriers are strongly bound by the potential valleys and the WS_2 channel shows semiconducting transport properties. For $V_g > V_c$, carriers are weakly bounded by the potential valleys and the WS_2 channel depicts metallic properties. It is expected that in a 2D system, $\alpha = 1.33$ ($4/3$). The estimated α (near the transition region) in the WS_2 nanoribbon FET at $V_{ds} = 2V$ is about 1.23 ± 0.1 , shown in Fig. 4c. In a strongly correlated system considering the percolation transport model, the carriers in the channel transport via the tunneling and hopping across the potential valleys, as presented schematically in the inset of Fig. 4c. As the electric field in the channel increases, the tunneling and hopping probability increase because of distortion and decrease of barrier height, and WS_2 nanoribbon FET shows MIT with gate voltage^{30–32}.

Further, we analysed the bias- and gate-induced MIT in nanoribbon WS_2 FET in light of a two-dimensional (2D) variable range hopping (VRH) model, where carriers hop through the traps states in the crystal structure, along the edges or at the WS_2/SiO_2 interface³⁵. The conductance (σ) in the VRH model can be expressed as

$$\sigma = AT^m e^{-\left(\frac{T_0}{T}\right)^\gamma} \quad (2)$$

where, A^* is constant, T_0 is a hopping parameter related to characteristics temperature, $\gamma = 1/3$ for 2D system and m is between -1 and -0.8 ^{30,35}. Figure 4d shows the Arrhenius plot of $\sigma T^{0.8}$ as a function of $T^{-1/3}$ along with the linear fitting to equation 2 for $V_{ds} = 0.25V$, $1V$ and $2V$, respectively at various V_g . 2D VRH has been reported in various 2D materials, where the localization length increases (ξ) due to efficient screening of the potential of trap states at higher carrier density^{30–32,35,36}. The estimated localization length (ξ) at different gate voltages with $V_{ds} = 0.25V$, $1V$, and $2V$ is depicted in Fig. 4e. It is conspicuous that at the lower $V_{ds} = 0.25V$ and $1V$ the ξ saturates around

8nm and 27nm, respectively with V_g . On the contrary, for $V_{ds} = 2V$ the localization length exponentially increases with V_g and a strong MIT is observed. These findings also support our presumptions of reducing the potential barrier of the trap states at the higher electric field in the percolation mediated transport, presented in Fig. 4c (inset). Here, higher V_{ds} (electric field) assist the gate voltage (V_g) to screen the trap sites (reducing the hopping mediated transport), thus transport takes place through unlocalized states.

Summary

The realization of ultra-narrow WS_2 FETs with atomically controlled zig-zag edges is promising for semiconductor science and technology. The adapted nanostructuring process is compatible with the current semiconductor manufacturing using a top-down approach of anisotropic wet etching in conjunction with physical etching techniques. The charge transport properties in the extremely narrow channels are found to be governed by the narrow channel effects, where the ON current and mobility decrease and V_{th} increase with reducing the channel width. Temperature dependent mobility infers a competitive trend between the phonon and defect mediated scattering, where the defect mediated scattering is dominant in narrower channels. Gate and bias-induced MIT with temperature is observed and attributed to percolation-driven transport in the nanoribbons. In conjunction with the narrow channel widths of TMD FETs demonstrated here, the development of nanostructuring techniques for monolayer materials in a large area will enable a further leap in the miniaturization of transistors. Furthermore, the use of 2D materials heterostructures can enhance the channel mobility and novel device architectures could help to reduce the channel length and gate dimensions to a sub-nm regime for cutting-edge nm-scale devices and electronic circuits⁴. Fabrication and characteristics of ultra-narrow WS_2 nanoribbon FETs open the platform for investigating electronic properties of edge structures in TMDs^{20,37} and the development of unique nanoscale devices.

Methods

First, WS_2 flakes were mechanically exfoliated from bulk crystals (Hq-graphene) onto SiO_2/Si substrate using the Scotch-tape method, and multilayer flakes were identified by their optical contrast on the Si/SiO_2 substrate (the thickness of SiO_2 is 285 nm). We performed reactive ion and chemical wet etching techniques to fabricate the nanoribbons with zig-zag edges as described in ref ¹⁹. For making nanoribbon WS_2 field-effect transistors (FETs), we prepared contacts of Ti (20 nm)/Au (90 nm) by standard electron beam lithography, electron beam evaporation, and lift-off technique. The $SiO_2/n-Si$ is used as a gate to control the carrier concentration in the WS_2 channel. The measured nanoribbon WS_2 FET is of width ~18-70 nm, thickness 35 nm, and channel length of ~600-800nm. The electrical transport measurements were carried out in a cryostat with variable temperatures. Keithley 2612B dual-channel source meter is used to apply V_{ds} , V_{gs} , and measure I_{ds} .

Acknowledgments

The authors acknowledge financial support from 2D TECH VINNOVA competence center (No. 2019-00068), EU Graphene Flagship (Core 3, No. 881603), Swedish Research Council VR project grants (No. 2021-04821), FLAG-ERA project 2DSOTECH (VR No. 2021-05925), Graphene center, EI Nano, and AoA Materials program at Chalmers University of Technology.

References

1. Salahuddin, S., Ni, K. & Datta, S. The era of hyper-scaling in electronics. *Nat. Electron.* **1**, 442–450 (2018).
2. Lundstrom, M. Applied physics: Moore's law forever? *Science* **299**, 210–211 (2003).
3. Avsar, A. *et al.* Optospintronics in Graphene via Proximity Coupling. *ACS Nano* **11**, 11678–11686 (2017).
4. Wu, F. *et al.* Vertical MoS₂ transistors with sub-1-nm gate lengths. *Nature* **603**, 259–264 (2022).
5. Sebastian, A., Pendurthi, R., Choudhury, T. H., Redwing, J. M. & Das, S. Benchmarking monolayer MoS₂ and WS₂ field-effect transistors. *Nat. Commun.* **2021** *12* **12**, 1–12 (2021).
6. Daus, A. *et al.* High-performance flexible nanoscale transistors based on transition metal dichalcogenides. *Nat. Electron.* **2021** *4* **4**, 495–501 (2021).
7. Li, N. *et al.* Large-scale flexible and transparent electronics based on monolayer molybdenum disulfide field-effect transistors. *Nat. Electron.* **2020** *3* **3**, 711–717 (2020).
8. Das, S. *et al.* Transistors based on two-dimensional materials for future integrated circuits. *Nat. Electron.* **2021** *4* **4**, 786–799 (2021).
9. Chhowalla, M., Jena, D. & Zhang, H. Two-dimensional semiconductors for transistors. *Nat. Rev. Mater.* **2016** *1* **1**, 1–15 (2016).
10. Akinwande, D. *et al.* Graphene and two-dimensional materials for silicon technology. *Nat.* **2019** *573* **7775** **573**, 507–518 (2019).
11. Zhang, F., Lee, C. H., Robinson, J. A. & Appenzeller, J. Exploration of channel width scaling and edge states in transition metal dichalcogenides. *Nano Res.* **2018** *11* **11**, 1768–1774 (2018).
12. Xu, K. *et al.* Sub-10 nm Nanopattern Architecture for 2D Material Field-Effect Transistors. *Nano Lett.* **17**, 1065–1070 (2017).
13. Chen, S. *et al.* Monolayer MoS₂ Nanoribbon Transistors Fabricated by Scanning Probe Lithography. *Nano Lett.* **19**, 2092–2098 (2019).
14. Jiang, J. *et al.* Ultrashort Vertical-Channel van der Waals Semiconductor Transistors. *Adv. Sci.* **7**, (2020).
15. Desai, S. B. *et al.* MoS₂ transistors with 1-nanometer gate lengths. *Science* (80-.). **354**, 99–102 (2016).
16. Chen, M. L. *et al.* A FinFET with one atomic layer channel. *Nat. Commun.* **2020** *11* **11**, 1–7 (2020).
17. Kotekar-Patil, D., Deng, J., Wong, S. L., Lau, C. S. & Goh, K. E. J. Single layer MoS₂ nanoribbon field effect transistor. *Appl. Phys. Lett.* **114**, 013508 (2019).
18. Liu, H., Gu, J. & Ye, P. D. MoS₂ nanoribbon transistors: Transition from depletion mode to enhancement mode by channel-width trimming. *IEEE Electron Device Lett.* **33**, 1273–1275 (2012).
19. Munkhbat, B. *et al.* Transition metal dichalcogenide metamaterials with atomic precision. *Nat. Commun.* **2020** *11* **11**, 1–8 (2020).
20. Ridolfi, E., Lima, L. R. F., Mucciolo, E. R. & Lewenkopf, C. H. Electronic transport in disordered MoS₂ nanoribbons. *Phys. Rev. B* **95**, 035430 (2017).
21. Kotekar-Patil, D., Deng, J., Wong, S. L. & Goh, K. E. J. Coulomb Blockade in Etched Single- And Few-Layer MoS₂ Nanoribbons. *ACS Appl. Electron. Mater.* **1**, 2202–2207 (2019).
22. Stankiewicz, J., Sesé, J., Balakrishnan, G. & Fisk, Z. Electrical transport properties of WS₂. *Phys. Rev. B - Condens. Matter Mater. Phys.* **90**, 8174–8181 (2014).
23. Chen, J.-R. *et al.* Control of Schottky Barriers in Single Layer MoS₂ Transistors with Ferromagnetic Contacts. *Nano Lett.* **13**, 3106–3110 (2013).
24. Dankert, A., Langouche, L., Kamalakar, M. V. & Dash, S. P. High-performance molybdenum disulfide field-effect transistors with spin tunnel contacts. *ACS Nano* **8**, 476–482 (2014).
25. Das, S., Chen, H. Y., Penumatcha, A. V. & Appenzeller, J. High performance multilayer MoS₂ transistors with scandium contacts. *Nano Lett.* **13**, 100–105 (2013).
26. Dankert, A. & Dash, S. P. Electrical gate control of spin current in van der Waals heterostructures at room temperature. *Nat. Commun.* **8**, 1–6 (2017).
27. Kroell, K. E. & Ackermann, G. K. Threshold voltage of narrow channel field effect transistors. *Solid State Electron.* **19**, 77–81 (1976).
28. Abbas, K. *Handbook of Digital CMOS Technology, Circuits, and Systems. Handbook of Digital CMOS Technology, Circuits, and Systems* (Springer International Publishing, 2020). doi:10.1007/978-3-030-37195-1
29. Radisavljevic, B. & Kis, A. Mobility engineering and a metal–insulator transition in monolayer MoS₂. *Nat. Mater.* **2013** *12* **12**, 815–820 (2013).
30. Patil, P. D. *et al.* Gate-Induced Metal-Insulator Transition in 2D van der Waals Layers of Copper Indium Selenide Based Field-Effect Transistors. *ACS Nano* (2019). doi:10.1021/acsnano.9b06846
31. Moon, B. H. *et al.* Anomalous conductance near percolative metal-insulator transition in monolayer

- MoS2 at low voltage regime. *ACS Nano* **13**, 6631–6637 (2019).
32. Chen, X. *et al.* Probing the electron states and metal-insulator transition mechanisms in molybdenum disulphide vertical heterostructures. *Nat. Commun.* **6**, 1–8 (2015).
 33. Ho, L. H., Micolich, A. P., Hamilton, A. R. & Sushkov, O. P. Ground-plane screening of Coulomb interactions in two-dimensional systems: How effectively can one two-dimensional system screen interactions in another. *Phys. Rev. B - Condens. Matter Mater. Phys.* **80**, 155412 (2009).
 34. Laturia, A., Van de Put, M. L. & Vandenberghe, W. G. Dielectric properties of hexagonal boron nitride and transition metal dichalcogenides: from monolayer to bulk. *npj 2D Mater. Appl.* **2018** **2**, 1–7 (2018).
 35. Ghatak, S., Pal, A. N. & Ghosh, A. Nature of electronic states in atomically thin MoS2 field-effect transistors. *ACS Nano* **5**, 7707–7712 (2011).
 36. Muchharla, B., Narayanan, T. N., Balakrishnan, K., Ajayan, P. M. & Talapatra, S. Temperature dependent electrical transport of disordered reduced graphene oxide. *2D Mater.* **1**, 011008 (2014).
 37. Li, Y., Zhou, Z., Zhang, S. & Chen, Z. MoS2 nanoribbons: High stability and unusual electronic and magnetic properties. *J. Am. Chem. Soc.* **130**, 16739–16744 (2008).

